Assessment and control of transition to turbulence in plane Couette flow

Anton Pershin
University of Leeds
School of Mathematics

Submitted in accordance with the requirements for the degree of
Doctor of Philosophy
June, 2020

Intellectual Property Statement

The candidate confirms that the work submitted is his own, except where work which has formed part of jointly authored publications has been included. The contribution of the candidate and the other authors to this work has been explicitly indicated below. The candidate confirms that appropriate credit has been given within the thesis where reference has been made to the work of others.

The work in Chapter 4 of the thesis has appeared in publication as follows:

- Anton Pershin, Cédric Beaume, and Steven M Tobias. Dynamics of spatially localized states in transitional plane Couette flow. *Journal of Fluid Mechanics*, **867**:414–437, 2019.

The work in Chapter 6 of the thesis has appeared in publication as follows:

- Anton Pershin, Cédric Beaume, and Steven M Tobias. A probabilistic protocol for the assessment of transition and control. *Journal of Fluid Mechanics*, **895**:A16, 2020.

The candidate was responsible for writing the papers, designing and performing research, writing the relevant code and analysing the data whose summaries were presented on regular meetings. The contribution of the other authors was in designing research, analysing the summary results and writing the paper.

Acknowledgements

First and foremost, I would like to thank sincerely my supervisors, Cédric Beaume and Steve Tobias, who has opened to me a fascinating subject of transition to turbulence and taught me how to be a scientist. It is clear that this thesis would not be possible without their guidance and their strong support and belief in me which has often induced the actions far beyond their duties. One can barely find a thought in this thesis not inspired by our thought-provoking discussions.

I would also like to thank all the researchers I have met during this scientific voyage and who have undoubtedly influenced this work: Peter Ashwin, Adrian Barker, Dwight Barkley, Mat Chantry, Predrag Cvitanović, Tom Eaves, Chris Jones, Mark Kelmanson, Rich Kerswell, Edgar Knobloch, Moritz Linkmann, Valerio Lucarini, Paul Manneville, Tobias Schneider, Benoît Semin, Jan Sieber, Priya Subramanian, Yue-Kin Tsang, Laurette Tuckerman, Jonathan Ward. In particular, I am indebted to John Gibson who gave the community his amazing code Channelflow.

I am very grateful to my family and my wife's family who have supported me throughout my years as a PhD student. Finally, I am thankful to my wife, Liza, for the fact of her existence: you are a lucky disturbance of the flow of my life.

Abstract

Transition to turbulence in shear flows is a puzzling problem regarding the motion of fluids flowing, for example, through the pipe (pipe flow), as in oil pipelines or blood vessels, or confined between two counter-moving walls (plane Couette flow). In this kind of flows, the initially laminar (ordered and layered) state of fluid motion is linearly stable, but turbulent (disordered and swirling) flows can also be observed if a suitable perturbation is imposed. This thesis concerns the assessment of transitional properties of such flows in the uncontrolled and controlled environments allowing for the quantitative comparisons of control strategies aimed at suppressing or trigerring transition to turbulence. Efficient finite-amplitude perturbations typically take the form of small patches of turbulence embedded in the laminar flow and called turbulent spots. Using direct numerical simulations, the nonlinear dynamics of turbulent spots, modelled as exact solutions, is investigated in the transitional regime of plane Couette flow and a detailed map of dynamics encompassing the main features found in transitional shear flows (self-sustained cycles, front propagation and spot splitting) is built. The map represents a quantitative assessment of transient dynamics of turbulent spots as a dependence of the relaminarisation time, i.e. the time it takes for a finite-amplitude perturbation, added to the laminar flow, to decay, on the Reynolds number and the width of a localised perturbation. By applying a simple passive control strategy, sinusoidal wall oscillations, the change in the spot dynamics with respect to the amplitude and frequency of the wall oscillations is assessed by the re-evaluation of the relaminarisation time for few selected localised initial conditions. Finally, a probabilistic protocol for the assessment of transition to turbulence and its control is suggested. The protocol is based on the calculation of the laminarisation probability, i.e. the probability that a random perturbation decays as a function of its energy. It is used to assess the robustness of the laminar flow to finite-amplitude perturbations in transitional plane Couette flow in a small computational domain in the absence of control and under the action of sinusoidal wall oscillations. The protocol is expected to be useful for a wide range of nonlinear systems exhibiting finite-amplitude instability.

Contents

List of Figures

List of Tables

Chapter 1

Introduction

In 1884, Osborne Reynolds, a British physicist from the University of Manchester, postulated a still unanswered question: what the conditions are under which the flow is inevitably laminar or sinuous. He conducted an experiment with a coloured streak of fluid immersed in clean water flowing through a long pipe [3] and speculated that the phase transition from the laminar regime to turbulent one may occur when a non-dimensional parameter, now known as Reynolds number, reaches a particular value:

$$Re = \frac{\rho U d}{\mu}, \tag{1.1}$$

where ρ is the density of the fluid, μ is the dynamic viscosity of the fluid, U is the mean streamwise velocity of the flow and d is the diameter of the pipe. He also managed to recognise that even if this hypothesised critical value is crossed, the laminar regime of the flow possesses, in his words, «residual stability» so one needs to impose certain finite-amplitude disturbances to trigger transition to turbulence. Therefore, there are at least two crucial parameters describing transition to turbulence: the Reynolds number and the form of finite-amplitude disturbances. Since then, many researchers have participated in developing our understanding of transition to turbulence and formed different approaches to this problem.

This thesis aims at contributing into the field by considering exact localised solutions and random states as finite-amplitude disturbances in another shear flow – plane Couette flow. It is a three-dimensional viscous flow confined between two parallel walls moving in opposite directions as shown in figure 1.1. It is governed by the Navier–Stokes equation

$$\partial_t \boldsymbol{U} + (\boldsymbol{U} \cdot \nabla)\boldsymbol{U} = -\nabla P + \frac{1}{Re}\nabla^2 \boldsymbol{U}, \tag{1.2}$$

where $\boldsymbol{U} = [U, V, W](t, x, y, z)$ is the velocity field, P is a scalar pressure field and Re is Reynolds number. The equation is non-dimensionalised by the speed of the walls U_{walls} and the gap $2h$ between them. The Reynolds number for plane Couette flow is defined as

$$Re = \frac{U_{walls} h}{\nu}, \tag{1.3}$$

where ν is the kinematic viscosity of fluid.

The Navier–Stokes equation is accompanied with the incompressibility condition:

$$\nabla \cdot \boldsymbol{U} = 0. \tag{1.4}$$

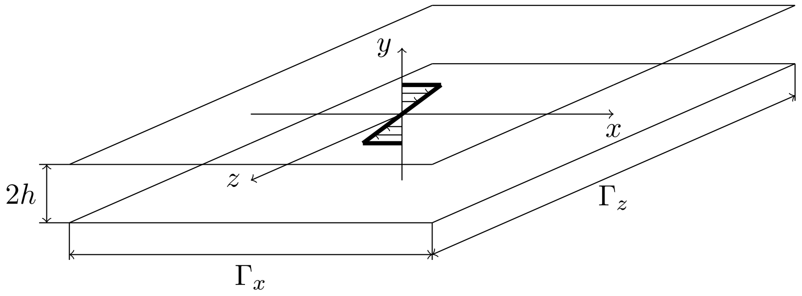

Figure 1.1: The layout of the domain for plane Couette flow and the laminar profile (bold black lines). Two parallel walls are separated from each other by the gap $2h$ and move along the x-direction with the fixed speed U_{walls}. Γ_x and Γ_z are streamwise and spanwise wavelengths of the domain respectively.

We call the x, y, z-directions the streamwise, wall-normal and spanwise directions respectively. To suit computational purposes, periodic boundary conditions are imposed in the streamwise and spanwise directions:

$$\boldsymbol{U}(t,x,y,z) = \boldsymbol{U}(t,x+\Gamma_x,y,z+\Gamma_z) \tag{1.5}$$

where Γ_x and Γ_z are corresponding wavelengths of the domain.

In the wall-normal direction, no-slip boundary conditions are used:

$$\boldsymbol{U}|_{y=-1} = [-1,0,0], \tag{1.6}$$

$$\boldsymbol{U}|_{y=1} = [1,0,0]. \tag{1.7}$$

Plane Couette flow possesses a simple laminar solution: a parallel flow with only one non-zero component of the velocity field and no pressure gradient:

$$\boldsymbol{U_{lam}} = [y,0,0], \tag{1.8}$$

$$P_{lam} = const. \tag{1.9}$$

In order to investigate the instability of the laminar state, the flow is decomposed into a base state (laminar profile) $\boldsymbol{U_{lam}}$ and a departure from it (fluctuations around the laminar state) $\boldsymbol{u} = [u,v,w](t,x,y,z)$ [4]:

$$\boldsymbol{U} = \boldsymbol{U_{lam}} + \boldsymbol{u}. \tag{1.10}$$

It is trivial to show that $\boldsymbol{u}$ satisfies the incompressibility condition (1.4). Substituting (1.10) into the Navier–Stokes equation (1.2) yields

$$\partial_t \boldsymbol{u} + v\boldsymbol{e}_x + y\partial_x \boldsymbol{u} + (\boldsymbol{u}\cdot\nabla)\boldsymbol{u} = -\nabla p + \frac{1}{Re}\nabla^2 \boldsymbol{u}, \tag{1.11}$$

$$\nabla\cdot\boldsymbol{u} = 0. \tag{1.12}$$

where $\boldsymbol{e}_x$ is a unit vector in the x-direction and v is the wall-normal component of the departure. They constitute the governing equations for the departure and hereafter we concentrate our attention on their dynamics unless we mention explicitly the full flow field.

Below we give an introduction into the field of transition to turbulence in subcritical shear flows in general and, whenever it is possible, mention the results regarding plane Couette flow.

1.1 Transition to turbulence: dynamical systems viewpoint

1.1.1 Routes to chaos

From the dynamical systems viewpoint, the laminar state is merely a fixed point attracting or repelling the flow depending on its stability. It is then reasonable to propose that the Reynolds number is a parameter in the dynamical Navier–Stokes equations and that the flow becomes turbulent when the laminar state, being linearly stable at low Reynods number, loses its stability at some critical Reynolds number Re_c. This idea, dated back to Stokes and Reynolds, was explored by Landau in 1944 [5] and Hopf in 1948 [6] to develop the first attempt to mathematically resolve the question about transition to turbulence. They suggested that the flow undergoes a sequence of Hopf-type bifurcations as Re is increased so that it becomes a quasi-periodic flow on a hypertorus and, therefore, contains of a large spectrum of independent frequencies which can be characterised as a turbulent state. However, Ruelle and Takens in 1971 showed that vector fields on tori of dimension three or higher have strange attractors on them [7] and, thus, claimed that the Landau–Hopf scenario is likely to end up with a strange attractor beyond three bifurcations.

Another scenario of transition known as *period-doubling* was developed by Feigenbaum in 1978 for a class of one-dimensional maps [8]. In this scenario, as a parameter is increased, the system undergoes a sequence of flip bifurcations such that, at the n-th bifurcation, a 2^{n-1}-cycle transforms into a 2^n-cycle and the sequence ends up with an aperiodic 2^∞-cycle where a k-cycle denotes a periodic orbit with the period of k iterations. This period-doubling cascade, accompanied with the universal constant of the convergence rate of bifurcations points, was indeed experimentally found in fluid systems such as Rayleigh–Bénard convection at low Prandtl numbers [9] and recently plane Couette flow for the upper Nagata solution branch [10]. In addition to the temporal period-doubling, a spatial period-doubling cascade has been recently experimentally observed in thin films made of ferroelastic materials [11].

A transition from a stable cycle was investigated by Pomeau and Manneville in 1980 in the context of the Lorenz system [12]. They found that the flow near the saddle-node bifurcation still exhibits a cyclic motion interrupted by windows of chaotic motion. As the control parameter moves farther from the saddle-node bifurcation, the chaotic windows last longer on average until their duration becomes infinite. This transition scenario, called the *intermittency route to chaos*, appeared to be a widespread phenomenon in many dynamical systems including Rayleigh–Bénard convection at high Prandtl numbers [13].

All these scenarios rely on the instability of base state (i.e. laminar state in shear flows or conductive state in convection) at some value of the control parameter of the system (e.g., the Reynolds number or the Rayleigh number). As the instability sets in, one of the scenarios may occur and lead to a chaotic attractor. However, they cannot be valid if the base state does not lose stability or loses it too far away from the point where the actual transition is observed. In this case, the transition to a chaotic state is *subcritical* and the corresponding flows are called *subcritical transitional flows*. Subcritical transition implies that not only parameter value must be large enough, but also finite-amplitude perturbations must be added to the laminar state in order for the flow to become turbulent. Therefore, the question of transition now turns to the question of finding appropriate perturbations.

Owing to their simplicity and industrial applicability, the following shear flows are usually used to investigate the subcritical transition to turbulence:

- *plane Couette flow* – shear-driven flow between two infinite plates moving in opposite directions;
- *plane Poiseuille flow* – pressure-driven flow between two infinite stationary par-

allel plates;

- *pipe flow (Hagen–Poiseuille flow)* – pressure-driven flow through an infinite cylindrical tube.

Plane Couette flow and pipe flow have linearly stable laminar states for all Reynolds number Re [14, 15] whereas turbulence can be sustained beyond $Re \approx 325 \pm 5$ [16] and $Re \approx 2040 \pm 10$ [17] respectively. In plane Poiseuille flow, the laminar state loses stability at a subcritical bifurcation at $Re \approx 5772$ [18] but sustained turbulence is obtained at Reynolds numbers as low as $Re \approx 830$ [19]. Nonlinear stability analysis based on the energy method, in turn, underestimates the critical Reynolds number and predicts the onset of instability of two-dimensional perturbations at $Re \approx 44.3$ (see [20] for a brief discussion and the latest results).

Even though the scenarios mentioned above may occur in these flows, they no longer describe the primary transition to turbulence. Thus, different ideas must be utilised to investigate the transition. It was first noticed that perturbations of the laminar state may exhibit transient algebraic growth due to the non-normality of the linearised operator of the Navier–Stokes equation (i.e., of the operator of the Orr–Sommerfeld/Squire system of equations in parallel flows) in spite of the linear stability of the laminar state (see [4] for details). It was then shown that this primary growth of the optimally chosen two-dimensional perturbations leads to their development into a flow pattern consisting of alternating streamwise vortices (*rolls*) and high-velocity *streaks* [21]. The resulting state is speculated to exhibit three-dimensional *secondary instabilities* which finally sends the flow to turbulent state [4]. Notwithstanding that this mechanism demonstrates how the flow can depart from a linearly stable laminar state, rigorous analysis of the secondary instability appears to be challenging.

1.1.2 Exact coherent states

As already said, the linear stability of the laminar state prevents us from considering bifurcation scenarios arising from it. However, one can speculate that transition to turbulence and the subsequent emergence of the chaotic attractor, which is often called the turbulent attractor in the literature, may occur due to the bifurcations of another non-laminar solution of the Navier–Stokes equations. It is clear that this solution is nonlinear. This has motivated a large body of research aiming at the numerical search for nonlinear solutions of the Navier–Stokes equations. Another attractive motivation stands from viewing a turbulent flow as a trajectory in phase space wandering between the saddle-type invariant sets[1] guided by their stable and unstable manifolds [22]. The simplest examples of such invariant sets are equilibria, travelling waves (i.e., equilibria under an appropriate Galilean transformation), periodic orbits and relative periodic orbits (i.e., periodic orbits under an appropriate Galilean transformation). These invariant sets have often been observed to replicate turbulent coherent structures, such as streak-roll pairs, found in numerical and experimental studies and, thus, were given a name of *exact coherent structures*[2] to emphasise that they are free of intermittent features of turbulent flow states and are exact (up to the available numerical accuracy) solutions of the Navier–Stokes equations [23]. For roughly 30 years, computing invariant numerical solutions has become a separate branch of computational fluid dynamics which has given many very promising results.

The first finite-amplitude solution in plane Couette flow was obtained by Nagata in 1990 [24]. Instead of directly looking for solutions in plane Couette flow, he considered Taylor–Couette flow in a narrow gap limit, i.e. plane Couette flow in a rotating frame of reference. This flow is known to display a supercritical scenario of transition to turbulence. There, the laminar state loses stability to the *Taylor vortex flow* made of counter-rotating toroidal vortices periodic in the direction of the cylinders axis. Nagata managed to show that the Taylor vortex flow bifurcates to a steady three-dimensional solution which was continued down to zero rotation rate corresponding to plane Couette flow. By a similar procedure, Clever and Busse in 1992 rediscovered this solution using Rayleigh–Bénard convection coupled with plane Couette flow [25]. In their case, numerical continuation was done for the wavy rolls down to zero Rayleigh number. In plane Couette flow, the found solutions form two branches now known as *lower and upper Nagata branches*. Figure 1.2 shows the lower and upper Nagata solutions for domain $\frac{32}{15}\pi \times 2 \times 4\pi$. In small periodic boxes, the lower Nagata branch solutions and the states structurally similar to them were later found to play a crucial role in transition to turbulence: their stable manifolds act as a boundary between the basin of attraction of the laminar state and turbulent saddle [26, 27].

---

[1] An invariant set is such a subset of the phase space that for each initial condition belonging to the invariant set, a trajectory emanating from it will stay in the invariant set forever.

[2] Terms "exact coherent structures", "exact coherent states" and "exact coherent solutions" are often interchangeable in the literature.

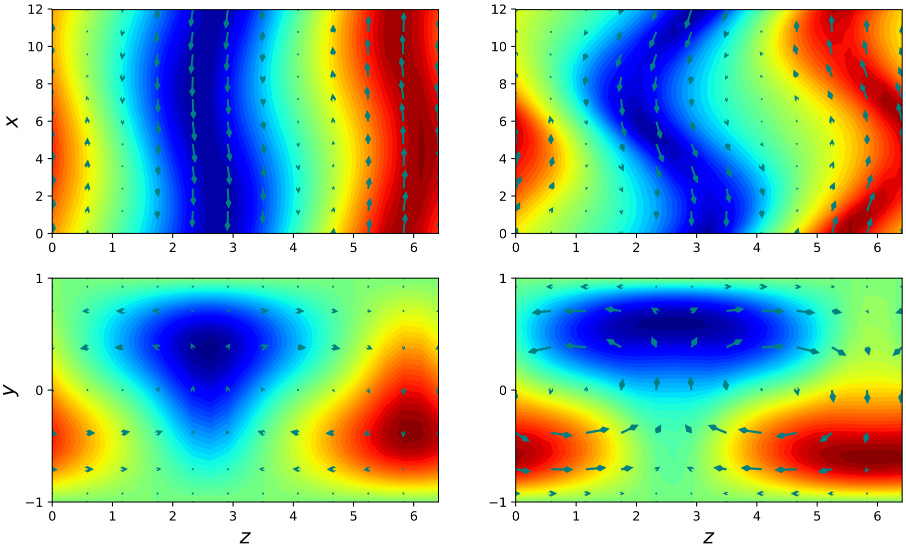

Figure 1.2: Lower Nagata solution at $Re \approx 202.278$ (left column) and upper Nagata solution at $Re \approx 202.297$ (right column). The contours show the streamwise component of the velocity fields. The arrows show the in-plane components on the y-averaged plane (top panels) and x-averaged plane (bottom panels).

A parallel branch of research was related to the mechanism by which a fixed spacing between the near-wall streaks is supported. Hamilton *et al.* [28], equipped by the minimal flow unit concept explored by Jiménez and Moin in 1991 [29], managed to reduce the violent dynamics of near-wall turbulence down to a relatively simple *regeneration cycle* by dynamically decreasing the Reynolds number. The regeneration cycle they found consisted of three subsequent steps:

1. formation of the streaks with a mild streamwise variation;
2. magnification of the streaks streamwise waviness;
3. breakdown of the streaks and their reconstruction.

A reduced model, encompassing all the ingredients of the regeneration cycle, was then built by Waleffe in 1997 [30]. It was derived using a reduction of what is now called Waleffe flow, i.e., the parallel shear flow with a sinusoidal body forcing and stress free boundary conditions, which is closely related to plane Couette flow [31–33]. The reduced model uncovered the mechanism named the *self-sustained process*: it describes the three phases of the regeneration cycle as a balance between the linear and non-linear terms associated with streaks, rolls and their fluctations. This balance allows for the existence of a certain class of non-linear equilibria now called the *SSP states*. Later, these non-linear equilibria were indeed numerically calculated in plane Couette flow and plane Poiseuille flow for various boundary conditions using a homotopy from Waleffe flow [34, 35]. Remarkably, they appeared to be the Nagata solutions for plane Couette flow. However, as was shown later, the Nagata solutions are not completely described by the self-sustained process. Indeed, only the lower Nagata branch solutions were shown to have the same scalings as the states obeying the self-sustained process [26]. Exact coherent states, obeying the scalings of the self-sustained process, were investigated in details by Beaume *et al.* in the context of Waleffe flow [32, 36].

Since the first discoveries of nonlinear equilibria in plane Couette flow, many other exact coherent solutions have been found. A number of equilibria and travelling waves (relative equilibria) was calculated by Schmiegel [37], Nagata [38], Waleffe [23, 35], Gibson *et al.* [39] and others. The heteroclinic connections between some of the equilibria, including the connection between lower and upper Nagata solutions, were found by Halcrow *et al.* [40]. Nonlinear solutions have been discovered in other shear flows (see [41] for a detailed review).

The first periodic orbits in plane Couette flow were calculated by Kawahara and Kida in 2001 in the minimal flow unit [42]. Exploiting the recurrent nature of the turbulent flows, they converged a recurrent turbulent trajectory to a periodic orbit whose dynamics repeats that of the regeneration cycle [28]. Moreover, the mean and RMS velocity of this periodic orbit compared remarkably well against the turbulent data. Another found periodic orbit was shown to bifurcate from the lower Nagata branch with respect to the decrease in the streamwise domain wavelength. A heteroclinic connection between the former and latter periodic orbits were linked to the bursting phenomenon. Given the importance of the lower Nagata branch for transition to turbulence, this fact can be interpreted as follows: transition to turbulence occurs via a bursting event. Later in 2007, Viswanath linked the bursting phenomenon to a set of periodic and relative periodic orbits embedded in the turbulent saddle [43]. Recurrent flow analysis was used by Cvitanović and Gibson in 2010 to calculate even more periodic orbits [44]. In this paper, the authors also sketched a program of how periodic orbit theory can be applied to the low Reynolds number turbulence to retrieve its statistics [22]. Periodic orbit theory was later thoroughly tested for the two-dimensional turbulence in Kolmogorov flow by Chandler and Kerswell in 2013 [45] and further by Lucas and Kerswell in 2015 [46] who showed that it requires a very large dataset of recurrent flows for reasonably good results and, thus, may be challenging to apply to the three-dimensional fluid systems. A remarkable period-doubling cascade at very low Reynolds numbers ($179 \lesssim Re \lesssim 188$) was presented by Kreilos and Eckhardt in 2012 [10]. For a nearly minimal flow unit and a symmetry-reduced phase space, the stable upper Nagata branch was shown to have a Hopf bifurcation giving rise to a stable periodic orbit which further undergoes period doubling. The periodic doubling cascade results in a chaotic attractor which becomes a chaotic saddle[1] through a boundary crisis.

One can notice that the aforementioned solutions have been discovered in relatively small domains which do not allow for spatial localisation. In plane Couette flow, spatially localised solutions were discovered using the technique known as *edge tracking*. Its description requires to discuss first the concept of *edge of chaos* which is of great importance for the understanding of transition to turbulence in shear flows.

1.1.3 Edge of chaos

In chaos theory, chaotic trajectories usually approach an attracting invariant set known as the *strange attractor*. It is then natural to suspect that turbulence is merely a strange attractor which, in shear flows, coexists with the stable laminar fixed point. Therefore, a particular finite-amplitude perturbation will be sent to turbulence if it lies in the basin of attraction of the strange attractor. Consequently, a well-defined (possibly fractal) boundary between the two basins of attraction exist. Transition to turbulence, however, appeared to be slightly more complicated than that. First of all, it was numerically shown by Schmiegel and Eckhardt in 1997 that turbulent flows in plane Couette flow spontaneously decay at low *Re* and, thus, have finite lifetimes [47]. Increasing the Reynolds number leads to increasing their lifetime, so the authors speculated that turbulence at a low Reynolds number is, in fact, imitated by these long-lasting transients.

---

[1] In the literature, turbulence associated with a chaotic saddle is often called "leaky" owing to the fact that a trajectory may be attracted by the chaotic saddle for a long, but only finite, time and must eventually approach a global attractor which is a laminar fixed point in shear flows.

Extensive experiments conducted by Hof *et al.* [48, 49] and numerical investigation by Avila *et al.* [17] confirmed this view for the case of pipe flow for transitional Reynolds numbers. It means that turbulence at low Reynolds number is rather confined to the strange saddle, not an attractor (it is however still "strange" due to the high sensitivity to initial conditions), which is dynamically connected to the laminar fixed point. In other words, the laminar state is highly likely a global attractor at low Reynods numbers even though turbulence can be sustained for very long time intervals. Consequently, the boundary between the chaotic saddle and the laminar fixed point cannot be defined in terms of their basins of attraction, so a different definition for partitioning is needed. It was introduced by Skufca *et al.* in 2006 [50] and arises from the concept of the *edge of chaos*, a manifold locally separating initial conditions resulting in quickly decaying trajectories from those resulting in long-lived ones. The authors investigated the edge of chaos for a 9-dimensional model of a shear flow, developed by Schmiegel in [37] and having transitional properties corresponding to plane Couette flow, and showed that the edge of chaos can be detected by measuring the lifetimes of the trajectories emanating from the parametrised initial conditions. For instance, one can sample a large number of initial conditions from the formula $\boldsymbol{u}_c = c\boldsymbol{u}_{turb}$, where $\boldsymbol{u}_{turb}$ is a turbulent initial condition, $c \in [0; 1]$ and $c = 0$ recovers the laminar fixed point. By measuring the lifetime as a function of c, one can find $\tilde{c}$ such that the trajectories emanating from $\boldsymbol{u}_c, c \lesssim \tilde{c}$ tend to the laminar fixed point, whereas the trajectories associated with $\boldsymbol{u}_c, c \gtrsim \tilde{c}$ become turbulent. The coefficient $\tilde{c}$ can in fact be found using the bisection method. A slightly more advanced approach, also introduced in [50], is now known as *edge tracking* – a bisection-like method for finding the trajectories confined to the edge of chaos. It was utilised by Skufca *et al.* to find periodic ($Re \lesssim 402$) and chaotic ($Re \gtrsim 402$) orbits which the edge trajectories converged to. By definition, these invariant sets have a 1-dimensional unstable manifold, one side of which is dynamically connected to the laminar fixed point and another points towards turbulence. As a result, the edge of chaos is formed by the codimension-1 stable manifold.

It must be mentioned that the edge does not divide phase space simply into laminar and turbulent subspaces, providing some isolated points for turbulent trajectories to relaminarise, but rather wraps around the chaotic saddle. The strong evidence for that was provided by Chantry and Schneider in 2014 for the edge in plane Couette flow in the small domain [51]. Therefore, the edge is dynamically connected to the chaotic

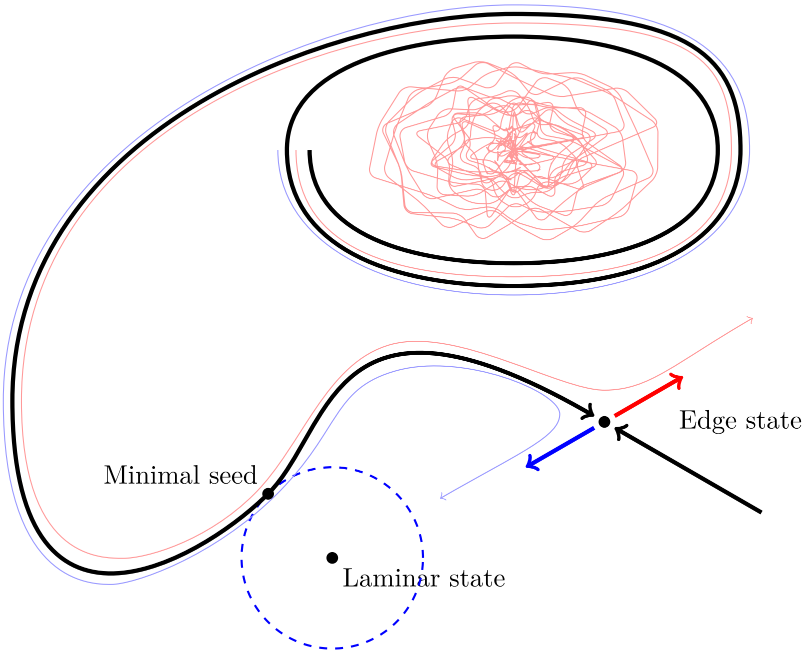

Figure 1.3: Illustration of the edge wrapped up around the turbulent saddle. Black and red/blue thick curves show stable and unstable manifolds of the edge state respectively. Blue and red thin curves illustrate laminarising and transitioning trajectories respectively. Dashed circle indicate the phase space segment where no perturbation resulting in a transitioning trajectory can be found.

saddle and is essentially a part of it which is illustrated by figure 1.3. Thus, the edge separates laminar trajectories from turbulent ones locally, but not globally.

Even though the definition of the edge of chaos was given rather informally, the edge tracking was powerful enough to be successfully used to explore the edge structure in many other flow configurations. In 2007, Schneider *et al.* used edge tracking to identify the chaotic edge trajectories lying on the laminar-turbulent boundary in pipe flow with a small streamwise extent [52]. The corresponding chaotic attractor was further analysed by Duguet *et al.* in 2008 [53] and Budanur and Hof in 2018 [54] and appeared to be built upon several travelling waves and the heteroclinic connections between them. The edge in plane Couette flow was investigated by Schneider *et al.* in 2008 [27] who identified the *edge states*, local attractors on the edge of chaos having only one unstable direction orthogonal to the edge. There, all edge trajectories were attracted by an equilibrium which is structurally the same as the lower Nagata branch solution shown in figure 1.2, but having doubled spanwise spatial period. Given the results by Wang *et al.* [26], it was concluded that the lower branch solution is the edge state only when it is once unstable. A step towards external flows was done by Cherubini *et al.* in 2011 who analysed the edge of chaos in boundary layers [55]. They showed that the approached edge states depend on the initial disturbances used in the edge tracking procedure: linearly optimal disturbances lead to an edge state dominated by streaks, whereas nonlinearly optimal disturbances lead to an edge state dominated by hairpin vortices. In addition, the latter edge state was found to have the lower energy compared to the former one. These results were extended by Duguet *et al.* by introducing a wider domain which allowed the discovery of a nearly periodic and fully localised edge state [56]. However, the spatial development of the boundary layer makes the closer investigation of the edge states computationally demanding. The typical way to suppress the spatial development is to consider the asymptotic suction boundary layer (ASBL). In 2013, Kreilos *et al.* investigated the edge state for ASBL which appeared to be a periodic orbit exhibiting slow-fast dynamics whose “fast” part corresponds to the bursting event [57]. By homotopy from plane Couette flow to ASBL, they also showed that this periodic orbit is born via a saddle-node infinite-period bifurcation of the edge state in plane Couette flow and the associated upper branch solution. Spatially localised counterparts of this periodic orbit were discovered by Khapko *et al.* in 2013 by considering a large enough spanwise extension of the domain [58]. The resulting edge states were periodic for relatively large streamwise spatial periods ($L_x \gtrsim 5\pi$) and chaotic for more confined domains. Eventually, fully localised chaotic edge states were identified by Khapko *et al.* in 2016 [59]. It was explicitly shown that the edge states are directly relevant to transition to turbulent boundary layers from small random perturbations [59, 60]. The formation of turbulent spots from noisy perturbations was explained as sliding along the stable manifold of the edge state, whereas the following nucleation of the turbulent spot was linked to the dynamics on the unstable manifold of the edge state.

In internal flows, such as pipe and plane Couette flows, the edge states in spatially extended domains also appear to be spatially localised. The study of the edge in a long enough pipe, carried out by Mellibovsky *et al.* in 2009, showed that the edge states in their domain correspond to localised puffs whose length does not depend on the Reynolds number [61]. For plane Couette flow, independent studies by Schneider *et al.* [62] and Duguet *et al.* [63] revealed the spatial localisation of the edge states in both spanwise-extended and doubly extended domains. Remarkably, the edge states in domains extended only in the spanwise direction are equilibria and travelling waves of the Navier–Stokes equation and can be numerically continued down in Re. Later, such continuation resulted in a discovery of the *homoclinic snaking* of the localised equilibria and travelling waves in plane Couette flow [64] which will be discussed further. A similar study allowed for the identification of the localised edge states in the form of periodic and relative periodic obrits in plane Poiseuille flow [65].

The attractive idea of the edge of chaos has spread out of the area of classical shear flows. The edge states have been recently identified in Taylor–Couette flow in the presence of magnetic field [66], viscoelastic channel flow [67], spatially extended plasma model [68], tokamak plasma [69], Earth climate system [70], droplet break-up [71], Hall magnetohydrodynamic equations in the context of magnetic reconnection [72] and shell buckling [73].

1.1.4 Localisation phenomenon

The spatial localisation of the edge states calculated in sufficiently large domains gave a strong motivation to study transition to turbulence from these states. The importance of the localised states for transitional regimes of the flow had however been appreciated a long time before their discovery. In 1951, Emmons gave a description of so-called "turbulent spots" ("turbulent sources" in Emmons' words) – tiny turbulent patches observed in the water flowing over an inclined plate [74]. They appeared at unpredictable locations on the plate and their growth in time led to turbulence downstream. Given two directions of spatial localisation and the absence of advection of the spots, plane Couette flow provides a suitable framework to study this phenomenon. Following the similar studies in plane Poiseuille flow and boundary layers, Lundbladh and Johansson in 1991 numerically simulated the evolution of finite-amplitude localised perturbations into turbulent spots [75]. By assessing the rate of their growth as a function of Reynolds number and associating the critical Reynolds number with zero growth rate, they found the critical Reynolds number to be approximately $Re_c \approx 375$, which is fairly close to the currently accepted result ($Re_c = 325 \pm 5$). Soon after, these results were reinforced by the experimental studies of turbulent spots in 1992 done by two independent research groups: Tillmark and Alfredsson [76] and Daviaud *et al.* [77]. In both papers, the remarkably close critical Reynolds number was reported: $Re_c = 360 \pm 10$ in the first study and $Re_c = 370 \pm 10$ in the second one. Later in 1995, Dauchot and Daviaud paid attention to the amplitude of localised perturbation [16]. In their study, the critical amplitude, needed to trigger turbulence, appeared to diverge as Reynolds number tended $Re_c = 325 \pm 5$ from above which is now the accepted critical Reynolds number.

The spanwise growth of turbulent spots was experimentally investigated by Tillmark in 1995 who reinforced the idea of the growth by destabilising surrounding laminar fluid by spanwise travelling waves entertaining the streamwise streaks located at the spot edges [78]. The importance of the latter had already been appreciated in [75].

The aforementioned spanwise waves, destabilising the laminar flow on the fronts, appeared to be linked to the large-scale flow surrounding a turbulent spot. This fact was first appreciated by Schumacher and Eckhardt in 2001 who investigated Waleffe flow, a model of plane Couette flow, in a sufficiently large domain and identified a quadrupolar shape of the large-scale flow [79]. They found that the large-scale flow indeed seems to destabilise the laminar flow adjacent to a turbulent spot. However, the spanwise velocity of the large-scale flow is smaller than the speed of the spot fronts. They however speculated that suppression of the large-scale flow deactivates the front growth. This hypothesis appeared to be incorrect – as shown by Duguet *et al.*, the nucleation of streaks on the spot edges is stochastic when a domain, confined in the streamwise direction and thus preventing the large-scale flow, is considered. Several later studies demonstrated that the quadrupolar shape of the large-scale flow can be explained by the mere linear momentum and mass convervation: the large-scale streamwise outflow from the spot must be compensated by the spanwise inflow [80, 81]. The large-scale flow was also shown to advect the growing streaks so that the spot is formed as an oblique pattern [81]. One step towards the connection between turbulent spots and large-scale flow and dynamical systems theory was done via the discovery of doubly localised equilibria by Brand and Gibson in 2014 [82]. Later, Couliou and Monchaux experimentally confirmed the existence of the large-scale flow [83, 84] and showed that the streamwise growth of a spot occurs via the competition of the positive growth rate due to the large-scale flow, located inside of the spot, and the negative growth rate corresponding to the outer large-scale flow [85]. Another important question regards the range at which the large-scale flow may act. Most of the studies suggest that the large-scale flow decays exponentially in both streamwise and spanwise directions which implies a short-range interaction between spots [79, 82]. Nonetheless, using analytical argument derived from the Navier–Stokes equation with free-slip boundary conditions at the walls, Wang *et al.* showed that the exponential decay should exist only in the very vicinity of a turbulent spot whereas the decay is algebraic in the far-field [86]. In this case, the algebraic decay of the large-scale flow implies the existence of the long-range interaction between turbulent spots.

Particularly interesting phenomena can be observed when the large-scale flow is suppressed by considering a small streamwise spatial periodicity ($1.7\pi \lesssim \Gamma_x \lesssim 4.2\pi$) while keeping the spanwise periodicity large enough ($L_z \gtrsim 16\pi$) [64, 87]. As was already mentioned in the previous section, such a domain allows for branches of spatially localised equilibria and travelling waves interwined in a bifurcation pattern known as *homoclinic snaking* [88]. The prototype system for studying homoclinic snaking is the generalised Swift–Hohenberg equation with quadratic-cubic nonlinearity:

$$\partial_t u = ru - \left(q_c^2 + \partial_{xx}\right)^2 u + au^2 - bu^3, \tag{1.13}$$

where u depends on an infinite spatial coordinate x and time t, i.e. $u = u(x, t)$; r is the main control parameter and q_c, a and b are fixed coefficients (for example, they could be chosen as $q_c = 0.5, a = 0.41, b = 1$ following [2]). The same equation, but with cubic nonlinearity, was originally suggested by Swift and Hohenberg in 1977 as a model describing Rayleigh–Bénard convection near the onset of instability of the conductive state to convective rolls [89, 90]. One can show that equation (1.13) has a Lyapunov functional $F[u]$, i.e. this system does not permit existence of periodic orbits nor persistent chaotic behaviour, and all trajectories must approach equilibria. Thus, by taking $\partial_t u = 0$ in equation (1.13), we get the differential equation

$$ru - \left(q_c^2 + \partial_{xx}\right)^2 u + au^2 - bu^3 = 0. \tag{1.14}$$

Equation (1.14) has a trivial solution $u = 0$ which is called the homogeneous state. In the context of plane Couette flow, we can associate it with the laminar flow. The homogeneous state is stable for $r < 0$ and unstable for $r > 0$ (note that the laminar flow is stable for all Reynolds numbers in plane Couette flow [14]). When a is chosen appropriately, three branches bifurcate subcritically from the homogeneous state at $r = 0$: spatially periodic states (P), spatially localised states with a fixed spatial

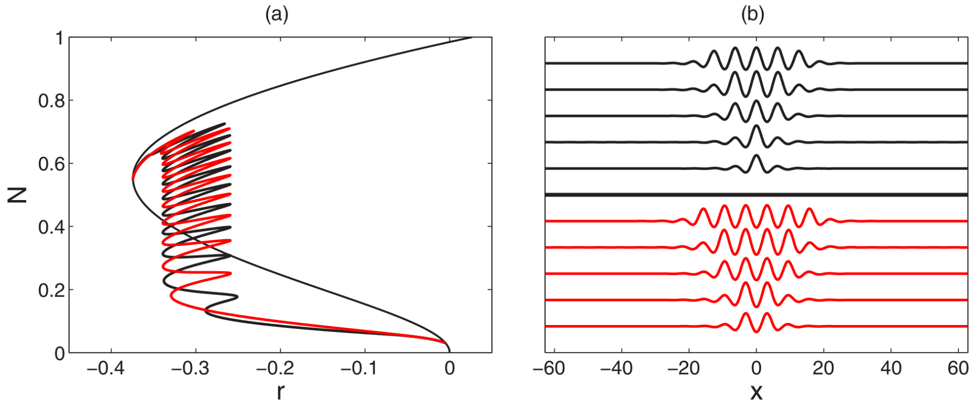

Figure 1.4: Bifurcation diagram showing homoclinic snaking in Swift–Hohenberg equation (a) and saddle-node states corresponding to the branches L_0 and L_π (b). The black/red colours correspond to L_0/L_π respectively. In panel (a), the thin black line stands for the branch of spatially periodic states P and N is the L_2 norm of u: $N = \left(\frac{1}{\Gamma}\int_{-\Gamma/2}^{\Gamma/2} u^2 dx\right)^{1/2}$, where Γ is the domain size. Taken from [1].

phase $\phi = 0$ (L_0) and spatially localised states with a fixed spatial phase $\phi = \pi$ (L_π). The states on these three branches have a reflection symmetry and the local maximum/minimum at $x = 0$ for L_0/L_π respectively as shown in figure 1.4(b). When continued down in $r < 0$, these branches undergo a series of saddle-node bifurcations which form a structure in the parameter space known as the homoclinic snaking and illustrated in figure 1.4(a). The region of r where the homoclinic snaking is located is called the *pinning region*.

In the context of the generalised Swift–Hohenberg equation, the homoclinic snaking was first investigated by Woods and Champneys in 1999 [91]. Later, Burke and Knobloch analysed the stability of these localised states and investigated depinning of the fronts observed outside the pinning region [2]. Depinning is the growth/contraction of the fronts of the localised structure via nucleation/annihilation of the side cells which is schematically shown in figure 1.5(a) as a transition from the lower part of the snaking to its upper part. They showed that a localised state, taken from one of the right saddle nodes and time-integrated at a parameter value taken at the distance δ from the right boundary of the pinning region, exhibits a depinning with the front speed c obeying a square-root law $c \propto \delta^{\frac{1}{2}}$. Equivalently, the time of nucleation one more cell on each side T obeys a law $T \propto \delta^{-\frac{1}{2}}$ which is demonstrated in figure 1.5(b).

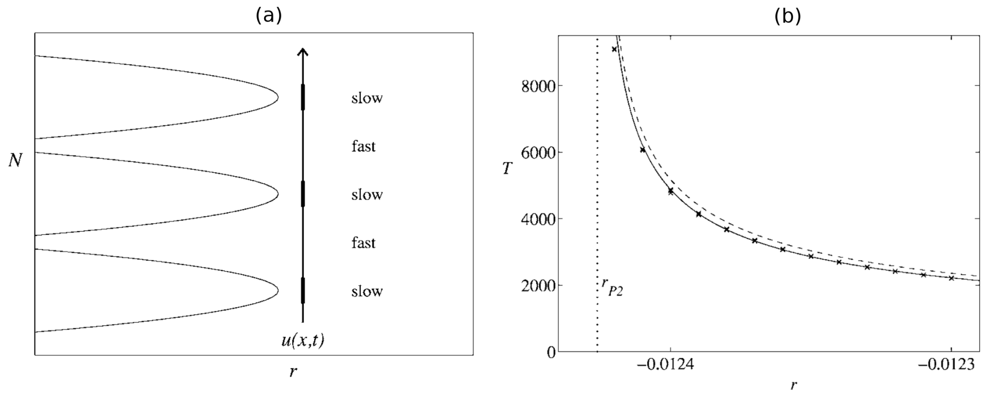

Figure 1.5: Schematic picture of depinning as evolution of $u(x, t)$ up along the snaking (a) and the time T it takes for a saddle-node state to nucleate one more cell on each side when time-integrated at r located at distance $\delta = r - r_{P2}$ from the right boundary of the pinning region r_{P2} (b). Nucleation occurs when going through the fast phase sketched in panel (a) as transition between two successive saddle-node states. In the slow phase, the state virtually replicates the saddle-node state it passes by. In panel (b), the dashed line shows the semi-analytical prediction, $T \propto \delta^{-\frac{1}{2}}$, and the crosses show numerically obtained values fitted by the solid curve. Taken from [2].

In plane Couette flow, depinning was investigated by Duguet *et al.* in 2011 [92]. They considered the growth of fronts of localised turbulent states at Reynolds numbers slightly to the right of the snaking region boundary and indeed recovered the square-root law for the speed of the fronts. The time-integrated states, however, were not exact solutions taken from the branches constituting the homoclinic snaking. They were carefully selected from a set of localised patches obtained by adiabatic reduction in Reynolds number starting from turbulent one. Nonetheless, they provided attractive evidence that depinning, as modelled in [2] for the Swift–Hohenberg equation, may be relevant to the transition from a localised spot to a domain-filling state which is usually observed in experiments.

It is worth mentioning that homoclinic snaking in plane Couette flow was rediscovered via nonlinear optimisation of perturbations at low *Re* [93]. This directly relates the localised states populating homoclinic snaking in spatially extended plane Couette flow to the optimal perturbations, i.e. the perturbations yielding the largest energy growth in a fixed finite time.

Homoclinic snaking is found in variety of other dissipative pattern-forming systems which include, as the most notable examples, doubly diffusive convection [94–99], Marangoni convection in binary fluids [100], ferrofluids [101], buckling of thin elastic structures [73, 102, 103], neuronal networks [104–108], optical cavity [109, 110], arterial calcification [111], urban crime model [112], reaction-diffusion models [111, 113, 114] and ecosystems [115–118]. In the case of three-dimensional doubly diffusive convection, the linear stability of primary and secondary snaking branches was shown to be helpful in understanding of transition to spatiotemporal chaos [99].

For further details about homoclinic snaking and the related phenomena, one should consult a comprehensive review by Knobloch [88].

1.2 Transition to turbulence: statistical viewpoint

Being built upon invariant solutions of the Navier–Stokes equation, a fully deterministic way of characterising transition to turbulence involves working with the microscopic features of the dynamics, i.e., the flow evolution at the scales of streaks and quasi-streamwise vortices. It is unsurprising then that many researchers concentrate their efforts on the macroscopic description of transition involving the spatial scales of localised spots or even the whole domain and the temporal scales of spot lifetimes or reaching the statistical equilibrium of the system. In an important series of numerical and experimental works regarding the lifetime of individual puffs in pipe flow, it was eventually shown that their mean lifetime grows superexponentially with respect to Re [48, 49, 119–122]. Thus, an individual puff may relaminarise even at large Reynolds number with an extremely small probability which is consistent with the view of transient, but long-lived turbulence [123]. It was also shown that the superexponential law for puff lifetimes can be derived using extreme value theory [124]. There, a puff was assumed to decay if the flow energy is below a certain threshold at all domain coordinates.

In these studies, however, the pipe length was kept comparable to the puff size, which is about $20D$, and did not exceed $50D$ where D is the pipe diameter [122]. As a result, they were not able to capture the intermittent nature of transitional regimes where turbulent regions, charaterised by puffs, and laminar regions alternate. Increasing the pipe length showed that intermittency is created due to puffs splitting [125] and, therefore, one needs to take into account the probabilities of both decay and splitting events to fully describe transition. This was done, accompanied with exhaustive experiments, by Avila *et al.* in 2011 and allowed them to obtain one of the most prominent results in the whole subject of transitional turbulence [17]. They discovered both numerically and experimentally that the time it takes for a puff to split into two puffs tends to zero superexponentially with respect to Reynolds number. The Reynolds number at which the mean time of puffs splitting is equal to the mean time of puffs decay can then be said to be the critical Reynolds number ($Re_c = 2040 \pm 10$ for the pipe flow [17]). This indeed explains how turbulence becomes sustained in an infinitely long pipe despite the fact that individual puffs have a non-zero relaminarisation probability at finite Reynolds numbers. To illustrate the idea, one could imagine an infinite pipe arbitrarily seeded by an infinite number of localised disturbances, i.e., puffs, and time-integrated at any value of the Reynolds number above critical. The probability that a particular puff splits before time T is larger than the probability it decays before time T. Therefore, given the infinite number of initial puffs, there are statistically more splitting events than decay events and, therefore, turbulence progressively contaminates the domain. Since the difference between splitting and decay probabilities diverges extremely fast as Re is increased beyond Re_c, the spreading rate increases accordingly, and transition appears to come on shorter time-scales.

Later in 2013, similar ideas were applied to plane Couette flow by Shi *et al.* who identified the critical Reynolds number $Re_c \approx 325$ [126] which is in-line with the experimentally established value $Re_c = 325 \pm 5$ [16]. To make simulations feasible, they used a domain tilted and confined in the streamwise direction which prevents the formation of the large-scale flow.

It is necessary to note that these studies have their roots in the non-equilibrium statistical mechanics, namely, non-equilibrium phase transition. Indeed, one may think of the intermittent regime of the flow as the coexistence of laminar and turbulent phases. One could also imagine the proliferation of turbulence as the excitation of cells on the lattice where the laminar state of a particular cell is globally stable. These two ideas lead to the view of transition to turbulence as directed percolation which was first noted by Pomeau in 1986 [127]. In this paper, Pomeau discussed how transition to turbulence could be shown to correspond to the directed percolation universality class and, essentially, foresaw the finite lifetime of individual puffs. A number of models supporting this view have been built. Indeed, as demonstrated by Sipos and Goldenfeld in 2011, the bond percolation process implemented in 3 spatial directions in a pipe geometry recovers all crucial features of transitional pipes, such as clustering of turbulent sites (i.e., puffs formation) and superexponentially diverging lifetime of puffs [128]. Another evidence comes from the simplified model invented by Barkley who treated the flow as excitable and bistable media similar to neurons [129, 130]. There, transition to turbulence was shown to be continuous and belong to the directed percolation universality class. Finally, directed-percolation-like transition and superexponential mean lifetime of localised spots was observed in a stochastic predator-prey model imitating the interaction between zonal flow and fluctuations in turbulence in pipe flow [131].

The demonstration that transition to turbulence follows directed percolation laws requires extensive computational studies for three-dimensional flows and appeared to be unfeasible for pipe flow due to very long timescales of puffs splitting and decay ($O(10^7)$ time units near the criticality). Plane Couette flow, in contrast, develops much smaller timescales associated with the spots dynamics ($O(10^4)$) but has two directions of localisation. Nonetheless, it was shown that flow configurations close to plane Couette flow exhibit scaling laws similar to those observed in problems involving the directed percolation. In 2016, Lemoult *et al.* demonstrated both experimentally (for a Taylor–Couette flow with a very small gap between the cylinders) and numerically (for a tilted domain) that the second-order phase transition characterised by the directed percolation scaling laws takes place if plane Couette flow is confined not only in the wall-normal direction, but also in the spanwise direction. Directed percolation in two spatial dimensions was also observed by Chantry *et al.* in 2017 for the case of Waleffe flow [132], known to mimic successfully many features of transitional plane Couette flow, such as tilted bands and large-scale flow around turbulence spots, and, in essence, represent the dynamics of the region away from the walls of plane Couette flow [33]. Recently, directed percolation was found to characterise the transition from laminar boundary layer to laminar separation bubbles for an airfoil flow configuration [133].

1.3 Control of transition to turbulence

Transition to turbulence is usually considered as an undesirable event in both open flows (e.g. flow over an airplane wing) and closed flows (e.g. flows in pipelines) since turbulent flow is characterised by a significantly larger dissipation rate, i.e. transport loss, than laminar flow. As a result, more energy is required to move an object through turbulent fluid or transport fluid through the pipeline. Moreover, in all these processes, fluid interacts with some structure (a wing surface or a pipe) and sends its fluctuations to it. In some extreme cases, the intermittent nature of transition to turbulence and large difference between the amplitude of fluctuations in laminar and turbulent regions may damage the structure. It is then beneficial to keep the flow laminar as long as possible.

There are two complementary ways how this goal can be achieved:

1. apply control to initially turbulent flow and drive it to the laminar state
2. apply control to initially laminar flow such that it is kept laminar even in the presence of noise

Historically, the first results were obtained in the context of laminarisation, i.e. transition from the turbulent state to the laminar one. This phenomenon was observed to occur naturally in many situations one of which is the acceleration of the flow [134]. When sufficiently large streamwise acceleration was imposed on the flow over a plate or a wing, boundary layers were found to laminarise due to the formation of an inner viscous layer, adjacent to the plate, where perturbations are strongly damped. The acceleration can be created by a sudden increase of the slope of the flat plate at a chosen streamwise location [135, 136] or by moving the plate or rotating cylinders on a wing [137]. Further, it was shown that the critical Reynolds number for pipe flow accelerated at a constant rate grows linearly with the value of acceleration [138]. Flow acceleration, i.e. creating the favorable pressure gradient, results in damping of the linearly optimal perturbations exhibiting algebraic growth and, thus, makes the laminar state more stable [139].

Manipulating the near-wall structures in the flow has also appeared to be fruitful for control purposes. The passive mechanisms of this type usually involve the modification of the surface of the flow boundaries, for example, by placing randomly shifted rows of protrusions [140] or adding thin water-repellent coatings [141]. An interesting experimental result was obtained in [142] where roughness elements, placed on the plate, induced linearly optimal perturbations which led to a stable streaky flow whose dissipation rate was only 3.5% larger than that of the laminar state.

Active mechanisms, instead, aim at reducing skin friction or complete laminarisation by putting the energy into the flow via external forcing. Most of the solutions based on feedback mechanisms employ linear control theory as the mathematically viable approach. The assumption behind this theory is the believe that the linearised Navier–Stokes equation (Orr–Sommerfeld/Squire system) or other linear systems describe well the production of turbulent energy and its reduction by means of some external forcing ("input" to the control system). Applying one of the linear control techniques, such as iterative adjoint-based optimization or direct Riccati-based feedback, allows for the construction of an optimal external forcing based on a given linear model such that the turbulent energy is minimised (see [143] for a comprehensive review of linear control techniques applied to fluid dynamics and [144] for a review of linear control applied to spatially developing flows). Linear feedback control can also be used to increase the stability of the laminar state by increasing the minimum amplitude of perturbations needed to trigger turbulence [145]. One of the drawbacks of this approach is a need for the sensing of and actuating on the full flow field or its significant part which makes it impractical in most of the cases. For example, a linear feedback control described in [146] and ensuring the global stability of the flow uses the full flow field sensing and acts on the wall-normal velocity.

Another branch of active mechanisms is related to the open-loop control where the control system only acts on the flow without getting any information from the sensors. A large body of research in this direction has been devoted to the oscillatory forcing. By applying a spanwise body force confined to a viscous sublayer producing a spanwise travelling wave, Du and Karniadakis demonstrated more than 50% drag reduction in plane Poiseuille flow owing to the destruction of the near-wall streaks [147]. Streamwise travelling waves induced by blowing and suction flowing downstream were shown to increase the stability of the laminar state and even cause laminarisation of fully turbulent flow at low Reynods numbers [148, 149]. Upstream travelling waves, in turn, appeared to trigger turbulence even for the initial conditions which laminarise in the uncontrolled flow.

An even simpler type of forcing is provided by the wall oscillations. In plane Poiseuille flow, the spanwise oscillations of the walls were shown to reduce drag by about 40% [150]. In later studies, the effect of spanwise oscillations travelling in the streamwise direction was taken into consideration [151]. It was shown that the waves travelling in the direction of the mean flow may lead to the drag increase whereas the waves travelling backward provide not only high drag reduction but may also cause laminarisation at low, though far beyond the criticality, Reynolds numbers (see figure 2 in [151] for a detailed map of drag reduction). Drag reduction of about 40% was obtained in the case of pipe flow where the pipe is oscillated around the longitudinal axis [152]. One can consult [153] for a deeper discussion of streamwise and spanwise waves induced by wall motion. Finally, an important paper by Rabin *et al.* demonstrated that the kinetic energy of the minimal seed of turbulence in plane Couette can be increased by 41% at a very modest cost in the presence of in-phase wall oscillations [154]. In other words, it was shown that spanwise wall oscillations may increase the basin of attraction of the laminar state given the appropriate parameters.

In long pipes allowing for spatial localisation of perturbations, laminarisation of individual puffs caused by flattening of their mean streamwise velocity profiles was demonstrated by Hof *et al.* in 2010 [155]. It was done by producing an additional puff by an injection of fluid downstream the target puff. More advanced versions of this technique result in complete laminarisation up to $Re = 6000$ in pipe flow [156]. Flattening the streamwise profile was also demonstrated by means of impulsive wall motions in the streamwise direction which allowed for the laminarisation up to $Re = 40000$ in pipe flow [157]. Moreover, the minimal seed calculated for the flattened profile in the presence of a similar forcing was shown to be significantly increased in comparison to the uncontrolled system [158].

1.4 Thesis outline

In this thesis, we assess transition to turbulence and the efficiency of its control using both spatially localised and random states as finite-amplitude disturbances applied to plane Couette flow. Our study is based on large campaigns of Direct Numerical Simulations (DNSs). Spatially localised states used as the initial conditions for the simulations are exact solutions of plane Couette flow calculated using Newton–Krylov method and numerical continuation which are discussed in Chapter 2 together with a solver used for DNSs. The exact localised states are located on the branches of the homoclinic snaking whose structure and properties are discussed in Chapter 3. When time-integrated at Re spanning from the right boundary of the pinning region up to transitional ones, they are found to exhibit several well-defined dynamical regimes involving oscillatory dynamics, splitting and front growth. The map of the dynamical regimes and their analysis are presented in Chapter 4. The most important parts of Chapters 3 and 4 were published in [159]. These results equip us with the quantitative picture of transition to turbulence and allow us to benchmark the efficiency of various control strategies. Being motivated by the paper by Rabin *et al.* [154], we choose spanwise oscillations of the walls as a control strategy for preventing transition to turbulence. We show how this control affects transient dynamics of the spatially localised initial conditions and suggest the metrics for the assessment of the control efficiency in Chapter 5. In Chapter 6, we introduce an alternative approach to the assessment of transition and control efficiency based on the extensive sampling of random perturbations and calculation of the laminarisation probability. The description of this probabilistic protocol was published in [160]. The thesis is concluded by Chapter 7.

Chapter 2

Methods

Our research heavily relies on the exploration of the phase space of plane Couette flow, i.e., its simulation for various initial conditions and Reynolds numbers. We time-integrate the system using direct numerical simulation (DNS) which implies that no turbulent model is used and all spatial and temporal scales of the flow are resolved in contrast to Reynolds-Averaged Navier–Stokes (RANS), where the mean velocity is found by approximating the Reynolds stresses, or Large-Eddy Simulation (LES), where the solution is searched for the large-scale flow by approximating the small-scale dynamics (see [161] for an easy-to-read introduction to the topic). In Section 2.1, we describe the pseudospectral method used to perform DNS in the code *Channelflow* [162].

In this thesis, the majority of the initial conditions used for time-integration are exact localised solutions of plane Couette flow. Initially, they are found using Newton–Krylov method with locally constrained optimal hookstep which is a deep modification of the classical Newton–Raphson method. We describe the Newton–Krylov method in Section 2.2. Since the Navier–Stokes equations depend on Re as a parameter, the whole branches of such solutions can be computed. This is done by means of numerical continuation, based on quadratic extrapolation and introduced in Section 2.3, and the aforementioned Newton–Krylov method. The linear stability analysis of these solutions is performed using Arnoldi iteration explained in Section 2.4. Finally, a important class of invariant solutions, known as the edge states, is computed using the edge tracking algorithm. We briefly discuss this algorithm in Section 2.5.

2.1 Direct Numerical Simulation: pseudospectral method

For performing DNS, we use the pseudospectral solver implemented in the code *Channelflow* [162] which also includes a set of tools for numerical continuation and stability analysis. Pseudospectral methods are wide-spread in solving partial differential equations due to their spectral, i.e., faster than any algebraic, convergence which allows to use significantly smaller number of degrees of freedom comparing to finite-differences to obtain the same accuracy [163]. We now present a brief description of the pseudospectral method implemented in *Channelflow*.

Since we are going to apply time-dependent control to the system, we rewrite equation (1.11) by considering the time- and wall-normal-dependent spanwise component of the laminar velocity field, i.e.,

$$\boldsymbol{U_{lam}} = [y, 0, W(t, y)], \tag{2.1}$$

which turns equation (1.11) into

$$\partial_t \boldsymbol{u} = -\nabla p - (\boldsymbol{U} \cdot \nabla)\boldsymbol{U} + \frac{1}{Re}\nabla^2 \boldsymbol{u} + \frac{1}{Re}\partial_{yy} W \boldsymbol{e}_z - \partial_t W \boldsymbol{e}_z, \tag{2.2}$$

where the nonlinear term is purposefully written with respect to the full flow field. To make numerical investigation of the system possible, we have to discretise the equation. Based on equation (2.2), we first define the linear operator $\boldsymbol{L}$, nonlinear term $\boldsymbol{N}(\boldsymbol{u})$ and constant term $\boldsymbol{C}$ independent on $\boldsymbol{u}$:

$$\boldsymbol{L} = \frac{1}{Re}\nabla^2, \tag{2.3}$$

$$\boldsymbol{N}(\boldsymbol{u}) = (\boldsymbol{U} \cdot \nabla)\boldsymbol{U}, \tag{2.4}$$

$$\boldsymbol{C} = \frac{1}{Re}\partial_{yy} W \boldsymbol{e}_z - \partial_t W \boldsymbol{e}_z. \tag{2.5}$$

Here, the nonlinear term is expressed in its convection form which does not conserve the linear momentum and the kinetic energy of the inviscid flow when equation (2.2) discretised according to collocation schemes [164]. Instead, we shall use the rotation form found to be optimal for collocation methods owing to lower aliasing errors (see [165, Chapter 7] for discussion and [164] for a thorough comparison of different forms of the nonlinear term):

$$\begin{aligned}\boldsymbol{N}(\boldsymbol{u}) &= (\nabla \times \boldsymbol{U}) \times \boldsymbol{U} + \frac{1}{2}\nabla(\boldsymbol{U} \cdot \boldsymbol{U}) \\ &= y\partial_x \boldsymbol{u} + W\partial_z \boldsymbol{u} + v\boldsymbol{e}_x + v\partial_y W \boldsymbol{e}_z + (\nabla \times \boldsymbol{u}) \times \boldsymbol{u} + \frac{1}{2}\nabla(\boldsymbol{u} \cdot \boldsymbol{u}).\end{aligned} \tag{2.6}$$

Finally, we define the modified pressure as $q = p - \frac{1}{2}\boldsymbol{u} \cdot \boldsymbol{u}$ so that the nonlinear term becomes

$$\boldsymbol{N}(\boldsymbol{u}) = y\partial_x \boldsymbol{u} + W\partial_z \boldsymbol{u} + v\boldsymbol{e}_x + v\partial_y W \boldsymbol{e}_z + (\nabla \times \boldsymbol{u}) \times \boldsymbol{u}, \tag{2.7}$$

which eventually yields

$$\partial_t \boldsymbol{u} = -\nabla q + \boldsymbol{L}\boldsymbol{u} + \boldsymbol{N}(\boldsymbol{u}) + \boldsymbol{C}. \tag{2.8}$$

Next, we expand the velocity field, $\boldsymbol{u}$, and the modified pressure field, q, into Fourier series in the periodic directions x and z:

$$\boldsymbol{u}(t,x,y,z) = \sum_{k_x=-N_x/2+1}^{N_x/2} \sum_{k_z=-N_z/2+1}^{N_z/2} \widehat{\boldsymbol{u}}_{k_x,k_z}(t,y) e^{2\pi i\left(\frac{k_x x}{\Gamma_x}+\frac{k_z z}{\Gamma_z}\right)}, \tag{2.9}$$

$$q(t,x,y,z) = \sum_{k_x=-N_x/2+1}^{N_x/2} \sum_{k_x=-N_z/2+1}^{N_z/2} \widehat{q}_{k_x,k_z}(t,y) e^{2\pi i\left(\frac{k_x x}{\Gamma_x}+\frac{k_z z}{\Gamma_z}\right)}. \tag{2.10}$$

Equation (2.8) must be satisfied for each pair (k_x, k_z), so we have

$$\partial_t \widehat{\boldsymbol{u}}_{k_x,k_z} = -\widehat{\nabla}_{k_x,k_z} \widehat{\boldsymbol{q}}_{k_x,k_z} + \widehat{\boldsymbol{L}}_{k_x,k_z} \widehat{\boldsymbol{u}}_{k_x,k_z} + \widehat{\boldsymbol{N}(\boldsymbol{u})} + \widehat{\boldsymbol{C}}. \tag{2.11}$$

where

$$\widehat{\nabla}_{k_x,k_z} = \left[2\pi i \tfrac{k_x}{\Gamma_x}, \qquad \partial_y, \qquad 2\pi i \tfrac{k_z}{\Gamma_z}\right]^T, \tag{2.12}$$

$$\widehat{\boldsymbol{L}}_{k_x,k_z} = \frac{1}{Re} \widehat{\nabla}^2_{k_x,k_z} = \frac{1}{Re}\left[-4\pi \frac{k_x^2}{\Gamma_x^2} + \partial_{yy} - 4\pi \frac{k_z^2}{\Gamma_z^2}\right], \tag{2.13}$$

$$\widehat{\boldsymbol{C}} = \boldsymbol{C} \delta_{k_x,0} \delta_{k_z,0}. \tag{2.14}$$

Here, $\delta_{l,m}$ is the Kronecker delta and the nonlinear term is written implicitly because of the convolutions it consists of. In fact, rather than calculating the convolutions at the cost of $O(N^2)$ operations, where $N = 3N_x N_y N_z$, it is computationally more efficient to compute the nonlinear term in physical space at the cost of $O(N \log N)$ operations which corresponds to two Fast Fourier Transforms (from spectral to physical space and back) [165, Chapter 3]. Given the rotation form of the nonlinear term, $\nabla \times \boldsymbol{u}$ is calculated in spectral space and then the cross product computation with $\boldsymbol{u}$ is carried out in physical space. This introduces aliasing errors which, however, can be efficiently treated by the 2/3 de-aliasing rule. On the whole, such a treatment of the nonlinear term makes the method *pseudospectral* which was first suggested by Orszag in 1971 [163].

We continue by discretising time in equation (2.11) using the semi-implicit third-order backward differentiation scheme treating the linear terms implicitly and the nonlinear term explicitly. The implicit third-order backward differentiation scheme reads

$$\begin{aligned} \frac{1}{\triangle t}\left(\frac{11}{6}\widehat{\boldsymbol{u}}^{n+1} - 3\widehat{\boldsymbol{u}}^{n} + \frac{3}{2}\widehat{\boldsymbol{u}}^{n-1} - \frac{1}{3}\widehat{\boldsymbol{u}}^{n-2}\right) + O(\triangle t^3) \\ = -\widehat{\nabla}\widehat{\boldsymbol{q}}^{n+1} + \widehat{\boldsymbol{L}}\widehat{\boldsymbol{u}}^{n+1} + \widehat{\boldsymbol{N}(\boldsymbol{u})}^{n+1} + \widehat{\boldsymbol{C}}^{n+1}, \end{aligned} \tag{2.15}$$

where $\triangle t$ denotes the time step, $\widehat{\boldsymbol{u}}^n$ is the approximation of $\widehat{\boldsymbol{u}}$ at time $t = n\triangle t$ and the subscripts k_x, k_z were dropped for the sake of readability. To preserve the third order, the semi-implicit adaptation of this scheme approximates the nonlinear term at step $n+1$ using polynomial interpolation through its values at steps n, $n-1$ and $n-2$:

$$\widehat{\boldsymbol{N}(\boldsymbol{u})}^{n+1} = 3\widehat{\boldsymbol{N}(\boldsymbol{u})}^{n} - 3\widehat{\boldsymbol{N}(\boldsymbol{u})}^{n-1} + \widehat{\boldsymbol{N}(\boldsymbol{u})}^{n-2} + O(\triangle t^3). \tag{2.16}$$

Substituting the latter expression into the implicit scheme (2.15) and dropping $O(\triangle t^3)$ terms gives the third-order semi-implicit scheme:

$$\begin{aligned} &\frac{1}{\triangle t}\left(\frac{11}{6}\widehat{\boldsymbol{u}}^{n+1} - 3\widehat{\boldsymbol{u}}^{n} + \frac{3}{2}\widehat{\boldsymbol{u}}^{n-1} - \frac{1}{3}\widehat{\boldsymbol{u}}^{n-2}\right) \\ &\qquad = -\widehat{\nabla}\widehat{\boldsymbol{q}}^{n+1} + \widehat{\boldsymbol{L}}\widehat{\boldsymbol{u}}^{n+1} + 3\widehat{\boldsymbol{N}(\boldsymbol{u})}^{n} - 3\widehat{\boldsymbol{N}(\boldsymbol{u})}^{n-1} + \widehat{\boldsymbol{N}(\boldsymbol{u})}^{n-2} + \widehat{\boldsymbol{C}}^{n+1}, \end{aligned} \tag{2.17}$$

whose final form is

$$\begin{aligned} &\left(\frac{11}{6\triangle t} + \widehat{\boldsymbol{L}}\right)\widehat{\boldsymbol{u}}^{n+1} + \widehat{\nabla}\widehat{\boldsymbol{q}}^{n+1} \\ &\qquad = \frac{1}{\triangle t}\left(3\widehat{\boldsymbol{u}}^{n} - \frac{3}{2}\widehat{\boldsymbol{u}}^{n-1} + \frac{1}{3}\widehat{\boldsymbol{u}}^{n-2}\right) \\ &\qquad\quad + 3\widehat{\boldsymbol{N}(\boldsymbol{u})}^{n} - 3\widehat{\boldsymbol{N}(\boldsymbol{u})}^{n-1} + \widehat{\boldsymbol{N}(\boldsymbol{u})}^{n-2} + \widehat{\boldsymbol{C}}^{n+1}. \end{aligned} \tag{2.18}$$

The terms on the right-hand side are known from the previous steps of time-integration, except for $\widehat{\boldsymbol{C}}^{n+1}$ which can be easily calculated at step $n+1$, so we denote them as $\widehat{\boldsymbol{R}}$ for simplicity:

$$\widehat{\boldsymbol{R}} = \frac{1}{\triangle t}\left(3\widehat{\boldsymbol{u}}^{n} - \frac{3}{2}\widehat{\boldsymbol{u}}^{n-1} + \frac{1}{3}\widehat{\boldsymbol{u}}^{n-2}\right) + 3\widehat{\boldsymbol{N}(\boldsymbol{u})}^{n} - 3\widehat{\boldsymbol{N}(\boldsymbol{u})}^{n-1} + \widehat{\boldsymbol{N}(\boldsymbol{u})}^{n-2} + \widehat{\boldsymbol{C}}^{n+1}. \tag{2.19}$$

Substituting the expression for $\boldsymbol{L}$ and dropping the superscripts give *the tau equations*:

$$\frac{1}{Re}\frac{d^2\widehat{\boldsymbol{u}}}{dy^2} + \lambda\widehat{\boldsymbol{u}} + \widehat{\nabla}\widehat{q} = \widehat{\boldsymbol{R}}, \tag{2.20}$$

$$\widehat{\nabla}\cdot\widehat{\boldsymbol{u}} = 0, \tag{2.21}$$

$$\widehat{\boldsymbol{u}}(\pm 1) = 0, \tag{2.22}$$

where λ is defined as follows

$$\lambda = \frac{11}{6\triangle t} - \frac{4\pi}{Re}\left(\frac{k_x^2}{\Gamma_x^2} + \frac{k_z^2}{\Gamma_z^2}\right). \tag{2.23}$$

We can decouple the equation for the pressure by taking the divergence of (2.20):

$$\frac{d^2\widehat{q}}{dy^2} - \frac{4\pi}{Re}\left(\frac{k_x^2}{\Gamma_x} + \frac{k_z^2}{\Gamma_z}\right)\widehat{q} = \widehat{\nabla}\cdot\widehat{\boldsymbol{R}}. \tag{2.24}$$

The boundary conditions for this equation are obtained by evaluating divergence (2.21) at the walls:

$$\begin{aligned} \widehat{\nabla}\cdot\widehat{\boldsymbol{u}}\Big|_{y=\pm1} &= \left(2\pi i\frac{k_x}{\Gamma_x}\widehat{u} + \frac{d\widehat{v}}{dy} + 2\pi i\frac{k_z}{\Gamma_z}\widehat{w}\right)\Bigg|_{y=\pm1} = 0 \\ \Longrightarrow \quad \frac{d\widehat{v}}{dy}\Big|_{y=\pm1} &= 0. \end{aligned} \tag{2.25}$$

Thus, we need the equation for $\widehat{v}$ from (2.20) to make a closure. As a system of two equations, this gives the so-called *A-problem* made of two inhomogeneous 1D Helmholtz equations:

$$\frac{d^2\widehat{q}}{dy^2} - \frac{4\pi}{Re}\left(\frac{k_x^2}{\Gamma_x} + \frac{k_z^2}{\Gamma_z}\right)\widehat{q} = \widehat{\nabla}\cdot\widehat{\boldsymbol{R}}, \quad \frac{d\widehat{v}}{dy}\Big|_{y=\pm1} = 0, \tag{2.26}$$

$$\frac{1}{Re}\frac{d^2\widehat{v}}{dy^2} + \lambda\widehat{v} + \frac{d\widehat{q}}{dy} = \widehat{R}_x, \quad \widehat{v}(\pm1) = 0. \tag{2.27}$$

We solve the A-problem following the method suggested by Kleiser and Schumann in 1980 in [166]. It starts by defining the complementary B-problem as the A-problem with the boundary conditions for the first equation replaced with $\widehat{q}(\pm1) = Q_\pm$. Here the unknowns $Q_\pm$ must be found such that they agree with the original boundary conditions. To do this, we find three solutions to the B-problem:

- $\widehat{q}_{I,0}, \widehat{v}_{I,0}$ for the original B-problem with homogeneous boundary conditions
- $\widehat{q}_{H,+}, \widehat{v}_{H,+}$ for the homogeneous B-problem with $\widehat{q}(-1) = 0, \widehat{q}(1) = 1$
- $\widehat{q}_{H,-}, \widehat{v}_{H,-}$ for the homogeneous B-problem with $\widehat{q}(-1) = 1, \widehat{q}(1) = 0$

Given the linearity of the Helmholtz equations, we can express the solution to the B-problem as a linear combination of these solutions:

$$\begin{bmatrix}\widehat{q}\\ \widehat{v}\end{bmatrix} = \begin{bmatrix}\widehat{q}_{I,0}\\ \widehat{v}_{I,0}\end{bmatrix} + Q_+\begin{bmatrix}\widehat{q}_{H,+}\\ \widehat{v}_{H,+}\end{bmatrix} + Q_-\begin{bmatrix}\widehat{q}_{H,-}\\ \widehat{v}_{H,-}\end{bmatrix}. \tag{2.28}$$

The boundary conditions of the A-problem are then used to find the proper values of Q_+ and Q_-:

$$\frac{d\widehat{v}}{dy}\Big|_{y=\pm1} = \frac{d\widehat{v}_{I,0}}{dy}\Big|_{y=\pm1} + Q_+\frac{d\widehat{v}_{H,+}}{dy}\Big|_{y=\pm1} + Q_-\frac{d\widehat{v}_{H,-}}{dy}\Big|_{y=\pm1} = 0, \tag{2.29}$$

which results in the matrix equation

$$\begin{bmatrix} \left.\frac{d\widehat{v}_{H,+}}{dy}\right|_{y=1} & \left.\frac{d\widehat{v}_{H,-}}{dy}\right|_{y=1} \\ \left.\frac{d\widehat{v}_{H,+}}{dy}\right|_{y=-1} & \left.\frac{d\widehat{v}_{H,-}}{dy}\right|_{y=-1} \end{bmatrix} \begin{bmatrix} Q_+ \\ Q_- \end{bmatrix} = \begin{bmatrix} -\left.\frac{d\widehat{v}_{I,0}}{dy}\right|_{y=1} \\ -\left.\frac{d\widehat{v}_{I,0}}{dy}\right|_{y=-1} \end{bmatrix}, \tag{2.30}$$

where the coefficient matrix on the left-hand side is known as *the influence matrix*. Once Q_+ and Q_- are found, we readily get the solution for $\widehat{v}$ and $\widehat{q}$ from (2.28). Finally, the solutions for $\widehat{u}$ and $\widehat{w}$ are obtained via solving two Helmholtz equations from (2.20) with the substituted solution for $\widehat{q}$.

To complete the description of the pseudospectral method, we need to explain how the aforementioned Helmholtz equations are solved. Let's consider the equation

$$\alpha\frac{d^2u}{dy^2} - \beta u = f, \quad u(\pm 1) = u_\pm. \tag{2.31}$$

Following [165, Chapter 5], we use the Chebyshev tau approximation to this problem, i.e., expand all the terms into Chebyshev polynomials $T_m(y)$:

$$u(y) \approx \sum_{m=0}^{N_y-1} \widetilde{u}_m T_m(y), \tag{2.32}$$

$$\frac{d^2u}{dy^2} \approx \sum_{m=0}^{N_y-3} \widetilde{u}_m^{(2)} T_m(y), \tag{2.33}$$

$$f(y) \approx \sum_{m=0}^{N_y-1} \widetilde{f}_m T_m(y). \tag{2.34}$$

The coefficients $\widetilde{u}_m^{(2)}$ are linked to $\widetilde{u}_m$ via

$$\widetilde{u}_m^{(2)} = \frac{1}{c_m} \sum_{\substack{p=m+2, \\ p+m \text{ even}}}^{N_y-1} p(p^2 - m^2)\widetilde{u}_p, \tag{2.35}$$

where $c_0 = 2$ and $c_m = 1, m > 0$. Thus, for the m-th component, equation (2.31) reads

$$\frac{\alpha}{c_m} \sum_{\substack{p=m+2, \\ p+m \text{ even}}}^{N_y-1} p(p^2 - m^2)\widetilde{u}_p - \beta\widetilde{u}_m = \widetilde{f}_m, \quad m = 0, \ldots, N_y - 3. \tag{2.36}$$

Given the properties of the Chebyshev polynomials $T_m(1) = 1$ and $T_m(-1) = (-1)^m$, the boundary conditions in problem (2.31) turn to:

$$\sum_{m=0}^{N_y-1} \widetilde{u}_m = u_+, \tag{2.37}$$

$$\sum_{m=0}^{N_y-1} (-1)^m \widetilde{u}_m = u_-. \tag{2.38}$$

Equation (2.36), together with (2.37) and (2.38), leads to a matrix equation with a nearly upper triangular matrix which is sufficient to find a solution for $\widetilde{u}_m$:

$$\begin{bmatrix} -\beta & 0 & 4\alpha & 0 & 32\alpha & \dots & \frac{1}{2}a_{0,N_y-3} & 0 & \frac{1}{2}a_{0,N_y-1} \\ 0 & -\beta & 0 & 0 & 60\alpha & \dots & a_{1,N_y-3} & 0 & a_{1,N_y-1} \\ 0 & 0 & -\beta & 0 & 48\alpha & \dots & a_{2,N_y-3} & 0 & a_{2,N_y-1} \\ \vdots & \vdots & \vdots & \vdots & \vdots & \dots & \vdots & \vdots & \vdots \\ 0 & 0 & 0 & 0 & 0 & \dots & -\beta & 0 & a_{N_y-1,N_y-1} \\ 1 & 1 & 1 & 1 & 1 & \dots & 1 & 1 & 1 \\ 1 & -1 & 1 & -1 & 1 & \dots & 1 & -1 & 1 \end{bmatrix} \begin{bmatrix} \widetilde{u}_0 \\ \widetilde{u}_1 \\ \widetilde{u}_2 \\ \vdots \\ \widetilde{u}_{N_y-3} \\ \widetilde{u}_{N_y-2} \\ \widetilde{u}_{N_y-1} \end{bmatrix} = \begin{bmatrix} \widetilde{f}_0 \\ \widetilde{f}_1 \\ \widetilde{f}_2 \\ \vdots \\ \widetilde{f}_{N_y-3} \\ u_+ \\ u_- \end{bmatrix}, \tag{2.39}$$

where $a_{l,m} = \alpha m(m^2 - l^2)$. However, equations (2.36) can be transformed such that the resulting coefficient matrix will be nearly tridiagonal. Indeed, one can make use of the following recursion relation [165, Chapter 2]:

$$c_{m-1}\widetilde{u}^{(q)}_{m-1} = \widetilde{u}^{(q)}_{m+1} + 2m\widetilde{u}^{(q-1)}_m, \tag{2.40}$$

which, for $q = 2$, reads

$$2m\widetilde{u}^{(1)}_m = c_{m-1}\widetilde{u}^{(2)}_{m-1} - \widetilde{u}^{(2)}_{m+1}. \tag{2.41}$$

Substituting $\widetilde{u}^{(2)}_{m-1}$ and $\widetilde{u}^{(2)}_{m+1}$, expressed via (2.36), into equation (2.41) yields

$$\widetilde{u}^{(1)}_m = \frac{c_{m-1}}{2m\alpha}(\widetilde{f}_{m-1} + \beta\widetilde{u}_{m-1}) - \frac{1}{2m\alpha}(\widetilde{f}_{m+1} + \beta\widetilde{u}_{m+1}), \quad m = 1, \dots, N_y - 4. \tag{2.42}$$

Similarly, relation (2.40) for $q = 1$ gives

$$2m\widetilde{u}_m = c_{m-1}\widetilde{u}^{(1)}_{m-1} - \widetilde{u}^{(1)}_{m+1}, \tag{2.43}$$

which, after substitution of (2.42) and simplifications, becomes

$$\begin{aligned} &\frac{c_{m-2}\beta}{2\alpha(m-1)}\widetilde{u}_{m-2} - \left[2m + \frac{\beta m}{\alpha(m^2-1)}\right]\widetilde{u}_m + \frac{\beta}{2\alpha(m+1)}\widetilde{u}_{m+2} \\ &= -\frac{c_{m-2}}{2\alpha(m-1)}\widetilde{f}_{m-2} + \frac{m}{\alpha(m^2-1)}\widetilde{f}_m - \frac{1}{2\alpha(m+1)}\widetilde{f}_{m+2}, \quad m = 2, \dots, N_y - 5. \end{aligned} \tag{2.44}$$

This recursion relation decouples even and odd coefficients and forms, thus, two tridiagonal matrices. In order to take the boundary conditions (2.37) and (2.38) into account, we note that their sum and the difference between them yield

$$\sum_{\text{even } m} \widetilde{u}_m = \frac{1}{2}(u_+ + u_-), \tag{2.45}$$

$$\sum_{\text{odd } m} \widetilde{u}_m = \frac{1}{2}(u_+ - u_-). \tag{2.46}$$

Each of these equations complement the corresponding tridiagonal matrix. The resulting two quasi-tridiagonal matrices can be independently solved via a slightly modified Thomas algorithm requiring only $O(N_y)$ operations.

To sum up, the described pseudospectral method solves for the velocity and pressure fields expanded into Fourier–Chebyshev–Fourier series:

$$\boldsymbol{u} \approx \sum_{k_x=-N_x/2+1}^{N_x/2} \sum_{k_y=0}^{N_y-1} \sum_{k_z=-N_z/2+1}^{N_z/2} \hat{\boldsymbol{u}}_{k_x,k_y,k_z} T_{k_y}(y) e^{2\pi i\left(\frac{k_x x}{\Gamma_x}+\frac{k_z z}{\Gamma_z}\right)}, \tag{2.47}$$

$$p \approx \sum_{k_x=-N_x/2+1}^{N_x/2} \sum_{k_y=0}^{N_y-1} \sum_{k_z=-N_z/2+1}^{N_z/2} \hat{p}_{k_x,k_y,k_z} T_{k_y}(y) e^{2\pi i\left(\frac{k_x x}{\Gamma_x}+\frac{k_z z}{\Gamma_z}\right)}. \tag{2.48}$$

where $k_x, k_y, k_z \in \mathbb{N}$, N_x (resp. N_z) is the even number of uniform nodes in the x (resp. z) direction, N_y is the number of Chebyshev nodes and $T_{k_y}(y)$ is the k_y-degree Chebyshev polynomial of the first kind. The solution is found independently for each pair (k_x, k_z) which implies parallelisation on up to $k_x \times k_z$ threads.

2.2 Numerical search for exact solutions: Newton–Krylov method

In this thesis, plane Couette flow is viewed as an infinite-dimensional dynamical system defined by equations (1.11), (1.12). The spatial discretisation described in the previous section transforms it to a finite-dimensional form which can be written as

$$\frac{d\hat{\boldsymbol{u}}}{dt} = \boldsymbol{F}(\hat{\boldsymbol{u}}, \hat{\boldsymbol{p}}, Re), \tag{2.49}$$

where $\hat{\boldsymbol{u}} \in \mathbb{R}^{3\times k_x\times k_y\times k_z}$, $\hat{\boldsymbol{p}} \in \mathbb{R}^{k_x\times k_y\times k_z}$ and $\boldsymbol{F}$ is a vector function appearing after pseudospectral discretisation and for which the pressure is found in a preliminary step by solving the A-problem (2.26) as described above. This system can now be treated as a finite-dimensional dynamical system with Re as a control parameter.

Equilibria can be found by equaling the right-hand side of (2.49) to zero and solving the correspoding system of non-linear equations. However, we are interested in a more general case allowing for the calculation of travelling waves and periodic orbits. The former requires considering the translations in the periodic directions x and z, which we do following [43]:

$$\begin{aligned}&\boldsymbol{u}(x \to x + \triangle x, z \to z + \triangle z)\\&\qquad = \sum_{k_x \in \mathbb{Z}} \sum_{k_y = 0}^{\infty} \sum_{k_z \in \mathbb{Z}} \hat{\boldsymbol{u}}_{k_x, k_y, k_z} T_{k_y}(y) e^{2\pi i \left(\frac{k_x (x + \triangle x)}{\Gamma_x} + \frac{k_z (z + \triangle z)}{\Gamma_z} \right)}. \end{aligned} \tag{2.50}$$

Expanding into Taylor series around the identity transformation results in the infinitesimal generators of the group of translations along x and z:

$$G_x \boldsymbol{u} = \sum_{k_x \in \mathbb{Z}} \sum_{k_y = 0}^{\infty} \sum_{k_z \in \mathbb{Z}} \frac{2\pi i k_x}{\Gamma_x} \hat{\boldsymbol{u}}_{k_x, k_y, k_z} T_{k_y}(y) e^{2\pi i \left(\frac{k_x x}{\Gamma_x} + \frac{k_z z}{\Gamma_z} \right)}, \tag{2.51}$$

$$G_z \boldsymbol{u} = \sum_{k_x \in \mathbb{Z}} \sum_{k_y = 0}^{\infty} \sum_{k_z \in \mathbb{Z}} \frac{2\pi i k_z}{\Gamma_z} \hat{\boldsymbol{u}}_{k_x, k_y, k_z} T_{k_y}(y) e^{2\pi i \left(\frac{k_x x}{\Gamma_x} + \frac{k_z z}{\Gamma_z} \right)}, \tag{2.52}$$

The finite translations are thus given by the following exponentials [43, 167]:

$$\boldsymbol{u}(x \to x + \triangle x) = e^{\triangle x G_x} \boldsymbol{u} = \sigma_{\triangle x} \boldsymbol{u}, \tag{2.53}$$

$$\boldsymbol{u}(z \to z + \triangle z) = e^{\triangle z G_z} \boldsymbol{u} = \sigma_{\triangle z} \boldsymbol{u}. \tag{2.54}$$

We now suppose that the solution of (2.8) produces a finite-time flow map $f^T(\boldsymbol{u})$, where $\boldsymbol{u}$ is an initial condition and T is time until which $\boldsymbol{u}$ is integrated. Then, given the invariance of plane Couette flow under the aforementioned translations, all exact equilibria, travelling waves and (relative) periodic orbits must satisfy the equation

$$\boldsymbol{G}(\boldsymbol{u}, \triangle x, \triangle z, T) = \sigma_{\triangle x} \sigma_{\triangle z} f^T(\boldsymbol{u}) - \boldsymbol{u} = 0, \tag{2.55}$$

where $\triangle x = \triangle z = T = 0$ for equilibria, $T = c\triangle x$ or $T = c\triangle z$ for travelling waves and $\triangle x = \triangle z = 0$ for periodic orbits. Out of generality, we shall consider the case of relative periodic orbits. Following [162], we denote the discretised versions of $\boldsymbol{G}$ and $\boldsymbol{F}$ as $\boldsymbol{G}_N$ and $\boldsymbol{F}_N$ respectively, where $N = 3 \times N_x \times N_y \times N_z$ is the number of degrees of freedom in the discretised system. We also introduce a vector $\boldsymbol{u}_N \in \mathbb{R}^{N+3}$ made of $\hat{\boldsymbol{u}} \in \mathbb{R}^N$ being the solution of (2.49) and augmented by $\triangle x, \triangle z$ and T. This transforms (2.55) into

$$\boldsymbol{G}_N(\boldsymbol{u}_N) = 0. \tag{2.56}$$

Our goal is to find $\boldsymbol{u}_N$ satifying this equation which we do by an iterative method described below. We expand $\boldsymbol{G}_N$ into Taylor series around an approximation $\boldsymbol{u}_N^{(k)}$, obtained at the k-th iteration, and evaluate it at $\boldsymbol{u}_N^{(k)} + \delta\boldsymbol{u}_N$:

$$\boldsymbol{G}_N(\boldsymbol{u}_N^{(k)} + \delta\boldsymbol{u}_N) = \boldsymbol{G}_N(\boldsymbol{u}_N^{(k)}) + \boldsymbol{J}(\boldsymbol{u}_N^{(k)})\delta\boldsymbol{u}_N + O(|\delta\boldsymbol{u}_N|^2), \tag{2.57}$$

where $\boldsymbol{J}(\boldsymbol{u}_N^{(k)})$ is the Jacobian of $\boldsymbol{G}_N$ evaluated at $\boldsymbol{u}_N^{(k)}$. Assuming that $\boldsymbol{u}_N = \boldsymbol{u}_N^{(k)} + \delta\boldsymbol{u}_N$ and $\delta\boldsymbol{u}_N$ is small enough yields

$$\boldsymbol{J}(\boldsymbol{u}_N^{(k)})\delta\boldsymbol{u}_N \approx -\boldsymbol{G}_N(\boldsymbol{u}_N^{(k)}). \tag{2.58}$$

Since $\boldsymbol{J}(\boldsymbol{u}_N^{(k)})$ has only N rows, this equation needs three more equations to be solved. We get them by constraining the Newton step $\delta\boldsymbol{u}_N$ to be orthogonal to the time and space directions:

$$\langle \delta\boldsymbol{u}_N, \frac{d\hat{\mathbf{u}}}{dt} \rangle = \langle \delta\boldsymbol{u}_N, \boldsymbol{F}_N(\boldsymbol{u}_N^{(k)}) \rangle = 0, \tag{2.59}$$

$$\langle \delta\boldsymbol{u}_N, \frac{d\hat{\mathbf{u}}}{dx} \rangle = \langle \delta\boldsymbol{u}_N, G_x\boldsymbol{u}_N^{(k)} \rangle = 0, \tag{2.60}$$

$$\langle \delta\boldsymbol{u}_N, \frac{d\hat{\mathbf{u}}}{dz} \rangle = \langle \delta\boldsymbol{u}_N, G_z\boldsymbol{u}_N^{(k)} \rangle = 0, \tag{2.61}$$

where $\langle \cdot, \cdot \rangle$ is the dot product. This yields an augmented system

$$\boldsymbol{A}\delta\boldsymbol{u}_N = \boldsymbol{b}. \tag{2.62}$$

Solving the latter equation for $\delta\boldsymbol{u}_N$ and defining the approximation on the next iteration as $\boldsymbol{u}_N^{(k+1)} = \boldsymbol{u}_N^{(k)} + \delta\boldsymbol{u}_N$ get the *Newton–Raphson method*. Usually, it requires the inversion of the Jacobian matrix which, given more than 10^6 degrees of freedom in our case, is computationally expensive. In addition, the Jacobian is poorly-conditioned at low Reynolds numbers due to the large condition number of the discretised Laplacian which complicates the inversion. In order to overcome these issues, a solution of the matrix equation is sought in a K-dimensional *Krylov subspace* $V = \{\boldsymbol{v}_1, \boldsymbol{v}_2, \dots, \boldsymbol{v}_K\} = \{\boldsymbol{b}, \boldsymbol{A}\boldsymbol{b}, \dots, \boldsymbol{A}^{K-1}\boldsymbol{b}\}$, where K is typically very small, namely, $K = O(100)$ at most [168]. It is constructed by an *Arnoldi iteration* which efficiently performs QR decomposition of the Krylov matrix $[\boldsymbol{v}_1|\boldsymbol{v}_2|\dots|\boldsymbol{v}_K]$. The resulting *Newton–Krylov method* searches for $\delta\hat{\mathbf{u}} \in \mathit{span}(V)$ such that (2.62) is satisfied. It should be noted that the Arnoldi iteration requires only repeated computation of $\boldsymbol{A}\boldsymbol{z}$ for some vector $\boldsymbol{z}$ which does not require assembling the whole matrix $\boldsymbol{A}$ and, more importantly, $\boldsymbol{J}(\boldsymbol{u}_N)$. For this reason, this Newton–Krylov method is often classified as a *matrix-free method.*

The solution in the Krylov subspace can be then found by a *generalised minimal residual method* (GMRES) which implies the minimisation of residual $||\boldsymbol{A}\delta\boldsymbol{u}_N - \boldsymbol{b}||$ with respect to $\delta\boldsymbol{u}_N$ belonging to the Krylov space, i.e. with respect to arbitrary N-dimensional vector $\boldsymbol{y}$ projected onto V: $\delta\boldsymbol{u}_N = V\boldsymbol{y}$. The minimisation leads to the normal equation

$$(\boldsymbol{A}V)^T(\boldsymbol{A}V)\boldsymbol{y} = (\boldsymbol{A}V)^T\boldsymbol{G}_N \tag{2.63}$$

which is solved for $\boldsymbol{y}$ using QR decomposition of the coefficient matrix. *Channelflow* implements GMRES as described in [169, Lecture 35].

The Newton–Krylov iteration is also accompanied with a *locally constrained optimal hookstep algorithm* [170] which was first employed for searching for the exact solutions in plane Couette flow by Viswanath in 2007 [43]. This algorithm is switched on when the residual in the Newton method does not decrease sufficiently fast. The optimal hookstep is obtained by minimising $||\boldsymbol{A}\delta\boldsymbol{u}_N - \boldsymbol{b}||$ subject to $||\delta\boldsymbol{u}_N|| \leq \delta$, where δ is a *trust region radius.* Following [162], we restrict $\delta\hat{\boldsymbol{u}}$ to lie within the Krylov space by defining $\delta\boldsymbol{u}_N = \boldsymbol{Q}_n\boldsymbol{y}$, where $\boldsymbol{y} \in \mathbb{R}^n$ and $\boldsymbol{Q}_n \in \mathbb{R}^{N\times n}$ is a matrix obtained at the nth Arnoldi iteration and whose columns form the orthonormal basis for the n-dimensional Krylov subspace. We note that the $(n+1)$th Arnoldi iteration implies the decomposition

$$\boldsymbol{A}\boldsymbol{Q}_n = \boldsymbol{Q}_{n+1}\boldsymbol{H}_n, \tag{2.64}$$

where $\boldsymbol{H}_n \in \mathbb{R}^{(n+1)\times n}$ is the upper Hessenberg matrix. Since $\boldsymbol{Q}_n$ is orthogonal, the norm in the minimisation problem will not be modified if we multiply the expression under the norm from the left by $\boldsymbol{Q}_{n+1}^T$. Together with (2.64), this gives

$$\min_{||\delta\boldsymbol{u}_N||\leq\delta} ||\boldsymbol{H}_n\boldsymbol{y} - \boldsymbol{Q}_{n+1}^T\boldsymbol{b}||. \tag{2.65}$$

Using the singular value decomposition $\boldsymbol{H}_n = \boldsymbol{U}\boldsymbol{D}\boldsymbol{V}^T$ results in

$$\min_{||\delta\boldsymbol{u}_N||\leq\delta} ||\boldsymbol{U}\boldsymbol{D}\boldsymbol{V}^T\boldsymbol{y} - \boldsymbol{Q}_{n+1}^T\boldsymbol{b}||. \tag{2.66}$$

Eventually, multiplying the expression under the norm from the left by $\boldsymbol{U}^T$ yields

$$\min_{||\delta\boldsymbol{u}_N||\leq\delta} ||\boldsymbol{D}\tilde{\boldsymbol{y}} - \tilde{\boldsymbol{b}}||, \tag{2.67}$$

where $\tilde{\boldsymbol{y}} \in \boldsymbol{V}^T \boldsymbol{y}$ and $\tilde{\boldsymbol{b}} = \boldsymbol{U}^T \boldsymbol{Q}_{n+1}^T \boldsymbol{b}$. This minimisation problem is solved via Lagrange multipliers [162]. The locally constrained optimal hookstep is then computed as $\delta \boldsymbol{u}_N = \boldsymbol{Q}_n \boldsymbol{V} \tilde{\boldsymbol{y}}$.

2.3 Numerical continuation

Since the Navier–Stokes equations, as well as equation (2.55), continuously depend on Re, the exact solutions of plane Couette flow should lie on the branches, i.e. smooth curves, in the $(\boldsymbol{u}, Re)$ space. Given some initial exact solutions, we can perturb a parameter Re (i.e., either increase or decrease it) and search for a new solution using the given ones as initial guesses. Repeating this many times reveals the branch of solutions. The corresponding numerical technique for finding such branches is called *numerical continuation* which has become a vital tool in numerical investigation of dynamical systems.

In *Channelflow*, the numerical continuation alrogithm is based on the predictor-corrector scheme where prediction is done using quadratic extrapolation of three previously calculated solutions and where correction is done by the Newton–Krylov method described above. To make a prediction, solutions $\hat{\boldsymbol{u}}$ lying on the branch and parameter Re are parametrised by arclength s:

$$\hat{\boldsymbol{u}} = \hat{\boldsymbol{u}}(s), \tag{2.68}$$

$$Re = Re(s). \tag{2.69}$$

Here, the arclength is related to the branch projected on the reduced space $(\mathcal{E}, Re)$, where $\mathcal{E}$ is the enstrophy defined for a continuous velocity field as

$$\mathcal{E} = \frac{1}{2\Gamma_x \Gamma_z} \int_0^{\Gamma_x} \int_{-1}^{1} \int_0^{\Gamma_z} |\nabla \times \boldsymbol{u}|^2 dx dy dz, \tag{2.70}$$

Let's assume that the exact solutions $\hat{\boldsymbol{u}}^{(k)}$, $\hat{\boldsymbol{u}}^{(k-1)}$ and $\hat{\boldsymbol{u}}^{(k-2)}$ have been already calculated. We associate the arclength $s^{(k-2)} = 0$ with $\hat{\boldsymbol{u}}^{(k-2)}$ and compute two other arclengths as

$$s^{(k-1)} = \sqrt{\left(\frac{\mathcal{E}^{(k-2)} - \mathcal{E}^{(k-1)}}{\mathcal{E}^{(k-1)}}\right)^2 + \left(\frac{Re^{(k-2)} - Re^{(k-1)}}{Re^{(k-1)}}\right)^2}, \tag{2.71}$$

$$s^{(k)} = s^{(k-1)} + \sqrt{\left(\frac{\mathcal{E}^{(k)} - \mathcal{E}^{(k-1)}}{\mathcal{E}^{(k-1)}}\right)^2 + \left(\frac{Re^{(k)} - Re^{(k-1)}}{Re^{(k-1)}}\right)^2}, \tag{2.72}$$

where $\mathcal{E}^{(k)}$, $\mathcal{E}^{(k-1)}$, $\mathcal{E}^{(k-2)}$ and $Re^{(k)}$, $Re^{(k-1)}$, $Re^{(k-2)}$ are the enstrophy and Reynolds numbers associated with $\hat{\boldsymbol{u}}^{(k)}$, $\hat{\boldsymbol{u}}^{(k-1)}$ and $\hat{\boldsymbol{u}}^{(k-2)}$ respectively. Given these values, we can build quadratic interpolants, $\hat{\boldsymbol{u}}(s)$ and $Re(s)$, such that they pass through the corresponding data at the iterations k, $k-1$ and $k-2$. Eventually, $\hat{\boldsymbol{u}}^{(k+1)}$ and $Re^{(k+1)}$ are predicted by evaluating the corresponding quadratic interpolants at $s^{(k+1)} = s^{(k)} + (s^{(k)} - s^{(k-1)})$ and then corrected by means of the Newton–Krylov method.

Channelflow implements these algorithms as a part of the main library. The programs *findsoln* and *continuesoln* are supplied for numerical search and continuation of equilibria, periodic orbits and their relative companions.

2.4 Linear stability analysis: Arnoldi iteration

Once we have found exact solutions, it is of prime interest to learn their stability properties. *Channelflow* implements this by means of Arnoldi iteration. Let's assume that $\boldsymbol{u}_N^*$ is an exact solution. Then, small random perturbations $\delta\boldsymbol{u}_N$ around this state would lead to the linearisation of $\boldsymbol{G}_N$. Indeed, evaluating (2.57) at $\boldsymbol{u}_N^* + \delta\boldsymbol{u}_N$ yields

$$\boldsymbol{G}_N(\boldsymbol{u}_N^* + \delta\boldsymbol{u}_N) \approx \boldsymbol{J}(\boldsymbol{u}_N^*)\delta\boldsymbol{u}_N. \tag{2.73}$$

As a result, the linear stability analysis of the exact solution is equivalent to finding the eigenvalues and eigenfunctions of $\boldsymbol{J}(\boldsymbol{u}_N^*)$. We do this by means of the Arnoldi iteration described above where the corresponding K-dimensional Krylov subspace is given by $\{\delta\boldsymbol{u}_N, \boldsymbol{J}(\boldsymbol{u}_N^*)\delta\boldsymbol{u}_N, \dots, \boldsymbol{J}(\boldsymbol{u}_N^*)^{K-1}\delta\boldsymbol{u}_N\}$. Arnoldi iteration leads to the calculation of the eigenvalues and eigenvectors of the Hessenberg matrix $\tilde{\boldsymbol{H}}_n$ obtained by removing the last row of $\boldsymbol{H}_n$ mentioned in (2.64). The corresponding eigenvalues are known as *Arnoldi estimates* and are typically expected to converge fast enough to the extreme eigenvalues of $\boldsymbol{J}(\boldsymbol{u}_N^*)$ [169, Lecture 34]. Owing to a small dimension, the eigendecomposition of $\tilde{\boldsymbol{H}}_n$ is done using QR decomposition.

As $\boldsymbol{G}_N$ was built from a finite-time map, this procedure does not calculate the eigenvalues of the Navier–Stokes equation linearised around the exact solution, but rather returns the characteristic multipliers $L_j = e^{\lambda_j T}$. The needed eigenvalues are thus given by the corresponding Floquet multipliers:

$$\lambda_j = \frac{1}{T} \ln L_j. \tag{2.74}$$

2.5 Edge tracking

The *edge tracking* is a bisection-like method used to compute the edge states. This algorithm is illustrated in figure 2.1. To start off, it only needs a pair of initial conditions one of which decays (laminarises) and another one goes turbulent (transitions) after being time-integrated (the leftmost trajectories in figure 2.1). We treat an initial condition as transitioning if the kinetic energy of the flow emanating from it exceeds the average turbulent kinetic energy E_{turb} calculated for a given flow configuration at a certain time; otherwise, we call an initial condition laminarising. By time-integrating ten incompressible perturbations $\boldsymbol{u_c} = c\boldsymbol{u_\perp}$, where $c \in \{0.1, 0.2, \dots, 1.0\}$ and $\boldsymbol{u_\perp}$ is a random component orthogonal to the laminar solution and satisfying $||\boldsymbol{u_\perp}|| = 1$, we select such a pair of laminarising/transitioning initial conditions associated with smallest c and denote them $\boldsymbol{u_{lam}}$ and $\boldsymbol{u_{turb}}$ respectively. If they are sufficiently close to the edge of chaos, the trajectories emanating from them should slide along the stable manifold of the edge state for some short amount of time and then diverge exponentially fast. We then look for the critical time t_1 when these trajectories are just about to diverge in the sense that the difference between them in the energy space exceeds a small prescribed threshold $E_{diff} = 1.25 \times 10^{-3}$. Once we find it, we take the flow states at time t_1, quadrasect between them producing thus three new initial conditions (three dots in the middle of figure 2.1) and again select among them the closer pair of laminarising/transitioning initial conditions $\boldsymbol{u_{lam}}$ and $\boldsymbol{u_{turb}}$. After that, the procedure described above is iteratively repeated until the convergence to the edge state is observed. At certain iterations, the selected pair of trajectories may diverge too fast, i.e., the energy difference exceeds E_{diff} for less than $t_{diff} = 50$ time units, despite the quadrasection we use at each iteration. In this case, it is beneficial for the convergence acceleration to quadrasect one more time between the corresponding initial conditions.

The main output of the edge tracking is a piecewise trajectory approximating the

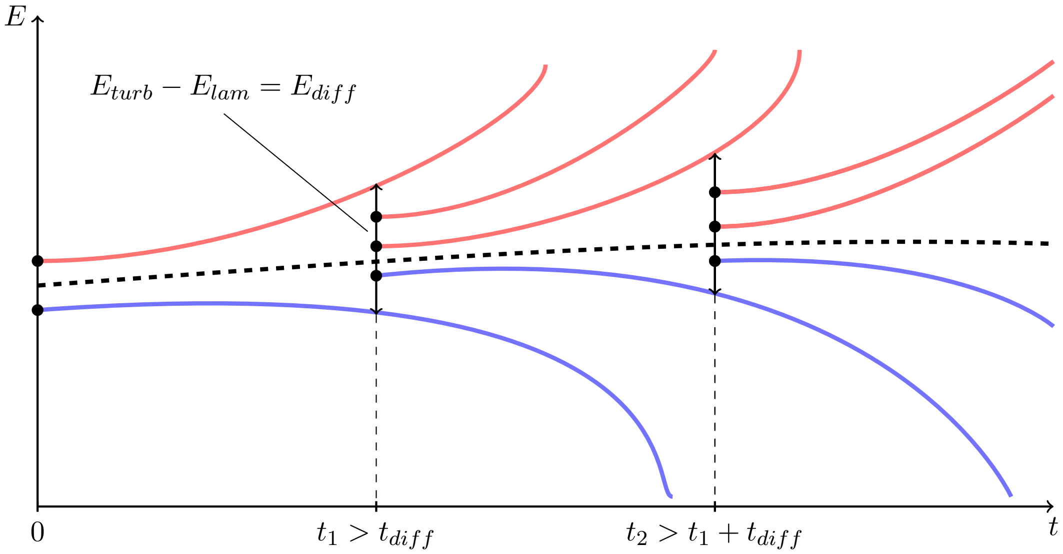

Figure 2.1: Illustration of the edge tracking algorithm explained in the text. The leftmost pair of initial conditions (black dots at $t = 0$) results in a pair of laminarising (blue curve) and turbulent (red curve) trajectories. When the difference between their energies exceeds E_{diff} at time $t_1 > t_{diff}$, we take the corresponding snapshots of the laminarising and turbulent trajectories and sample three initial conditions $\boldsymbol{u}_c, c \in \{\frac{1}{4}, \frac{1}{2}, \frac{3}{4}\}$ (black dots at t_1) equally spaced on the straight line connecting these snapshots. After time-integrating $\boldsymbol{u}_c$, we find a new pair of laminarising/transitioning trajectories and repeat the same iteration. The piecewise-defined trajectory confined between the laminarising and transitioning pieces (dashed curve) approximates the edge trajectory approaching the corresponding edge state for large enough t.

edge trajectory:

$$\boldsymbol{u_{edge}}(t) = \frac{1}{2}\left[\boldsymbol{u}\left(t; \boldsymbol{u}^{(j)}_{\boldsymbol{lam}}\right) + \boldsymbol{u}\left(t; \boldsymbol{u}^{(j)}_{\boldsymbol{turb}}\right)\right], \quad t \in [t_{j-1}; t_j], \tag{2.75}$$

where j denotes the j-th iteration of the algorithm, $\boldsymbol{u}^{(j)}_{\boldsymbol{lam}}$ and $\boldsymbol{u}^{(j)}_{\boldsymbol{turb}}$ are a pair of laminarising/transitioning initial conditions at the j-th iteration and $\boldsymbol{u}(t; \boldsymbol{u_{IC}})$ denotes a trajectory emanating from an initial condition $\boldsymbol{u_{IC}}$. Owing to the definition of the edge of chaos, the edge trajectory slides along the stable manifold of a local attractor confined to the edge of chaos, i.e., the edge state, and is expected to approach it as $t \to \infty$. Two parameters of the algorithm, E_{diff} and t_{diff}, determine the properties of the convergence of the edge trajectory to the edge state. The former, E_{diff}, specifies the small neighbourhood of the edge manifold within which the edge trajectory is guaranteed to lie, whilst the latter, t_{diff}, defines how much time $\boldsymbol{u_{edge}}(t)$ is guaranteed to be within this neighbourhood during one iteration of the algorithm. Increasing t_{diff} and decreasing E_{diff} clearly stabilise the algorithm while requiring more computational time due to the increased number of iterations, and their particular values are found empirically. Finally, the convergence properties may strongly depend on Re, and the values of t_{diff} and E_{diff} should be changed correspondingly (the values mentioned above are useful for $Re = 500$). For example, trying to compute the edge state in the domain $4.08\pi \times 2 \times 1.05\pi$ at $Re = 1000$ (the flow configuration used in [154]) in the absence of control, we found that the edge tracking algorithm with $E_{diff} = 1.25 \times 10^{-3}$ does not converge to a steady state for at least $t = 3000$ time units and requires to lower E_{diff} down to $E_{diff} = 6.25 \times 10^{-4}$ to exhibit convergence within $t = 2000$ time units. At the same time, one must remember that the speed of convergence depends on the random initial condition $\boldsymbol{u}_{\perp}$ we use to initialise the edge tracking, so one is advised to do several edge tracking runs with different initialising perturbations.

Chapter 3

Homoclinic snaking

The cornerstone of our research of spatially extended plane Couette flow (Chapters 4 and 5) is using exact solutions of plane Couette flow as the initial conditions for time-integration. Most of the exact solutions considered in this thesis are spatially localised and found on interwined branches known as homoclinic snaking branches which were already introduced in Chapter 1. In Section 3.1, we discuss homoclinic snaking found in plane Couette flow and explain how it can be used as a source of initial conditions. Linear stability analysis of the snaking branches is presented in Section 3.2. Despite the incompleteness of this analysis, it appears to be useful for further chapters. One of the snaking branches is shown to have a subcritical Hopf bifurcation which gives rise to a branch of spatially localised periodic orbits whose manifolds seem to orchestrate the dynamics of spatially localised states in the vicinity of the snaking region. We discuss the dynamics of one of these time-periodic orbits in Section 3.3, concluding the chapter, in detail.

3.1 Homoclinic snaking as a source of initial conditions

In plane Couette flow, homoclinic snaking was first computed by Schneider *et al.* in domain $\Gamma_x \times 2 \times \Gamma_z = 4\pi \times 2 \times 16\pi$ by numerical continuation of localised equilibria (EQ) and travelling waves (TW), both found at $Re = 400$ [64]. The latter were edge states found using edge tracking algorithm and possessing a shift-reflect symmetry: $[u, v, w](x, y, z) \longrightarrow [u, v, -w](x + \Gamma_x/2, y, -z)$. The former, while still lying on the edge of chaos, had an additional unstable eigendirection connected to the stable manifolds of the TW solutions and were reflection-symmetric: $[u, v, w](x, y, z) \longrightarrow [u, v, w](-x, -y, -z)$. The two resulting snaking branches, EQ and TW, inherited the reflection and shift-reflect symmetries respectively. We also label their lower parts, associated with the edge states and populated by the smallest localised solutions, as EQ_LOW and TW_LOW respectively.

Since our prime goal is to investigate the dynamics of the localised solutions and their possible growth, we doubled the size of this domain in the spanwise direction and recomputed the snaking branches. To do this, we took one solution from each branch computed in the aforementioned domain and first continued them in Γ_z from 16π to 32π. Then, the localised solutions in the larger domain were continued in *Re* up and down so that the snaking branches were recovered. The resulting homoclinic snaking is shown in figure 3.1 where we used the enstrophy $\mathcal{E}$ to characterise the solutions ($\mathcal{E} = 1$

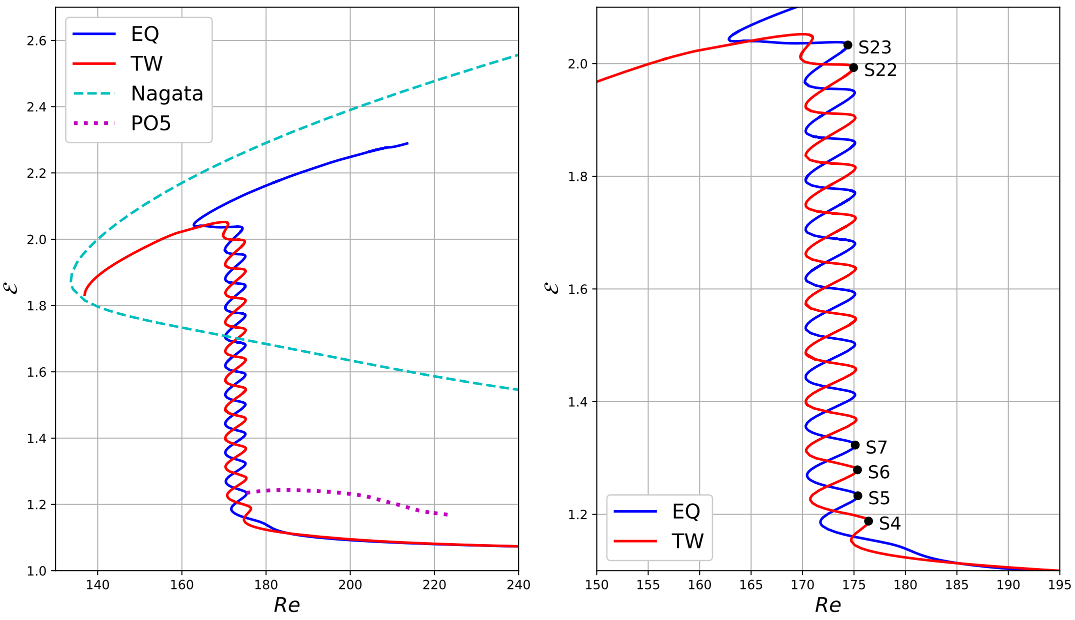

Figure 3.1: Bifurcation diagram showing homoclinic snaking in plane Couette flow. The homoclinic snaking consists of the oscillating branches of equilibria (EQ, shown in blue) and travelling waves (TW, shown in red). The right saddle-node states are purposefully named Si, where i denotes the number of rolls in a particular state. The travelling waves branch reconnects the lower branch of Nagata solutions (dashed line), one example of which is shown in figure 1.2. The dotted line denotes the branch of spatially localised periodic orbits PO5 bifurcating from EQ.

corresponds to the laminar state).

With each oscillation of the branches in the parameter space, localised states gain one additional wavelength of the streak and roll pattern. Due to the finite size of the domain, this process terminates at the top of the snaking where localised states are nearly domain-filling. There, the branch TW turns to lower Reynolds numbers and reconnects the spatially periodic branch of lower Nagata solutions where the bifurcation point is associated with the Eckhaus-type instability [171]. In contrast, the branch EQ does not seem to connect any spatially periodic branch, but rather grows along the upper Nagata branch to larger Re preserving a small localised defect close to the periodic boundaries as shown in figure 3.2(a). This situation is similar to the homoclinic snaking in doubly diffusive convection with non-periodic [98] and periodic [171]

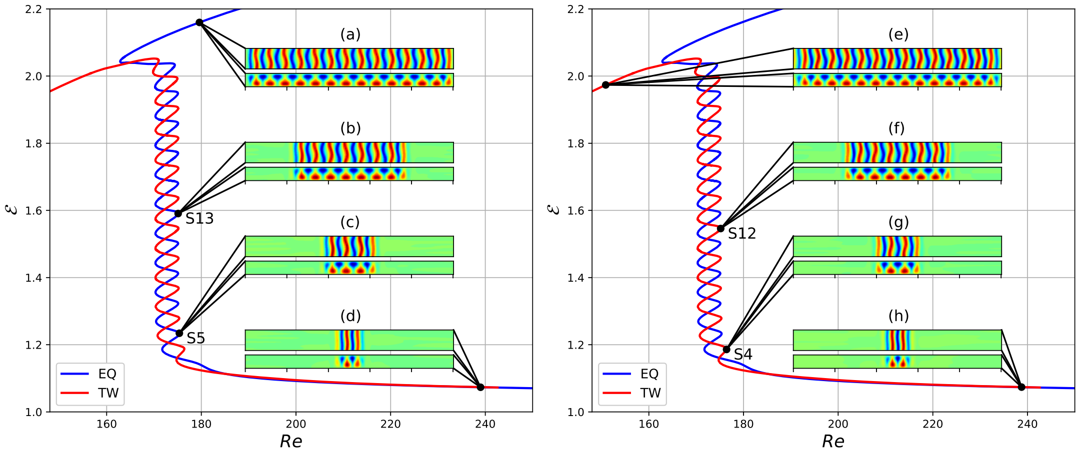

Figure 3.2: Same bifurcation diagram as in figure 3.1 with the flow field representations of the localised equilibria (a–d) and travelling waves (e–h). See figure 1.2 for the definition of the representation scheme of the insets.

boundary conditions. For some reason, the system finds it energetically preferable to retain the localised defect in all these cases in contrast to the homoclinic snaking in the Swift–Hohenberg equation where both branches reconnect the corresponding spatially periodic branches [171]. This phenomenon is however sensitive to changes in the aspect ratio of the domain as pointed out in [171]. Additionally, we note that the left and right boundaries of the snaking branches appear to converge to the fixed values $Re \approx 170.30$ and $Re \approx 175.16$ respectively as $\mathcal{E}$ is increased which defines the boundaries of the pinning region. Such an asymptotic behaviour of the snaking in a finite-size domain was addressed in [87] for the case of plane Couette flow where the boundaries were found to scale as $\mathcal{E}^{-1}$.

The right saddle-node states of both branches are of particular importance for us since we will use them as initial conditions for time-integration in the following chapters. As shown in the left plate in figure 3.1, we mark them as S4, S5, etc., where the number after S denotes the number of rolls the corresponding localised state possesses. Since the rolls are only weakly dependent of the x-coordinate in our solutions, we employ the vorticity averaged in the streamwise direction to count the number of rolls:

$$\langle \boldsymbol{\omega} \rangle_x = \frac{1}{\Gamma_x} \int_0^{\Gamma_x} (\nabla \times \boldsymbol{u}) dx, \tag{3.1}$$

where $\boldsymbol{\omega} = [\omega_x, \omega_y, \omega_z]$. The local maxima of its streamwise component, $\langle \omega_x \rangle_x$, when

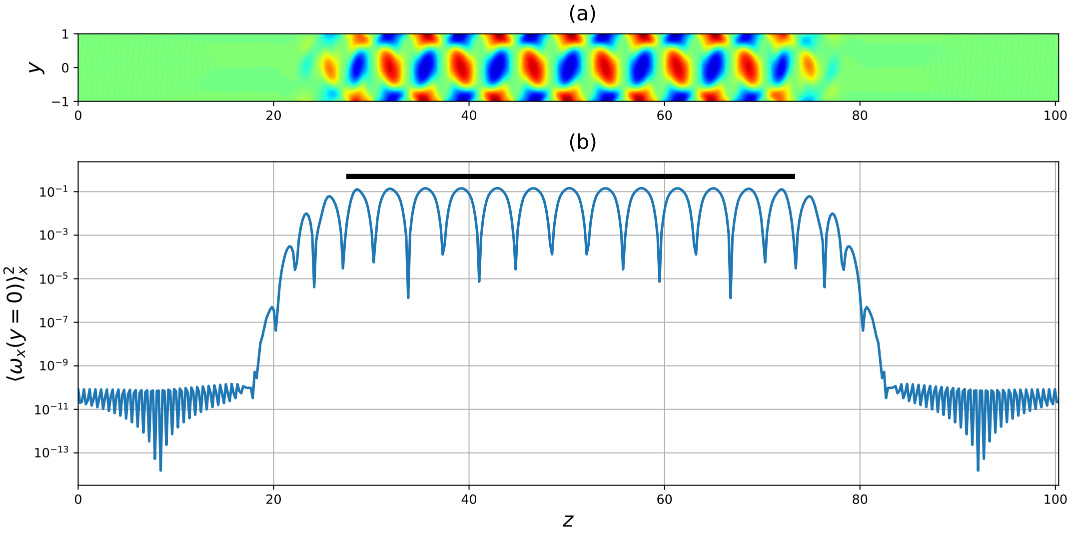

Figure 3.3: The top panel shows the streamwise vorticity of S13 averaged in the streamwise direction. The colored blobs of vorticity in the middle between the walls define the regions occupied by rolls. The bottom plate corresponds to the same quantity, but evaluated at $y = 0$ and squared. The local maxima of the resulting function are associated with the locations of the roll centres. The oscillations on the tails of the localised structure occur due to the numerical inaccuracy. Their magnitude, $O(10^{-10})$, gives an estimation for the numerical error involved in the calculation of this exact solution.

squared and evaluated at the midplane $y = 0$, can be associated with the roll centre locations as one can notice comparing the insets (a) and (b) in figure 3.3. The number of rolls is thus defined as the number of local maxima in the core region of the localised state [87]. For the localised equilibrium S13, figure 3.3(b) shows that the number of rolls in the core region, highlighted by the black line, is 13 which justifies the name of this solution.

Our choice of Si, $\mathrm{i} = 4, 5, \ldots, 23$, as initial conditions is motivated by several reasons. First of all, the right saddle-node states were found to exhibit depinning, i.e. a steady front growth, in the case of the Swift–Hohenberg equation as explained in Section 1.1.4. Thus, these are a natural choice to perform numerical experiments in the very vicinity of the right boundary of the snaking which could potentially reveal a presence of depinning in plane Couette flow and, therefore, establish a strong link between the spanwise growth of the fronts of turbulent spots and depinning. This motivation is

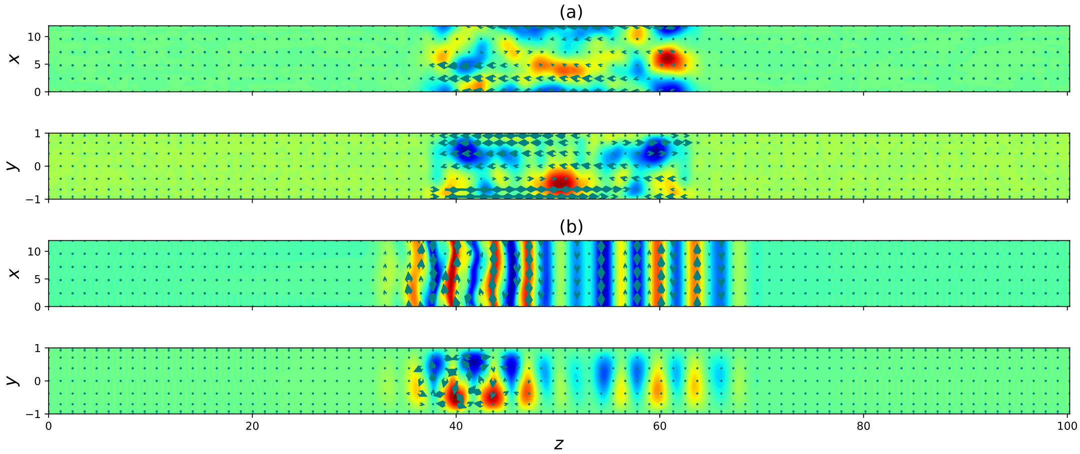

Figure 3.4: Two snapshots of the velocity field taken from the time-integration of a random localised perturbation in the domain $\Gamma_x \times 2 \times \Gamma_z = 4\pi \times 2 \times 32\pi$ at the subcritical Reynolds number $Re = 300$ at $t = 0$ (a) and $t = 200$ (b). See figure 1.2 for the definition of the representation scheme of the insets. The random perturbation was generated by sampling the spectral coefficients uniformly and then localising the central spot using the rectangular function.

further reinforced by the work by Duguet *et al.* demonstrating depinning-like front growth in plane Couette flow in a slightly smaller domain [92].

Secondly, our initial conditions are made of streaks and rolls, dominant features characterising near-wall turbulence (the buffer layer of wall-bounded turbulence) [41, 172, 173]. Many experimentalists mention a formation of streaky flow around localised perturbations such as permanent beads [83, 84, 174] or brief transverse jet streams [175]. This phenomenon can be easily replicated by the time-integration of a random localised perturbation where the internal tools of Channelflow were employed for its generation [162]. Figure 3.4 shows that, for 200 time units, it relaxes to streaky flow organised into two clusters one of which exhibits viscous decay characterised by the streamwise-independent streaks and another one resembles an intermediate state between localised equilibria shown in panels (c) and (d) in figure 3.2. The formation of clusters or spots, which we call splitting, and their spontaneous growth and decay will be discussed in Section 4.3.

Thirdly, the selected states form a discrete set of initial conditions well-parameterised by the number of rolls i. Given that this problem is infinite-dimensional, it has always been of prime importance to find a way to parameterise initial conditions such that one only needs to scan one- or two-dimensional space while investigating a particular aspect of transition to turbulence. For example, in one of the earliest numerical studies on the turbulent spot formation in plane Couette flow, Lundbladh and Johansson used an analytical function, parameterised by an amplitude and imitating four pairs of rolls to find the critical Reynolds number [75]. A similar function was later used by Duguet *et al.* to discover the localised edge states [63] and statistically quantify the front growth [92] and by Couliou and Monchaux to analyse turbulent spot dynamics. A fractal structure of the laminar-turbulent boundary was identified by Schmiegel and Eckhardt by means of another function, vortex ring, which was again parameterised by an amplitude [47]. Many studies have used either linearly or nonlinearly optimal perturbations, typically composed of streamwise vortices or oblique waves, to investigate the transition boundary [52, 55, 176]. In statistical studies, a large number of initial conditions can often be obtained from the snapshots of turbulence simulated at higher Reynolds numbers [92, 121, 122, 126]. Finally, uncorrelated noise has been employed to study statistics of lifetimes in pipe flow [119], oblique turbulent bands near the onset of transition [177] and statistical features of turbulent spot growth [178], where a square, cut from a snapshot of turbulence, was embedded into the laminar flow to mimic a turbulent spot. Our initial conditions are fixed in amplitude, but allow for a distrete variation of the width quantified by the number of rolls.

The concluding motivation for our choice of initial conditions is that all of these states are reproducible even for wider domains which makes them particularly suitable for assessment and comparison of the efficiency of control strategies. We must however notice that the states are robust only to the increase of the spanwise wavelength. Its decrease may result in the significant changes of the tails and even interior of the localised structure. Furthermore, since our states are localised in the spanwise direction only, any changes of the streamwise wavelength of the domain also significantly affect them as well as the whole homoclinic snaking [87].

3.2 Stability analysis

In this section, we present linear stability analysis of a segment of branch EQ from its lower part, named EQ_LOW, to S7 and that of all EQ solutions Si, $\mathrm{i} = 5, 7, \dots, 23$. Figure 3.5 shows the evolution of leading eigenvalues for the solutions found at EQ_LOW (bottom), a segment between EQ_LOW and S5 (middle) and around S5 (top) as a function of $\mathcal{E}$ and Re. First of all, for all the EQ solutions, we find two marginal eigenvalues associated with the streamwise and spanwise translations owing to the periodic boundaries: such translations do not change the stability of a solution. These two real eigenvalues may collide into one complex eigenvalue with a negligible real part (see, for example, the marginal eigenvalues at $Re = 182$ in figure 3.5). We then note that for $Re \gtrsim 200$, branch EQ_LOW is twice unstable. The leading unstable eigenmode is the amplitude mode associated with depinning and denoted D1 on the figure. It has the same reflection symmetry as all the equilibria found at EQ. The second unstable eigenmode for these Reynolds numbers is the phase mode associated with the TW solutions and denoted P1 on the figure. Indeed, following the analysis by Schneider *et al.* in [62], we can expect that perturbing an EQ_LOW solution along the phase eigenmode would lead the flow to a TW solution via a heteroclinic connection which implies that TW_LOW (the lower part of branch TW) is only once unstable and, thus, more stable than EQ_LOW for $Re \gtrsim 200$. In contrast, perturbing an EQ_LOW solution along the depinning eigenmode results in either quick decay or temporary depinning of the flow state typical for the edge state (see Section 4.6 for details). In other words, we can say that a perturbation along the depinning/phase modes is orthogonal/tangential to the edge manifold respectively for the EQ_LOW solutions. To illustrate the dynamics associated with the depinning mode, figure 3.6 shows the space-time plot of the xy-averaged kinetic energy, defined as

$$E_{xy}(z) = \frac{1}{4\Gamma_x} \int_0^{\Gamma_x} \int_{-1}^{1} |\boldsymbol{u}|^2 dx dy, \tag{3.2}$$

for the flow obtained via a slight perturbation of the EQ_LOW solution at $Re = 186.17105$ along this eigenmode. One can observe that the flow exhibits clear depinning for the first 1000 time units and then, after the flow readjustment, it starts approaching the periodic orbit correspoding to a PO5 solution. Thus, figure 3.6 presents a heteroclinic connection between the EQ and PO5 solutions.

At $Re \approx 200$, the eigenvalue associated with the phase mode crosses zero making the mode stable for $Re \lesssim 200$. This causes a bifurcation associated with a branch of so-called rung solutions connecting EQ and TW branches and not computed in this study (see figure 6 in [179], figure 2 in [64] and figure 7 in [88] for examples of rung branches). We continue studying linear stability of the EQ solutions in the middle

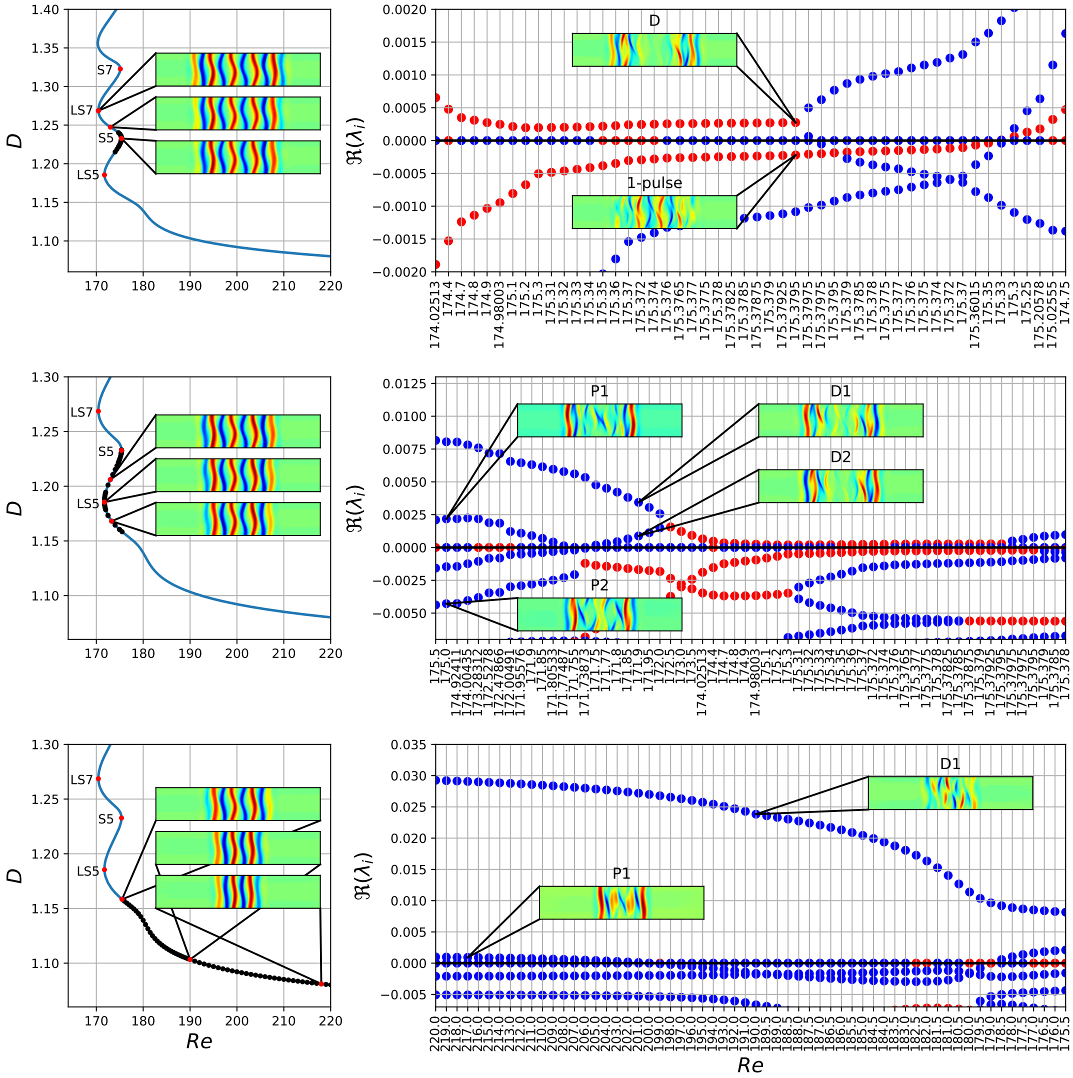

Figure 3.5: Right plots show the evolution of the real parts of the leading eigenvalues λ_i of the EQ solutions along lower segments of branch EQ, namely, EQ_LOW (bottom), a segment between EQ_LOW and S5 (middle) and a segment around S5 (top). Blue and red dots denote real and complex eigenvalues respectively. Insets show the real parts of the eigenfunctions of selected eigenvalues. Left plots show the bifurcation diagrams of the lower segment of EQ branch (black dots correspond to the solutions whose leading eigenvalues are plotted on the right).

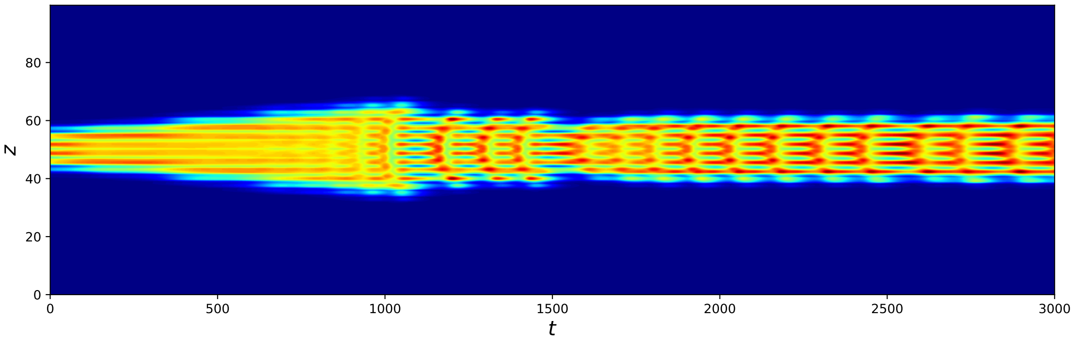

Figure 3.6: Time-evolution of the xy-averaged kinetic energy E_{xy} for the flow along a heteroclinic connection between the lower branch of EQ and PO5 obtained by perturbing the localised equilibria found at the lower part of EQ at $Re = 186.17105$ and perturbed along the depinning eigendirection. Blue color in the contours corresponds to the laminar regions and red color corresponds to the maximum values of the turbulent regions.

part of figure 3.5 which shows a segment of branch EQ between EQ_LOW and S5. Following the evolution of the phase mode along the branch, we can notice that it becomes unstable at $Re \approx 179$ (figure 3.5(bottom)) and then stabilises back close to the left saddle-node at $Re \approx 171.755$ figure 3.5(middle): both bifurcation points are associated with rung branches. Soon after that, the associated real eigenvalue collides with another real eigenvalue, denoted P2, producing the complex eigenvalue associated with the phase mode. This stable eigenvalue remains complex until it starts approaching the right saddle-node bifurcation S5, where at $Re \approx 175.3$, it splits back into two real eigenvalues. Collision of two real eigenvalues, associated with the phase mode, into a complex one and its further splitting back into two real ones were already observed in linear stability analysis of snaking branches in doubly diffusive convection [99, 180]. Similar situation occurs for the depinning mode. One can observe that the leading unstable eigenvalue D1, associated with this depinning mode, collides with another real and unstable eigenvalue D2 just above the left saddle-node at $Re \approx 172.5$ making the depinning mode oscillatory. The saddle-node bifurcation LS5, in turn, occurs because the real eigenvalue D2 crosses zero at $Re \approx 171.73873$.

One can notice that the amplitude mode is the only unstable mode on the branch segment between LS5 and S5 in figure 3.5(middle). In the close vicinity of S5, analysed in figure 3.5(top), the complex eigenvalue D associated with the depinning mode splits into two real ones D1 and D2 at $Re \approx 175.3795$ and then one of them, D2, crosses zero at $Re \approx 175.37975$: this bifurcation point corresponds to the saddle-node bifurcation S5. The stabilised depinning mode D2 will cross zero again at the next left saddle-node LS7 and then collide with D1 producing again the oscillatory amplitude mode D. On the branch segment from LS7 to S7, the stability scenario associated with the amplitude and phase modes is the same as on the segment from LS5 to S5 with only one exception: the oscillatory depinning mode D stabilises through the Hopf bifurcation in the middle of the segment between LS7 and S7 and destabilises again through another Hopf bifurcation extremely close to S7, at the distance $\triangle Re \propto O(10^{-7})$ from the saddle-node. Similar to the S5 scenario, the oscillatory depinning mode then splits into two real eigenvalues one of which stabilises giving rise to the saddle-node bifurcation associated with S7. Given an extremely small distance between the second Hopf and saddle-node bifurcations, our linear stability analysis around S7 may be numerically unreliable. Nonetheless, this stability scenario for the right saddle-node bifurcations is strikingly similar to that identified by Watanabe *et al.* in the case of the snaking branch of equilibria in two-dimensional binary fluid convection (see figure 7 in [180]). In their case, the Hopf bifurcations occur at the distance $O(10^{-3})$ from the right saddle-node bifurcations. One may suspect that in our case, this distance can be increased by changing the streamwise wavelength of the domain which would make the stability analysis in the proximity of S7 more reliable.

In addition to the amplitude and phase modes, we can find so called n-pulse modes, oscillatory modes which subsequently destabilise and thus increase the dimension of the unstable manifold as we move up along the snaking (see figure 10 in [87]). The first such mode, 1-pulse mode, destabilises slightly above S5 at $Re \approx 175.33$ (see figure 3.5(top) where it is denoted as "1-pulse") through a Hopf bifurcation which gives rise to PO5 discussed in detail in Section 3.3. This oscillatory mode remains the leading unstable eigenmode for all the right saddle-node equilibria and, thus, dominates the dynamics in the close vicinity of the snaking region as will be demonstrated in Section 4.2. From figure 3.8 showing the eigenvalues associated with linear stability of n-pulse modes and evaluated at the saddle-node solutions, we can also read that for $n \geq 2$, n-pulse mode destabilises between saddle-nodes $\mathrm{S}(4n+1)$ and $\mathrm{S}(4n+3)$. An important property of

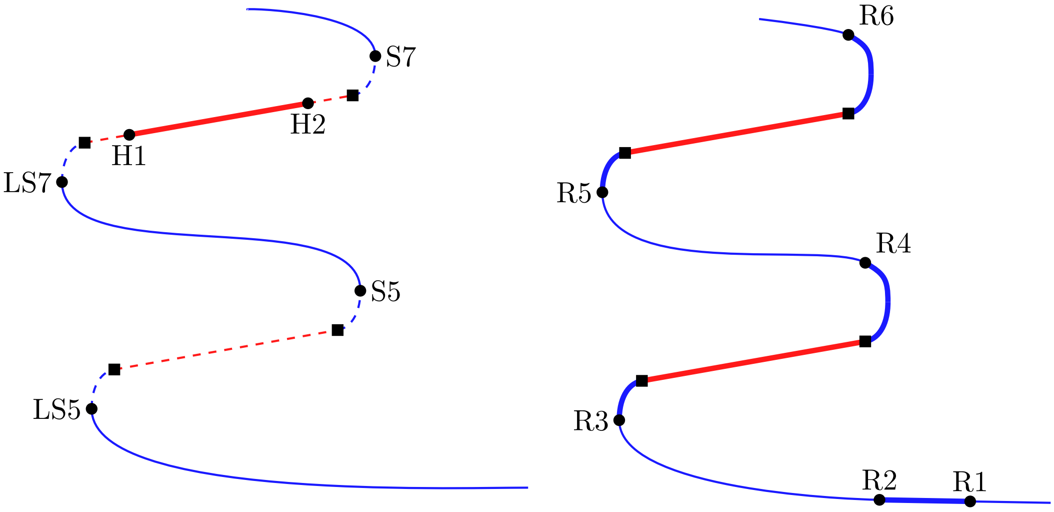

Figure 3.7: Illustration of the stability of the depinning (left) and phase (right) modes. Each mode is associated with two eigenvalues which can be both real (blue) or form a pair of complex conjugates (red). Real depinning (phase) modes correspond to D1 and D2 (P1 and P2) in figure 3.5. Oscillatory depinning mode corresponds to D in figure 3.5. By the curve type, we illustrate one of three cases of the mode stability: both eigenvalues associated with the mode are stable (thick solid), one eigenvalue is stable and another one is unstable (thin solid) and both eigenvalues are unstable (thin dashed). Dots denote saddle-node (LS5, S5, LS7, S7), Hopf (H1, H2) and symmetry-breaking rung (R1, R2, R3, R4) bifurcations. Note that the distance between H2 and S7 in the parameter space is of order of $O(10^{-7})$ and the stability analysis for a segment between H2 and S7 may thus be unreliable due to possible numerical inaccuracy.

all the n-pulse modes is that they seem to remain unstable for all the solutions located above the associated bifurcation points at EQ branch, where a particular mode becomes unstable, with the growth rates increasing as the width of a localised solution becomes larger.

To exemplify the dynamics induced by the n-pulse modes, we perturb EQ solution S17 within the plane spanned by the real and imaginary parts of the complex n-pulse eigenvector $\boldsymbol{e_{np}}$ and use the following initial condition for time-integration:

$$\tilde{\boldsymbol{u}}_{\boldsymbol{n}} = \boldsymbol{u_{S17}} + c \max_{x,y,z} |\boldsymbol{u_{S17}}| \left[\frac{\operatorname{Re}(\boldsymbol{e_{np}})}{\max\limits_{x,y,z} |\operatorname{Re}(\boldsymbol{e_{np}})|} + \frac{\operatorname{Im}(\boldsymbol{e_{np}})}{\max\limits_{x,y,z} |\operatorname{Im}(\boldsymbol{e_{np}})|} \right], \tag{3.3}$$

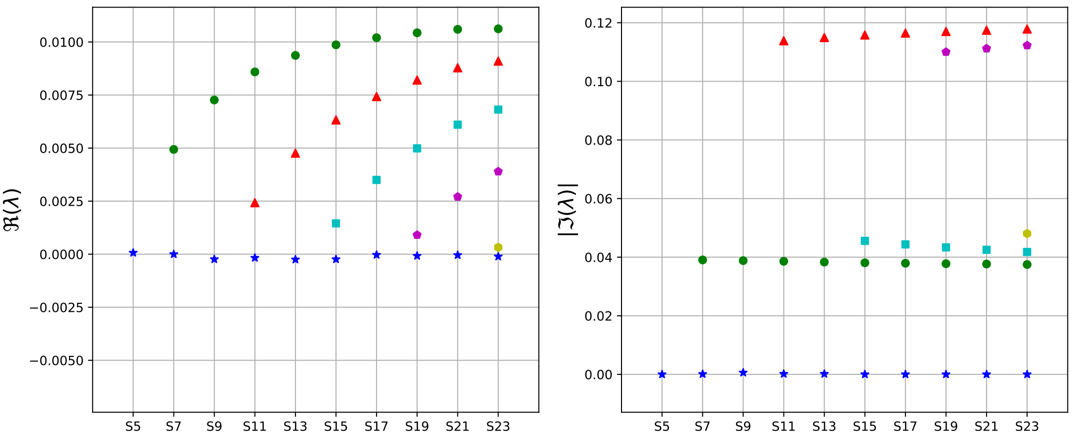

Figure 3.8: Left and right panels show the real and absolute imaginary parts of the unstable eigenvalues λ of the saddle-node EQ solutions respectively. Blue stars correspond to the depinning mode. Green circles, red triangles, cyan squares, purple pentagons and yellow hexagon correspond to the 1-, 2-, 3-, 4- and 5-pulse modes.

where $c = 10^{-3}$ sets a small magnitude of the perturbation. Figure 3.9 shows the resulting dynamics for $n = 1$ (c) and $n = 2$ (f) as the time-evolution of the fluctuations of the xy-averaged kinetic energy E_{xy} around its mean. As space-time plot (c) demonstrates, the dominant 1-pulse mode induces the oscillations of the whole localised pattern with the period $T \approx 165$, predicted by the linear stability analysis (figure 3.8) and close to the period of PO5 solutions found at similar Reynolds numbers (see Section 3.3). In contrast to the 1- and other odd-pulse modes, the even-pulse modes break the reflection symmetry of EQ solutions and may thus lead to the asymmetrical evolution of the flow. Figure 3.9(f) confirms this speculation for the case of the 2-pulse mode. Perturbing S17 with $\tilde{\boldsymbol{u}}_{\mathbf{2}}$ initially results in the flow readjustment ($t \lesssim 150$), characterised by the linear dynamics related to the 2-pulse mode, after which the influence of the leading instability, the 1-pulse mode, becomes dominant and the flow settles into an oscillatory motion resembling an asymmetrical version of the oscillations in figure 3.9(c): during the first half of the period of the oscillations, one half of the localised structure strengthens and another half weakens, and vice versa during the second half of the period.

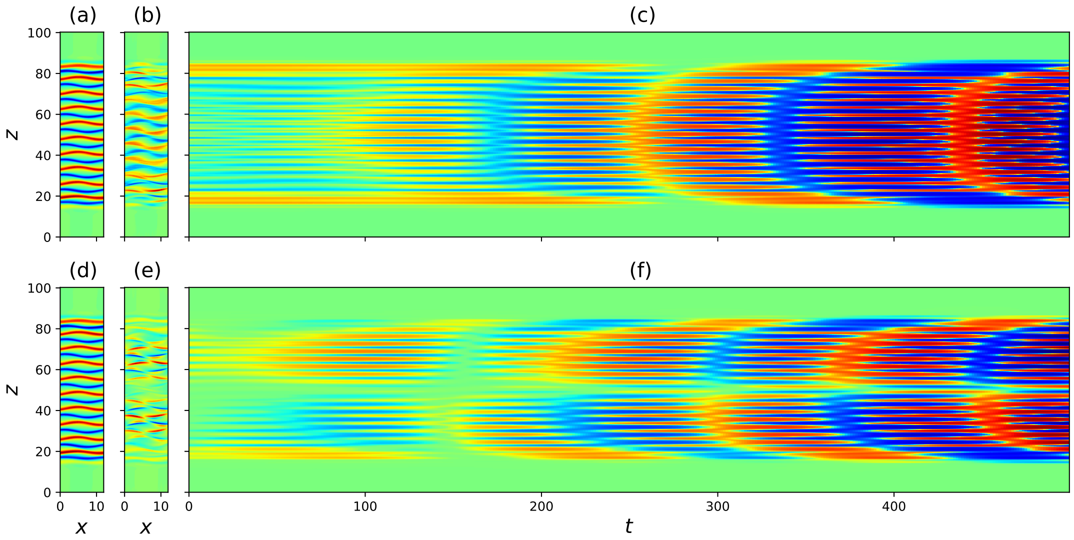

Figure 3.9: (c, d) Space-time plots of the time-evolution of the fluctuations of the xy-averaged kinetic energy E_{xy} around its mean obtained by perturbing EQ solution S17 (a, d) with $\tilde{\boldsymbol{u}}_\mathbf{1}$ (b) and $\tilde{\boldsymbol{u}}_\mathbf{2}$ (e) respectively. Contours (a, b, d, e) show the streamwise velocity at the mid-plane $y = 0$. Note that the fluctuations in space-time plots (c, d) are shown in the symmetrical logarithmic scale so that red/blue/green colors correspond to positive/negative/close-to-zero values.

3.3 Localised periodic orbits PO5

Slightly above the saddle-node bifurcation corresponding to S5, a subcritical Hopf bifurcation associated with the 1-pulse mode occurs and gives rise to a branch of spatially localised periodic orbits named PO5 and denoted by the dotted line in figure 3.1. It is not the first time when the oscillatory instability is observed near the lowest saddle-node in snaking branches – its presence was in fact observed in [181] in the case of the extended Swift–Hohenberg equation. Close to the bifurcation point, the period of the periodic orbit is $T \approx 162.6$ and grows almost linearly as the Reynolds number is increased ($T \approx 222$ at $Re = 223.65838$). Oscillatory dynamics with period $T \approx 200$ was indeed reported for Reynolds number adiabatically decreased down to $Re = 210$ in a similar spanwise-extended domain [182]. At much higher Reynolds numbers, the turbulent cycle was found to have period $O(100)$ [28, 29] which is also consistent with the period of PO5.

Figure 3.10(a) shows the xy-averaged kinetic energy of the localised periodic orbit taken from PO5 at $Re = 200.41072$ for several periods $T \approx 189$. Since the flow dynamics at the considered Reynolds numbers is mostly described via streaks and rolls and their interaction, it is sensible to analyse them separately from the remaining flow features. We find it useful to associate the streak and roll dynamics with the particular Fourier modes following Wang *et al.* [26]. We then decompose the flow into Fourier series

$$\boldsymbol{u} = \sum_{k=0}^{\infty} \boldsymbol{u}_k(y,z)e^{i\alpha k x} + c.c., \tag{3.4}$$

where $\boldsymbol{u}_k(y,z) = [u_k(y,z), v_k(y,z), w_k(y,z)]$, $\alpha = 2\pi/\Gamma_x$ and k is a non-negative integer, and associate the streaks with $u_0(y,z)$ and the rolls with $[v_0(y,z), w_0(y,z)]$. The fluctuations of the streaks and rolls are thus defined as $u_1(y,z)$ and $[v_1(y,z), w_1(y,z)]$ respectively. To eliminate the influence of the fronts, we will analyse the streak-roll dynamics of the central wavelength of the pattern which is equal to $l_z \approx 6.8$. As a result, we define the energy of the streaks and the rolls, E_u and E_v, and their fluctuations, $\widetilde{E}_u$ and $\widetilde{E}_v$, as follows:

$$E_u = \int\limits_{-1}^{1} \int\limits_{\Gamma_z/2}^{\Gamma_z/2+l_z} u_0^2(y,z)dydz, \tag{3.5}$$

$$E_v = \int\limits_{-1}^{1} \int\limits_{\Gamma_z/2}^{\Gamma_z/2+l_z} \left[v_0^2(y,z) + v_0^2(y,z)\right] dydz, \tag{3.6}$$

$$\widetilde{E}_u = \int\limits_{-1}^{1} \int\limits_{\Gamma_z/2}^{\Gamma_z/2+l_z} u_1^2(y,z)dydz, \tag{3.7}$$

$$\widetilde{E}_v = \int\limits_{-1}^{1} \int\limits_{\Gamma_z/2}^{\Gamma_z/2+l_z} \left[v_1^2(y,z) + v_1^2(y,z)\right] dydz. \tag{3.8}$$

The energy of the streaks is two orders of magnitude larger that the energy of the rolls, so space-time plots of the xy-averaged energy contain mostly information about the streak dynamics. Visually, we can isolate two phases of each period in figure 3.10(a). The first phase located between $t = T_{-}^{+} - T \approx 70$ and $t = T_{+}^{-} \approx 178$ is characterised by the weakly time-dependent flow structure. The roll energy is minimum in this phase and positively correlates with the streak growth rate which can be observed

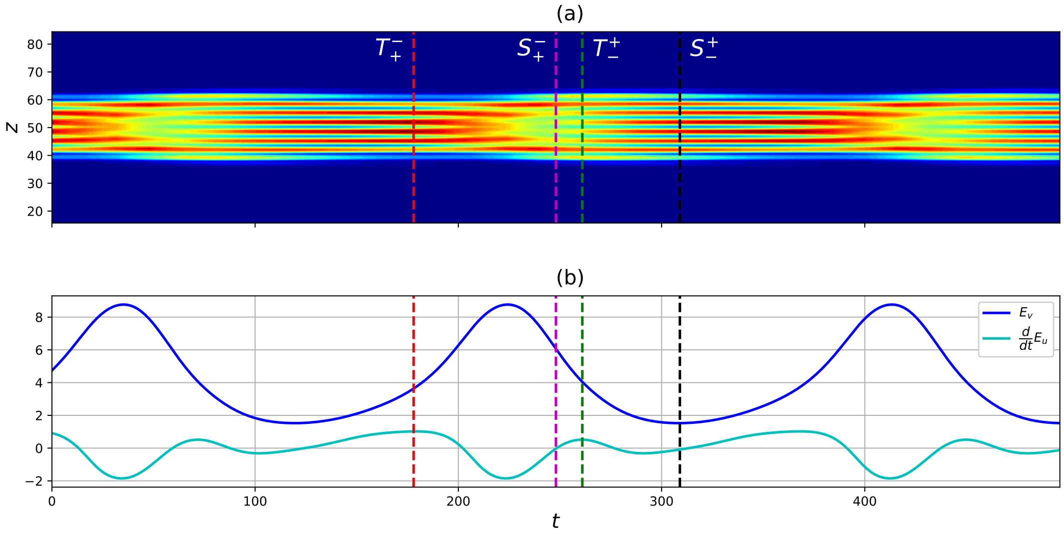

Figure 3.10: Top plot shows the time-evolution of the xy-averaged kinetic energy E_{xy} of the localised periodic orbit found at PO5 at $Re = 200.41072$. Bottom plot shows the time-evolution of the growth rate of the streaks dE_u/dt and the roll energy E_v, where E_u and E_v are defined in equations (3.5) and (3.6) respectively.

from figure 3.10(b). The second phase occuring between T_+^- and T_-^+ is characterised by the significant growth of rolls and anticorrelation between the roll energy and the streak growth rate which results in the decay of the streak energy. The boundaries of these parts, T_+^- and T_-^+, are defined as the inflection points of E_u to emphasise the transition from the correlation between dE_u/dt and E_v to the anticorrelation and vice versa. During the bursting in the second phase, we can observe the nucleation event on the fronts of the localised state which, however, is subsequently annihilated in the coming first phase.

In order to further elaborate the interaction between the streaks and the rolls, we demonstrate the most significant correlations between $E_u(t)$, $E_v(t)$, $\widetilde{E}_u(t)$ and $\widetilde{E}_v(t)$ in figure 3.11. We first note that the growth of streaks in the first phase promotes the growth of their fluctuations with a delay $\triangle t = 6$ (see plot figures 3.11(b)) which can be understood as the instability of streaks. This triggers the growth of the rolls with a delay $\triangle t = 8$ owing to a strong positive correlation between the fluctuations of streaks and those of rolls shown in 3.11(c). Shortly after that, with a delay $\triangle t = 9$, the growing roll fluctuations lead to the growth of the rolls themselves owing to a similar

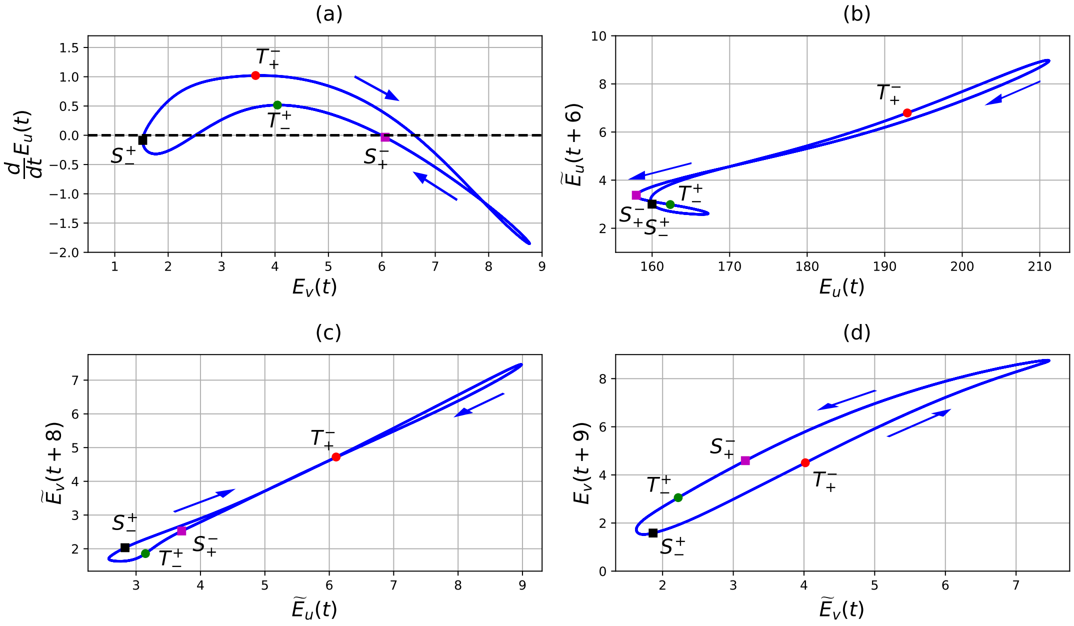

Figure 3.11: Selected correlation curves built for $E_u(t)$, $\widetilde{E}_u(t)$, $E_v(t)$, $\widetilde{E}_v(t)$ for the localised periodic orbit shown in figure 3.10(a). Since the considered flow is a periodic orbit, the curves are necessarily closed. Points T_+^-, T_-^+, S_+^- and S_-^+ and their colors correspond to those in figure 3.10.

positive correlation as demonstrated in plot 3.11(d). In the first phase, the growing rolls increase the growth rate of the streaks so that the streaks stop decaying and start growing which can be seen from figures 3.11(a) and 3.10(b). This process, however, terminates when the amplitude of rolls grows above $E_v \approx 3.63$ so that the further growth of rolls leads to the decrease of the growth rate of streaks and, consequently, to the decrease of streak energy beginning at $t \approx 202$. This turning point corresponds to $t = T_+^-$ and defines the beginning of the second phase. In the second phase, the roll energy reaches its maximum and then decays which, due to the anticorrelation between dE_u/dt and E_v in this phase, results in the increase of the growth rate of streaks so that it becomes positive at $t = S_+^-$. The anticorrelation turns to the positive correlation when the roll energy decays down to $E_v \approx 4.05$ in the vicinity of $t = T_-^+$ which signifies the end of the second phase and the beginning of the next period where all considered quantities, E_u, $\widetilde{E}_u$, E_v, $\widetilde{E}_v$, decay owing to the positive correlations between them in the first phase. It should be noted that the second phase is connected to the first phase

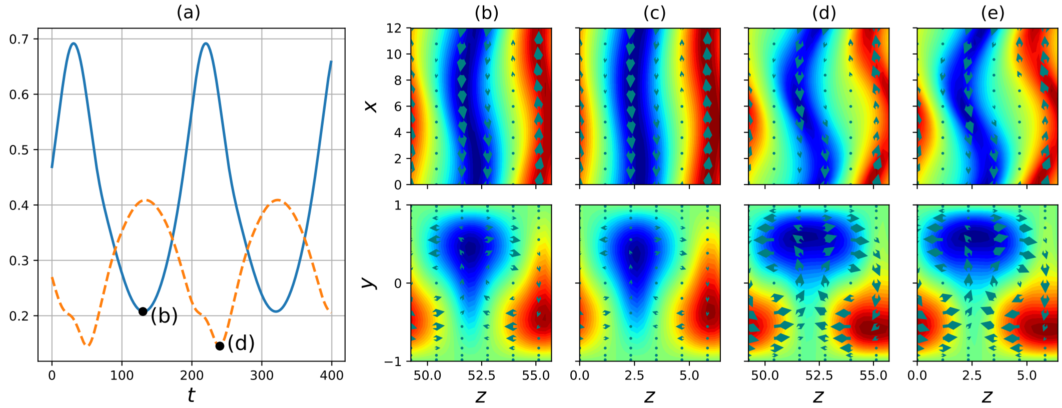

Figure 3.12: Plot (a) shows the time-evolution of the distances $||\boldsymbol{u}-\boldsymbol{u_{LN}}||/||\boldsymbol{u_{LN}}||$ (solid curve) and $||\boldsymbol{u}-\boldsymbol{u_{UN}}||/||\boldsymbol{u_{UN}}||$ (dashed curve) between the instantaneous state of the localised periodic orbit shown in figure 3.10(a) and the lower (c) and upper (e) Nagata solutions respectively. The minima of these distances, marked as (b) and (d) in plot (a), correspond to the flow states of the periodic orbit shown in contours (b) and (d). One can visually appreciate the similarity between (b) and (c) as well as between (d) and (e).

through the streak readjustment found between $t = S_+^-$ and $t = S_-^+$ which manifests as an oscillation of the growth rate of the streaks around zero (figure 3.10(b)) and the anticorrelation between the energy of streaks and their fluctuations (figure 3.11(b)).

Closer inspection of the flow states reveals that the first and second phases can be associated with approaching the lower and upper Nagata solutions respectively. In the spirit of the algorithm for verification of heteroclinic connections [40], this can be demonstrated by calculating normalised distances between the instantaneous flow state $\boldsymbol{u}$ and the lower and upper Nagata solutions $\boldsymbol{u_{LN}}$ and $\boldsymbol{u_{UN}}$, i.e., $||\boldsymbol{u}-\boldsymbol{u_{LN}}||/||\boldsymbol{u_{LN}}||$ and $||\boldsymbol{u}-\boldsymbol{u_{UN}}||/||\boldsymbol{u_{UN}}||$, where the L_2-norm is defined as

$$||\boldsymbol{f}|| = \langle \boldsymbol{f}, \boldsymbol{f} \rangle^{1/2} = \left(\frac{1}{V} \int_{\Omega} \boldsymbol{u} \cdot \boldsymbol{u} \partial\Omega \right)^{1/2}, \tag{3.9}$$

where Ω is the considered domain and V is its volume. Figure 3.12(a) shows the evolution of these distances in time. One can notice that the flow becomes close to the lower Nagata solution approximately in the middle of the first phase, $t = 130$, which corresponds to the minimum of $||\boldsymbol{u}-\boldsymbol{u_{LN}}||/||\boldsymbol{u_{LN}}||$ on the plot. The corresponding flow state, shown in figure 3.12(b), indeed resembles the lower Nagata solution which can be seen by comparing figures 3.12(b) and 3.12(c). When leaving the first phase, the flow escapes the vicinity of the lower Nagata solution and starts approaching the neighborhood of the upper Nagata solution so that $||\boldsymbol{u} - \boldsymbol{u_{UN}}||/||\boldsymbol{u_{UN}}||$ reaches its minimum close to the middle of the second phase at $t = 240$. One can compare figures 3.12(d) and 3.12(e) to verify the striking similarity between the flow state at $t = 240$ and the upper Nagata solution. We thus conclude that, locally in space, the localised periodic orbit travels between the lower and upper Nagata solutions in a nearly heteroclinic cycle where the path from $\boldsymbol{u_{LN}}$ to $\boldsymbol{u_{UN}}$ is characterised by the growing rolls and bursting whilst the backward path from $\boldsymbol{u_{UN}}$ to $\boldsymbol{u_{LN}}$ is associated with decaying rolls and relaxation of the flow.

Transition from the first phase to the second phase may correspond to the EQ1-EQ2 heteroclinic connection found by Halcrow et al. [40], where EQ1 and EQ2 denote the lower and upper Nagata solutions respectively. Bursting dynamics similar to PO5 was also observed in the relative periodic orbits found by Viswanath [43], namely solutions P2 to P6, so our periodic orbit PO5 may act as their localised analog. Finally, locally in space, the dynamics of PO5 closely resembles the regeneration cycle [28, 42] whose analysis gave rise to the self-sustained process (SSP) [30, 183]. The latter is a three-step loop describing the mechanism how the exact equilibria and travelling waves can exist and support themselves in shear flows. The SSP states are characterised by particular scalings, namely $O(1)$ streaks and $O(Re^{-1})$ rolls, which were confirmed to be true for the lower Nagata solutions [26], but not for the upper ones. Consequently, the considered periodic orbit may be related to the SSP only in the first phase whilst the second phase demonstrates transition from the SSP. While some self-sustained mechanism must support the existence of PO5, it is not precisely the same process described by Waleffe [30] and can be thought of as a time-dependent extension of the SSP.

Chapter 4

Relaminarisation of localised states in plane Couette flow

In this chapter, we report the results of a large numerical study of the dynamics of the exact localised states Si, i $= 4, 5, \ldots, 23$, i.e., the right saddle-node states of the homoclinic snaking discussed in the previous chapter. The concept of the relaminarisation time, which will be defined below, and using exact solutions as initial conditions are among the cornerstones of this thesis. Together with the quantitative outputs of this chapter, they set up a framework for the assessment of control strategies employed in Chapter 5. The main summarising result, the map of dynamics, is introduced in Section 4.1. Different regions of this map are associated with different dynamical regimes typical for the localised states: oscillations (Section 4.2), splitting of the initial spot and transient chaotic dynamics (Sections 4.3 and 4.4) and front propagation (Section 4.5). We conclude the Chapter by Section 4.6 where we present a study of transition to chaotic dynamics from the solutions found at the lower part of the branch EQ and, thus, related to the edge states.

We characterise each simulation with the corresponding relaminarisation time t_{relam}, i.e., the time it takes for the flow to reach a small neighbourhood of the laminar fixed point where the dynamics is well described by the linearised Navier–Stokes equation. In this definition, the notion of "a small neighbourhood of the laminar fixed point" remains to be explained. We shall approximate this neighbourhood by a portion of the phase space where the maximum kinetic energy of the flow, $E_{\max}(t) = \frac{1}{2}\max_{x,y,z}|\boldsymbol{u}(x, y, z, t)|^2$, is less than a properly selected threshold E_{lam}. The threshold E_{lam} should be chosen such that the flow monotonically decays once its maximum kinetic energy decreases down to E_{lam}, i.e.

$$E_{\max}(\tau) < E_{lam} \implies \frac{d}{dt}E_{\max}(\tau + \triangle\tau) < 0, \quad \triangle\tau > 0. \tag{4.1}$$

We choose a pointwise quantity, the maximum kinetic energy, rather than an integral quantity as a scalar proxy of the flow to avoid the dependence on the size of a localised state.

In order to find a suitable value for E_{lam}, we time-integrate two initial conditions, S5 and S7, for a range of Reynolds numbers evenly spaced from $Re = 183$ to $Re = 293$ with a spacing $\triangle Re = 5$. Figure 4.1 shows the time-evolution of $E_{\max}$ for all of the simulations during their final stage of relaminarisation. It can be noticed that the flow is in the regime of the exponential decay when its maximum kinetic energy drops down to 0.1 independently of the initial condition and the Reynolds number. This confirms that the flow is in the small neighbourhood of the laminar fixed point, so

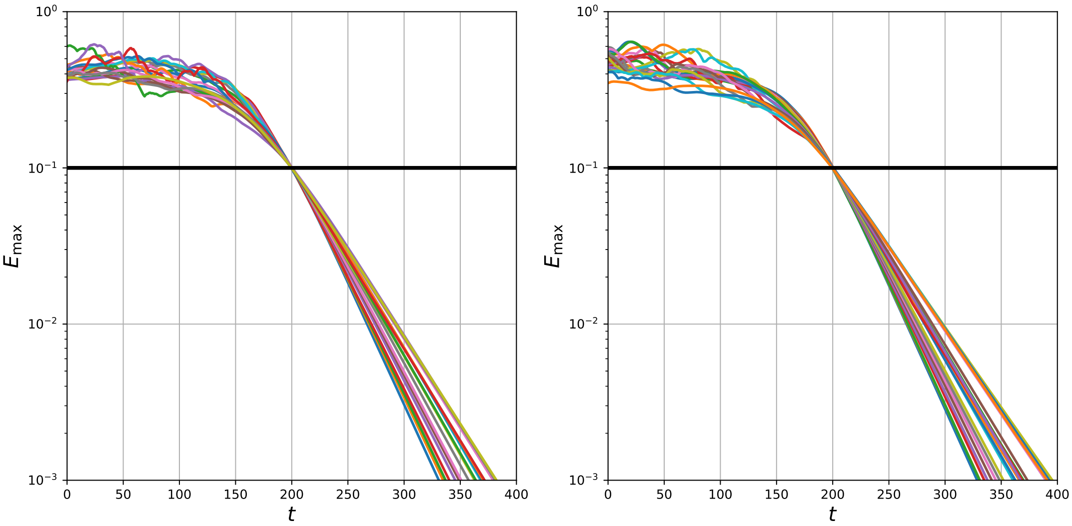

Figure 4.1: Final stage of relaminarisation of S5 (left) and S7 (right) time-integrated for Reynolds numbers evenly spaced from $Re = 183$ to $Re = 293$ with a spacing $\triangle Re = 5$. Each coloured curve corresponds to the maximum kinetic energy $E_{\max}$ plotted as a function of time for a simulation at a particular Re. The black horizontal line denotes the selected threshold for the maximum kinetic energy $E_{lam} = 0.1$. For all simulations, the time is shifted such that $E_{\max}(200) = 0.1$. Simulations sustained for more than 1000 time units are omitted.

we choose $E_{lam} = 0.1$. The relaminarisation time t_{relam} is then defined such that $E_{\max}(t_{relam}) = E_{lam}$ up to numerical accuracy.

4.1 The map of dynamics

In order to characterise the dynamics at pre-transitional Reynolds numbers, we scan the phase space by performing DNS with Si, i $= 4, 5, \ldots, 23$ as initial conditions for $Re \in (Re(\mathrm{i}); 350)$. For each simulation, we compute the relaminarisation time which results in a set of relaminarisation time curves $t_{relam}(Re)$ each of which is associated with the corresponding initial condition Si. The spacing in Re is adapted as necessary to resolve the relaminarisation time curves up to reasonable accuracy.

All the resulting relaminarisation time curves are grouped and shown in figure 4.2. Since the vertical axis can be thought of as the width of an initial condition, we

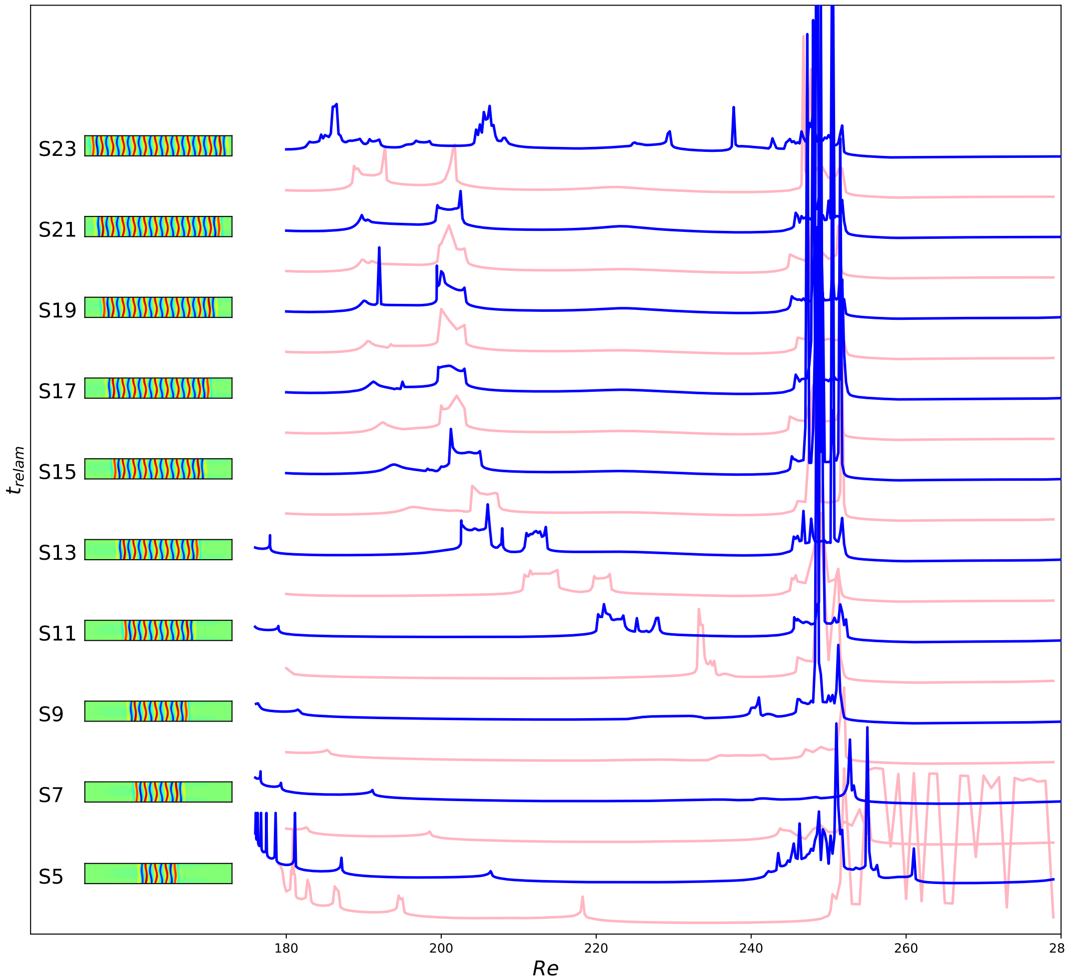

Figure 4.2: Relaminarisation time curves for localised equilibria S5, S7, . . . , S23 (blue) and travelling waves S4, S6, . . . , S22 (light pink). The contours on the left correspond to the equilibria (EQ) initial conditions and show the top view of the streamwise component of the velocity field. To align the relaminarisation time curves with the corresponding initial conditions on the left, we shifted them for each initial condition Si as follows: $t_{relam} \to t_{relam} + 1000(\mathrm{i} - 4)$.

can treat figure 4.2 as the map of the parameter space where (Re, i) is mapped into the relaminarisation time. The map demonstrates a non-trivial macroscopic structure where several regions, separated by irregularities, can be identified in the parameter space (Re, i). The close examination of the irregularities of the relaminarisation curves may be a valuable sources of information as will be shown in the remaining part of the chapter.

We first note the region adjacent to the snaking and populated by peaks in the relaminarisation time curves. This region, called R1, appears for all considered initial conditions and becomes smaller for large initial conditions. At larger Reynolds numbers, we find the region of sharply increased relaminarisation time ($500 \lesssim t_{relam} \lesssim 1500$) called R2 and charaterised by the splitting of the initial spot into two. For smaller localised states, its boundaries become closer in Re to another region named R3. This region, located roughly between $Re \approx 245$ and $Re \approx 252$, has almost no dependence on the initial condition. It is characterised by occasionally occuring long-lasting chaotic transients with large relaminarisation times ($t_{relam} \sim O(10^4)$). Similar to R2, the initial phase of the simulations in R3 is associated with the splitting of the localised state into two spots, so R3 is present only for S8 and wider localised states. We can notice that S5, S6 and S7 also produce chaotic transients with large relaminarisation times for Reynolds numbers similar to R3. However, their dynamics is not associated with splitting because of the small width of S5, S6 and S7, so we denote the corresponding region R3a to make the taxonomy clearer. The last region, called R4 and corresponding to $Re \geq 280$, is associated with eventual transition to turbulence. It is not shown in figure 4.2 and will be discussed in section 4.5. The boundaries of the aforementioned regions are presented in table 4.1. The regions are separated by smooth plateaux, hereafter called P, where the relaminarisation time is relatively small ($200 \lesssim t_{relam} \lesssim 400$) and constant. We find it sufficient to characterise them by their local minima reported in table 4.2 for all initial conditions except for S23 which does not seem to exhibit a clear organisation of regions and plateaux. Finally, it can be noted that the relaminarisation time curves do not depend on whether the initial condition is an equilibrium (S5, S7, etc.) or a travelling wave (S4, S6, etc.), so the dynamics of these localised states is also likely to be independent of the type of the initial condition. Closer examination of the simulations of the travelling waves confirms this speculation, so only equilibria S5, S7, etc. will be considered in the forthcoming discussions.

To ease the navigation among the aforementioned regions, we simplify figure 4.2 down to a schematic plotted in figure 4.3. In the following sections, we discuss the regions R1, R2, R3, R3a, R4 and the plateaux P in more details.

Si	$\max_{Re}$ R1	$\min_{Re}$ R2	$\max_{Re}$ R2	$\min_{Re}$ R3 (R3a)	$\max_{Re}$ R3 (R3a)	$\max_{Re}$ R4
S5	206.375	–	–	242.25	261	280
S7	191.125	–	–	252.75	253.25	286.5
S9	181.6875	240.0625	241	246	251.25	291.25
S11	178.98031	220.25	228	245.5625	252.25	291.75
S13	177.90536438	202.5625	213.5	245.5	251.75	287.75
S15	–	201.25	205	245.25	251.5	292
S17	–	199.625	203	245.75	251.75	289
S19	–	190	203	245.25	252	287.25
S21	–	189.75	202.5	245.75	251.75	294.5

Table 4.1: Reynolds numbers for boundaries of regions R1, R2, R3 (R3a for S5 and S7) and R4.

Si	P12	P23 or P13a	P34 or P3a4
S5	–	284.5	263
S7	–	293	229.5
S9	312.5	388.5	220.0
S11	358.0	372.5	229.5
S13	383.5	376.5	234.5
S15	393.5	378	236
S17	401.5	376	240.5
S19	404.5	379	239
S21	407.5	376.5	239.5

Table 4.2: Local minima of t_{relam} at the plateaux between regions R1 and R2 (plateau P12), R2 and R3 (plateau P23), R3 and R4 (plateau P34). Due to the absence of R2 and the replacement of region R3 with region R3a for S5 and S7, we have plateaux P13a and P3a4 for them instead of P23 and P34 respectively.

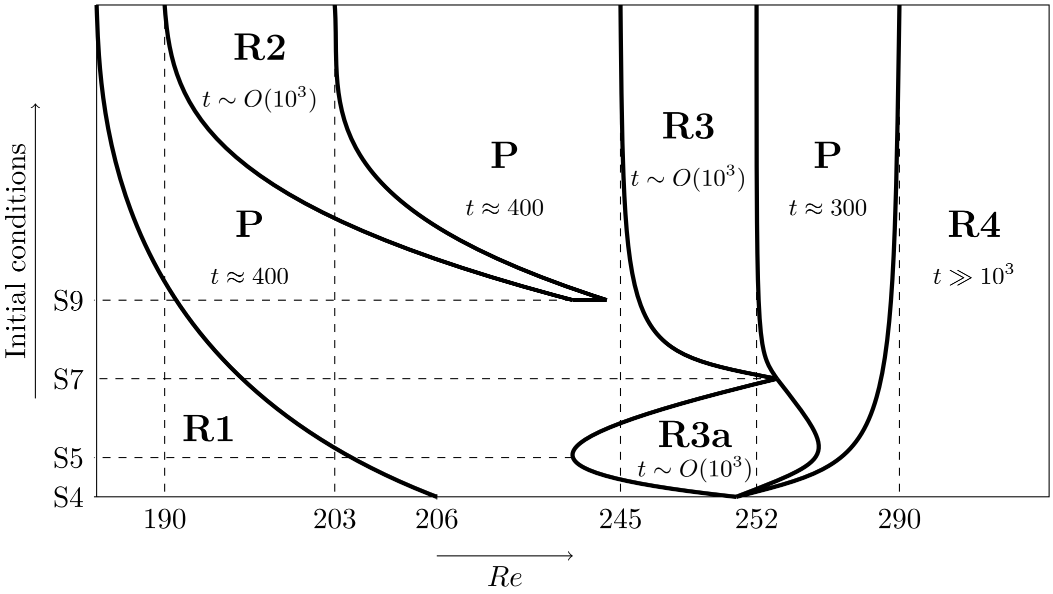

Figure 4.3: Schematic of the map of the relaminarisation time shown in figure 4.2. For most of the regions, we give an estimate of the typical relaminarisation time.

4.2 Dynamics in the vicinity of the snaking: region R1

Region R1 is adjacent to the right boundary of the snaking and, therefore, dynamics in R1 is directly influenced by the stable and unstable manifolds of the exact localised solutions. In particular, dynamics is R1 is dominated by the leading unstable eigenmode of the majority of EQ solutions, the oscillatory one-pulse mode discussed in Section 3.2. The part of a relaminarisation time curve, containing this region, is characterised by a sequence of peaks converging to Re_s(i), i.e., the right boundary of the snaking, which defines the left boundary of R1. The right boundary of R1 is then defined as the Reynolds number at which the rightmost peak is found. As can be seen from figure 4.4, the right boundary of R1 converges almost geometrically to the right boundary of the snaking as the number of rolls of an initial condition is increased.

Two representative examples of region R1 are displayed in figure 4.5. For the smallest considered equilibrium, S5, the relaminarisation time at the peaks tends to infinity (figure 4.5(a)). This is in contrast to the peaks for S7 and wider initial conditions which correspond to the finite t_{relam} and are consequently smoothed. At the Reynolds number found between the peaks, the flow exhibits several cycles of oscillations

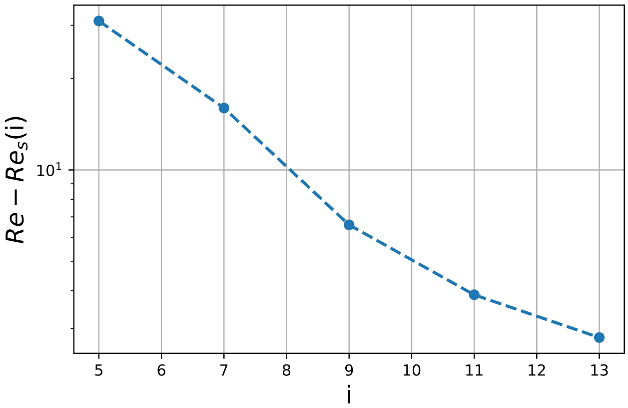

Figure 4.4: The width of region R1, defined as the distance between the rightmost peak of region R1 for the initial condition Si and Re_s(i), is plotted as a function of the number of rolls i. Owing to the vertical logarithmic scale, the width seems to converge to zero geometrically as the number of rolls increases.

and a subsequent decay. These oscillations closely resemble those exhibited by the localised periodic orbits PO5 and thoroughly discussed in Chapter 3. The decay, in turn, is characterised by a quick decay of rolls and, as a result, straightened and slowly diffusing streaks. The same decay mechanism can be observed in the case of a small domain (e.g., see figure 6 in [184] for an illustration). Crossing a peak in the direction towards the snaking corresponds to the gain of one more cycle which increases the local minimum of the relaminarisation time (green circle in figure 4.5(a)) found between two adjacent peaks (red squares in figure 4.5(a)). Consequently, for initial condition Si, the local minimum of t_{relam} tends to infinity as Re becomes closer to Re_s(i). It is clear that the relaminarisation time must be infinite at $Re = Re_s$(i) since such a simulation would correspond to the time-integration of the exact solution. Finally, if we escape region R1 by crossing the rightmost peak in the direction of increasing Re, we enter the plateau P where the flow performs only 2 oscillations.

In order to illustrate the key features of the dynamics in this region, we consider simulations to the right ($Re = 181.1875$) and to the left ($Re = 180.875$) of the peak marked by Re_n in figure 4.5(a). Figure 4.6(a) shows the trajectories of both simulations in the reduced phase space defined as $(||u||, \widetilde{v}, \widetilde{w})$ where $\widetilde{v} = ||w|| \sin 70^\circ + ||v|| \cos 70^\circ$ and $\widetilde{w} = ||w|| \cos 70^\circ - ||v|| \sin 70^\circ$ are the L_2-norms of v and w in the rotated frame

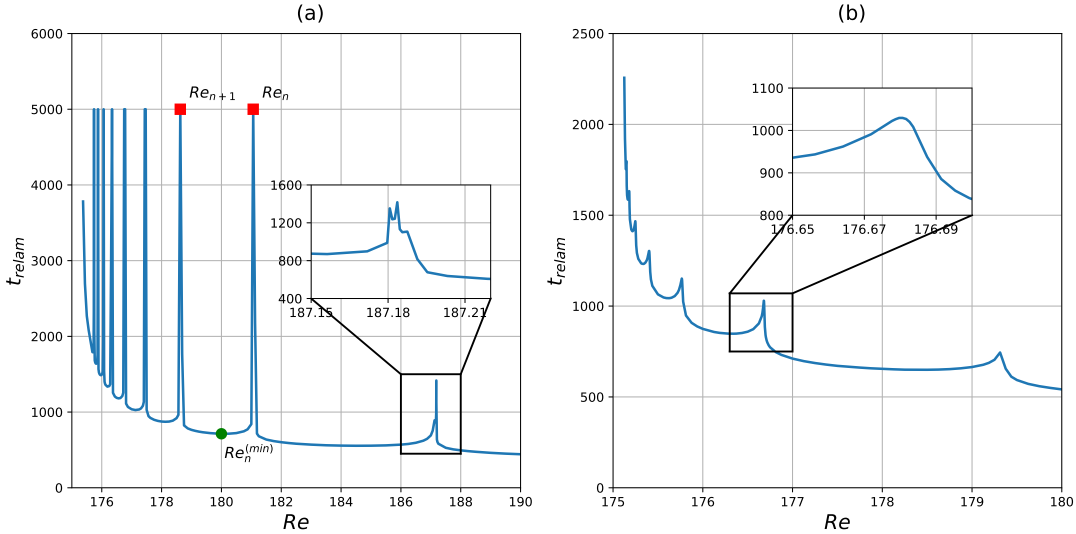

Figure 4.5: Enlargements of the relaminarisation time curves in figure 4.2 for S5 (a) and S7 (b) and corresponding to region R1. For S5, this region contains a set of diverging peaks two of which are marked by the red squares and named Re_n and Re_{n+1} where $n = 0$ corresponds to the rightmost peak in region R1 and $Re_n \to Re_s(\mathrm{i})$ as $n \to \infty$. Between any two peaks, one can find a local minimum of the relaminarisation time curve marked by the green circle and named $Re_n^{(min)}$. The inset in plot (a) shows a complex, highly sensitive to change in Re, structure of the relaminarisation time curve typical for two rightmost peaks for S5 and all the resolved peaks for S4. Wider initial conditions have only smoothed peaks associated with finite t_{relam} which is illustrated by the inset in plot (b).

of reference. The trajectories, both emanating from S5, perform 4 cycles together and then diverge. The trajectory corresponding to the simulation to the right of the peak decays whereas another trajectory goes for one more cycle and decays only after completing this additional cycle. Similarly, the addition of a cycle can be observed from the space-time plots of the xy-averaged kinetic energy E_{xy} shown in figure 4.6(b, c) and corresponding to the trajectories in figure 4.6(a). Diverging trajectories imply that some invariant structure exists in the neighbourhood where the trajectories start moving in opposite directions in the reduced phase space. Indeed, the time-integration of S5 at Reynolds number corresponding to the peak Re_n in figure 4.5(a) reveals a trajectory that escapes from this neighbourhood and seems to be attracted by a new invariant

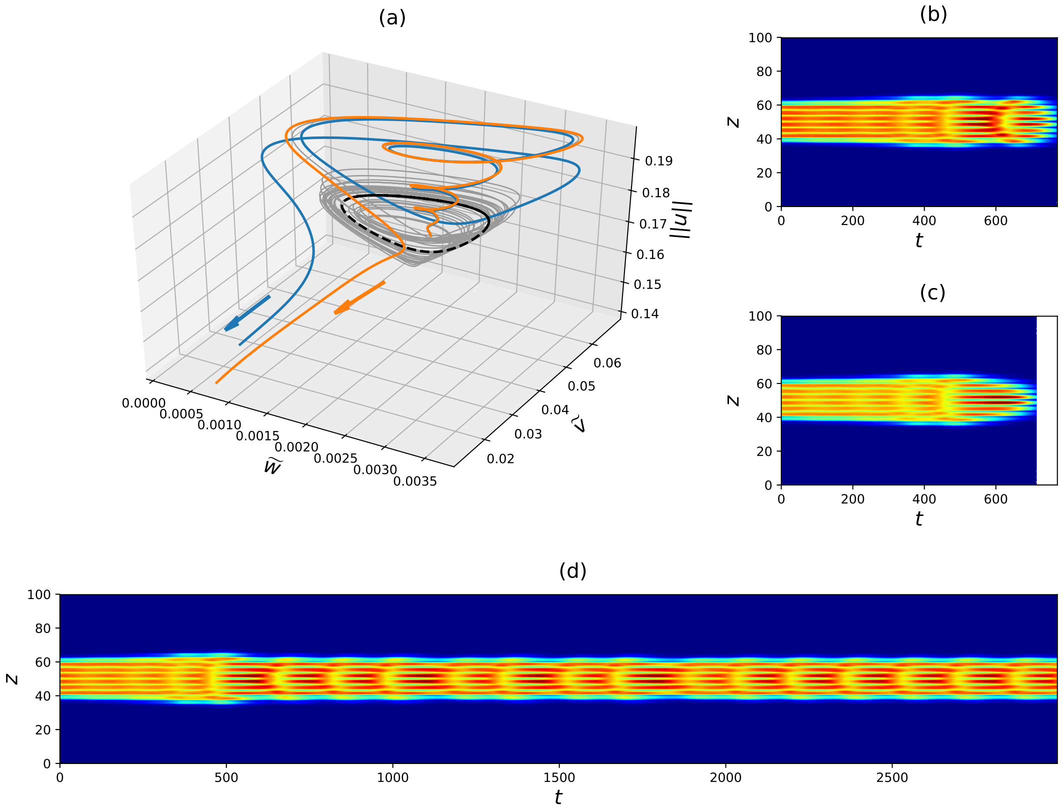

Figure 4.6: Time-evolution of S5 integrated at the Reynolds number to the right of the peak Re_n in figure 4.5(a) (orange curve in plot (a) and the space-time plot for E_{xy} in plate (c)) and to the left of the same peak (blue curve in plot (a) and the space-time plot for E_{xy} in plate (b)). Plot (a) shows the trajectories in the reduced phase space explained in the text whose direction is emphasised by the arrows of the corresponding colors. One can observe that the trajectory corresponding to Re to the right of the peak has one less cycle of oscillations so crossing a peak can be associated with the gain of one additional cycle. The trajectory obtained by time-integration of S5 at the peak (gray curve in plot (a) and the space-time plot for E_{xy} in plate (d)) appears to be attracted by a spatially localised periodic orbit (dashed black curve in plot (a)) belonging to the branch PO5.

set. Looking at the time-evolution of E_{xy} shown in figure 4.6(d), we can observe that the flow converges to a spatially localised periodic orbit. Using a representative part of the flow as a guess for the Newton–Krylov search, we confirm that the corresponding periodic orbit lies on PO5, a branch of spatially localised periodic orbits discussed in Section 3.3. This periodic orbit is shown in figure 4.6(a) by a dashed closed curve and can be observed to attract the trajectory corresponding to the peak Re_n which can be thus understood as the trajectory located sufficiently close to the stable manifold of the PO5 periodic orbit.

The picture described above remains valid for S4, where the flow corresponding to a peak converges to a spatially localised relative periodic orbit which was confirmed by the Newton-Krylov search. This relative periodic orbit lies on the branch analogous to PO5, but bifurcating from the TW branch. In contrast, wider initial conditions Si, i > 5, are not found to converge to any periodic orbits even when the peaks are well-resolved as shown in the inset in figure 4.5(b). This means that t_{relam} at the peaks is finite and the relaminarisation time curve is smooth around the peaks for these initial conditions. One may speculate that the flow found around these peaks still exhibits an influence of hypothetical periodic orbits PO7, PO9, etc., but they have additional unstable directions preventing the flow from converging to them. We must also note that, under sufficient zooming, the two rightmost peaks of R1 for S5 (see the inset in figure 4.5(a)) and all the resolved peaks for S4 (see the lowest curve in figure 4.2) appear to have several local maxima, i.e., several tightly located peaks. At each local maximum, the flow is still attracted by the stable manifold of PO5 and performs few cycles around the periodic orbit, similar to those observed in figure 4.6(d) from $t \approx 500$, but then spontaneously decays. Closer inspection shows that the number of finished cycles does not seem to be a smooth function of Re within these peaks which results in high sensitivity of t_{relam} to changes in Re observed in the inset in figure 4.5(a). One may suspect that other S5 peaks also have complex inner structure unresolved because of the insufficiently small spacing in Re.

For all initial conditions, the peaks in R1 can be observed to accumulate according to the following geometric law as $Re_n \to Re_s(\mathrm{i})$:

$$Re_{n+1} - Re_s(\mathrm{i}) = \alpha_{\mathrm{i}} \left[Re_n - Re_s(\mathrm{i}) \right], \tag{4.2}$$

where α_{i} is the convergence rate which is slower for wider initial conditions and probably converging to $\alpha_\infty \approx 0.2$ (see figure 4.7(b)). Figure 4.7(a) confirms the asymptotical law (4.2) for the case of S7. Since the right boundary of R1 tends geometrically to $Re_s(\mathrm{i})$ as i is increased, this asymptotical law approximates the peak accumulation in R1 especially well for wide initial conditions.

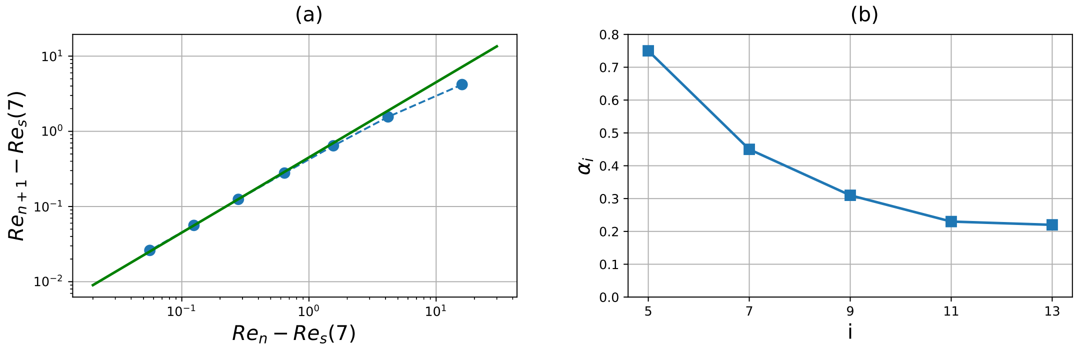

Figure 4.7: Verification of the peak accumulation law (4.2) is shown in plot (a) where the real data is plotted in blue color and green line shows the asympotic law (4.2) with the number of rolls i = 7 and the convergence rate $\alpha_7 = 0.45$. The dependence of the convergence rate α_i on the number of rolls a particular initial condition is made of is shown in plot (b). One may speculate that the convergence rate asymptotically approaches $\alpha_\infty \approx 0.2$ as the number of rolls grows.

Another simple asympotic law can be inferred for the local minima t_n of t_{relam} which is located between two peaks Re_n and Re_{n+1} at the Reynolds number $Re_n^{(min)}$ (see figure 4.5(a)). As the n-th peak is crossed in the direction of decreasing Re, its value is found to be increased on an almost constant value β_i which can be seen from the top row of plots in figure 4.8 where the dependence of t_n on n is shown for S5, S7, S9, S11 and S13. This suggests the following linear law:

$$t_n = t_0 + \beta_\mathrm{i} n. \tag{4.3}$$

While t_0 monotonically increases as the initial condition becomes wider (see figure 4.9(a)), the rate coefficient β_i has a more complicated dependence. We first note from the bottom row of plots in figure 4.8 that β_i in fact depends on n and can be assumed constant only for those n for which Re_n is close enough to $Re_s(\mathrm{i})$. The dependence of β_i on n for S5 is, however, different from all other cases (see the leftmost plot in the second row in figure 4.8). It seems to be constant with respect to n and fluctuates around a smaller value than in the case of other saddle-note states. This difference is unsurprising since the lowest part of the homoclinic snaking is populated by small localised solutions whose structure, including the amplitude of streak and rolls, is not yet asymptotically converged. Their structural and stability properties may thus significantly deviate from

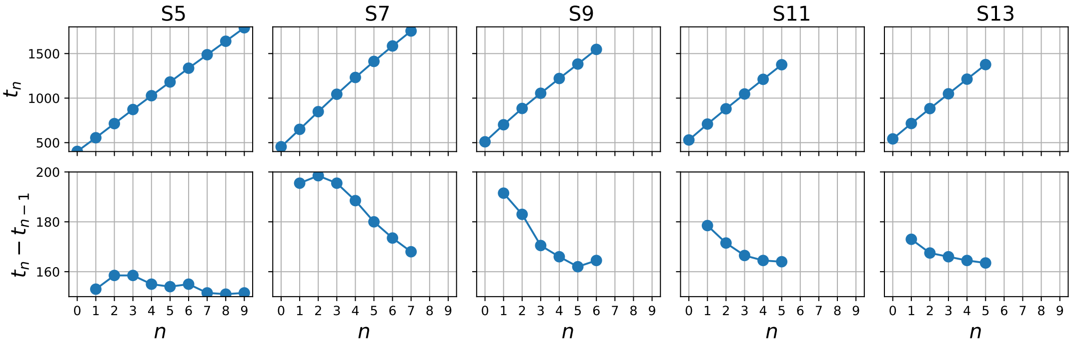

Figure 4.8: The local minima of t_{relam} found between the n-th and $(n+1)$-th peaks (top row) and the increase of the local minimum while crossing the n-th peak (bottom row) plotted for S5, S7, S9, S11 and S13 (from the left to the right). The local minima of t_{relam} exhibit almost linear dependence on n for all initial conditions as described by the law (4.3). Closer inspection of $\beta_\mathrm{i} \approx t_{n+1} - t_n$, which should be equal to a constant value according to the law (4.3), shows that it is true only for S5 and large enough n for other initial conditions. For S11, S13 and, perhaps, wider initial conditions, we can observe convergence of β_i to some constant value for $n \gtrsim 4$.

those of much wider localised solutions found somewhere in the middle of the snaking [2, 87]. This explains a non-monotonic dependence of the least-squares-fitted β_i on the number of rolls shown in figure 4.9(b). Similar to α_i, the rate coefficient β_i can be seen to approach an asymptotical value which, however, is hard to predict from the available data.

Based on the laws (4.2) and (4.3), an asymptotical law for the lower bound of the relaminarisation time can be derived. Indeed, if we assume that the Reynolds number of the local minimum of t_{relam} is located exactly at the middle between two adjacent peaks, i.e., $Re_n^{(min)} = 1/2\,(Re_n + Re_{n+1})$, and notice that the solution of (4.2) is $Re_n - Re_s(\mathrm{i}) = \alpha_\mathrm{i}^n\,[Re_0 - Re_s(\mathrm{i})]$, we get

$$Re_n^{(min)} = Re_s(\mathrm{i}) + \frac{\alpha_\mathrm{i}}{2}\,[Re_0 - Re_s(\mathrm{i})]\,(1+\alpha_\mathrm{i}). \tag{4.4}$$

Expressing n from this and substituting the result into (4.3) yields

$$t_n(Re_n^{(min)}) = t_0 + \frac{\beta_\mathrm{i}}{\ln\alpha_\mathrm{i}} \ln\frac{Re_n^{(min)} - Re_s(\mathrm{i})}{[Re_0 - Re_s(\mathrm{i})]\,(1+\alpha_\mathrm{i})}, \tag{4.5}$$

which, after replacing t_n with t_{relam} and $Re_n^{(min)}$ with Re, gives an asymptotical law for

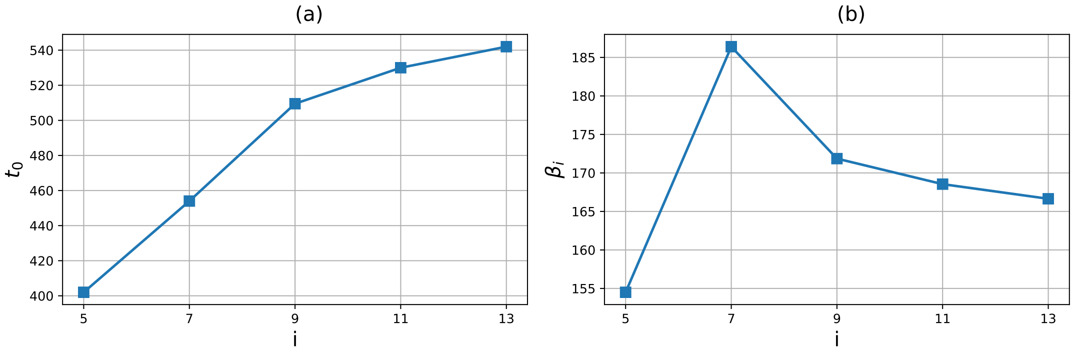

Figure 4.9: The dependence of two main constants of the linear law (4.3), the rightmost local minimum of the relaminarisation time curve t_0 (a) and the rate of increase of the local minima β_i (b), on the number of rolls. We can suspect that both values saturate as the initial condition gets wide enough, but more resolved peaks and the initial conditions with $\text{i} > 13$ need to be considered to evidence this.

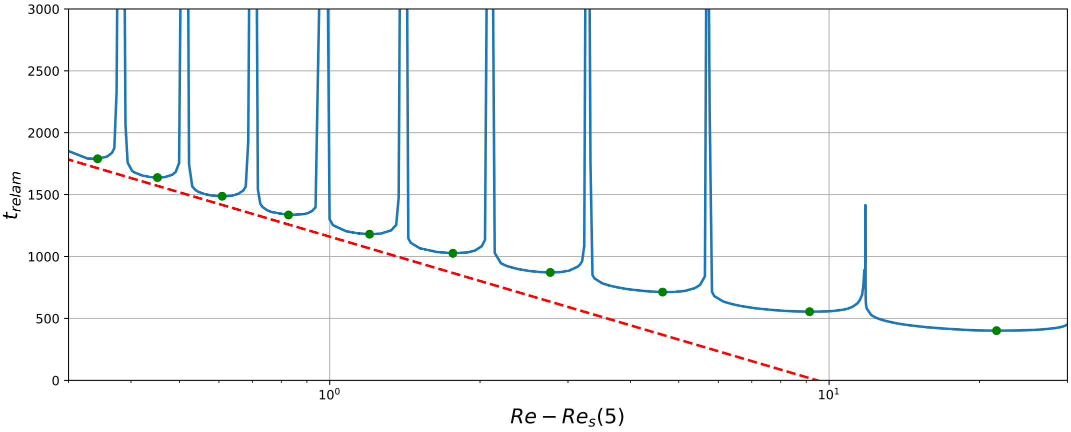

Figure 4.10: Verification of the law (4.5) for the lower bound of t_{relam} (dashed red line) for the case of S5. The relaminarisation time curve for S5 is shown in blue whilst green dots denote the local minima t_n. The following values were substituted in the law (4.5): $t_0 = 402, \beta_5 = 155, \alpha_5 = 0.74, Re_s(5) = 175.375$ and $Re_0 = 180.375$.

the lower bound of t_{relam}. Figure 4.10 illustrates it for the case of S5 and confirms that the law approximates the lower bound of t_{relam} well for Re asympotically close to $Re_s(\text{i})$. Finally, we note that the law predicts that t_{relam} grows with the rate $dt_{relam}/dRe \propto O([Re - Re_s(\text{i})]^{-1})$ as Re approaches $Re_s(\text{i})$.

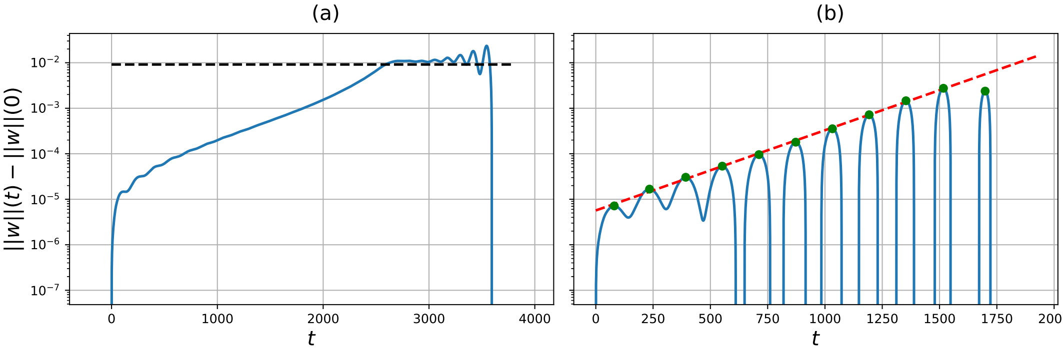

Figure 4.11: The time-evolution of $||w||(t)-||w||(0)$ for S5 (a) and S7 (b) time-integrated at $Re = 175.375$ and $Re = 175.1328125$ respectively. The black dashed line in plot (a) corresponds to the L2-norm of $||w||$ for S7. The green dots in plot (b) denote the local maxima of $||w||$ and the red dashed line corresponds to a function $Ae^{\gamma t}$, where the constants $A = 5.6 \times 10^{-6}$ and $\gamma = 4.1 \times 10^{-3}$ were obtained via least-square fitting to the local maxima.

Additional insights about dynamics in R1 can be gained if we look the time-evolution of the L_2-norm of the spanwise velocity component, $||w||$. Figure 4.11(b) shows that it performs clear oscillations as we expect in the case of the leading oscillatory instability. Our way of counting the number of cycles is based on counting the number of local maxima of $||w||$. One can notice that the last local maximum does not lie on the line corresponding to the envelop fitting. As the Reynolds number is decreased towards the left peak, the last local maximum increases until it hits the envelope fitting. The corresponding Reynolds number is equal to that of the peak. If we cross the peak towards the snaking, this local maximum becomes stuck to the envelope fitting and a new small-amplitude local maximum appears and the described scenario is repeated.

Interestingly, S5 dynamics in R1 does not exactly follow the described scenario as can be seen from figure 4.11(a). Instead, this initial condition exhibits one event of depinning, i.e., transitions to S7, and only after that performs oscillations described above. This can be well explained by the linear stability of EQ solutions. For S7 and wider initial conditions, the dominant instability is an amplitude mode, different from the depinning mode and introduced as the one-pulse mode in Section 3.2, which becomes unstable due to the subcritical Hopf bifurcation giving rise to PO5. This amplitude mode is responsible for the oscillations observed in figure 4.11(b). The leading instability of S5, in contrast, corresponds to the depinning mode (see figure 3.8) which manifests itself in one nucleation of rolls on the side which transforms S5 into S7 ($t \lesssim 2600$ in figure 4.11(a)) and which becomes dominated by the one-pulse mode after that ($t \gtrsim 2600$ in figure 4.11(a)).

4.3 Onset of chaotic transients: region R2

If the initial condition has 9 or more rolls, it starts splitting into two spots separated by the laminar flow as the Reynolds number is increased beyond region R1. The spots quickly decay (as shown in panel 4.12(a1)) until, at a certain Reynolds number, they get activated and exhibit the same type of oscillations as we discussed in region R1. This denotes the beginning of region R2 which manifests as a sharp increase of relaminarisation time from $t_{relam} \approx 500$ to $t_{relam} \approx 1000$. The flow dynamics inside region R2 depends on the width of a localised state, so we will first describe the most general case exemplified by region R2 for S13 and then highlight peculiarities of other initial conditions.

Figure 4.12 shows the part of the relaminarisation time curve for S13 corresponding to region R2. To ease the description of the region, we divide it into three subregions: R2a, R2b, R2c. Subregion R2a starts from the left boundary of region R2 and is characterised by the splitting event at $t \approx 300$ after which the spots perform few oscillations (panel 4.12(a2)). As the Reynolds number is increased from the left boundary, we can notice that less rolls decay in the middle part of the localised pattern during the splitting which can be seen as the contraction of the laminar gap between the spots (one can compare panels 4.12(a2, a3)). If the Reynolds number is increased even further, the laminar gap stops forming at $t \approx 300$ and splitting now occurs at $t \approx 420$ as shown in panel 4.12(b1). This suppresses the spot activation and, thus, sharply decreases t_{relam} which denotes the beginning of subregion R2b. In this subregion, a flow state is different from R2a and R2c: it has one more oscillation in comparison to the flow at the preceding plateau P and typically does not have splitting (panels 4.12(b1, b3)) which yields a relative low relaminarisation time ($t_{relam} \approx 500$). Panel 4.12(b2) shows an exceptional case where the activated spots significantly increase the relaminarisation time which correponds to the peak at $Re = 207.875$ in the top left plot in figure 4.12. As we move to the right within subregion R2b, the central rolls start weakening at $t \approx 300$ so that the laminar gap is eventually formed and the spots get activated again

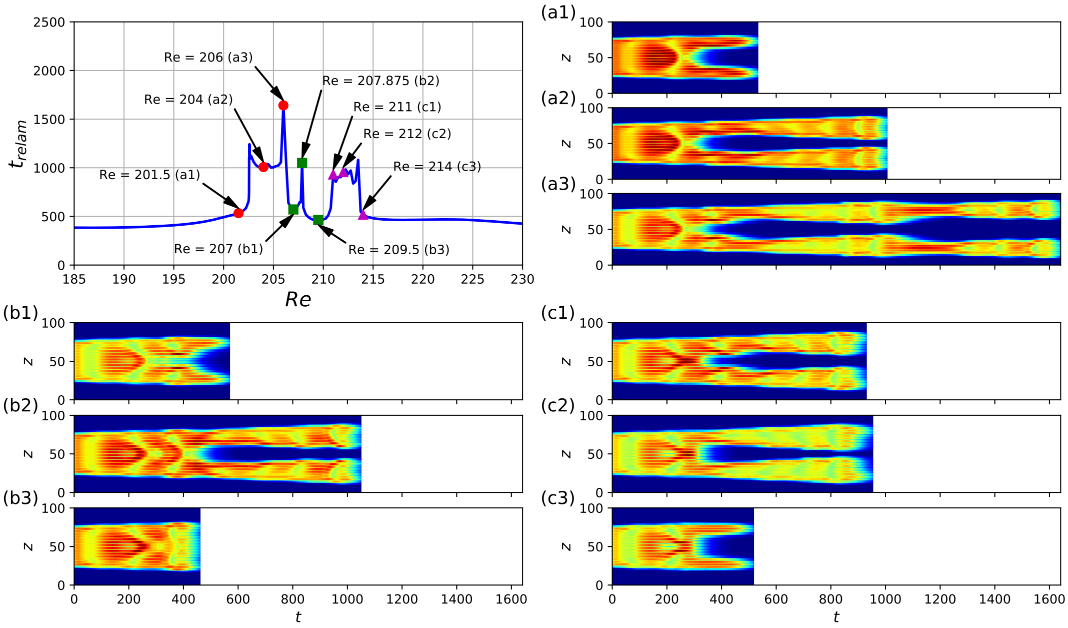

Figure 4.12: Relaminarisation times in region R2 for S13 (upper left plot). Panels (a1-a3) show the xy-averaged kinetic energy of the flow and demonstrate the splitting event at $t \approx 300$ which results in decaying spots for Re to the left of region R2 (a1) and activated spots within subregion R2a with narrowing laminar gap (a2, a3). The disapperance of the laminar gap at $t \approx 300$ gives rise to subregion R2b whose dynamics is demonstrated in panels (b1-b3). As Re is increased further, the initial condition again splits at $t \approx 300$ and the laminar gap starts growing which results in subregion R2c (c1, c2) similar to R2a in its dynamics. Region R2 ends when the spots get deactivated (c3).

which, in turn, suddenly increases t_{relam}. This marks the beginning of subregion R3c whose right boundary is also the right boundary of the whole region R2. One can notice from panels 4.12(c1, c2) that the dynamics in this subregions is very similar to that in R2a with only one major difference: the laminar gap in this subregions widens with increasing Re. Finally, further increase of Re will lead to crossing the right boundary of region R2 after which the spot oscillations suddenly terminate (panel 4.12(c3)) and the relaminarisation time drops down to $t_{relam} \approx 500$.

The description above holds for the localised states narrower than S13 without major changes. For them, subregions R2a and R2c become smaller as the width of an

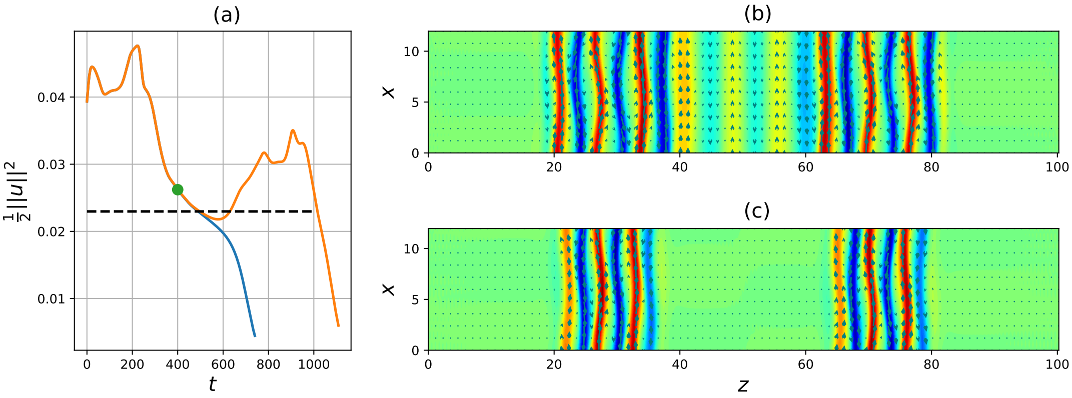

Figure 4.13: Plot (a) shows the time-evolution of the kinetic energy of S13 time-integrated at $Re = 202.546875$ (blue) and $Re = 202.5625$ (orange) located slightly to the left and to the right of the left boundary of R2 respectively. The dashed line shows the kinetic energy of the two-pulse solution converged by the Newton–Krylov search (panel (c)). The snapshot of the flow at $t = 400$, marked by the green dot in plot (a) and shown in panel (b), was used as a guess for the Newton–Krylov search.

initial condition is decreased so that subregion R2b essentially fills the whole region R2 for S9. For localised states smaller than S9, region R2 cannot be detected anymore. Region R2 for initial conditions wider than S13 have similar structure to that of S13 with only one difference: subregion R2a collapses into a peak so that the spots exhibit only one oscillation at the peak. One can notice from figure 4.2 that subregion R2a seems to be take its original form for initial condition S22 which is, however, a finite-size effect. There, the spot fronts nearest to the periodic boundaries reach each other at the left boundary of R2 and thus excite further oscillations of the spots.

The boundaries of region R2 deserve additional consideration. First of all, the spanwise width of the spots near the boundaries is found to be independent of an initial condition and equal to the width of the solutions of EQ_LOW for similar Reynolds numbers. It implies that the drastic increase of t_{relam} at the boundaries of R2 given the smooth variation of Re may be caused by crossing the stable manifold of the associated two-pulse exact solution. Indeed, if we take the appropriate snapshot from the simulation at the boundary of R2 and use it as a guess for the Newton–Krylov search, we can converge it to the two-pulse solution as shown in figure 4.13. By comparing 4.13(c) and 3.2(d), one can convince oneself that each pulse is virtually indistinguishable from the solutions found on EQ_LOW. In addition, it was found that slight changes of Re close to the boundaries of R2 lead to drastic changes in t_{relam} which may be explained by the fractal structure of the stable manifold of the two-pulse solution. Lastly, figure 4.2 shows that the boundaries of R2 monotonically decrease in Re as the width of an initial condition grows and seem to approach $Re \approx 190$ and $Re \approx 203$ for the left and right boundaries respectively.

It should be noted that region R2 can be thought of as a window to the oscillatory dynamics of two-pulse EQ_LOW states which are, in turn, directly related to the edge states (see the explanation in Chapter 3). This oscillatory dynamics in fact closely resembles what we observed in region R1 (see Section 4.6 for details). This view can be supported a simple numerical experiment: if we take the snapshot of the two-pulse state from a chaotic simulation in R2 as an initial condition and time-integrate it at Reynolds numbers beyond the boundaries of R2, R1-like oscillations will still be observed given $Re \gtrsim 180$. In other words, it is necessary for wide spots to evolve into spots whose width is close to the edge state (e.g., via partial decay yielding one or two small spots) to exhibit chaotic dynamics. This may explain why the random localised perturbation shown in figure 3.4 first decays down to the state resembling the edge state before transitioning to turbulence.

4.4 Long-lasting chaotic transients: region R3

When the Reynolds number is increased beyond the right boundary of R2, the splitting of the initial spot is still present even though it does not result in the activation of spots. Spot oscillations will be triggered again when the left boundary of R3 is crossed and disappear as Re is increased beyond its right boundary. This draws a similarity to region R2. Indeed, we can interpret crossing the R3 boundaries as crossing the stable manifold of the associated two-pulse state as explained in the previous section. Moreover, since region R3 appears as a result of splitting of the initial spot, it exists only for sufficiently wide initial conditions starting from S8. We however note two main differences between R2 and R3. In contrast to R2, region R3 is characterised by much higher sensitivity of the relaminarisation time to changes in Re which results in long-lasting chaotic transients whose lifetime may exceed $t_{relam} \approx 2 \times 10^4$. Moreover, the laminar gap formed due to the splitting of the initial spot does not seem to depend on Re as it does in region R2 which makes it difficult to define any subregions in region

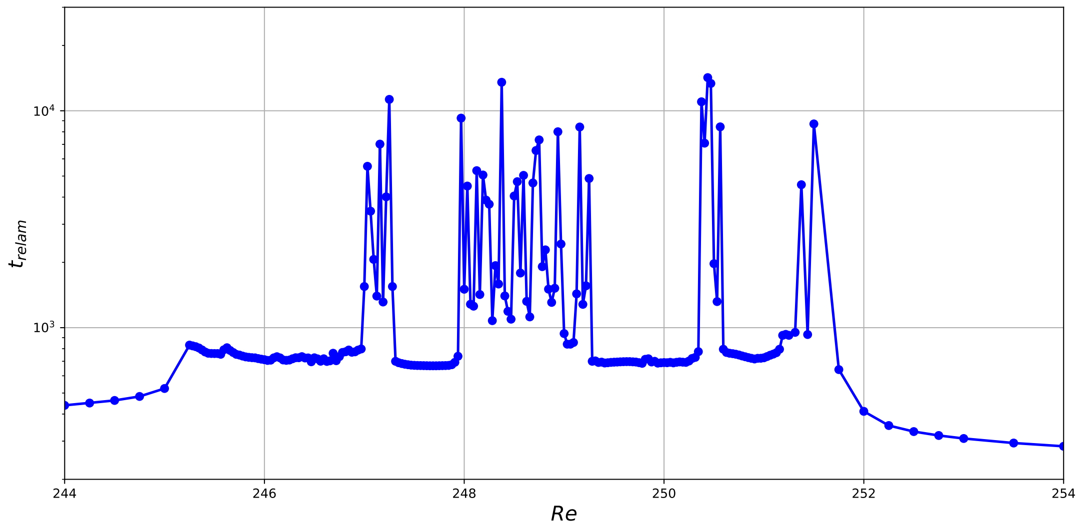

Figure 4.14: Relaminarisation times for region R3 for S15 plotted in the logarithmic scale as a function of the Reynolds number. The Re-step between points is $\triangle Re = 1/32$.

R3. Lastly, the boundaries of R3 virtually do not depend on the width of localised states so that region R3 is confined between $Re \approx 245.5$ and $Re \approx 252$ for all initial conditions.

An enlargement of region R3 for S15 is shown in figure 4.14. It demonstrates the intermittency of two types of subregions: the first one is associated with relatively low and only slightly varied relaminarisation time, $t_{relam} \approx 750$, and the second one exhibits large variations of t_{relam} with respect to Re. The latter regions act as windows in the parameter space leading to long-lasting chaotic dynamics. The number of such windows depend on a particular initial condition in a non-trivial way from 2 (S9, S17) to 4 (S11, S13, S15). Similarly, the location and width of the windows as a function of the number of rolls do not seem to follow any trivial pattern. Finally, some windows might have been smaller than the spacing in Re we used to resolve region R3 and are thus missed.

Consequently, we decide to use a statistical approach to quantify the relaminarisation time variations in region R3. Suppose that $D = \{Re_i\}$ is a set of Reynolds numbers lying inside R3 for a particular initial condition and $t_{relam}(Re)$ is the relaminarisation time at a given Reynolds number. We then divide R3 into two parts: $L = \{Re_i : t_{relam}(Re_i) < 2m\}$ and $H = \{Re_i : t_{relam}(Re_i) \geq 2m\}$, where m is the median of the induced dataset $t_{relam}(D)$ and $D = L \cup H$. Subset L corresponds to Reynolds numbers where the relaminarisation time is relatively low and constant. Even though t_{relam} is mildly sensitive to small changes in Reynolds number within this subset, its variation is tiny. To capture these observations statistically, we calculate the mean relaminarisation time μ_L and the standard deviation σ_L for the induced dataset $t_{relam}(L)$. In contrast, subset H contains Reynolds numbers for which the relaminarisation time variation becomes extremely large. Calculating the mean relaminarisation time does not seem to be useful for this case and we are rather interested in the maximum relaminarisation time $\max H$ and the fraction of Reynolds number associated with long-lived simulations, i.e. $f_H = \dfrac{|H|}{|L \cup H|}$. The latter is equivalent to the probability of getting a long-lasting chaotic transient at a random Reynolds number in R3.

We build the datasets D for all localised equilibria having R3 such that they consist of evenly spaced Reynolds numbers with spacing $\triangle Re = 1/32$. Since the boundaries slightly vary for different initial conditions, all datasets have different number of points. The resulting statistics are summarised in table 4.3. One can notice that the statistics of L only weakly depend on the number of rolls of an initial condition and show that the typical relaminarisation time outside of chaotic windows in R3 is $\mu_L \approx 780$ with a standard deviation $\sigma_L \approx 160$.

The statistics of H are much more sensitive to initial conditions since H contains a relatively small number of points. We can however note that long-lasting transients associated with H are not just rare events: depending on an initial condition, a probability of getting such simulations varies from 9.5% to 20.3%. The majority of them have the relaminarisation time which is one order of magnitude larger than t_{relam} in L with the largest relaminarisation time, $t_{relam} \approx 22181.5$, witnessed for S9 time-integrated at $Re = 249.21875$. Figure 4.15 shows one of such long simulations obtained by time-integrating S9 at $Re = 248.5$ and resulting in $t_{relam} \approx 12505$. Similar to the simulations in R2 shown in figure 4.12, we notice the splitting of the initial spot at $t \approx 200$ into two spots and their subsequent activation. They oscillate and extend their fronts until $t \approx 600$ where they collide and a cluster of several rolls in the middle of the structure dies out. Unlike R2, the spots continue to exhibit front growth after that and collide again at $t \approx 1800$ which results in a decay of a large cluster of rolls at $t \approx 2500$. This competition between the growth of the fronts and the decay of the roll

	N	m	μ_L	σ_L	$\max H$	f_H
S9	169	759.0	802.901	154.129	21319.5	0.160
S11	201	732.5	782.461	162.041	22181.5	0.164
S13	201	734.5	779.407	155.159	17164.5	0.095
S15	197	753.5	796.669	191.269	14219.0	0.203
S17	193	741.0	780.407	146.545	19732.5	0.109
S19	217	723.5	764.050	163.264	15543.0	0.175

Table 4.3: Statistics of R3 for the localised equilibria S9, S11, . . . , S19. For each initial condition, its own dataset D, containing N points and divided into L and H, was built. For dataset L, associated with low t_{relam}, we present the mean relaminarisation time μ_L and its standard deviation σ_L. For dataset H, associated with long-lasting chaotic transients, we report the maximum observed relaminarisation time $\max H$ and the fraction (or, equally, the probability of observing) of long-lasting transients f_H in the original dataset D. The initial condition S23 is excluded from the consideration since we cannot reliably define region R3 for it.

clusters continues further and yields spatiotemporal intermittency similar to directed percolation dynamics [127, 130, 132, 185]. In region R3, the decay of rolls overwhelms the front growth owing to too low Reynolds numbers and, thus, turbulence can never be sustained. It should be noted that the discovery of long-lasting dynamics at such low Re is not new. Similar results were obtained by means of adiabatic decrease of Re in the studies by Schmiegel and Eckhardt, who report $Re = 240$ as the lowest Re for the sustained turbulence in a minimal box [186] and Barkley and Tuckerman, who managed to sustain turbulence for $t \gtrsim 4200$ at $Re = 220$ in a spanwise extended domain similar to ours [182].

Large relaminarisation times in region R3 allow for the first time in our study to investigate the deviation of the flow from the symmetry subspace which can be quantified by

$$q(t) = \left(\frac{1}{2\Gamma_x \Gamma_z} \int\int\int_{\Omega} [u(x, y, z, t) + u(-x, -y, -z, t)]^2 \, dxdydz \right)^{\frac{1}{2}}. \tag{4.6}$$

Since the considered initial conditions from the branch EQ are reflection-symmetric, their dynamics is confined to the symmetry subspace during the initial phase of the

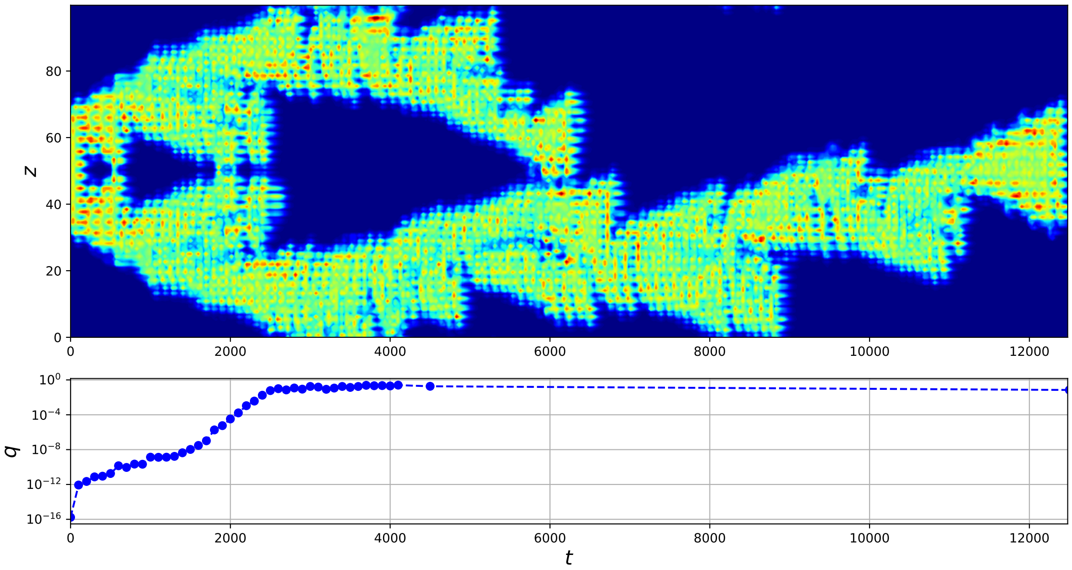

Figure 4.15: The top plane corresponds to the time-evolution of the xy-averaged kinetic energy E_{xy} for S9 time-integrated at $Re = 248.5$. The bottom plane shows the time-evolution of the deviation of the flow from the reflection symmetry subspace, defined in (4.6), for the same simulation.

simulation which can be observed from the time-evolution of $q(t)$ in the bottom plot in figure 4.15. Here, the deviation starts at $O(10^{-16})$ at $t = 0$ and grows almost monotonically until $O(1)$ at $t \approx 2500$ and is only $O(10^{-4})$ at $t_{relam} = 2000$. Given that all our simulations in R1 and R2, except for R1 peaks approaching the reflection-symmetric periodic orbit and one exceptional simulation in R2 for S19, and the majority of simulations in R3 have $t_{relam} < 2000$, we can safely say that the dynamics of the initial conditions taken from EQ is confined to the reflection symmetry subspace even though no symmetry constraints were imposed during the simulations. To confirm this, we recalculated the relaminarisation curve for one of the initial conditions with imposed reflection symmetry which appeared to be identical to the original one except for few Reynolds numbers in R3 where the relaminarisation time was significantly larger than 2000 in the original relaminarisation time curve.

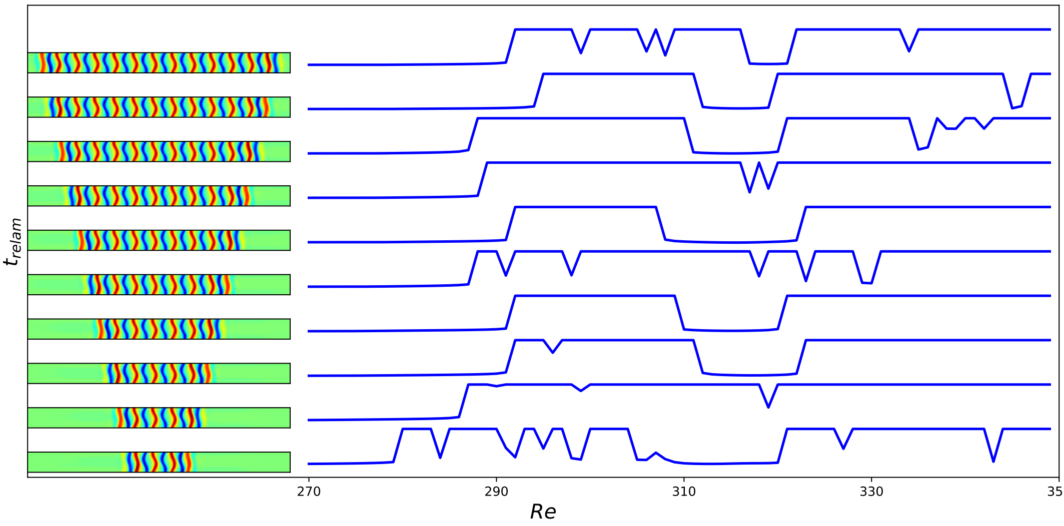

Figure 4.16: Relaminarisation times in region R4 plotted for localised equilibria S5, S7, . . . , S23 (blue) as a function of *Re*. The relaminarisation time was cut off at $t_{relam} = 2000$ to aviod cluttering (typical relaminarisation times are $O(10^4)$ in this region). See figure 4.2 for the explanation of the alignment of the curves and contours.

4.5 Transition to turbulence: region R4

For Reynolds numbers larger than $Re \approx 280$, one finds region R4 associated with eventual transition to turbulence and shown in figure 4.16. Similar to R2 and R3, the left boundary of this region is associated with splitting of the initial conditions which now occurs even for S7. Transition to turbulence occurs abruptly: right before the onset of R4, the relaminarisation time is very low ($t_{relam} \approx 230$), whereas it is immediately increased to $t_{relam} \propto O(10^4)$ once the boundary of R4 is crossed. As will be shown later, such a difference occurs because the flow quickly becomes domain-filling once the initial condition is time-integrated within region R4. Even though the relaminarisation time curves in figure 4.16 contain continuous ranges of *Re* with low t_{relam} (e.g., $Re \in [312; 322]$ for S9), the vast majority of the simulations in this region exhibit domain-filling turbulent states. It can also be noted that the critical Reynolds number for the onset of transition depends on the number of rolls of an initial condition and varies from 280 for S5 to 294.5 for S21.

The key difference of long-lasting chaotic transients in R4 from those in R3 is the

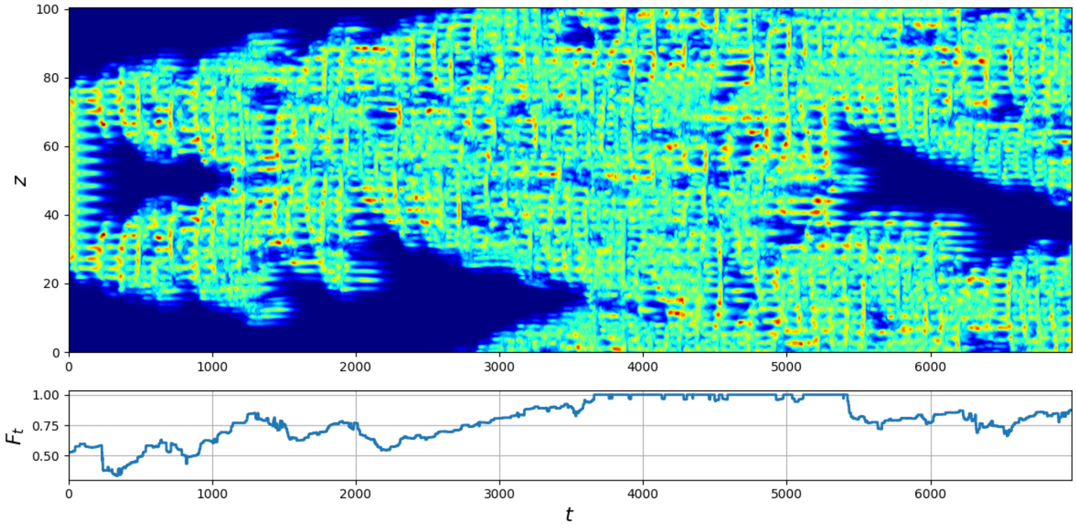

Figure 4.17: The top plane shows the time-evolution of the xy-averaged kinetic energy of S13 time-integrated at $Re = 300$. The bottom plot shows the corresponding time-evolution of the turbulent fraction.

dominating front propagation. To demonstrate this, we show an example of a chaotic transient in figure 4.17 obtained by time-integration of S13 at $Re = 300$. One can observe that the initial part of the simulation, $t \lesssim 1000$, is similar to that shown in figure 4.17. However, for $t \gtrsim 1000$, we see a significant difference: the decaying clusters have much smaller number of rolls so that the front growth can successfully compensate the decaying turbulent phase. As a result, the growing turbulent phase eventually fills the domain at $t \approx 3600$. It does not mean, however, that the flow state will be forever turbulent at each point of the domain beginning from $t \approx 3600$. Instead, laminar gaps of different sizes may appear. For example, we find a laminar gap in the middle of the domain starting from $t \approx 5400$ in figure 4.17. Nevertheless, the laminar gaps typically survive for a relatively short time and are quickly replaced by turbulent flow owing to the prevalence of front propagation.

To further characterise the front propagation in this region, we shall compute the turbulent fraction evolution for each simulation. Given the the streamwise and wall-normal confinement of our domain, we only need to determine the fraction of the domain occupied by the turbulent phase in the spanwise direction. We distinguish the laminar and turbulent patches of the flow by introducing a threshold $\epsilon_{xy}^{(lam)} = 5 \times 10^{-2}$ such that a range of z at a particular time t corresponding to $E_{xy}(t, z) \leq \epsilon_{xy}^{(lam)}$ is said to be a laminar patch. In order to avoid counting the low-energy space between the streaks as the laminar phase, we impose an additional constraint requiring the laminar patches to be continuous regions of z with the length at least 3. The fraction of the domain not occupied by the laminar phase is consequently said to be a turbulent fraction F_t. The bottom plot in figure 4.17 displays the time-evolution of the turbulent fraction calculated from the simulation shown in the top plane. The decay of roll clusters, including the splitting of the initial spot, is now easy to detect since it manifests as a sudden drop of F_t. We also notice that the turbulent flow becomes domain-filling when $F_t(t) = 1$ for some time t.

Using the turbulent fraction, the speed of front propagation can be estimated as $c = \Gamma_z dF_t/dt$. Given the irregular dependence of the turbulent fraction on time, it is necessary to smooth c by averaging it in time:

$$\langle c \rangle_t = \frac{\Gamma_z}{t_2 - t_1} \int_{t_1}^{t_2} \frac{dF_t}{dt} dt = \Gamma_z \frac{F_t(t_2) - F_t(t_1)}{t_2 - t_1}, \tag{4.7}$$

where we set $t_1 = 500$ to exclude the effect of the initial splitting and define t_2 as the smallest time t for which $F_t(t) = 1$. If the domain-filling turbulent state is not observed for a simulation, we set t_2 to be the final time of the simulation.

Figure 4.18 shows the time-averaged speed of fronts $\langle c \rangle_t$ and the corresponding linear regression for all localised equilibria as a function of the Reynolds number in R4. Here, the simulations with $t_{relam} \leq 2000$ were excluded from consideration not to contaminate the statistics with quick relaminarisation results. First of all, we can note a large variation of $\langle c \rangle_t$ which mostly falls between 0 and 0.04. The variation is one order of magnitude larger for S21 and S23 which is a direct consequence of the use of the finite domain: the adjacent fronts of S21 (S23) located near the periodic boundary are very close which results in their quick contact in the very beginning of a simulation intensifying further front growth. We then exclude S21 and S23 from further analysis of the front growth. For other initial conditions, linear regression shows that the correlation between $\langle c \rangle_t$ and Re strongly depends on an initial condition: it can be both positive (S5 and S7) and negative (S11, S15, S17, S19) whereas the absolute value of the Pearson's correlation coefficient is lower than 0.35 for all cases. We thus find it useful to average $\langle c \rangle_t$ with respect to Re for each initial condition which gives $\langle c \rangle_{t,Re}$ plotted in the rightmost plot in figure 4.18. One can observe that it grows from $\langle c \rangle_{t,Re} \approx 0.15$ for S5 to $\langle c \rangle_{t,Re} \approx 0.26$ for S13 and then similarly decreases starting

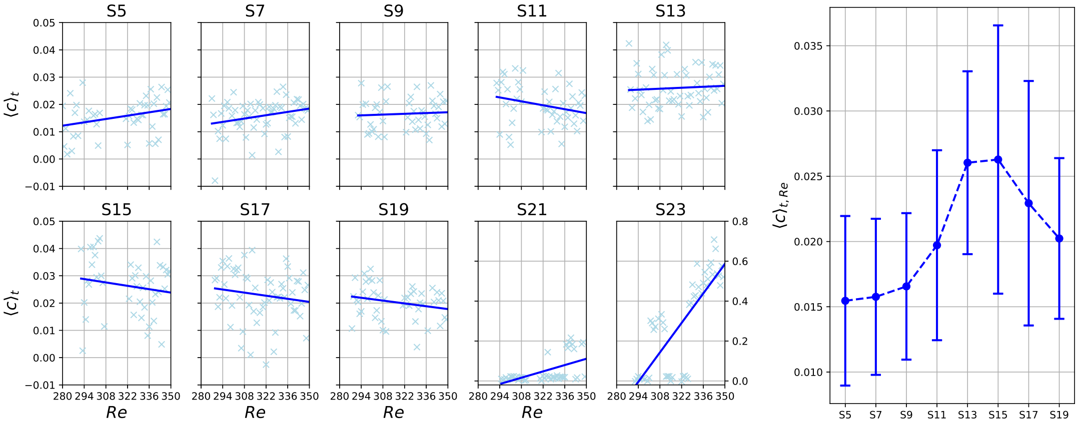

Figure 4.18: Ten leftmost plots show the time-averaged speed of fronts for S5, S7, . . . , S23 (light blue crosses) and the linear functions (blue lines) fitted to them via linear regression and used to obtain any trend in the front speed of the initial conditions with respect to Re. Note that the plots for S21 and S23 have a different vertical scale, shown to the right of them and used to emphasize the sudden increase of the speed of fronts. The rightmost plot shows the rate of front propagation, averaged in time and Re, for all initial conditions except for S21 and S23 for the reason explained in the text. The error bars in this plot corresponds to the standard deviation.

from S15. The bell-shaped structure of this curve may be explained by the following fact. Since we track the front propagation from $t_1 = 500$, i.e. right after the splitting, we could say that $\langle c \rangle_t$ actually corresponds to the speed of fronts for a two-pulse state formed after the splitting. Close inspection of the splitting shows that the two-pulse state is going to be evenly spaced for an initial condition whose width is between S13 and S15 owing to the periodic boundary. Consequently, the laminar gap between two pulses decreases as we decrease the width of an initial condition beginning from 13 rolls, but similarly, it decreases as the width of an initial condition increases beginning from 15 rolls. This observation allows us to interpret the results from the rightmost plot in figure 4.18 in the following way: the t, Re-averaged speed of fronts is maximised when the spacing between the spots in the two-pulse state is as large as possible and vice versa. One should however note that it is not equivalent to simply saying that the further the spots from each other, the larger the front speed in average. The explanation above is valid only for a two-pulse state fitting into one spanwise period of the domain.

Similarly, it does not work for S21 and S23 since their fronts closest to the periodic boundary start interacting at time $t < 500$. In the view of the above, it seems sensible to average $\langle c \rangle_{t,Re}$ among initial conditions S5, . . . , S19 which yields 0.02 agreeing very well with the front speed in the statistical study by Duguet *et al.* in [92] for the case termed «deterministic regime of growth» in this paper.

4.6 Transition from the EQ_LOW states

We close this chapter by considering transition to chaotic dynamics from the solutions found at the lower part of the branch EQ named EQ_LOW. In contrast to the localised solutions of different width found within the pinning region of the homoclinic snaking, the localised states belonging to EQ_LOW always have 3 rolls and are exact solutions for all Reynolds numbers being of interest in our study ($180 \lesssim Re < 350$). Thus, we employ a different approach to investigate transition used by many authors to study the heteroclinic connections between the exact solutions [40, 180, 187, 188] and based on perturbing the EQ_LOW solutions along the most unstable eigenvector. Linear stability analysis performed in Section 3.2 shows that the EQ_LOW solutions are once unstable for $Re \lesssim 200$ and twice unstable for higher Reynolds numbers. In the first case, the EQ_LOW solutions may be thought of as the edge states and, consequently, their only unstable eigendirection $\boldsymbol{e_1}$ must point outside the edge of chaos. In the second case, the leading unstable mode is the same as in the first case ($\boldsymbol{e_1}$), whilst the second unstable eigenmode is associated with the perturbations within the edge of chaos pointing to a TW_LOW state which is known to be the edge state in this situation [62]. Importantly, the second mode has an order-of-magnitude smaller growth rate in comparison to the leading unstable eigenmode (see the bottom plots in figure 3.5). Therefore, we can say that the perturbations along the leading unstable eigendirection of the EQ_LOW solutions are valid enough to investigate how the flow transitions from the edge states. Even though the edge states and, thus, the edge of chaos as a concept are ill-defined for such low Reynolds numbers due to the absence of turbulence, we will show that there is still a clear distinction between the dynamics of perturbations taken at different sides of the leading unstable eigendirection and the main features of this distinction stay the same even when larger Reynolds numbers are concerned.

We then build our initial conditions $\tilde{\boldsymbol{u}}$ by perturbing the EQ_LOW solution

$\boldsymbol{u_{EQ\_LOW}}(Re)$ calculated at given Re along its most unstable eigendirection $\boldsymbol{e_1}$:

$$\tilde{\boldsymbol{u}} = \boldsymbol{u_{EQ\_LOW}} + \sigma c \boldsymbol{e_1}, \tag{4.8}$$

where $\sigma \in \{-1, 1\}$ defines the "side" of the eigendirection with respect to $\boldsymbol{u_{EQ\_LOW}}$ and c quantifies how far the initial condition departs from the exact solution:

$$c = \alpha \frac{\max\limits_{x,y,z} |\boldsymbol{u_{EQ\_LOW}}|}{\max\limits_{x,y,z} |\boldsymbol{e_1}|}. \tag{4.9}$$

Since $\boldsymbol{e_1}$ is computed numerically by means of the Arnoldi method, the leading eigenvectors calculated for two nearby solutions $\boldsymbol{u_{EQ\_LOW}}$ on the EQ_LOW branch may appear nearly identical, but differ by a factor of -1. To ensure $\boldsymbol{e_1}$ changes continuously as a function of Re, we define it as

$$\boldsymbol{e_1} = \operatorname{sign}(\langle \boldsymbol{u_{EQ\_LOW}}, \tilde{\boldsymbol{e}}_{\boldsymbol{1}} \rangle) \cdot \tilde{\boldsymbol{e}}_{\boldsymbol{1}}, \tag{4.10}$$

where $\tilde{\boldsymbol{e}}_{\boldsymbol{1}}$ is the leading eigenvector computed originally by the Arnoldi method. Finally, we wish to keep the perturbations around the exact solutions close enough to the unstable manifold and then set $c = 0.1$.

Initial conditions are generated as defined in (4.8) for $Re \in [175; 300)$, where a pair of initial conditions with $\sigma = 1$ and $\sigma = -1$ is made for each Re. We find that at each Re, one of the initial conditions quickly decays ($t_{relam} < 250$) as shown in figure 4.20(a), whereas another one exhibits front growth and may lead to long-lived dynamics. We then say that that the first initial condition lies on the "laminar side" of $\boldsymbol{u_{EQ\_LOW}}$ and the second one on its "turbulent side". To characterise the dynamics on two sides, we build separate relaminarisation time curves for the "laminar" and "turbulent" sides of $\boldsymbol{u_{EQ\_LOW}}$ and show them in figure 4.19. Interestingly, it can immediately be noted that the laminar and turbulent sides cannot be strongly associated with the sign of σ, i.e., $\sigma = 1$ can correspond to the laminar and turbulent sides for two adjacent Reynolds numbers.

Starting from $Re = 175$, the relaminarisation times associated with the laminar side smoothly decay with Re until virtually stagnating at $t_{relam} \approx 100$ for $Re \gtrsim 190$. In contrast, the relaminarisation times associated with the turbulent side exhibit erratic variations and defining regions, as we did for the relaminarisation time curves for S5, S7 etc. by inspecting figure 4.2, appears to be complicated. Closer examination of the simulations, however, allows for the identification of few Re-dependent features of the

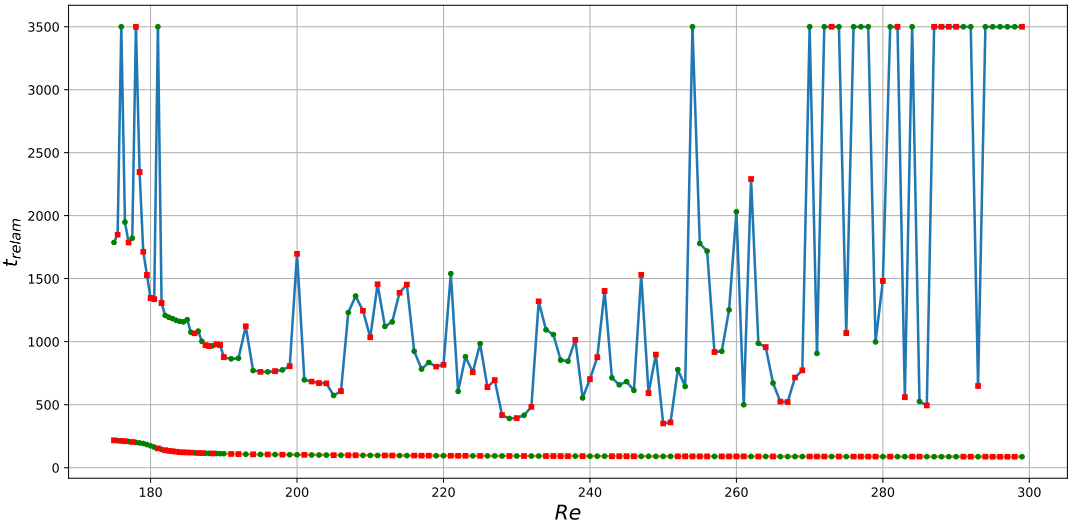

Figure 4.19: The relaminarisation times for the laminar (lower curve) and turbulent (upper curve) sides of $\boldsymbol{u_{EQ\_LOW}}$. The green dots and red squares correspond to $\sigma = 1$ and $\sigma = -1$ respectively and show that we cannot infer whether the initial condition of the form (4.8) is on the laminar or turbulent side based on the sign of σ.

flow. First of all, we note a region for $Re \leq 206$ where the relaminarisation time can diverge at the peaks and its lower bound decreases with the Reynolds number. This region can be directly related to region R1 for S5 where the flow is characterised by the oscillations and found to approach PO5 at the peaks of t_{relam}. Figure 4.20(b) shows one of the simulations corresponding to a peak. One can observe that the initial condition in the beginning of the simulation nucleates a pair of rolls at $t \approx 300$ which is the main difference between the dynamics at the laminar and turbulent sides of $\boldsymbol{u_{EQ\_LOW}}$ as one can confirm by comparing planes 4.20(b, c, d) corresponding to the dynamics on the turbulent side and plane 4.20(a) corresponding to the laminar side. This initial depinning event essentially makes the state close to S5 in the terms of the number of rolls. Following the discussion of S5 dynamics in R1 in Section 4.2, it is unsurprising then that the second depinning event, increasing the number of rolls up to 7, occurs at $t \approx 1500$ and triggers oscillations typical for R1. After that, the readjustment of the flow at $t \approx 1900$ results in approaching a periodic orbit from PO5. In this case, given the definition of our initial conditions in (4.8), the approach of the PO5 state in fact reveals a heteroclinic connection between EQ_LOW and PO5 at a particular Reynolds

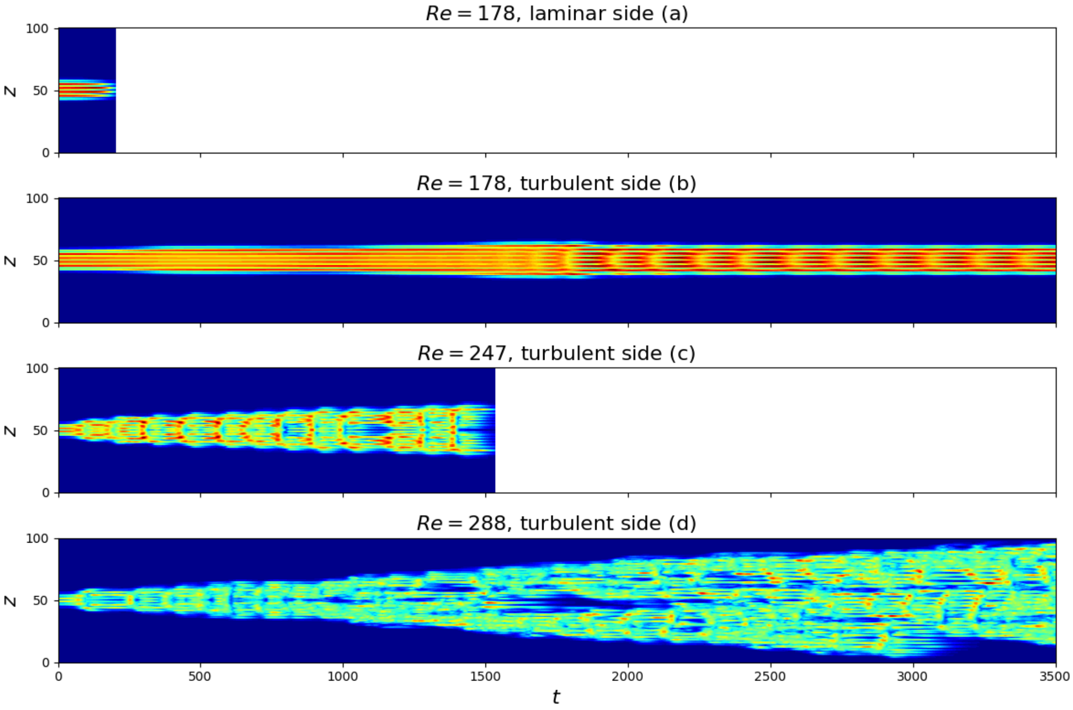

Figure 4.20: Space-time plots of the xy-averaged kinetic energy for simulations of initial conditions located at the turbulent side of $\boldsymbol{u_{EQ\_LOW}}$ which can be associated with regions R1 (b), R3 (c) and R4 (d). Space-time plot in (a) shows the simulation associated with the laminar side of $\boldsymbol{u_{EQ\_LOW}}$ for the same Reynolds number as in (b). All the simulations associated with the laminar side exhibit exactly the same quick decay via annihilation of rolls as that shown in (a).

number.

Beginning from $Re = 207$, instead of approaching PO5, the flow starts exhibiting the front growth which may lead to very long-lived chaotic transient, e.g., at $Re = 254$. However, for $Re < 270$, the spontaneous decay of roll clusters prevents us from observing the domain-filling states even though we can observe an almost steady speed of the fronts for substantial amount of time (plane 4.20(c)). It is thus natural to associate this region with region R3. Finally, for $Re \geq 270$, we observe transition to turbulence as it is explained for region R4: here the front growth overwhelms the decay of the clusters of rolls which allows the turbulent phase to fill the whole domain as exemplified by space-time plot 4.20(d) for a simulation at $Re = 288$.

Chapter 5

Relaminarisation of localised states in the presence of wall oscillations

Controlling the dynamics of localised states, i.e., either suppressing or enhancing their growth, is a natural step after studying their dynamics in the uncontrolled system which was done in the previous chapter. The map of dynamics shown in figure 4.2 appears to be of great use for this purpose: tracking how the map changes as a function of control parameters, we can both qualitatively and quantitatively (by means of the relaminarisation times, Reynolds numbers for region boundaries and front speed) assess the effect of a chosen control strategy on the dynamics. To exemplify this, we choose a well-known control strategy, spanwise wall oscillation, parameterised by its amplitude, frequency and phase and introduce it in Section 5.1. The metrics necessary to assess the effect of wall oscillations on transient dynamics of localised states are then defined in Section 5.2. By increasing the amplitude from 0, we investigate the homotopy from plane Couette flow by means of the relaminarisation times and show in Sections 5.3 and 5.4 how regions R1, R2, R3 (R3a) deform, unite and then disappear for large enough amplitudes. The only region left in the case of large amplitudes of wall oscillations is region R4 denoting transition to domain-filling turbulence. Its left boundary is then the critical Reynolds number for the onset of transition to turbulence for our particular initial conditions. In the concluding section of this chapter, we assess its dependence on the amplitude and frequency of wall oscillation.

5.1 Control strategy: spanwise wall oscillations

Spanwise wall oscillation is one of the standard open-loop control strategies. By varying the amplitude, frequency and type of oscillations, one may significantly reduce the total drag and suppress transition to turbulence for some perturbations (see Section 1.3 for details). We introduce the spanwise oscillations by modifying the original no-slip boundary conditions (1.6) and (1.7):

$$\boldsymbol{U}(x, \pm 1, z, t) = [\pm 1, 0, A_\pm \sin(\omega_\pm t + \phi_\pm)], \tag{5.1}$$

where $A_\pm, \omega_\pm$ and $\phi_\pm$ denote the amplitude, frequency and phase of the oscillations of the top ("+") and bottom ("−") walls. As shown in Appendix A, such boundary conditions modify the laminar flow into:

$$\boldsymbol{U_{lam}} = [y, 0, W(y, t)], \tag{5.2}$$

where the time-dependent spanwise component is given by the expression

$$\begin{aligned}
W(y,t) = {} & \frac{A_+}{\cosh^2 2\Omega_+ - \cos^2 2\Omega_+} \left[(\sin 2\Omega_+ \cosh \Omega_+(y-1) \sin \Omega_+(y+1) \right. \\
& + \sinh 2\Omega_+ \sinh \Omega_+(y+1) \cos \Omega_+(y-1)) \sin(\omega_+ t + \phi_+) \\
& + (\sinh 2\Omega_+ \cosh \Omega_+(y+1) \sin \Omega_+(y-1) \\
& \left. - \sin 2\Omega_+ \sinh \Omega_+(y-1) \cos \Omega_+(y+1)) \cos(\omega_+ t + \phi_+) \right] \\
& + \frac{A_-}{\cosh^2 2\Omega_- - \cos^2 2\Omega_-} \left[(- \sinh 2\Omega_- \cos 2\Omega_- \sinh \Omega_-(y-1) \cos \Omega_-(y-1) \right. \\
& - \cosh 2\Omega_- \sin 2\Omega_- \cosh \Omega_-(y-1) \sin \Omega_-(y-1)) \sin(\omega_- t + \phi_-) \\
& + (- \sinh 2\Omega_- \cos 2\Omega_- \cosh \Omega_-(y-1) \sin \Omega_-(y-1) \\
& \left. + \cosh 2\Omega_- \sin 2\Omega_- \sinh \Omega_-(y-1) \cos \Omega_-(y-1)) \cos(\omega_- t + \phi_-) \right],
\end{aligned} \tag{5.3}$$

where $\Omega_\pm = \sqrt{\frac{\omega_\pm Re}{2}}$ and $\delta_\pm = 1/\Omega_\pm$ is the depth of penetration of the transverse wave created by the top or bottom oscillating wall and travelling to the bulk of the flow. Consequently, the Navier–Stokes equation (1.11) written for the departure $\boldsymbol{u} = \boldsymbol{U} - \boldsymbol{U_{lam}}$ reads:

$$\partial_t \boldsymbol{u} + (\boldsymbol{U} \cdot \nabla)\boldsymbol{U} = -\nabla p + \frac{1}{Re}\nabla^2 \boldsymbol{u} + \frac{1}{Re}\partial_{yy} W \boldsymbol{e}_z - \partial_t W \boldsymbol{e}_z, \tag{5.4}$$

where the nonlinear term is consciously left unexpanded since Channeflow treats the nonlinear term in this form (see Section 2.1 for the explanation). The last term on the right-hand side, $\partial_t W \boldsymbol{e}_z$, was incorporated as a body force while implementing this control strategy in Channelflow.

In this thesis, we will consider two simplest particular cases of the wall oscillations: in-phase ($A = A_+ = A_-, \omega = \omega_+ = \omega_-, \phi = \phi_+ = \phi_-$) and antiphase ($A = A_+ = A_-, \omega = \omega_+ = \omega_-, \phi_- = \phi_+ + \pi$) ones. The expression for the spanwise component of the laminar flow in the presence of in-phase wall oscillations with amplitude A, frequency ω and phase ϕ is given by

$$\begin{aligned}
W(t,y) = {} & \frac{A}{\cosh 2\Omega + \cos 2\Omega} \left[[\cosh \Omega(y+1) \cos \Omega(y-1) \right. \\
& + \cosh \Omega(y-1) \cos \Omega(y+1)] \sin(\omega t + \phi) \\
& \left. + [\sinh \Omega(y+1) \sin \Omega(y-1) + \sinh \Omega(y-1) \sin \Omega(y+1)] \cos(\omega t + \phi) \right],
\end{aligned} \tag{5.5}$$

which is a simplification of (5.3). A similar expression can be derived for antiphase

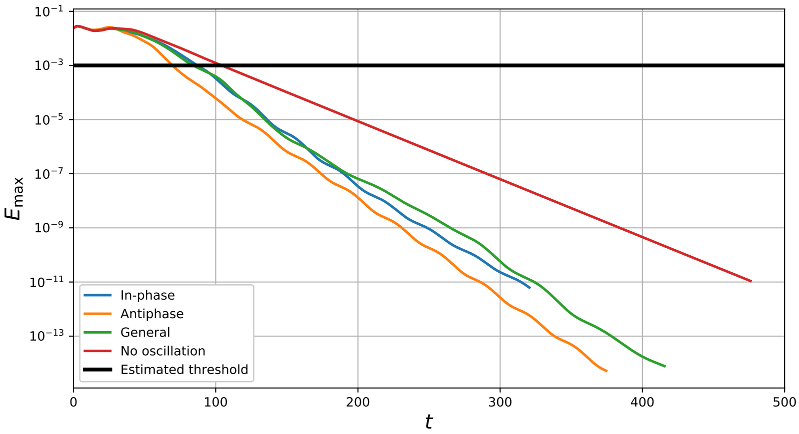

Figure 5.1: Time-evolution of the maximum pointwise kinetic energy of the flow computed in the presence of different types of wall oscillations at $Re = 200$ using a random initial condition. For in-phase and antiphase wall oscillations, the following parameter values are used: $A = 0.35$, $\omega = 0.1$, $\phi = 0.4\pi$. For the general case of oscillations, the random parameter values are used: $A_+ = 0.300587371312$, $A_- = 0.290422611548$, $\omega_+ = 0.0605525929595$, $\omega_- = 0.091739177893$, $\phi_+ = 0.1305025511422\pi$, $\phi_- = 0.09151800021 24\pi$. The black line denotes the threshold $E_{lam} = 10^{-3}$ we will use to detect a relaminarisation event.

wall oscillations:

$$\begin{aligned} W(t,y) = \frac{A}{\cosh 2\Omega - \cos 2\Omega} & [[\cosh \Omega(y+1) \cos \Omega(y-1) \\ & - \cosh \Omega(y-1) \cos \Omega(y+1)] \sin(\omega t + \phi) \\ & + [\sinh \Omega(y+1) \sin \Omega(y-1) - \sinh \Omega(y-1) \sin \Omega(y+1)] \cos(\omega t + \phi)] \,. \end{aligned} \tag{5.6}$$

The details of the derivation and simplification of these expressions can be found in Appendix A. Figure 5.1 demonstrates examples of relaminarising trajectories emanating from the same random initial condition but under the action of different types of wall oscillations. Since the presence of wall oscillations may shrink the neighbourhood of the laminar flow within which the linearised Navier–Stokes equation describes the departure dynamics well, we act out of caution and lower the threshold E_{lam} defining this neighbourhood and introduced in the beginning of Chapter 4 down to $E_{lam} = 10^{-3}$.

The spanwise component of the oscillatory laminar flow can safely be thought of as a combination of two Stokes boundary layers developed by the walls if the depth of

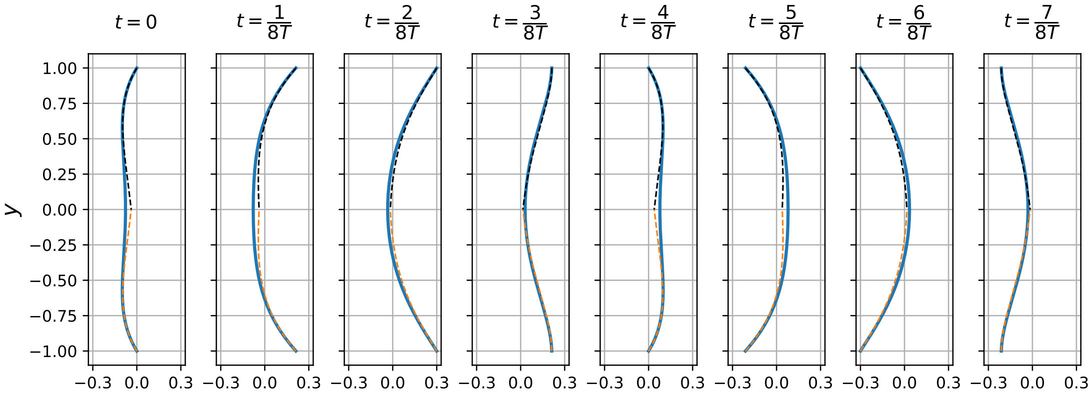

Figure 5.2: Time-evolution of the spanwise component of the laminar flow (blue curves) in the presence of in-phase wall oscillations at $A = 0.3$ and $\omega = 1/64$ plotted for 8 stages of one period $T = 2\pi/\omega$ of oscillations (the Reynolds number is 500). The orange and black dashed curves denote the Stokes boundary layers associated with the bottom and top walls respectively and defined by the following expressions: $W(y,t) = Ae^{-\Omega\tilde{y}} \sin(\omega t - \Omega\tilde{y})$, where $\tilde{y} = y + 1$ for the bottom wall and $\tilde{y} = 1 - y$ for the top wall. The depth of penetration is $\delta \approx 0.5$.

penetration is small enough ($\delta_\pm \lesssim 0.5$) or, equivalently, the frequency is large enough ($\omega \gtrsim 1/64$ for $Re = 500$). This is illustrated by figure 5.2 showing the time-evolution of the spanwise component of the laminar flow in the presence of in-phase wall oscillations at amplitude $A = 0.3$ and frequency $\omega = 1/64$ together with the Stokes boundary layers at different times. It is however reasonable to expect that too large frequencies have no effect on the interior of the flow. We may assume that the effect of the oscillations with the depth of penetration less than 0.1 (the kinetic energy of the flow is at least one order of magnitude smaller within this distance from the wall compared to the interior of the flow) is negligible which encourages to examine frequencies $\omega \lesssim 1/3$. For the sake of caution, we will then consider frequencies $\omega \leq 1$. On the other hand, the period of oscillations should be less than the timescale associated with transition to turbulence which is $O(10^3)$ for our wide domain (see Section 4.5). It is then sensible to consider only those frequencies which are larger than 1/128. This gives the following range of frequencies $\omega \in [1/128; 1]$.

5.2 Assessment of the effect of control

The main purpose of this chapter is to understand how the map of dynamics discussed in Chapter 4 changes when wall oscillations are applied. Here we present the results for the simplest type of such a control, in-phase wall oscillations, which involves only three parameters (A, ω and ϕ). Our approach is based on the reproduction of the relaminarisation time curves shown in figure 4.2. Since the exploration of the whole parameter space for all localised initial conditions is computationally unreasonable, we find it sensible to choose only one control parameter while keeping other parameters fixed and to restrict the set of initial conditions to be investigated as much as possible. In particular, we choose the amplitude as a homotopy parameter and fix the frequency at $\omega = 1/16$, which is in line with the study by Rabin *et al.* [154], and the phase ϕ at zero. This value of the frequency gives a fairly deep penetration of the transverse waves ($\delta \approx 0.25$) whereas it is not too small to require a thorough consideration of non-zero phases (the period of such oscillations is $T \approx 100$ whilst the relaminarisation times can be expected to be larger than 300). It will be shown further in Chapter 6 (see Sections 6.4 and 6.5) that, in a small domain, this frequency is sub-optimal in terms of the laminarisation probability and leads to chaotic and time-periodic edge states depending on the amplitude of the oscillations. Finally, we significantly restrict the set of initial conditions by considering only S5 and S13. The former initial condition acts as a representative of small spots exhibiting no splitting and has the most detailed description of region R1 (see Section 4.2). On the other hand, the results presented in Chapter 4 show that, excluding the peculiarities related to the subregions of R2 and the largest initial condition S23 having a localised defect, the equilibria featuring the splitting (i.e., S9 and wider localised equilibria) exhibit qualitatively similar dynamics. This means that it may be sufficient to consider only one initial condition allowing for splitting and then extrapolate the qualitative and some of the quantitative conclusions about its dynamics under the action of control to other wide localised states. Among these initial conditions, S13 yields the richest dynamics (it has all three subregions in region R2 and the maximum number of chaotic windows in region R3) and nearly equally spaced spots after the splitting maximising the front speed in region R4 (see Section 4.5). Another suitable candidate would be S15: it results in the largest number of long-lived chaotic transient in R3 and almost the same average front speed as S13 in region R4. However, since S15 has a less rich region R2, we make a choice in favor of S13. Our preliminary calculations showed that there is no need to complement S5 and S13 with any of the localised travelling waves: similar to the uncontrolled system, there is no qualitative difference between the dynamics of the equilibria and travelling waves taken as initial conditions in the presence of in-phase wall oscilations.

To allow for a quantitative comparison between the uncontrolled and controlled systems, we need to introduce some metrics for the assessment of the effect of control. Given the plan described above, the most natural way is to compare the relaminarisation time curves. They are defined at specific Reynolds numbers, whereas, in real-life systems, the Reynolds number can only be specified within a limited accuracy. To account for this uncertainty, we suggest using the expected value of a given single-valued quantity assessing the dynamics of the flow at a particular Re, such as the relaminarisation time and the front speed. The expected value is obtained by averaging within the range $[Re - \triangle Re; Re + \triangle Re]$ using the following operator:

$$\mathrm{E}[f] = \frac{1}{2\triangle Re} \int_{Re-\triangle Re}^{Re+\triangle Re} f(\widetilde{Re}) d\widetilde{Re}, \tag{5.7}$$

where f is an arbitrary Re-dependent function and we assume that the specified Reynolds number is uniformly distributed in $[Re - \triangle Re; Re + \triangle Re]$. We found the following references to the accuracy in experimental studies of plane Couette flow:

- “The accuracy on the determination of Re is within 3%”, where $100 \lesssim Re \lesssim 400$ [174]
- “The accuracy on Re is [...] at best 2.5% and at worst 4%”, where $100 \lesssim Re \lesssim 400$ [175]
- “A constant Reynolds number ±0.25 over the long observation times” [185]
- “The uncertainties [...] lead to an Re-uncertainty of 5” [84]

Taking into account our range of Reynolds numbers, we take $\triangle Re = 5$ as an intermediate value. To give an example, we show the expected relaminarisation times $\mathrm{E}[t_{relam}]$ for S5 in Figure 5.3 in comparison with the non-smoothed t_{relam}. The effect of the control can then be assessed by calculating the difference between the expected relaminarisation times in the uncontrolled and controlled systems, i.e., $\mathrm{E}[t_{relam}^{ctrl}] - \mathrm{E}[t_{relam}]$. Averaging

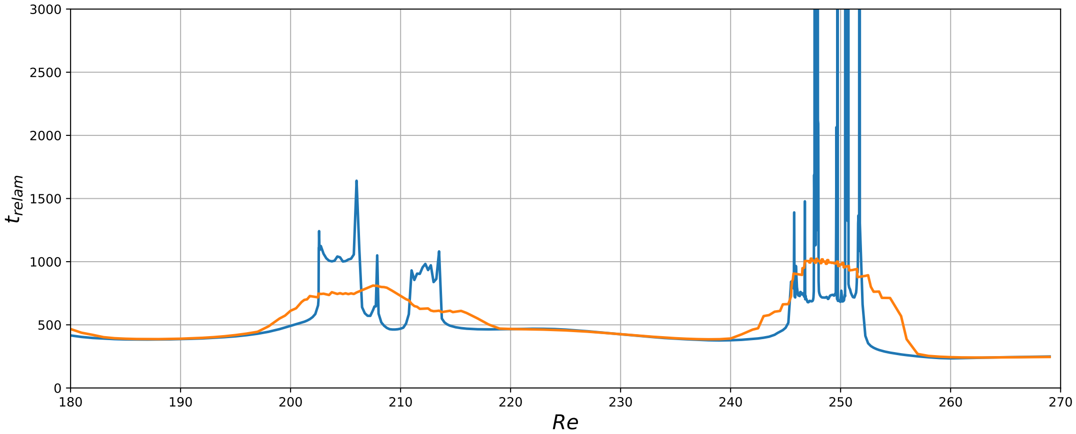

Figure 5.3: Expected relaminarisation times $\mathrm{E}[t_{relam}]$ (orange) and original, non-smoothed, relaminarisation time curve (blue) calculated for S5 in the absence of wall oscillations using $\triangle Re = 5$.

this difference within the considered range of Re, we get a single-value quantity assessing the control action which we denote t_{incr}. Given that regions R1, R2 and R3 (R3a) in the uncontrolled system are found for $Re \lesssim 270$, we will compute t_{incr} by averaging over $Re \in [180; 270]$.

Comparing the relaminarisation time curves makes sense only for regions R1, R2, R3 and plateaux where the time-integration is performed until complete relaminarisation in all the simulations (except for the peaks in region R1 for S5 where the relaminarisation time diverges). In contrast, the simulations in region R4 are typically performed until $t = 3000$ to save computational time. Since region R4 is first of all characterised by the front growth, it is sensible to assess how the control affects the front speed. Similar to the relaminarisation time, we find it useful to compare the expected front speed $\mathrm{E}[\langle c\rangle_t]$ accounting for the uncertainty in Re and also track a single-value metric c_{incr} assessing the overall effect of the control on the front speed:

$$c_{incr} = \frac{\int\limits_{Re_1}^{Re_2} \left(\mathrm{E}[\langle c\rangle_t^{ctrl}] - \mathrm{E}[\langle c\rangle_t]\right) dRe}{\int\limits_{Re_1}^{Re_2} \mathrm{E}[\langle c\rangle_t] dRe}, \tag{5.8}$$

where $\mathrm{E}[\langle c\rangle_t]$ and $\mathrm{E}[\langle c\rangle_t^{ctrl}]$ are the expected front speeds in the uncontrolled and controlled cases respectively and $[Re_1; Re_2]$ denotes the interval within which regions R4

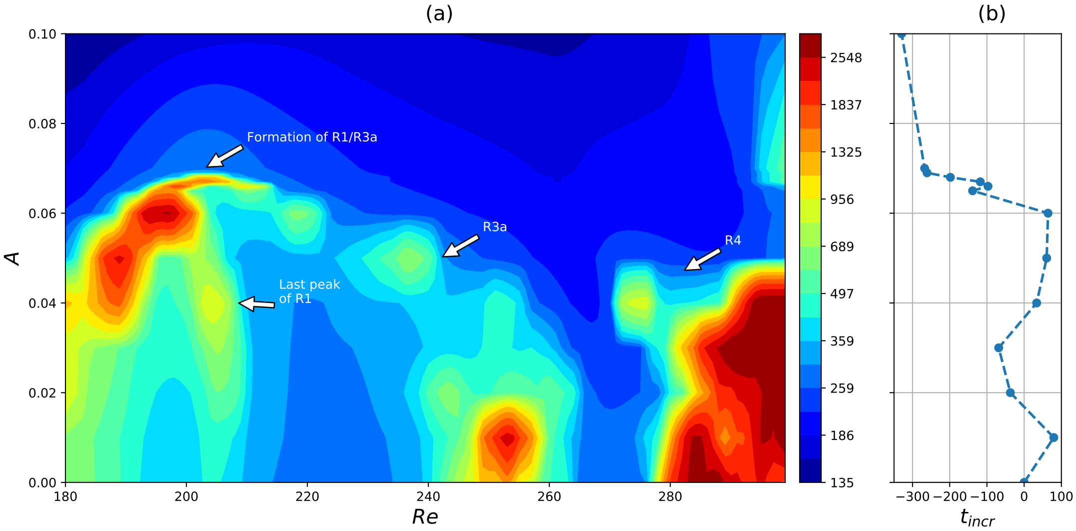

Figure 5.4: Expected relaminarisation times plotted as a function of Re and of the amplitude A of the wall oscillations (a) and the dependence of t_{incr}, quantifying the effect of the control on relaminarisation within regions R1, R2 and R3a, on the amplitude (b). In contours (a), we used $\triangle Re = 3$ to compute $\mathrm{E}[t_{relam}]$ and a logarithmic scale for the sake of visibility.

overlap for both the uncontrolled and controlled cases.

5.3 Homotopy from the uncontrolled system for S5

We start the discussion of the homotopy from the uncontrolled system for S5, one of the smallest localised equilibrium investigated in Chapter 4. Figure 5.4(a) shows the dependence of the expected relaminarisation time on the Reynolds number and the amplitude of wall oscillations. We first note that a slight departure from the uncontrolled system by introducing small-amplitude oscillations at $A = 10^{-2}$ expands regions R1 and R3a a little and increases the relaminarisation times in region R3a, even though the location of the peaks in region R1 barely changes. The phase change as well as the frequency change do not affect dynamics nor the R1 peak locations at this value of the amplitude. Even though an additional small increase of the amplitude ($A = 2 \times 10^{-2}$) again slightly expands the regions, for the amplitudes $A > 2 \times 10^{-2}$, both regions start shrinking and region R3a starts moving towards lower Reynolds

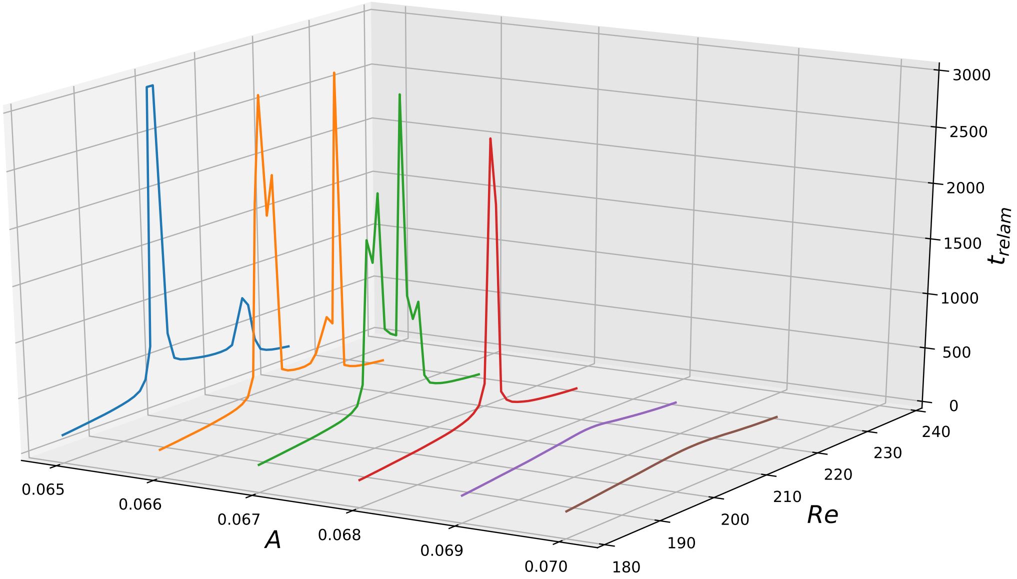

Figure 5.5: The relaminarisation time curves for S5 computed for various amplitudes from $A = 6.5 \times 10^{-2}$ (blue) to $A = 7 \times 10^{-2}$ (brown).

numbers so that these regions meet at $(A, Re) \approx (6.8 \times 10^{-2}, 203)$ and disappear for the amplitudes larger than $A \approx 6.8 \times 10^{-2}$. Beyond this amplitude, the only remaining region is region R4 whose onset starts moving towards larger Reynolds numbers as the amplitude is increased above $A \approx 4 \times 10^{-2}$. These transformations of the regions are correspondingly reflected in the dependence of t_{incr} on the amplitude shown in figure 5.4(a). It illustrates that the wall oscillations mainly destabilise the system when the amplitude is strictly below $A \approx 6.5 \times 10^{-2}$ which corresponds to positive values of t_{incr}. For larger amplitudes, instead, we can observe that the flow becomes gradually more stable as the amplitude is increased yielding $t_{incr} \approx -330$ at $A \approx 10^{-1}$.

To get a more detailed look at the formation of regions R1 and R3a, we plot the non-smoothed relaminarisation time curves in figure 5.5 in the vicinity of $A = A_{cr} = 6.8 \times 10^{-2}$. At $A = 6.5 \times 10^{-2}$, we can observe two peaks: one peak, located at lower Re and corresponding to the combined peaks of region R1 (note how peaks in region R1 collide as the amplitude is increased from 5×10^{-2} to 6×10^{-2} in figure 5.4), and another peak, located at higher Re and corresponding to region R3a. Increasing the amplitude from $A = 6.5 \times 10^{-2}$ forces these peaks to move towards each other until they eventually collide at $A_{cr} = 6.8 \times 10^{-2}$ into a single peak at $Re \approx 203$ which disappears if we increase the amplitude slightly above A_{cr}. The observation of this homotopy suggests that region R3a in the uncontrolled system is directly related to R1 and can be thought of as an additional R1 "peak" which, due to relatively large Reynolds numbers at which R3a is located, splits into a set of other peaks. The latter should not surprise since the rightmost peaks of region R1 in the uncontrolled system have very similar structure (see 4.2 for details). Moreover, if we compare the number of cycles the flow performs at the plateaux P13a and P3a4, we will see that the flow loses one oscillation as region R3a is crossed towards larger Re which is consistent with what happens when a peak in R1 is crossed. We should also note that all the simulations associated with the peaks capped at $t = 3000$ in figure 5.5 exhibit long-lasting oscillatory dynamics resembling the solution in figure 5.6(d) and discussed below.

We will now focus on the flow dynamics at the amplitude $A = 5 \times 10^{-2}$ to appreciate the effect of wall oscillations. Figure 5.6(a) shows the corresponding relaminarisation time curve put in comparison with the one in the uncontrolled system. One can notice that region R1 still keeps the same structure as for $A = 0$, albeit it is shifted towards larger Reynolds numbers and peaks are rather replaced by small subregions of large t_{relam} separated by the plateaux. Nonetheless, region R1 for $A = 5 \times 10^{-2}$ possesses its main distinguishing feature: the number of cycles the flow performs increases (decreases) as Re is shifted to the left (right) between two adjacent plateux. The space-time plot in figure 5.6(b) shows the solution at $Re = 190$ located at the plateau corresponding to 4 cycles of the flow. If we cross a small adjacent region of large t_{relam} to the right, we appear at the plateau associated with 3 cycles which is confirmed by figure 5.6(c) showing the solution at $Re = 193$. Even though the change of the number of cycles may be hard to be seen with the naked eye, the counting procedure explained in the end of Section 4.2, applied without any adaptation, confirms the result above. Similar to the uncontrolled case, between the plateaux, we find a set of simulations whose relaminarisation time exceeds 3000 in most of the cases. They all exhibit persistent oscillatory dynamics closely resembling that of PO5 solutions (see Section 3.3 for details) and accompanied by oscillations whose frequency is that of the walls and front deformation. One example is demonstrated by figure 5.6(d) showing the solution at $Re = 191$ located between the solutions corresponding to space-time plots 5.6(b, c). We can observe that the front locations slightly oscillate at the frequency of the walls

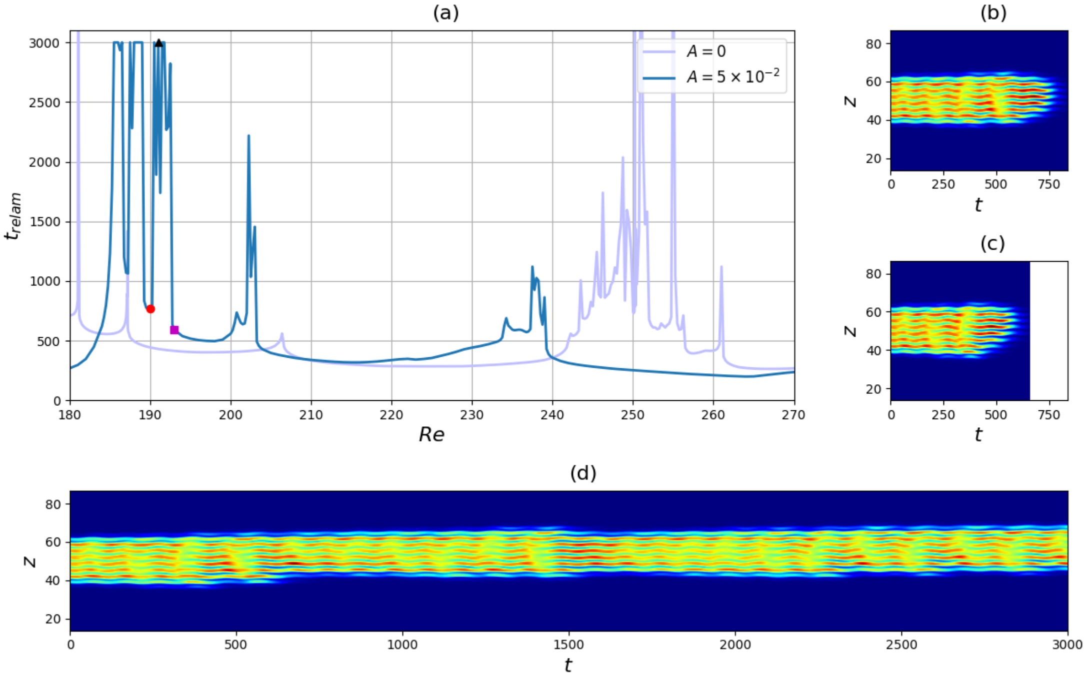

Figure 5.6: Plot (a) shows the relaminarisation time curves for S5 obtained at $A = 0$ (light blue) and $A = 5 \times 10^{-2}$ (dark blue). To exemplify the dynamics typical of region R1 in the latter case, space-time plots (b, c, d) show the evolution of the xy-averaged kinetic energy for simulations at $Re = 190$ (b), $Re = 191$ (d) and $Re = 193$ (c), i.e., before (red dot in plot (a)), within (black triangle) and after (magenta square) the chaotic window, associated with a peak in the uncontrolled case, respectively.

and the fronts themselves may asymmetrically nucleate and annihilate rolls resulting in the shift of the flow state and the change of its width. If we examine the peaks located at smaller Reynolds numbers, we will see that the deformation of the fronts becomes less and less significant as Re is descreased until the fronts become virtually immovable at the leftmost peak ($Re = 185.5$).

The solution at $Re = 185.5$ is a good candidate for more detailed analysis owing to its simplicity in comparison to other long-lived solutions in region R1 at $A = 5 \times 10^{-2}$. For this solution, the time-evolution of the fluctuations of the xy-averaged streamwise velocity, shown in figure 5.7(a) and mostly associated with the streak amplitude, exhibit clear oscillations synchronised with the oscillations of the base flow at the middle plane $y = 0$ (figure 5.7(b)) at the wall frequency $\omega_{walls} = 1/16 = 6.25 \times 10^{-2}$. Fourier time-decomposition of the L_2-norms of all three components of the velocity fields (figure 5.7(c)) confirms that the wall oscillations make a prime influence on the intensity of the streaks associated with $||u||$: the amplitude of the Fourier cofficient associated with $||u||$ is roughly one order of magnitude larger than those associated with $||v||$ and $||w||$ at frequency $2\omega_{walls}$ (the wall frequency is half the frequency observed because the Fourier transform was applied to the time-evolution of the L_2-norm). Importantly, this frequency is superimposed to another smaller frequency shown by the dashed line and primarily associated with a peak in $||w||$ which we attribute to the rolls. This second frequency exactly coincides with the frequency of a PO5 solution, $\omega_{PO5} \approx 3.6 \times 10^{-2}$, taken at a very close Reynolds number $Re = 185.56433$. To emphasise this link between the solution at $Re = 185.5$ and the PO5 solution, we additionally demonstrate the Fourier transform of the latter in figure 5.7(c). There, we observe the same peak at frequency ω_{PO5} and several peaks of smaller amplitudes at its subharmonics which seem to be suppressed in figure 5.7(d). In view of the above, we can say that in-phase wall oscillations induce strong oscillations of the streak intensity, clearly seen in figure 5.7(a), and superimpose them onto the typical oscillatory dynamics of the uncontrolled system associated with PO5 solutions. For relatively small amplitudes ($A \lesssim 6.8 \times 10^{-2}$) and Reynolds numbers ($Re \lesssim 220$), this action of the wall oscillations on the streaks may play a constructive role: it seems to oppose laminarisation in certain simulations which results in positive t_{incr} (see figure 5.4(b)) and long-lasting transients with very coherent dynamics (see figure 5.6(d)). For larger amplitudes, however, it breaks the self-sustained mechanism understood in the context of the PO5 solutions (see Section 3.3) and supporting the oscillatory dynamics in regions R1 and R3a so that these regions disappear for $A \gtrsim 6.8 \times 10^{-2}$. It is also worth noting that the fair counting of the number of cycles which we mentioned describing figure 5.6(a) becomes possible because, as follows from the Fourier decomposition in figure 5.7(d), the L_2-norm of the spanwise velocity exhibits clear oscillations at frequency ω_{PO5} just as in the uncontrolled system, whereas wall oscillations introduce only order-of-magnitude smaller subharmonics in the time-evolution of $||w||$.

Given such a strong influence of wall oscillations on the streaks at $A = 5 \times 10^{-2}$, it is natural to suggest that their phase may have a significant effect on the relaminarisation times. An appropriately chosen phase may strengthen the streaks during the last oscillation of the flow right before relaminarisation which, in turn, would support the

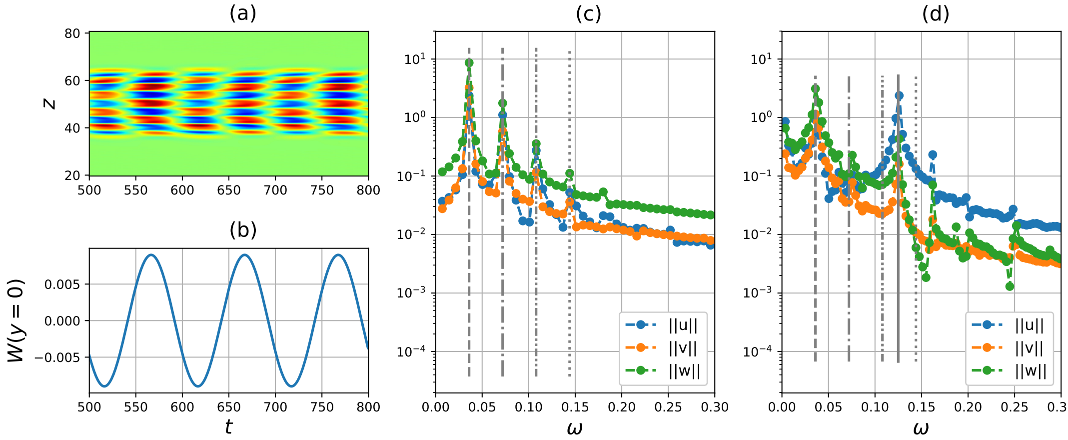

Figure 5.7: Plane (a) shows the space-time plot of the fluctuations of the xy-averaged streamwise velocity about its mean (blue/red/green colors correspond to negative/positive/zero values respectively) for the solution computed at $Re = 185.5$ in the presence of wall oscillations at amplitude $A = 5 \times 10^{-2}$, frequency $\omega_{walls} = 1/16$ and zero phase. These fluctuations are synchronous with the oscillations of the base flow at $y = 0$ shown in plot (b). Plots (c, d) show the absolute values of the Fourier coefficients associated with the L_2-norms of velocity components u, v and w computed for the solution taken at branch PO5 at $Re = 185.56433$ in the absence of wall oscillation (plot (c)) and the solution from plane (a) (plot (d)). The dashed, dash-dotted and dotted gray lines in plots (c, d) denote the multiples of $\omega_{PO5} \approx 3.6 \times 10^{-2}$ (the dashed line corresponds to ω_{PO5}). The solid gray line denotes $2\omega_{walls}$.

rolls, thus, preventing the break-up. To verify this, we take a simulation slightly to the right of the left boundary of the plateau between R1 and R3a, namely, at $Re = 203.5$ and investigate how the flow dynamics changes as the phase is increased. As plot 5.8(a) shows, the original simulation performs two cycles after which $||w||$ seems to stagnate for some time at $t \approx 280$ around low value $||w|| \approx 10^{-2}$ and then decays signifying a relaminarisation event. A tiny increase of the phase from 0 to $1/64\pi$ allows the flow to overcome this stagnation and, thus, relaminarisation and results in a long-lived solution, similar to the simulation shown in figure 5.6(d), as if we shifted the Reynolds number to the left. Similar trajectories are produced if the phase is increased further until $\phi = 5/64\pi$: at this phase, the flow starts exhibiting three cycles as if the Reynolds number is lowered down to $Re \approx 200$. Owing to the reflection symmetry of S5, the

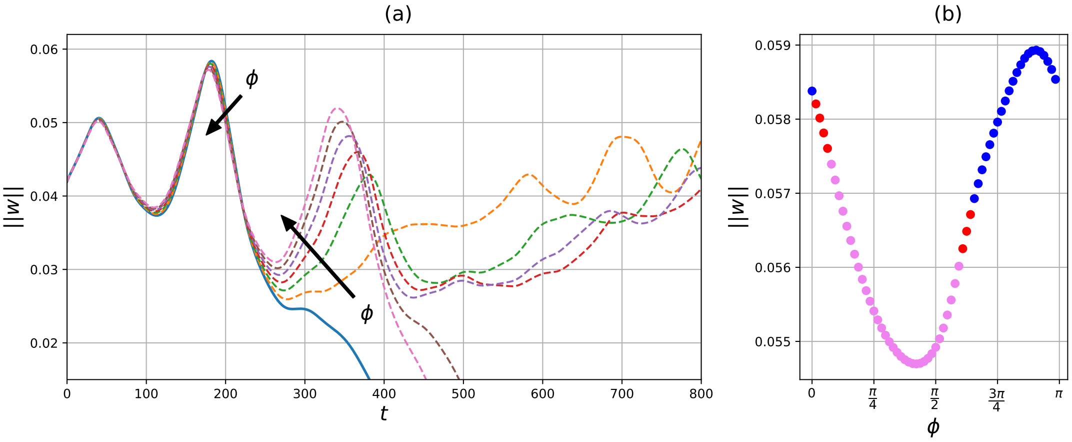

Figure 5.8: Time-evolution of the L_2-norm of the spanwise velocity (a) for different values of the phase of wall oscillations, from $\phi = 0$ (blue) to $\phi = 6/64\pi$ (pink). Plot (b) shows the dependence of the second local maximum of $||w||$ on the phase and illustrates which phase values lead to two-cycle (blue), three-cycle (pink) or long-lasting (red) dynamics of the flow. The step in ϕ is $1/64\pi$ for both plots.

flow dynamics must be invariant under the phase shift $\phi \to \phi + \pi$ modulo reflection in the spanwise direction, so further increase of the phase returns the flow dynamics back to the two-cycle dynamics through a window of ϕ where long-lasting simulations are observed. Thus, the overall effect of changing the phase in our particular experiment resembles that of "moving" the relaminarisation time curve, shown in figure 5.6(a), to the right, when ϕ is increased towards $\pi/2$, and back to the left when it is further increased towards π. It is also important to note that the change of the phase lowers and raises the local extrema of $||w||$ which can be used to predict whether the flow goes for one more cycle or not. Too large values of the local maxima of $||w||$ can be associated with the break-up of the self-sustained mechanism giving rise to oscillations in the flow. In particular, in the case of zero phase, the overshooting of the second local maximum $||w||$ around $t \approx 190$ in figure 5.8(a) results in a subsequent decay of the flow. A small increase of the phase from 0 lowers the second local maximum which helps overcome laminarisation of the flow. Thus, we find it useful to associate the regime of the flow with the value of the second local maximum which is shown in figure 5.8(b). One can observe that the clear threshold in $||w||$, separating the two-cycle regime and three-cycle regimes from the long-lasting one, cannot be identified here. Moreover, the effect of changing the phase on the second local maximum is quite limited: it allows for the decrease of the maximum by less than 10%. Similar experiment carried out at $Re = 215$, i.e., closer to the middle of the plateau, where the value of the second local maximum is larger than at $Re = 203.5$, shows that the phase change is not able to trigger the third cycle of the flow.

It is necessary to mention that changing the frequency may significantly affect the picture of the dynamics described above. For example, lowering the frequency from $\omega = 1/16$ down to $\omega = 1/32$ compresses region R1 and slightly shifts its left boundary towards larger Reynolds numbers. At the same time, it eliminates the long-lasting simulations with relaminaristion time above 1500 and introduces a steady spanwise drift of the localised states observed in some of the simulations.

5.4 Homotopy from the uncontrolled system for S13

We now turn to considering the homotopy from the uncontrolled system built using the second initial condition, S13. In the case of no wall oscillations, the dynamics of the flow emanating from S13 is first of all characterised by splitting of the initial spot into two spots. This process gives rise to regions R2 and R3 absent in the case of S5 and appears to be very sensitive to the presence of wall oscillations. In contrast to S5 where wall oscillations at a tiny value of the amplitude $A = 10^{-2}$ only slightly affect the structure of the relaminarisation time curve, they provoke the activation of the spots appearing after the splitting in the case of S13 and, as a consequence, lead to an expansion of region R2: its right boundary nearly reaches the left boundary of R3 at $A = 10^{-2}$ as one can see from figures 5.9(a) and 5.10(a). More specifically, it is subregion R2c that is expanded towards larger Reynolds numbers whereas subregions R2a and R2b are mostly unchanged at $A = 10^{-2}$ (except for a small shift of their boundaries towards smaller Re). At this amplitude, again unlike S5, the phase or frequency change may have a significant influence on the boundaries and statistics of the regions. For example, figure 5.10(c) shows that decreasing the frequency down to $\omega = 1/32$ destroys subregion R2a, similar to S15 and wider initial conditions in the uncontrolled system (see Section 4.3), and move region R3 to larger Reynolds numbers ($Re \approx 260$) which drastically increases the number of long-lasting simulations in R3. The change of the phase, in turn, has a less dramatic effect: for instance, setting the phase $\phi = \pi/2$ results in the connection of regions R2 and R3 whose boundaries were

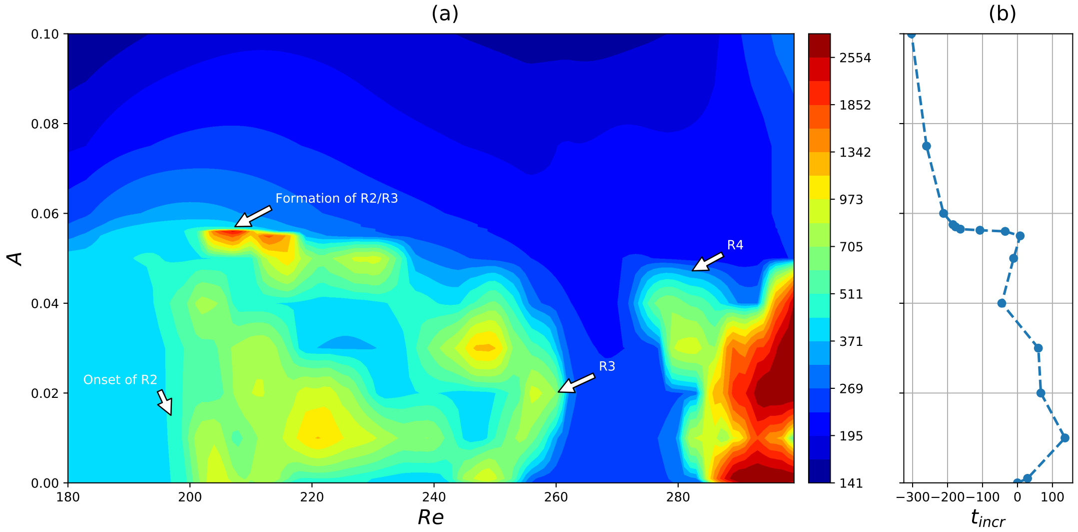

Figure 5.9: Same as figure 5.4, but built for initial condition S13.

already close to each other at zero phase (see figure 5.10(b)).

Inspecting figure 5.9(a) further, we can see that an additional increase of the amplitude first results in the connection of regions R2 and R3 ($A = 2 \times 10^{-2}$) and then their separation and movement to lower Reynolds numbers as A is increased above $A = 2 \times 10^{-2}$. These regions start approaching each other for $A \gtrsim 5 \times 10^{-2}$, collide into a peak at $(A, Re) \approx (5.625 \times 10^{-2}, 207)$ and eventually disappear for amplitudes larger than $A \approx 5.625 \times 10^{-2}$. One can note that this scenario is very close to that of transformations of regions R1 and R3a for S5. In particular, the collision of regions R2 and R3 into a peak occurs in the same fashion as shown in figure 5.5 and one can similarly associate this peak with a simulation exhibiting long-lasting oscillatory dynamics resembling the solution in figure 5.6(d). It is also expected that, given much finer resolution in A and Re than the one we have, one can track how region R1 for S13 connects to the peak at $(A, Re) \approx (5.625 \times 10^{-2}, 207)$ similar to region R1 for S5. Finally, we can notice from figure 5.9(b) that the relaminarisation time in the presence of control increases on average with respect to the uncontrolled system for $A \lesssim 4 \times 10^{-2}$ which reinforces our observation, made initially for the case of S5, that wall oscillations typically destabilise the system when their amplitude is below some threshold ($A \approx 6.5 \times 10^{-2}$ for S5 and $A \approx 4 \times 10^{-2}$ for S13) and significantly stabilise it for larger values of the amplitude.

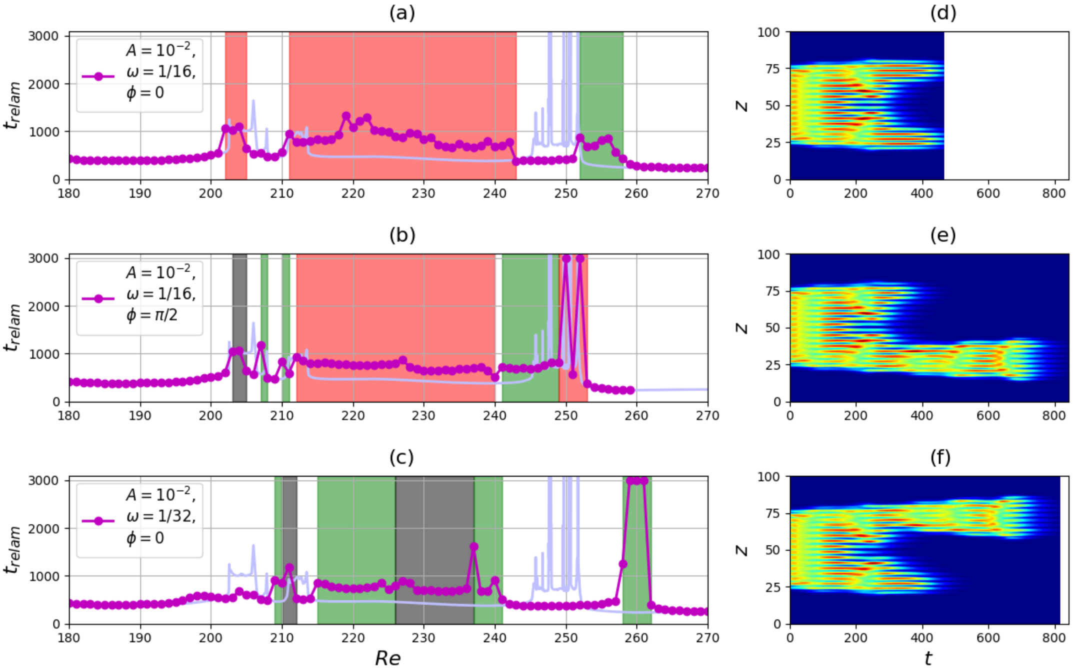

Figure 5.10: Plots (a, b, c) show the relaminarisation time curves for S13 for different combinations of the frequency and phase of wall oscillations at $A = 10^{-2}$ (magenta curves) put in comparison to the relaminarisation time curve in the uncontrolled case (light blue). Coloured bands correspond to ranges of Re within which the flow exhibits two-spot (gray) or one-spot (red and green for a long-lived spot located around $z = 25$ and $z = 75$ respectively) oscillations after the splitting of the initial spot (the right boundaries of the bands are not included in the corresponding ranges). Space-time plots (d, e, f) compare the evolution of the xy-averaged kinetic energy of the flow emanating from S13 at $Re = 220$ for three configurations: no control (d), $(A, \omega, \phi) = (10^{-2}, 1/16, \pi/2)$ (e) and $(A, \omega, \phi) = (10^{-2}, 1/32, 0)$ (f).

Since in-phase wall oscillations break the reflection symmetry, typical for the dynamics in the uncontrolled system (see Section 4.4), it is sensible to expect that the splitting of the initial spot in the presence of control will lead to the asymmetrical evolution of the resulting two spots. Indeed, depending on the control parameters and Reynolds number, one of the spots may decay right after the splitting whereas the second one may continue to evolve for much longer time and even approach self-sustained oscillations similar to the solutions in figures 5.6(d) and 5.7(a). Two examples of such asymmetrical spot dynamics are shown in space-time plots 5.10(e, f) for control parameters $(A, \omega, \phi) = (10^{-2}, 1/16, \pi/2)$ and $(A, \omega, \phi) = (10^{-2}, 1/32, 0)$ respectively for S13 time-integrated at the same Reynolds number $Re = 220$. One could note that wall oscillations at $\omega = 1/16$ do not seem to alter the initial stage of the splitting, i.e., the formation of the laminar gap in the middle of the initial spot (compare plots 5.10(d) and 5.10(e) for $200 \lesssim t \lesssim 350$), but rather stimulate one or both of the spots, which have short lifetime in the absence of control, to perform additional oscillations on the time-scale typical for region R2. We can expect that the analysis, similar to that shown in figure 5.8, but carried out with respect to A and separate spots, would reveal that wall oscillations strengthen decaying streaks of one or both of the spots and, thus, refuel the self-sustained mechanism via the nonlinear interaction between streaks and rolls producing subsequent spot oscillations.

Even though we observe this phenomenon for all investigated control parameter values for which regions R2 and R3 can be defined, a regime of splitting at a given Re is predictably sensitive to changes in control parameter values. The coloured bands in plots 5.10(a, b, c) exemplify this by comparing the relaminarisation time curves obtained by changing phase and frequency at $A = 10^{-2}$. For example, increasing the phase up to $\pi/2$ at frequency $\omega = 1/16$ (plot 5.10(b)) stimulate both spots to get activated for the simulations around $Re \approx 203$ whereas only one of them was activated at zero phase for the same Re (plot 5.10(a)). Even more dramatic difference is caused by a frequency decrease from $\omega = 1/16$ (plot 5.10(a)) to $\omega = 1/32$ (plot 5.10(c)) given zero phase: in the former configuration, only one spot located around $z = 25$ get activated for $Re \in [211; 242]$ whilst in the latter configuration, either two spots simultaneously ($Re \in [211; 212) \cup [226; 237)$), only one spot located around $z = 75$ ($Re \in [215; 226) \cup [237; 241)$) or no spot whatsoever ($Re \in [212; 215) \cup [241; 242]$) exhibit oscillatory dynamics. On the other hand, plots 5.10(a, b, c) show that the regime of splitting has a non-trivial dependence on the Reynolds number given a fixed amplitude, frequency and phase of wall oscillations.

It is also necessary to note that similar phenomenon can be observed if we merely break the reflection symmetry of the initial condition. For example, the shift of region boundaries and asymmetrical evolution of the spots after the splitting can both be recovered if we reproduce the relaminarisation time curves for S13 slightly deformed

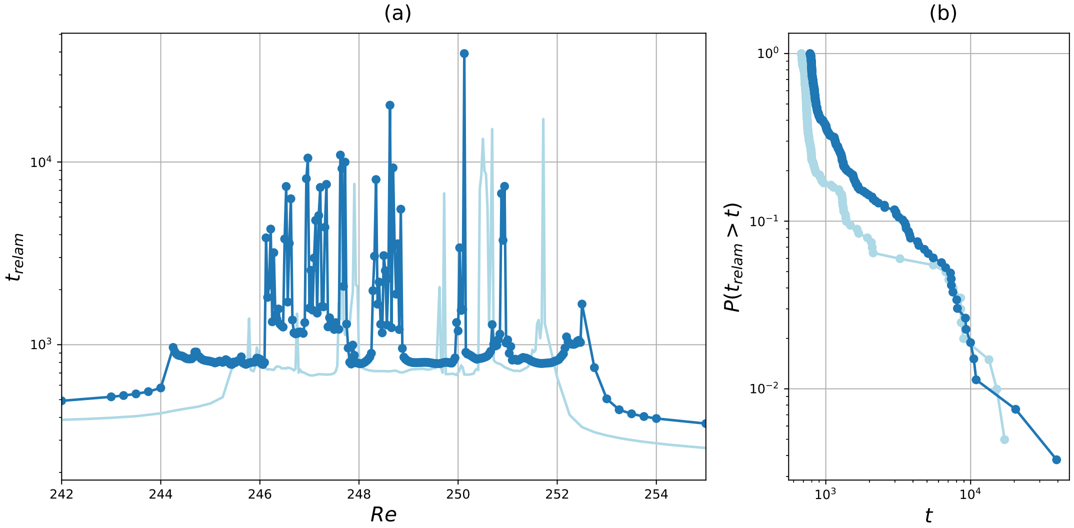

Figure 5.11: Relaminarisation times (a) and survival function $P(t_{relam} > t)$ (b) computed within region R3 for S13 and plotted for two cases: no control (light blue) and wall oscillations at $(A, \omega) = (10^{-3}, 1/16)$ (dark blue).

along the spanwise coordinate:

$$\tilde{\boldsymbol{u}}_{S13}(z) = [1 + p \tanh(s(z - \Gamma_z/2))]\, \boldsymbol{u}_{S13}(z),$$

where $\boldsymbol{u}_{S13}$ is the flow-field of S13, $s = 0.3$ controls the sharpness of the asymmetry and $p = 10^{-2}$ quantifies added disturbance to S13.

We have already noticed that wall oscillations at amplitude 10^{-2} significantly modify the structure of regions R2 and R3. The original structure of regions R2 and R3 can be recovered if we lower the amplitude down to 10^{-3}: at this amplitude, region boundaries only slightly differ from those in the uncontrolled case. Nonetheless, the asymmetrical evolution of the spots after the splitting is still present. In contrast to larger amplitude values, however, the one-spot regime, i.e., when only one spot gets activated after the splitting, is now observed only in the vicinity of region boundaries which are slightly expanded in comparison to the uncontrolled case. The latter statement is supported by figure 5.11(a) showing the relaminarisation times in region R3 for both the uncontrolled and controlled cases. Importantly, one can observe that the relaminarisation times are mostly larger in the controlled case at the same Reynolds numbers. To assess this observation statistically, we follow the scheme for the analysis of the relaminarisation

	N	m	μ_L	σ_L	$\max H$	f_H
Maximum at $A = 0$	217	759.0	802.901	191.269	22181.5	0.203
S13 ($A = 0$)	201	734.5	779.407	155.159	17164.5	0.095
S13 ($A = 10^{-3}$)	265	856.0	939.379	213.404	39241.0	0.155

Table 5.1: Statistics of R3 gathered for S13 in the case of no control (second row) and wall oscillations at $(A, \omega) = (10^{-3}, 1/16)$ (third row). The first row contains the maximum values of the statistics found among all the initial conditions in the uncontrolled case (see table 4.3). For the explanation of the statistics meaning, see Section 4.4.

times in region R3 explained in Section 4.4 and applied there for the uncontrolled case. Namely, we recalculate statistics m (the median of the whole distribution of t_{relam} in region R3), μ_L, σ_L (the mean and standard deviation of t_{relam} associated with relatively quick simulations), $\max H$ (the largest t_{relam}) and f_H (the probability of getting a long-lived chaotic transient) using the same spacing in Re as we did for $A = 0$ and report our results in table 5.1. It can be seen that all these quantities are significantly increased at $A = 10^{-3}$ and, except for f_H, take values larger than those found among all the initial conditions investigated at $A = 0$. This clearly signifies that even very small-amplitude wall oscillations substantially destabilise the system. The same conclusion can be made if we look at the survival function $P(t_{relam} > t)$ plotted in figure 5.11(b) and estimating the probability that a simulation in region R3 will not exhibit relaminarisation for at least t time units: for all $t \lesssim 6000$, the probability of surviving is clearly larger at $A = 10^{-3}$. Interestingly, the survival functions seem to overlap for $t_{relam} \gtrsim 6000$ which, however, may be a mere coincidence given that such very long-lasting simulations are essentially rare events in region R3.

We finish this section by discussion of how wall oscillations affect the front speed in region R4. We have just seen that, in general, wall oscillations even at small amplitudes increase the relaminarisation time and we may reasonably expect that they similarly increase the front speed in region R4. This logic, however, appears to be misleading in our case. Figure 5.12 shows that wall oscillations, on average, significantly decrease the expected front speed $\mathrm{E}[\langle c \rangle_t]$ even at $A = 10^{-2}$ reducing it to virtually zero at $A = 5 \times 10^{-2}$. Only at $A = 10^{-3}$ we find a marginal decrease in the expected front

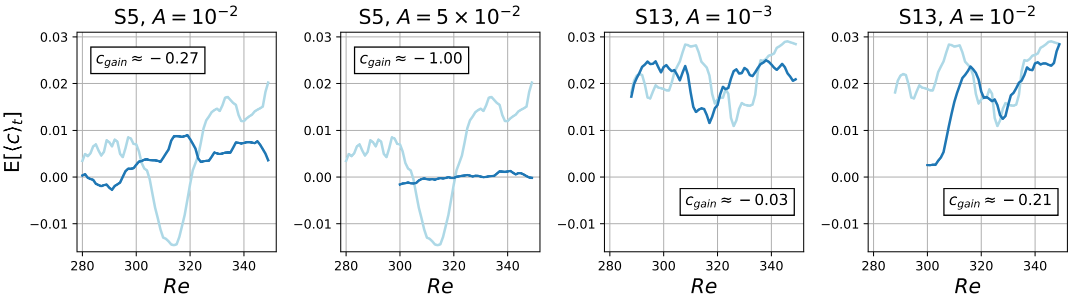

Figure 5.12: The dependence of the expected front speed on Re in region R4 for S5 and S13 plotted for various amplitudes of wall oscillations at frequency $\omega = 1/16$ and zero phase (dark blue) and put in comparison to the uncontrolled case (light blue).

speed ($c_{incr} \approx -3\%$). Interestingly, one can observe that the expected front speed at amplitude $A = 10^{-2}$ for S13 and $Re \lesssim 316$ is significantly lower in comparison to the uncontrolled case, whereas for $Re \gtrsim 316$, the expected front speeds nearly coincides for both cases. This fact is explained by the aforementioned asymmetrical evolution of the spots occuring after the initial splitting: for $Re \lesssim 316$, we always find a one-spot regime of the splitting within region R4 which yields the front speed close to S5, whilst for $Re \gtrsim 316$, both spots get activated after the splitting which matches the S13 dynamics in the uncontrolled setup. Finally, we note that the previously discussed increase of t_{relam} in regions R1, R2, R3(a) in the presence of wall oscillations and the reduced front speed in region R4 are not contradictory, but rather complementary facts: the former may be expected to take place in region R4 too, once we continue all the simulations until relaminarisation, as a direct consequence of the latter.

5.5 Onset of transition to turbulence

We have so far investigated the flow dynamics for relatively small values of the amplitude, $A < 10^{-1}$, and learnt that for larger amplitudes, regions R1, R2 and R3(a) disappear so that only region R4, associated with transition to turbulence, persists and moves to higher Reynolds numbers. The dependence of the left boundary of region R4, i.e, the critical Reynolds number for a particular initial condition, on the control parameter values thus becomes the main criterion to assess the efficiency of control. Preliminary calculations showed that, for $A > 10^{-1}$, the left boundary of region R4

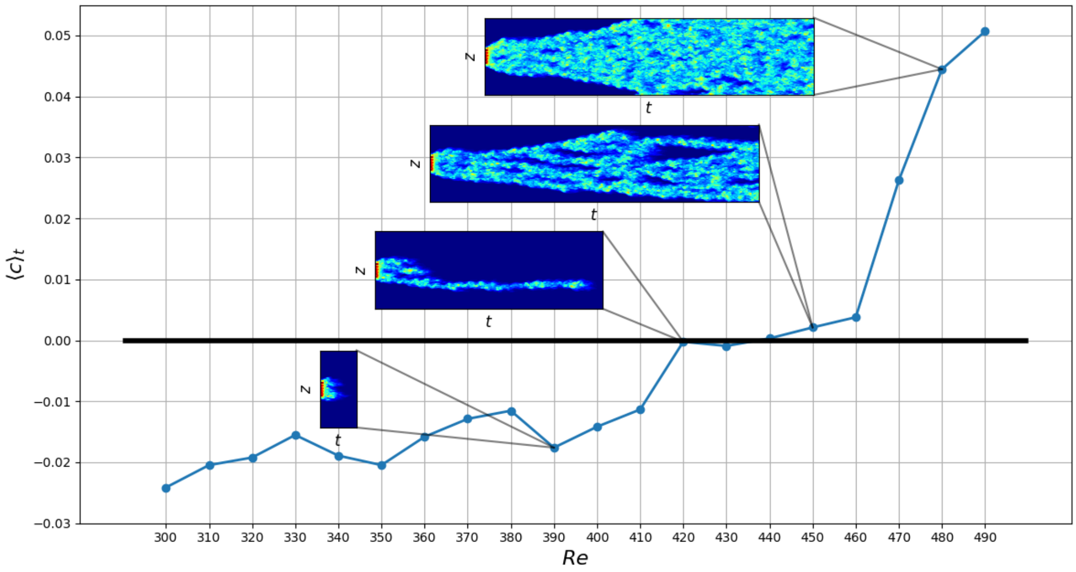

Figure 5.13: Dependence of the averaged front speed $\langle c\rangle_t$ on the Reynolds number for the flow emanating from S5 in the presence of wall oscillations at amplitude $A = 0.3$ and frequency $\omega = 1/16$. The insets show the time-evolution of the xy-averaged kinetic energy of the flow obtained at the corresponding Reynolds number.

can no longer be associated with an abrupt increase of t_{relam} as for the uncontrolled case (see figure 4.16). We then determine the boundary of region R4 as the smallest Reynolds number at which the flow emanating from a particular localised state exhibit a positive front speed and denote it Re_{cr}. Using initial condition S5 as an example, figure 5.13 shows the dependence of the averaged front speed on Re in the presence of wall oscillations at $(A, \omega) = (0.3, 1/16)$. One can notice that $\langle c\rangle_t(Re)$ first grows from negative values around $\langle c\rangle_t = -0.02$ associated with a very quick decay of the initial spot as demonstrated by the simulation at $Re = 390$. Getting closer to $Re = 430$, the averaged front speed almost vanishes and crosses zero between $Re = 430$ and $Re = 440$ which gives the following estimation of the critical Reynolds number: $430 \lesssim Re_{cr} \lesssim 440$. To get a more accurate value, we assume that the front speed varies approximately monotonically in the vicinity of Re_{cr} and find $Re_{cr} = 439.5$ by bisecting the interval $Re \in [430; 440]$. Slightly to the left of Re_{cr}, the flow exhibits long-lasting dynamics associated with a chaotic evolution of one or few spots, neither growing nor decaying for a substantial amount of time (see the simulation at $Re = 420$

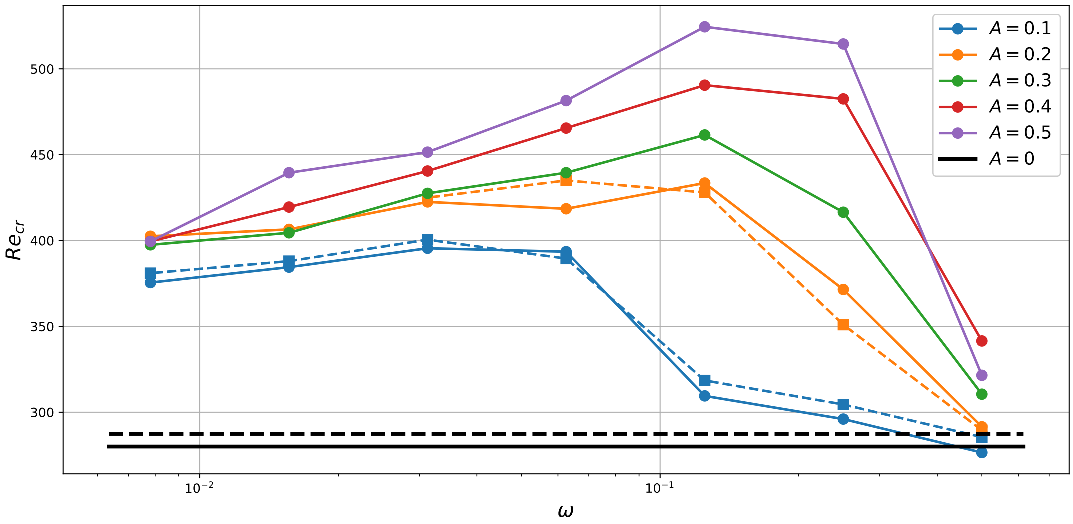

Figure 5.14: Dependence of the critical Reynolds number Re_{cr}, associated with the onset of transition to turbulence and calculated for S5 (solid curve) and S13 (dashed curve), on the amplitude A and frequency ω of wall oscillations.

in figure 5.13). When Re_{cr} is crossed, these spots can be observed to grow, split and collide thus resulting in a significant growth of the turbulent fraction which is still non-zero for at least $t = 3000$ time units just above Re_{cr} (see the simulation at $Re = 450$ in figure 5.13) and quickly approaches 1 if the Reynolds number is increased further (see the simulation at $Re = 480$ in figure 5.13). One may notice that this scenario of transition is clearly different from the uncontrolled system where a tiny decrease of Re from the left boundary of region R4 would result in quick relaminarisation of the flow whilst crossing the boundary almost inevitably leads to a domain-filling state. In contrast, wall oscillations favour directed-percolation-like transition where the turbulent fraction gradually increases when the Reynolds number crosses the critical value Re_{cr}. It should be noted that transition to turbulence in uncontrolled plane Couette flow is already suspected to fall into directed percolation universality class [132] but only in the case of very large and doubly extended domains. In the case of our wide domain extended in the spanwise direction only, transition in the uncontrolled system is rather abrupt (see figure 4.16) and the addition of wall oscillations induces features typical for the continuous transition. This may be related to the modification of the laminar solution, occurring due to wall oscillations, which can indeed turn the transition from discontinuous to continuous as exemplified by a coupled-map lattice model in [132].

Using the same scheme for the determination of Re_{cr} as described above, we can recover how it changes as the amplitude and frequency are varied for the case of initial conditions S5 and S13. Figure 5.14 shows this dependence for amplitudes $A \in \{0.1, 0.2, \dots, 0.5\}$ and frequencies $\omega \in \{2^{-1}, 2^{-2}, \dots, 2^{-7}\}$. First of all, we note the stabilising role of the amplitude: increasing the amplitude of wall oscillations leads to delaying the onset of transition of turbulence at almost any frequency. The dependence of Re_{cr} on the frequency is instead convex: the critical Reynolds number grows if we decrease the frequency from $1/2$ and takes its maximum value at frequencies $1/8$ or $1/16$ depending on the amplitude (the expection is Re_{cr} for S13 at $A = 0.1$, where the optimal frequency is $\omega = 1/32$). Further decrease of the frequency results in a monotonic decay of Re_{cr}. Overall, the largest delay of transition is achieved at $(A, \omega) = (0.5, 1/8)$ which allows for the shift of the onset up to $Re_{cr} \approx 524.5$ for S5. One should also notice that $Re_{cr}(A, \omega)$ depends on the choice of the initial condition, but it does not change the qualitative picture described above. We note that these results are insensitive to the phase change because, close to Re_{cr}, the time-scale of flow relaminarisation is at least one order of magnitude larger than the period of oscillations (except for the case $\omega = 1/128$ which is thus treated as unreliable).

Chapter 6

Probabilistic protocol for designing control of transition

While designing any type of flow control, it is important to have an objective measure of the control efficiency as a function of its parameter values. In the case of finite-amplitude instabilities in general and transition to turbulence in particular, such a measure could be the size of the basin of attraction of the laminar state (or, generally speaking, of any invariant set exhibiting finite-amplitude instability). Since we cannot calculate the size of the basin of attraction directly, we are interested in a scalar proxy either approximating or being proportional to this size. Recent advances in nonlinear stability theory suggest that the minimal seed energy may be a good candidate [189]. The framework for designing control based on this idea suggests that the robustness of the laminar flow to finite-amplitude perturbations is maximised (minimised) if the flow control minimises (maximises) the energy of the minimal seed. Similarly, one may consider the energy of the edge state, directly related to the edge of chaos separating laminarising and transitioning perturbations, as a scalar proxy for the size of the basin of attraction and suggest its minimisation or maximisation. However, both the minimal seed and the edge state are merely points or sets belonging to the basin of attraction, and their energy does not necessarily change in a direct proportion to the basin size. In this chapter, we propose using the laminarisation probability, i.e., the probability that a random finite-amplitude perturbation decays as a function of its energy, as a more robust proxy for the size of the basin of attraction of the laminar state. Our notion of the laminarisation probability is very close to that of the basin stability introduced in [190]. In Section 6.1, we describe the design and sampling of the random perturbations. We then introduce in Section 6.2 a probabilistic protocol for the assessment of the control efficiency based on the calculation of the laminarisation probability and discuss its estimation, employed to make the flow control design feasible, in Section 6.3. Using in-phase spanwise wall oscillations, already introduced in Chapter 5, as an example of a control strategy [154] and a small domain $\Gamma_x \times \Gamma_y \times \Gamma_z = 4\pi \times 2 \times 32/15\pi$, we demonstrate in Section 6.4 how our protocol can be employed to find optimal parameter values of the control aimed at suppressing or triggering transition to turbulence at $Re = 500$ and relate these results to the control design based on the maximisation of the edge state energy in Section 6.5. The domain we will use has the same streamwise extent as the one in the previous chapters, but its spanwise extent is now equal to one spanwise wavelength of spatially periodic solutions in the wide domain. Such a choice of the domain size will allow us to make a comparison of transitional properties of the flow altering as a function of the amplitude and frequency of wall oscillations for the cases of small and wide domains.

6.1 Design of random initial conditions

Our probabilistic protocol necessitates the calculation of the laminarisation probability $P_{lam}(E)$ as a function of the energy of a random finite-amplitude perturbation (RP) $\boldsymbol{u}$. We express an RP as a linear combination of the laminar solution $\boldsymbol{U_{lam}} = [y, 0, 0]^T$ and a random component orthogonal to the laminar solution:

$$\boldsymbol{u} = B\boldsymbol{U_{lam}} + C\boldsymbol{u}_{\perp}, \tag{6.1}$$

where $\langle \boldsymbol{u}_{\perp}, \boldsymbol{U_{lam}} \rangle = 0$ and $||\boldsymbol{u}_{\perp}|| = 1$ (see (3.9) for definition of the L_2-norm and the scalar product). We generate the random orthogonal component $\boldsymbol{u}_{\perp}$ by means of routine *randomfield* embedded in Channelflow which samples its spectral coefficients from the uniform distribution and guarantees that the homogeneous boundary conditions are satisfied. The coefficients B and C, in turn, must be chosen so that $\boldsymbol{u}$ possesses kinetic energy E, i.e.,

$$\begin{aligned} & ||\boldsymbol{u}||^2 = 2E \\ \implies \quad & C^2 + B^2||\boldsymbol{U_{lam}}||^2 = 2E. \end{aligned} \tag{6.2}$$

Our testing calculations showed that $P_{lam}(E)$ is especially sensitive to the sign of B and, thus, to the asymmetry of the distribution. They also revealed that the RPs corresponding to $C \approx 0$ inevitably laminarise both in the uncontrolled and in the controlled cases which makes sampling of RPs in the vicinity of $C = 0$ meaningless. We address both issues by drawing B from the uniform distribution defined by the following probability density function (pdf)

$$f_B(b) = \frac{||\boldsymbol{U_{lam}}||}{2\sqrt{2E}}, \quad b \in \left(-\frac{\sqrt{2E}}{||\boldsymbol{U_{lam}}||}; \frac{\sqrt{2E}}{||\boldsymbol{U_{lam}}||} \right), \tag{6.3}$$

and then computing $C = \sqrt{2E - B^2||\boldsymbol{U_{lam}}||^2}$. The resulting pdf for C can then be derived as the distribution of the monotonic transformation of the random variable B (see Theorem 2.1.8 in [191]):

$$f_C(c) = \frac{c}{\sqrt{4E^2 - 2Ec^2}}, \quad c \in (0; \sqrt{2E}). \tag{6.4}$$

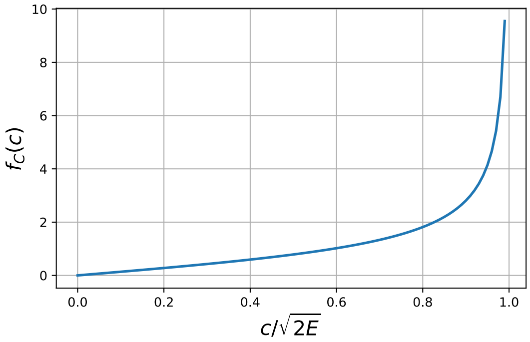

Figure 6.1: Probability density function of C obtained by assuming that B is drawn from the uniform distribution.

Figure 6.1 shows the pdf for C and confirms that the probability of sampling C in the vicinity of $C = 0$ tends to 0. We also note that it is sufficient to consider only positive C since the sign of C is implicitly included into $\boldsymbol{u}_\perp$.

One could notice that an RP as defined in (6.1) does not satisfy the homogeneous boundary conditions in the case when $C \neq 0$. To impose the boundary conditions, we make use of the numerical scheme used (see Chapter 2 for details) and preprocess RPs by performing two small time-steps. After the first time-step, the state is forced to satisfy the boundary conditions, but, due to the discontinuity embedded in an initial condition, the tau correction of the Chebyshev coefficients produces the solution with a large amplitude in the highest mode yielding a saw-like profile. The highest mode, however, decays away after the second time-step (see figure 6.2 for the comparison). By RP, we hereafter understand the state formed after these two time-steps.

The preprocessing procedure leads to a slight change of the RP energy. To assess how large this change is, we preprocessed 4000 RPs generated for 40 energy levels $\widetilde{E}_j$, $j = 1, \dots, 40$ equally spaced between 0 and $(2/3)E_{turb}$, where $E_{turb} \approx 6 \times 10^{-2}$ is the average turbulent kinetic energy, and calculated the average deviation per each energy level. Figure 6.3 shows the relative change of the kinetic energy as a function of the RP energy prior to preprocessing and demonstrates that, on the average, the energy drops by less than 0.3% due to the preprocessing of RPs. We will then shift all the energy levels $\widetilde{E}_j$ after sampling RPs according to the average deviation resulting from the preprocessing procedure which gives 40 energy levels E_j at which we will assess the laminarisation probability. It can similarly be shown that the values of B and C

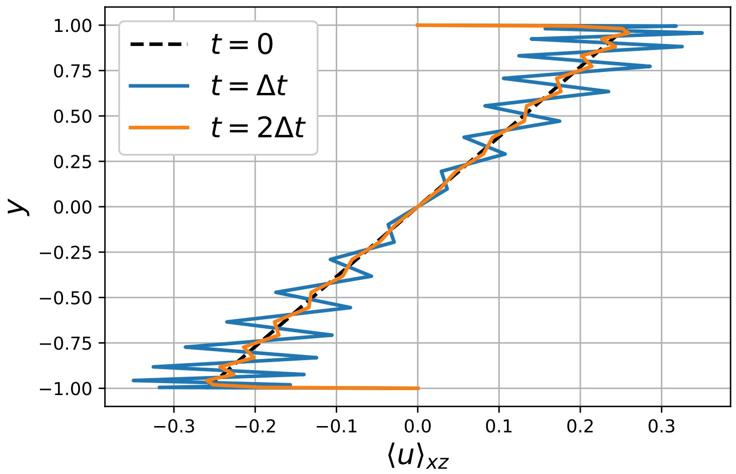

Figure 6.2: The xz-averaged profile of the streamwise component of the velocity field of the initial RP violating the homogeneous boundary conditions (dashed black line) and its evolution after the first (blue line) and second (orange line) time-steps.

change by less than 0.1% which we treat as negligible.

6.2 Laminarisation probability in uncontrolled and controlled cases

Eventually, we approximate $P_{lam}(E)$ at 40 discrete energy levels $E_j,\ j = 1, \dots, 40$. For each energy level $\widetilde{E}_j$, we generate 200 RPs: 100 of them have negative B and other 100 RPs have positive B. The former and latter RPs form the sets which we call RP$-$ and RP$+$ respectively. By time-integrating each RP at Re, we classify RPs as laminarising if the kinetic energy of flow emanating from an RP drops below $E_{lam} = 6 \times 10^{-4}$ during the first 400 time units of time-integration. The last condition is necessary to capture the “laminarisation via overshooting” which we witnessed in our preliminary simulations: the kinetic energy of the flow may grow significantly above the average turbulent kinetic energy and then quickly decay down to zero which we also wish to count as a laminarisation event. Other RPs whose energy are classified as transitioning to turbulence. The remaining RPs whose energy fluctuates between E_{lam} and E_{turb} for more than 400 time units, are thus left unclassified, but we have not observed such cases: they would correspond to the trajectories wandering around the edge manifold.

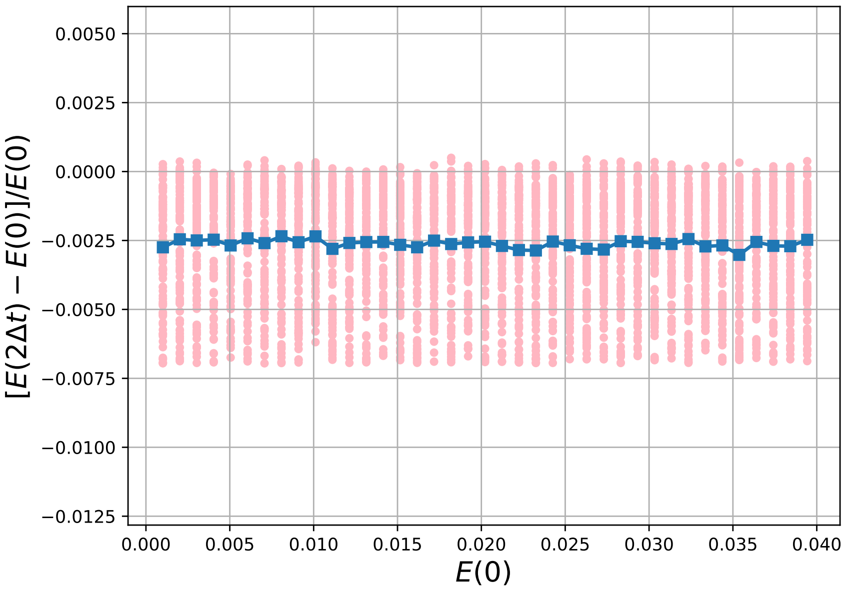

Figure 6.3: Relative change in kinetic energy $\left[E(2\triangle t) - E(0)\right]/E(0)$ after two small time-steps plotted versus the initial energy $E(0)$, where $E(t) = \frac{1}{2}||\boldsymbol{u}(t)||^2$. Pink circles show the relative change for all the RPs and blue line shows the relative change averaged over the RPs at a given energy level. Time-integration was carried out at $Re = 500$.

The laminarisation probability $P_{lam}(E_j)$ at energy level E_j is then approximated by the fraction of laminarising RPs at the given energy level.

Figure 6.4(a) shows the resulting distribution of the laminarisation probability in uncontrolled plane Couette flow in a small computational domain $\Gamma_x \times \Gamma_y \times \Gamma_z = 4\pi \times 2 \times 32\pi/15$ where all the simulations were performed at $Re = 500$. The laminarisation probability expectedly starts from 1 at the first two energy levels which means that all the RPs having such energies laminarise. The first transitioning RPs appears at the third energy level which then defined the upper bound for the energy of the minimal seed: $E_{min} < 4 \times 10^{-3}$. Beginning from E_3, we can observe that P_{lam} descreases nearly monotonically until it reaches a plateaux at $P_{lam} \approx 0.08$ for energies larger than the edge state energy $E_{edge} \approx 1.82 \times 10^{-2} \approx (1/3)E_{turb}$ (see Section 6.5 for the discussion of the edge states). Our decomposition of the RPs into the laminar solution and a random orthogonal component allows for an important observation: RP$-$, characterised by a weakened bulk shear which is typical for averaged turbulent profiles, are found to have

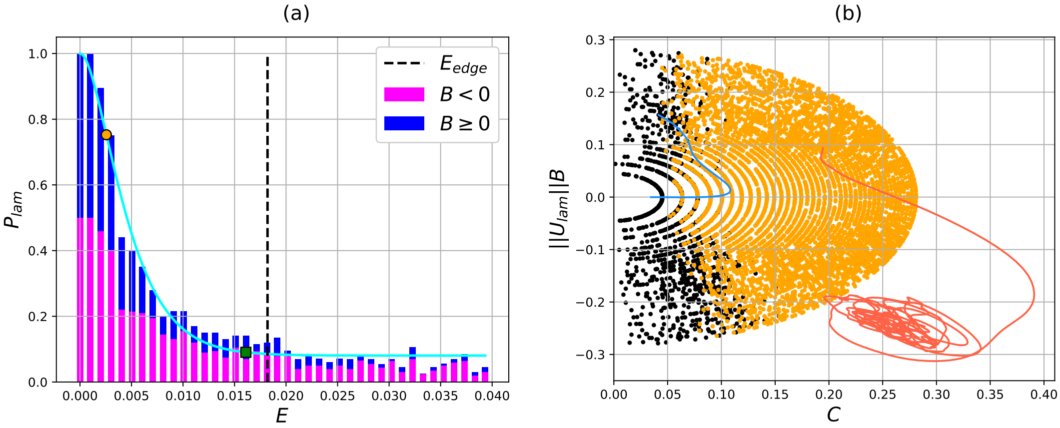

Figure 6.4: The left plot shows the laminarisation probability P_{lam} as a function of the energy of RPs (bars) and the fitting function (6.5) with $a = 0.0805$, $\alpha = 2.05$ and $\beta = 412$ found via least-squares approximation (solid line). The fitting function is additionally characterised by the inflection energy $E_{flex} \approx 2.5 \times 10^{-3}$ (orange circle) and energy $E_a \approx 1.6 \times 10^{-2}$ (green square) above which the fitting function is in the asymptotic regime. The right plot shows all the RPs used to construct $P_{lam}(E)$ projected onto the reduced (B, C)-subspace where black and orange dots denote laminarising and transitioning RPs respectively. To give an example, a pair of laminarising (blue curve) and transitioning (red curve) trajectories is plotted. Note that the laminarising trajectory ends up in the vicinity of $(B, C) = (0, 0)$, which correspond to the laminar fixed point, whereas the the transitioning trajectory is mostly located in a small region in the lower right corner associated with the turbulent saddle.

larger laminarisation probability compared to RP+. In fact, figure 6.4(a) demonstrates that RP− are almost solely responsible for non-vanishing P_{lam} for large values of RP energy. This is a fairly counterintuitive result: the closer the RP bulk shear is to the bulk shear of the averaged turbulent profile, the more likely the RP laminarises. The same conclusion can be made by looking at figure 6.4(b) which shows all the RPs in the reduced (B, C)-space. One can notice that laminarising RPs are concentrated in the region adjacent to $C = 0$ and only rare ones can be found beyond this regions. We will denote this region $\mathrm{R_{lam}}$ for a future use. The part of $\mathrm{R_{lam}}$ associated with RP− is clearly larger than that associated with RP+ which explains the difference in their laminarisation probability. Figure 6.4(b) demonstrates the laminarisation of one of the RPs from region $\mathrm{R}_{\mathrm{lam}}$. Inspecting laminarising trajectories reveals that the kinetic energy of the flow, B and C can all evolve non-monotonically during laminarisation, except for the terminate phase where the dynamics is linear and thus dominated by the exponential decay. We however note that the vast majority of laminarising trajectories demonstrate a monotonic decay of the kinetic energy. In the exceptional cases where the kinetic energy of the laminarising flow evoles non-monotonically, it is still significantly lower than the averaged turbulent kinetic energy at any time and can at best reach the values compared to the edge state energy. Figure 6.4(b) also shows a typical turbulent trajectory emanating from one of the RPs classified as transitioning and trapped into a small region roughly confined between by $||\boldsymbol{U_{lam}}||B \in [-0.3; -0.2]$ and $C \in [0.2; 0.3]$. This region is associated with a projection of the turbulent saddle onto the (B, C)-subspace. We can thus say that the dynamics on the turbulent saddle is associated with negative B which justifies our physical explanation of the sign of B and again confirms the importance of our decomposition of RPs.

The dependence of P_{lam} on energy can be approximated by the following fitting function:

$$p(E) = 1 - (1 - a)\gamma(\alpha, \beta E), \tag{6.5}$$

where $\alpha, \beta, a, E > 0$ and $\gamma(\alpha, \beta E)$ is the lower incomplete gamma function. Figure 6.4(a) shows the least-squares fitted function $p(E)$ with $a = 0.0805$, $\alpha = 2.05$ and $\beta = 412$. We find it useful to charaterise this evolution by the following scalar quantities:

- Energy $E_{99\%}$ at which the predicted laminarisation probability is 0.99.
- Energy E_{flex} at which the fitting function has an inflection point.
- Asymptotic laminarisation probability a: $\lim_{E \to \infty} p(E) = a$.
- Energy E_a, at which $|p(E) - a| = 0.01$.
- Weighted average laminarisation probability $\langle p \rangle_f = \frac{1}{E_{max}} \int_0^{E_{max}} f(E)p(E)dE$, where $f(E)$ is a weight function.

Here, we can associate $E_{99\%}$ with the smallest energy of transitioning RPs and E_a with the smallest energy above which the laminarisation probability is asymptotically close to a. The inflection energy E_{flex} then defines an intermediate energy for a given fitting function and is calculated from the equation

$$\begin{aligned} \left.\frac{d^2}{dE^2}p(E)\right|_{E=E_{flex}} &= 0 \\ \implies \quad E_{flex} &= \frac{\alpha-1}{\beta}. \end{aligned} \tag{6.6}$$

Once we have the laminarisation probability for the uncontrolled system, we can calculate that for the controlled system and assess the efficiency of control by comparing the corresponding P_{lam}. To demonstrate this, we apply in-phase wall oscillations to plane Couette flow with the amplitude $A = 0.3$ and frequency $\omega = 1/16$ known to be efficient in suppressing transition to turbulence (see Chapter 5 for the discussion of this control strategy) and recalculate the laminarisation probability using the protocol above and the same energy levels. Since the system now explicitly depends on the initial value of t, we decide to generate a random phase $\phi \in [0; 2\pi]$ for each RP emphasizing that the phase ϕ should not be considered as one of the control parameters in such a study. This results in the distribution of the laminarisation probability shown in figure 6.5(a). Similar to the uncontrolled case, P_{lam} decays from 1 nearly monotonically as the RP energy increases and approaches a constant value $P_{lam} \approx 0.29$. The difference between the laminarisation probabilities in the uncontrolled and controlled cases is relatively small for small-energy RPs and becomes apparent for $E \gtrsim 7 \times 10^{-3}$. In contrast to 6.4(a), we can notice that the difference in P_{lam} between RP+ and RP− disappears for sufficiently large energies. Figure 6.5(b) reveals why this happens: in addition to region $\mathrm{R_{lam}}$ of the concentration of laminarising RPs in figure 6.4(b), the laminarising RPs are now found all over the (B, C)-space. Laminarisation of many RPs located outside region $\mathrm{R_{lam}}$ follows a different scenario from that typical for laminarising RPs found in $\mathrm{R_{lam}}$. As demonstrated in figure 6.5(b), some RPs can laminarise via "overshooting": their energy significantly grows in the initial stage similar to transitioning trajectories, but then, instead of being attracted by the turbulent saddle, their trajectories approach the laminar fixed point. One may think that this is a consequence of a fortunate choice of the phase of the wall oscillations, but we found no such correlation. Another important difference with the uncontrolled case is found for the turbulent saddle attracting the transitioning trajectories. As can be seen from figure 6.5(b), it is located at smaller B and C, i.e., it is associated with smaller kinetic energy, in comparison to the uncontrolled case.

To assess the difference in the location of laminarising RPs in figures 6.4(b) and

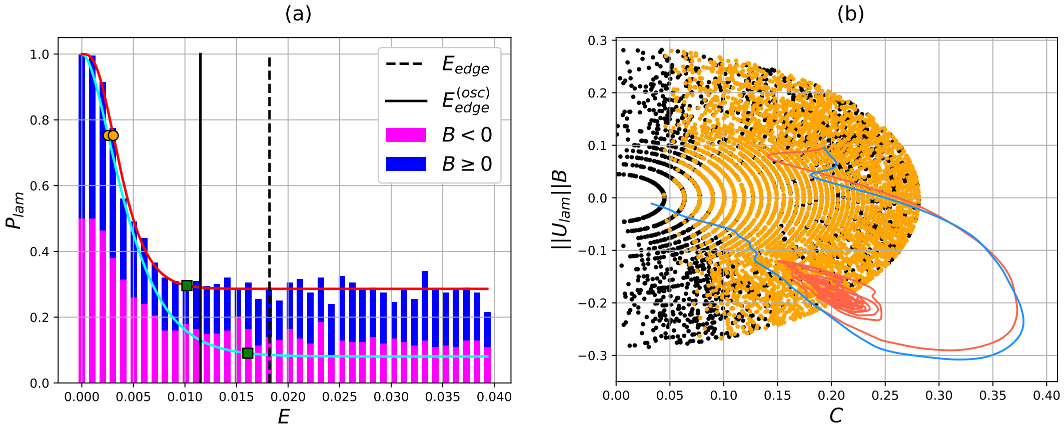

Figure 6.5: Same as figure 6.4 but in the presence of in-phase wall oscillations at the amplitude $A = 0.3$ and frequency $\omega = 1/16$. The edge state energy in the presence of control is shown in (a) by the black solid line.

6.5(b), we approximate the boundary of region $\mathrm{R_{lam}}$ by a linear function $C = \lambda(1 - \mu||\boldsymbol{U_{lam}}||B)$, where $\lambda = 3/40$ and $\mu = 10/9$, and introduce an auxiliary function $g(B,C)$ defined as

$$g(B,C) = \frac{C^2}{(1-\mu||\boldsymbol{U_{lam}}||B)^2} - \lambda^2. \tag{6.7}$$

This function acts as a classifier: a set $\{(B,C) : \ g(B,C) < 0\}$ approximates $\mathrm{R_{lam}}$, i.e., the region of laminarising RPs in the uncontrolled system, whereas the remaining (B,C) are associated with transitioning RPs in the uncontrolled system. We can then assess the difference between the distributions of laminarising RPs on the (B,C)-plane for the uncontrolled and controlled cases. Figure 6.6 shows a histogram of values of $g(B,C)$ computed for both cases and for all laminarising RPs. We can observe that, in the absence of control, the vast majority of the laminarising RPs correspond to $g(B,C) < 0$, i.e., region $\mathrm{R_{lam}}$, and only about 22.6% of RPs yield $g(B,C) > 0$. The activation of control almost does not affect the number of laminarising RPs associated with region $\mathrm{R_{lam}}$. Instead, it forces the RPs located outside of this region to laminarise: the majority of the laminarising RPs now correspond to $g(B,C) > 0$ (about 58.6%). We can thus extend our conclusion about the efficiency of the considered control made from figure 6.5(a) by saying that the considered control is successful in suppressing transition of RPs whose parameters B and C correspond to $g(B,C) > 0$, whereas it is statistically neutral to the RPs associated with $g(B,C) < 0$, i.e., region $\mathrm{R_{lam}}$.

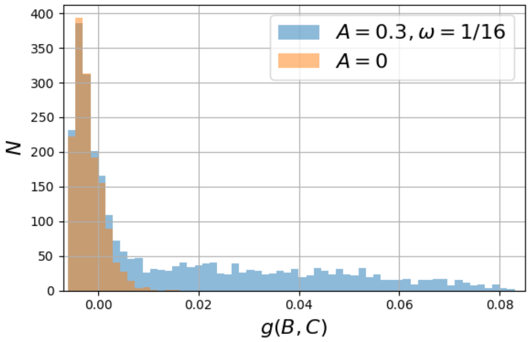

Figure 6.6: Histogram of the values of $g(B, C)$ calculated for laminarising RPs in the uncontrolled (orange) and controlled (blue) cases. Random perturbations with B and C yielding $g(B, C) < 0$ are approximately located in region $\mathrm{R}_{\mathrm{lam}}$. In contrast to the uncontrolled cases, the number of laminarising RPs in the controlled case only weakly depends on the value of positive $g(B, C)$ (the slow decrease of N for $g(B, C) \gtrsim 0.05$ is a consequence of our allocation of RPs: they cover circles rather than rectangles on the (B, C)-plane).

To be able to compare the uncontrolled and controlled systems or two differently controlled systems quantitatively, we need to introduce scalar metrics of efficiency assessing the effect of control. Depending on the problem at hand, different metrics induced by the scalar quantities characterising the fitting function $p(E)$ can be suggested. We will focus on the general metrics induced by the weighted average laminarisation probability which we will call the weighted relative probability change C_f. Given the fitting function $p(E)$ for P_{lam} for the uncontrolled system and the fitting function $p_{ctrl}(E)$ for the controlled system, we define the weighted relative probability change as follows:

$$C_f = \frac{1}{E_{max}} \int_0^{E_{max}} f(E) \frac{p_{ctrl}(E) - p(E)}{p(E)} dE, \tag{6.8}$$

where we take $E_{max} = 2E_{edge}$ out of simplicity. It is natural to expect a weight function $f(E)$ to be the distribution of the energy of disturbances in a particular system, e.g., known from the experimental observations. In this case, $\langle p \rangle_f$ and C_f can be interpreted as the expected laminarisation probability and the expected relative probability change for a given system. For the sake of simplicity, we assume that the source of disturbances is white noise in our case, i.e, $f(E) = 1$, which yields $C_f = 1.72$ after the substitution of (6.5) with the parameter values for the uncontrolled and wall-oscillated cases into

	$E_{99\%}$	E_{flex}	E_a	a	$\langle p \rangle_f$	C_f
$A = 0$	4.07×10^{-4}	2.55×10^{-3}	1.61×10^{-2}	0.0805	0.208	1
$A = 0.3, \omega = 1/16$	8.87×10^{-4}	3.05×10^{-3}	1.02×10^{-2}	0.286	0.369	1.72

Table 6.1: The values of the scalar metrics characterising the fitting function (6.5) ($E_{99\%}$, E_{flex}, E_a, a and $\langle p \rangle_f$) and assessing control efficiency (C_f) which were were calculated for the uncontrolled ($A = 0$) and controlled ($A = 0.3, \omega = 1/16$) cases.

(6.8). This means that the laminarisation probability almost doubles on average when the control is switched on. It should be noted that if $f(E) = 1$ and E_{max} is large enough, $C_f \to (a_{ctrl} - a)/a$, where a and a_{ctrl} are the asymptotic laminarisation probabilities for the uncontrolled and controlled caes. In this case, one attempts to assess the efficiency of the control with respect to large-energy RPs and can readily use $(a_{ctrl} - a)/a$ as a scalar metric of efficiency.

For a reference, we report all the values of the scalar metrics mentioned above in table 6.1 assuming that $f(E) = 1$.

6.3 Estimation of the laminarisation probability

Calculation of the laminarisation probabilities shown in figures 6.4(a) and 6.5(a) requires a great number of simulations. To build any of these figures, we time-integrated 8000 initial conditions where the laminarising and transitioning ones required simulating the flow for about 100 and 400 time units respectively. Ultimately, we are interested in finding optimal values of the control parameters (A and ω in the case of wall-oscillated plane Couette flow), so, as the first attempt, we need to scan the parameter space with at least $O(10)$ combinations of the parameter values. In this case, calculating P_{lam} for all these combinations and then solving the optimisation problem becomes computationally infeasible. We address this issue by relying on estimation theory which we employ to estimate $p(E)$ defined in (6.5) using a much smaller number of RPs.

First of all, we note that calculation of $P_{lam}(E)$ at fixed E using a finite number of RPs N is equivalent to saying that we observe $P_{lam}(E)$ at a particular E with some observation error $e_N(E)$ which implicitly depends on N. In this case, our observation is $\tilde{P}^N_{lam}(E) = P_{lam}(E) + e(E, N)$. Following the results from the previous section, we can reasonably assume that $P_{lam}(E) = p(E)$, where $E \geq 0$, for optimally chosen parameter values a, α and β and large enough N. Thus, we aim to estimate the parameters of $p(E)$ using observations $\tilde{P}_{lam}(E_j)$ obtained at the energy levels E_j, $j = 1, \ldots, 40$, which are defined as in the previous section. The observation error depends on a random sampling of RPs used to compute $\tilde{P}_{lam}(E)$ and, thus, is a random variable. To justify the choice of an estimator, it is important to find the distribution of the observation errors. We derive this distribution by first realising that time-integrating an RP with energy E and classifying it as laminarising or transitioning is a Bernoulli trial with the probability of success $P_{lam}(E)$. Let the number of laminarising RPs with energy E out of N Bernoulli trials be the random variable X. Then the probability that n of N RPs laminarise is given by the binomial distribution:

$$P(X = n \mid N, P_{lam}(E)) = \binom{N}{n} (P_{lam}(E))^n \, (1 - P_{lam}(E))^{N-n}, \quad n = 0, 1, \ldots, N. \tag{6.9}$$

We can thus define the observation error simply as a linear transformation of X, $\mathcal{E} = \frac{X}{N} - P_{lam}(E)$, which has the following distribution:

$$P(\mathcal{E} = e \mid N, P_{lam}(E)) = \binom{N}{N(e+p)} (P_{lam}(E))^{N(e+p)} \, (1 - P_{lam}(E))^{N(1-e-p)}, \\ e = \frac{0}{N} - P_{lam}(E), \frac{1}{N} - P_{lam}(E), \ldots, 1 - P_{lam}(E). \tag{6.10}$$

The latter is merely a scaled-and-shifted binomial distribution and should approach the normal distribution under the same conditions as (6.9). It is known that the binomial distribution can be well approximated by the normal distribution if N is large enough and $P_{lam}(E)$ is not close to 0 or 1 (the rule of thumb is $\min(N P_{lam}(E), N(1 - P_{lam}(E))) \geq 5$; see Chapter 3 in [191] for details). Since the laminarisation probability tends to 1 for small-energy RPs, these conditions cannot be satisfied for $E \to 0$. In addition, we may expect that $P_{lam}(E)$ is close to zero when $A \to 0$ and E is sufficiently large which can be deduced by comparing figures 6.4(a) and 6.5(a). Using larger N at the smallest and largest energy levels would compensate the extreme values of P_{lam}, but, as the first step towards the estimation, we can assume that the observation error is normally distributed. We then choose the least-squares estimator, known to be suitable for the nonlinear regression with Gaussian observation errors [192, 193].

To assess the reliability of our approach to the estimation, we first estimate P_{lam} for two already elaborated cases, $A = 0$ and $A = 0.3, \omega = 1/16$, by drawing random samples of $40 \times N$ RPs (N RPs per each of the 40 energy levels) from the already time-integrated and classified 8000 RPs. Making 2000 random samples with replacement and estimating the corresponding functions $p(E)$ for each of the samples, we can computationally assess the distribution of fitting functions for a fixed N. For relatively small N, this approach allows for the assessment of how the errors in approximating the accurate fitting function $p_{acc}(E)$ scale with N, where we hereafter assume that $p_{acc}(E)$ is obtained by considering all 8000 RPs and shown in figures 6.4(a) and 6.5(a). In particular, we will track the relative errors with respect to E_{flex}, a and E_a, denoted as e_{flex}, e_a, e_{E_a} respectively, and two additional errors induced by the weighted average laminarisation probability $\langle p \rangle_f$:

$$e_{\langle p \rangle} = \frac{1}{E_{max}} \left| \int_0^{E_{max}} f(E) \frac{p(E) - p_{acc}(E)}{p_{acc}(E)} dE \right|, \tag{6.11}$$

$$e_{\langle p \rangle, \mathrm{abs}} = \frac{1}{E_{max}} \int_0^{E_{max}} f(E) \frac{|p(E) - p_{acc}(E)|}{p_{acc}(E)} dE. \tag{6.12}$$

The last two errors evaluate the average relative deviation from $p_{acc}(E)$ and, thus, assess the overall accuracy of the estimation of $p_{acc}(E)$. We however note that the former error, e_f, is a better estimate of accuracy in the case when C_f is used as a criterion for assessing the control efficiency.

The dependence of the errors on N resulting from the aforementioned sampling procedure for both uncontrolled and controlled cases is displayed in figure 6.7. The largest inaccuracy is observed for E_a and E_{flex} whose corresponding relative errors may exceed 100% for certain samples. This is a consequence of the large variation in α and β which are heavily correlated ($\beta \approx k\alpha$, where $250 \lesssim k \lesssim 300$ for the uncontrolled case). This fact will be appreciated in more details further. Owing to the smoothing, inaccurate estimation of E_a and E_{flex} has only limited effect on the more representative errors $e_{\langle p \rangle}$ and $e_{\langle p \rangle, \mathrm{abs}}$: they are less than 30% and 15% for 80% samples for the uncontrolled and controlled cases respectively and $N = 10$. Such a difference between the uncontrolled and controlled cases is explained by the small value of a for $A = 0$ which encourages us to be more skeptical about the results of estimation for small amplitudes of wall oscillations. Finally, all the errors seem to follow the power law $e \propto N^{-\eta}$, where $\eta \approx 1/2$ for the most representative errors $e_{\langle p \rangle}$ and $e_{\langle p \rangle, \mathrm{abs}}$.

To elaborate these results further, we report the expectation, the interquartile and interdecile ranges of the fitting function $p(E)$ for the uncontrolled and controlled cases resulting from the sampling procedure for $N = 10$ in figure 6.8. The interdecile range

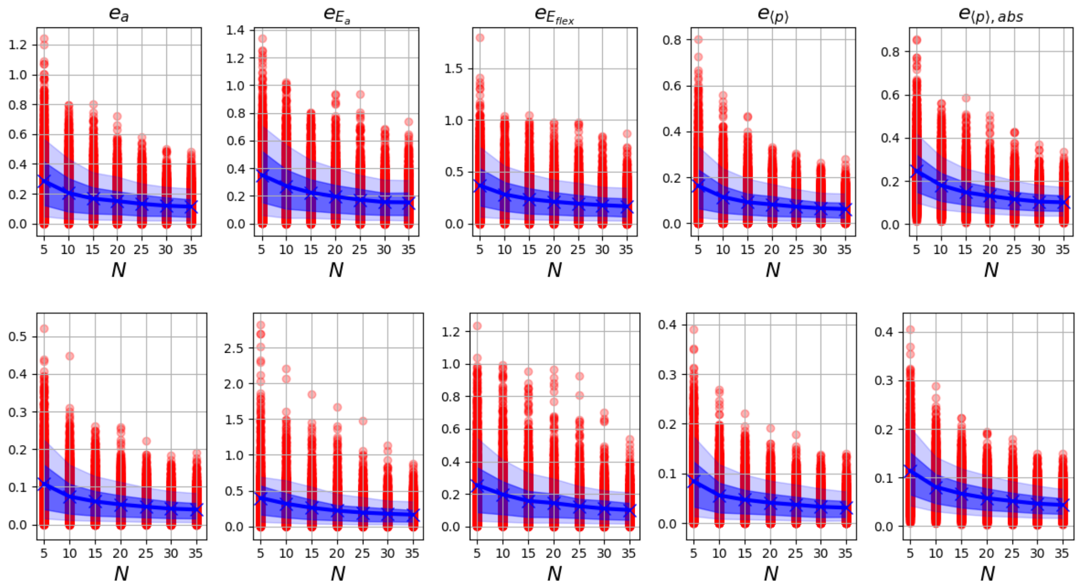

Figure 6.7: Relative errors with respect to E_{flex}, a and E_a (e_{flex}, e_a and e_{E_a} respectively) and the weighted average laminarisation probability $\langle p \rangle_f$ ($e_{\langle p \rangle}$ and $e_{\langle p \rangle,\mathrm{abs}}$) resulting from the estimation of $p_{acc}(E)$ using randomly chosen N RPs per energy level. The errors associated with the uncontrolled (controlled) system are shown in the top (bottom) row (the parameter values of the control are $A = 0.3, \omega = 1/16$). Red circles correspond to individual samples whereas the dark (light) blue bands correspond to the interquartile and interdecile ranges. The dark blue line shows the expectation of an associated error as a function of N.

will hereafter be treated as the confidence band of the fitting function. Owing to the sampling procedure, the expectations of the fitting function in both cases virtually coincide with $p(E)$ shown in figures 6.4(a) and 6.5(a). The distribution of the fitting function, assessed by the interquartile and interdecile ranges, seems to be fairly concentrated around the expectation: the variation of $p(E)$ is typically around 0.02 within the interdecile range. Exceptions are observed for very small ($E \lesssim 3 \times 10^{-3}$) and moderate ($5 \times 10^{-3} \lesssim E \lesssim 9 \times 10^{-3}$) energy levels where this variation may go beyond 0.1 and are explained by large fluctuations of α and β from sample to sample.

We thus reckon that the laminarisation probability can successfully be estimated using as small as $N = 10$ RPs per energy level which is expected to yield the error in C_f, the key indicator of the control efficiency, within 30% with the probability 80%

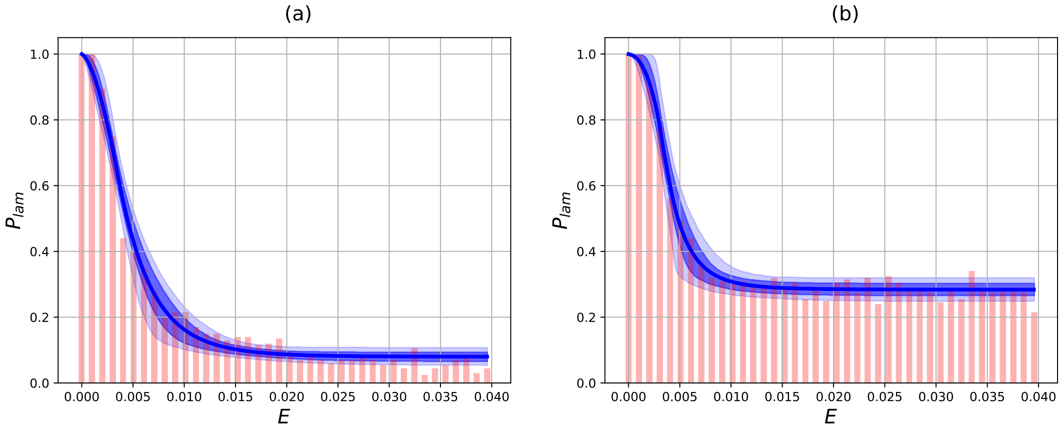

Figure 6.8: The expectation (solid line) of the distribution of fitting function (6.5) and its interquartile (dark band) and interdecile (light band) ranges for the uncontrolled (a) and controlled (b) cases (see the text for the details of the generation of this distribution). The pink bars show the laminarisation probability P_{lam} calculated for all available RPs. The interquartile and interdecile ranges help visualise the extent of the spread of the distribution. The probabilities that a fitting function falls into the interquartile and interdecile ranges are 50% and 80% respectively.

in the worst scenario when $A \approx 0$. This allows for the reduction of the number of simulations needed to approximate the laminarisation probability from 8000 to 400 or, in other words, to reduce the computing time from 32000 to 1600 core-hours, where we realistically assumed 4 core-hours per simulation. It is however still important to build an approach for the approximation of the confidence band of the fitting function and the corresponding confidence intervals for its main scalar metrics given only a single sample. This necessitates constructing the confidence regions for the parameters of nonlinear regression, namely, α, β and a, given this sample. The choice of a particular method for this kind of approximation strongly depends on the nonlinear function used for regression, the distributions of the parameters and observation errors. The simplest class of methods, so called linearisation methods, is based on the linearisation of the fitting function and then applying a statistical theory to the linear least-squares problem (see Chapter 2 in [194] for an introduction). They are valid for asymptotically large samples and well-known to be inferior for nonlinear least-squares problems [195]. Instead of linearising the fitting function, one can make use of the exact formulation of

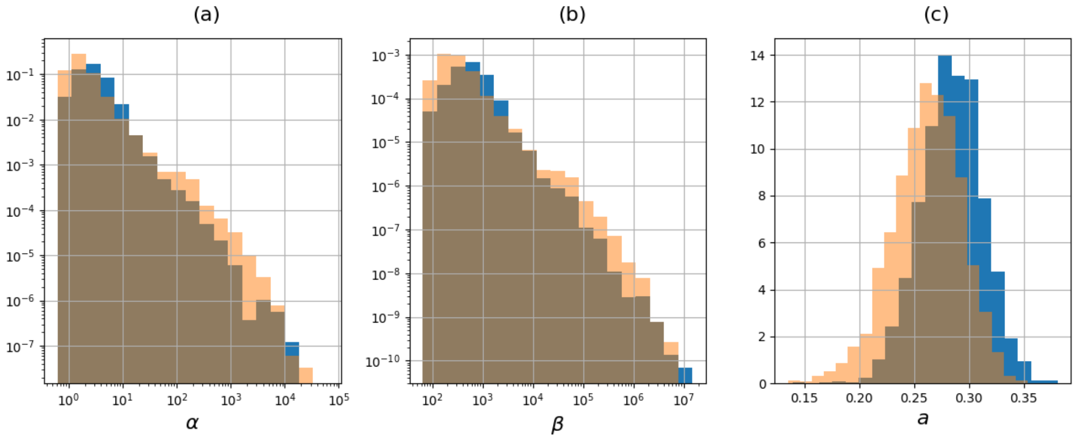

Figure 6.9: Normed histrograms for α (a), β (b) and a (c) built by making 2000 random samples of 400 RPs out of 8000 RPs (blue) and by bootstrapping applied to a single, randomly chosen sample of 400 RPs (orange). In both cases, we sampled 10 RPs per each energy level. Note the log-log scale used for the distributions for α and β, emphasising the Pareto tails.

the confidence regions for the linear least-squares problem and adapt it to the nonlinear case which yields the likelihood method. This method was shown to provide sufficiently accurate approximation when the error is normally distributed [195]. In our case, however, observation errors are not generally normally distributed, especially at small and large energy levels. Additionally, the aforementioned methods may suffer from the non-normality of the parameter distributions which takes place in our problem: even though the distribution of the observation errors and a (see figure 6.9(c)) can be treated as Gaussian to some extent, the situation is clearly different with the distributions of α and β which have Pareto tails (see figure 6.9(a, b)). We thus decide to adapt a more general and easy-to-implement approach known as bootstrap, i.e., multiple resampling of a given sample able to produce the empirical parameter distributions for α, β and a [196]. The bootstrap method needs only a single random sample, i.e., a set of 400 RPs evenly spread among 40 energy levels in our case, to get started. We then generate a large number of samples by resampling the initial sample with replacement such that each generated sample has again 10 RPs at each of 40 energy levels. By performing nonlinear regression with respect to each generated sample, we get three distributions for α, β and a. Figure 6.9 compares the resulting empirical distributions for a randomly chosen initial sample to those yielding the distribution of the fitting functions in figure 6.8(b). One can observe that bootstrapping captures well the shapes and scales of the distributions in our case. Nevertheless, the shifts are not necessarily well approximated which will however be compensated by mentioning the confidence intervals for any quantities calculated using these empirical distributions. Despite the fact that this result highly depends on a particular choice of the initial sample, it shows that bootstrapping is capable of giving a reasonable approximation of the confidence region.

Figure 6.10(b) showing the expectation of the fitting function and its interquartile and interdecile ranges helps further appreciate that the empirical distributions built via bootstrapping yield a decent approximation of the distribution of fitting functions consistent with figure 6.10(a) obtained by a more reliable approach (note that figures 6.10(a) and 6.8(b) are the same; the former was added simply to ease the comparison). However, few important features of the empirical distribution of fitting functions should be noted. First of all, one can notice that a relatively large variation of the fitting function for very small and intermediate energies, observed in figure 6.10(a), intensifies even further in figure 6.10(b) which is the direct consequence of the fat tails in the distributions of α and β. This leads to the overestimation of the confidence band (i.e., the interdecile range) which is by no means a critical drawback in our case. In addition, the asymptotic value of P_{lam} is sligtly underestimated in accordance with the underestimated mean of the distribution of a (see figure 6.9(c)).

Once the confidence region is approximated, we can readily get the confidence band for the fitting function and the confidence intervals for all the scalar metrics by assessing them within the confidence region and calculating their minima and maxima. For the sake of completeness, it should be said that one could instead assume some distribution for the quantities of interest (e.g., C_f) and then employ bootstrapping to estimate the necessary parameters of this distribution (e.g., mean and variance for the normal distribution) which should increase the accuracy of the approximation. Similarly, the distribution for the parameters of the fitting function can be assumed.

6.4 Control design based on the probabilistic protocol

Using the estimation of the laminarisation probability and the algorithm for calculating confidence regions, we can now address the problem of finding optimal control

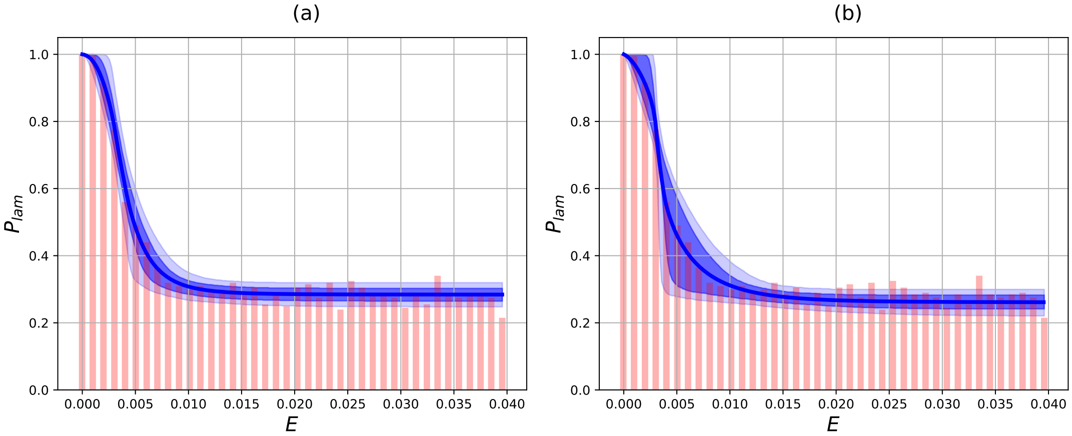

Figure 6.10: The visualisation of the empirical distribution of fitting functions built via bootstrapping (right) and compared to the distribution from figure 6.8(b) (left). See figure 6.8 for the explanation of this visualisation.

parameter values (amplitude A and frequency ω) with respect to C_f given by (6.8) for $f(E) = 1$ which can in general be replaced by other suitable metrics of the control efficiency. We estimate the depedence of C_f and the associated confidence intervals on the amplitude and frequency of the wall oscillations by sampling $N = 10$ RPs per each energy level and then bootstrapping them for all the pairs from the set $\{(A, \omega) : A \in \{0.1, 0.2, \ldots, 0.5\}$ and $\omega \in \{2^{-1}, 2^{-2}, \ldots, 2^{-5}\}\}$. To gain more information about the fitting functions and their dependence on the amplitude and frequency of wall oscillations, we additionally calculate E_a and E_{flex}. The summarising results are shown in figure 6.11. We emphasise that the confidence intervals of the vast majority of the estimates of C_f do not intersect which allows us to suggest that the qualitative features of the dependence of C_f on A and ω and the points at which the extrema of C_f lie are well approximated. One can note two main trends in C_f as a function of A and ω. First of all, C_f grows with respect to A for any ω which is in agreement with the studies of turbulent channel and pipe flows under the action of similar wall oscillations where the drag reduction was observed to intensify as the amplitude of oscillations increases [152, 197]. This seems to be contradictory to the study by Rabin *et al.* [154] who reported $A = 0.35$ as an optimal amplitude by maximising the minimal seed energy in plane Couette flow subjected to the same type of control at a different Reynolds number ($Re = 1000$). Secondly, C_f has a clear maximum at $\omega = 1/8$ for all

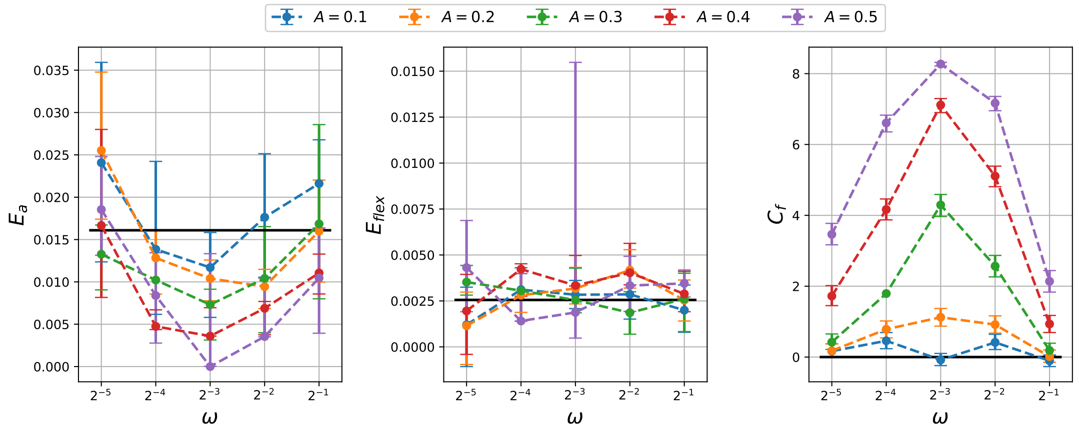

Figure 6.11: Estimates of the energy E_a above which the laminarisation probability is asymptotically close to a, inflection energy E_{flex} and relative probability change C_f, where $f = 1$, as functions of the amplitude A and frequency ω of the oscillations. The error bars show the confidence intervals (interdecile ranges in this case) calculated via bootstrapping of random samples. The control at $A = 0.5, \omega = 1/8$ results in almost complete laminarisation of all RPs ($p(E) \approx 1$), so that $p(E)$ only weakly depends on E. This explains an abnormal variation of E_{flex}, vanishing E_a and its confidence interval and the close-to-zero confidence interval for C_f for these parameter values.

values of the amplitude, except for $A = 0.1$, and monotonically decays when $\omega \to 0$ or $\omega \to \infty$ from $\omega = 1/8$. The most efficient flow control configuration in our case, $A = 0.5, \omega = 1/8$, results in essentially inevitable laminarisation of the RPs (only 3 out of 400 RPs were classified as transitioning to turbulence for these parameter values). Owing to the definition of C_f, it cannot infinitely grow and is bounded between -1 ($p_{ctrl}(E) = 0$, i.e., the control makes transition to turbulence inevitable) and 8.35 ($p_{ctrl}(E) = 1$, i.e., the control makes laminarisation inevitable). The control configuration $A = 0.5, \omega = 1/8$ thus results in the largest possible value of C_f. In fact, the control strategy is so efficient for $A = 0.5$ that the concept of the laminarisation probability becomes ill-posed since turbulence is hard to be sustained for the substantial amount of time and the logical separation of laminarising and turbulent trajectories vanishes.

The estimates of two other quantities, E_a and E_{flex}, cannot be considered as reliable owing to the large confidence intervals associated with them. Nevertheless, some useful information can still be read from them. We can notice that the inflection energy fluctuates between 0 and 5×10^{-3} without any clear dependence on A or ω. In contrast, the energy E_a designating the beginning of the asymptotic regime of $p(E)$ seems to be negatively correlated with C_f and, thus, is minimised at $A = 0.5$ and $\omega = 1/8$. These observations suggest that the efficient control tends to increase the laminarisation probability at the plateau of $p(E)$ whilst E_a is automatically adjusted to account for the increased a and keep E_{flex} unchanged. This is partly reflected in the fact that the parameters of the fitting function α and β are still strongly correlated for the data shown in figure 6.11 (the Pearson's correlation coefficient is about 0.99).

Unsurprisingly, the increase of the probability of laminarisation comes at a cost of the increased consumption of energy needed to perform the wall oscillations against viscous dissipation. For a flow control designer to find a trade-off between the improved laminarisation and energy consumption, it is necessary to get a measure of the required energy compared to the uncontrolled system. Following the ideas expressed by Rabin *et al.* [154], we quantify the consumed energy as the dissipation rate $\epsilon(A, \omega)$ which takes the following form for the laminar flow $\boldsymbol{u}$:

$$\begin{aligned}\epsilon_{lam}(A, \omega) &= \frac{\omega}{4\pi \Gamma_x \Gamma_z Re} \int\limits_0^{2\pi/\omega} \int\limits_0^{\Gamma_x} \int\limits_{-1}^{1} \int\limits_0^{\Gamma_z} |\nabla \times \boldsymbol{u}|^2 dt dx dy dz \\ &= \frac{1}{Re}\left[1 + \frac{A^2\Omega}{2} \cdot \frac{\sinh(2\Omega) - \sin(2\Omega)}{\cosh(2\Omega) + \cos(2\Omega)}\right],\end{aligned} \tag{6.13}$$

where $\Omega = \sqrt{\omega Re/2}$ and the time-averaging is performed over one period of wall oscillations. The dissipation rate of the laminar flow in the uncontrolled case is then $\epsilon_{lam}(A = 0) = 1/Re$. For the considered range of A and ω and fixed $Re = 500$, the term involving hyperbolic and trigonometric functions is very close to 1 so the laminar dissipation rate can be taken to scale as $O(A^2, \omega^{1/2})$. Following Rabin *et al.* [154], we assume that the average turbulent dissipation rate ϵ_{turb} only weakly depends on A and ω and is close to the turbulent dissipation rate in the uncontrolled case: $\epsilon_{turb} \approx 2.9/Re$. The energy saving can thus occur as the benefit of keeping the flow laminar at the expense of spending some energy on wall oscillations. We introduce the ratio

$$S = \frac{\epsilon_{turb} - \epsilon_{lam}(A, \omega)}{\epsilon_{turb} - \epsilon_{lam}(A = 0)}, \tag{6.14}$$

as a proxy assessing the energy efficiency under the assumption that the flow is kept laminar. Note that $S < 0$ means that the energy one spends to perform oscillations in

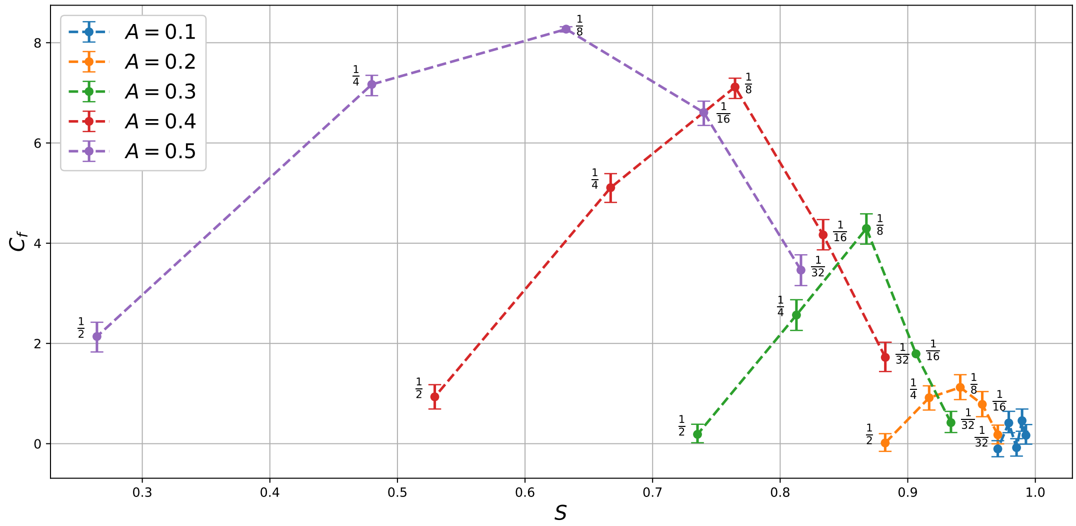

Figure 6.12: Relative probability change C_f plotted against S associated with the energy saving for the same amplitudes and frequencies as in figure 6.11. The values of the frequency of the wall oscillations are shown next to the points (the frequencies are omitted for $A = 0.1$ to avoid cluttering).

the laminar regime is larger the turbulent dissipation. For the uncontrolled system, we have $S = 1$ and, thus, can expect to consider control configurations yielding S in the range $(0; 1)$.

Figure 6.12 shows the relative probability change C_f plotted against S. One can observe that the perfect control configuration, maximising both C_f and S, cannot be found here since S decreases when the amplitude and frequency of the wall oscillations are increased. Nevertheless, some conclusions about choosing parameter values towards optimality can still be made. Since both S and C_f descrease monotonically for $\omega > 1/8$, there is in general no reason to consider frequencies larger than $\omega = 1/8$ for the purpose of transition control (excluding any engineering/experimental restrictions). Another important observation is that it makes sense to consider only those amplitudes which are smaller than $A = 0.5$. The largest possible C_f is already achieved at $A = 0.5$, so further increase of A would only increase the energy consumption without improving the laminarisation probability.

Bearing these two logical restrictions in mind, the appropriate choice of the amplitude and frequency will depend on particular restrictions of a problem at hand. Some moderate options, for example, $A = 0.3, \omega = 1/8$, significantly increase the laminarisation probability making transition less likely than laminarisation (the average laminarisation probability is $\langle p \rangle_{f=1} \approx 0.60$ for this flow configuration) while only slightly increasing the dissipation rate of the laminar flow in comparison to plane Couette flow without any control ($\epsilon_{lam}(A = 0.3, \omega = 1/8) \approx 1.25/Re$ versus $\epsilon_{lam}(A = 0) = 1/Re$ which yields $S \approx 0.87$). However, a flow control designer may conclude that the effect of transition to turbulence is so damaging (e.g., due to the extreme events occurring in turbulent flows) that it is better to pick $A = 0.5, \omega = 1/8$ yielding essentially stable oscillating laminar flow ($\langle p \rangle_{f=1} \approx 0.99$) while sacrificing the energy efficiency ($\epsilon_{lam}(A = 0.5, \omega = 1/8) \approx 1.70/Re$ and $S \approx 0.63$).

Finally, we find it interesting to compare the effect of wall oscillations on transitional properties of the flow for the cases of small (investigated in this chapter) and wide (investigated in Chapter 5) domains. To do this, we make use of two metrics assessing transition to turbulence: the relative probability change C_f for the small domain and the critical Reynolds number Re_{cr} for S5 for the wide domain. We thus combine the results for C_f taken from figure 6.11 and Re_{cr} for S5 taken from figure 5.14 and show the resulting relation between C_f and Re_{cr} in figure 6.13. Despite the fact that we used completely different protocols to compute C_f and Re_{cr} and different, but related, domain sizes, we get a significant positive correlation between these quantities implying that some of the conclusions of our analysis of transition to turbulence in the small, close to minimal, periodic box can be extrapolated to the case of the wide domain allowing for localisation of flow states and causing a complicated transition scenario (see figure 5.13). First of all, we note that both C_f and Re_{cr} generally grow with respect to the amplitude implying that the increase of A is beneficial for the purpose of suppressing transition to turbulence for both domain types. One can also notice that for $A > 0.1$, both C_f and Re_{cr} take their maxima at $\omega = 1/8$ suggesting that this particular frequency may be optimal for transition control in both domains. The only significant difference between the dependences of C_f and Re_{cr} on A and ω which we can observe is that the frequency change has a more dramatic effect on Re_{cr} in the wide domain for small amplitudes: Re_{cr} grows almost monotonically at $A = 0.1$ with respect to ω whereas C_f does not show any clear dependence on ω.

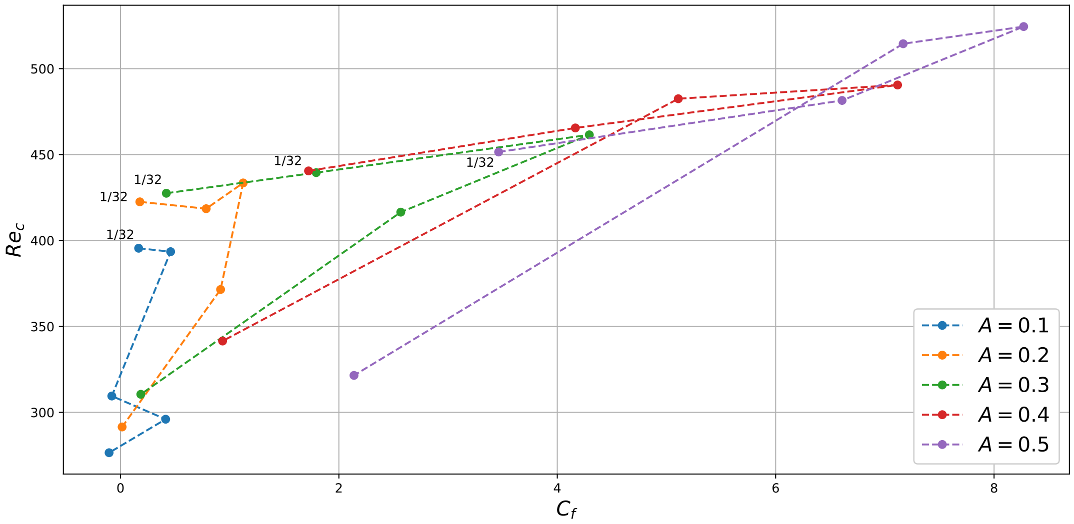

Figure 6.13: Relative probability change C_f plotted against the critical Reynolds Re_{cr} associated with the onset of transition to turbulence of S5.

6.5 Comparison to control design based on the edge state energy

In the previous sections, we have presented the probabilistic protocol for assessing the efficiency of control and demonstrated that the optimal flow configurations it yields may be different from those predicted via the maximisation of the minimal seed energy as done in [154], a default approach to control design proposed in the framework of modern nonlinear stability theory [189]. As noted in the introduction to this Chapter, one could also use the edge state energy as an alternative to the minimal seed owing to its connection to the edge of chaos separating the parts of the phase space associated with laminarising and transitioning perturbations. In this section, we will show that the results produced by this approach are inconsistent with the probabilitic protocol as well which additionally highlights the importance of calculating the laminarisation probability while designing control.

To start exploring the space of parameter values with respect to the edge state energy, we need to compute the edge states for the pairs of parameter values from the set $\{(A, \omega) : A \in \{0.05, 0.1, 0.2, \dots, 0.5\}$ and $\omega \in \{2^0, 2^{-1}, \dots, 2^{-7}\}\}$ which slightly extends the range of parameter values explored in the last section. We do this by computing the edge trajectories using the edge tracking algorithm explained in Section 2.5 for these parameter values and identify the associated edge states assuming that the edge trajectories manage to come sufficiently close to them for 1000 time units. The edge state may be an equilibrium, periodic orbit, relative periodic orbit or chaotic depending on A and ω. The general trend, which can be read from figure 6.15(b), suggests that, at the fixed amplitude of wall oscillations, the edge state is transformed from a steady state, virtually identical to the edge state in the uncontrolled system, at large frequencies ($\omega \geq 1/4$; see figure 6.14(a)) to a periodic orbit at $\omega = 1/8$ (see figure 6.14(b)) and then to a chaotic state as the frequency is decreased down to $\omega = 1/16$ ($\omega = 1/32$ for $A = 0.1$ and $\omega = 1/64$ for $A = 0.05$) or lower (see figure 6.14(d)). For the smallest amplitudes, $A = 0.05$ and $A = 0.1$, we also report the presence of relative periodic orbits for the intermediate frequencies between those associated with periodic orbits and chaotic edge states. All four types of edge states are shown in figure 6.14 for different amplitudes. We expect that the edge states taking the form of relative periodic orbits can be identified for other amplitudes as well if one considers more intermediate frequencies. Based on the continuity argument, one can argue that all non-chaotic edge states are actually relative periodic orbits with either very small spanwise group velocity ("periodic orbit") or both spanwise group velocity and period ("equilibrium") which become larger as the frequency of wall oscillations is decreased. For the sake of classification, we thus use the terms "equilibrium" and "periodic orbit" not in the strict sense in the context of our edge states assuming that the amplitudes of the edge state oscillations less than 10^{-4} and the group velocities less than 10^{-5} are negligible. It is also clear that further decrease of ω should transform the edge state back to the same steady state as we observe for large frequencies since the case $\omega \to 0$ recovers the uncontrolled plane Couette flow. To verify this, one would need to consider the wall oscillations with a period much larger than the time it takes for the algorithm to approach the edge state (typically, from 500 to 1000 time units). We may thus speculate that the edge state in the presence of wall oscillations starts approaching the edge state in the uncontrolled system for $\omega < O(10^{-4})$.

Bearing different types of edge states in mind, we calculate the edge state energy as the average kinetic energy of the edge trajectory starting from $t = 1000$:

$$E_{edge}(A, \omega) = \frac{\omega}{4n\pi} \int\limits_{1000}^{1000+2n\pi/\omega} ||\boldsymbol{u_{edge}}(t; A, \omega)||^2 dt, \tag{6.15}$$

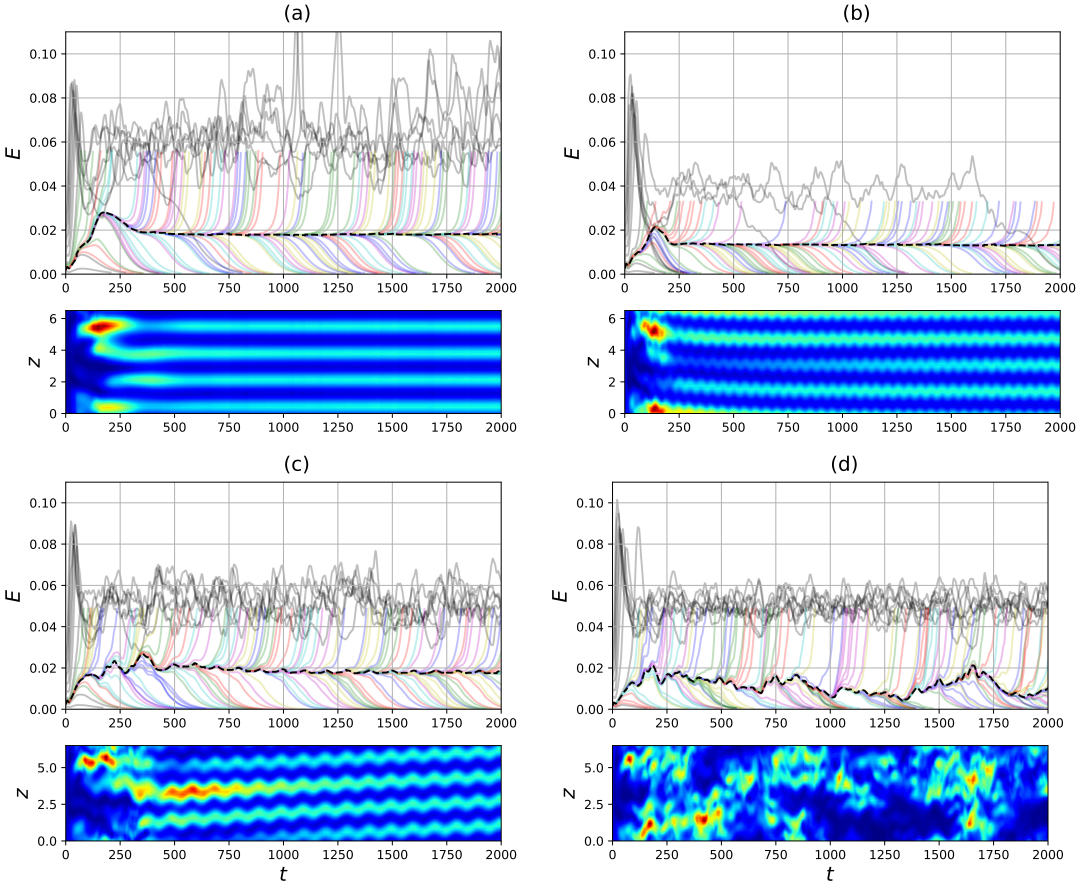

Figure 6.14: The visualisation of the edge tracking procedure for $A = 0.4, \omega = 1$ (a), $A = 0.3, \omega = 1/8$ (b), $A = 0.1, \omega = 1/16$ (c), $A = 0.2, \omega = 1/16$ (d). In each subfigure, the top plot shows the time-evolution of the kinetic energy of initial trajectories (gray), used to get the edge tracking started, trajectories associated with the iterations of the algorithm (colors) and the approximate edge trajectory (black dashed curve). The bottom plots show the time-evolution of the xy-averaged kinetic energy of the edge trajectory. The edge trajectories are found to appoach the edge states of different types: equilibrium (a), periodic orbit (b), relative periodic orbit (c) and chaotic trajectory (d) depending on the amplitude and frequency of wall oscillations (see diagram 6.15(b) for details). Note that the periodic orbit (b) and relative periodic orbit (c) bear clear structural resemblance to the steady edge state at larger frequencies (a) which, in turn, are virtually indistinguishable from the edge state in the uncontrolled system.

where n denotes the number of periods of wall oscillations we wish to average for ($n = 2$ for the smallest frequency $1/128$ and $n \geq 4$ for larger frequencies). The resulting dependence of the edge state energy on the amplitude and frequency of wall oscillations is displayed in figure 6.15(a). One can observe that in-phase wall oscillations decrease the edge state energy in the vast majority of control cases. Contrary to the laminarisation probability, the edge state energy decreases almost monotonically when the amplitude and frequency of wall oscillations are increased and decreased respectively. If a flow control designer assumed that maximising the edge state energy is associated with preventing transition to turbulence, the optimal control configuration would be $A = 0.05, \omega = 1/16$ which is clearly inconsistent with our results regarding the laminarisation probability, a more objective measure of the robustness of the laminar flow (based on figure 6.11, one can extrapolate the dependence of the laminarisation probability on A). Furthermore, figure 6.15(a) may be misinterpreted as a complete failure of the control by in-phase wall oscillations since almost all parameter values decrease the edge state energy compared to the uncontrolled system. One may think that the edge state energy can still be linked to the laminarisation probability via some correlations, which is supported by figure 6.5 where E_a seems to follow E_{edge}, but it appears to be a mere coincidence. We thus conclude that, at least in our case, the edge state energy cannot safely be used as a proxy assessing the size of the basin of attraction of the laminar solution.

To complete the comparison between the probabilistic protocol and the protocol considered in this section, we report the main non-dimensional estimates of control efficiency associated with these protocols (the relative change of the laminarisation probability C_f for the probabilistic protocol and the relative change of the edge state energy with respect to the uncontrolled system for the second protocol) in table 6.2.

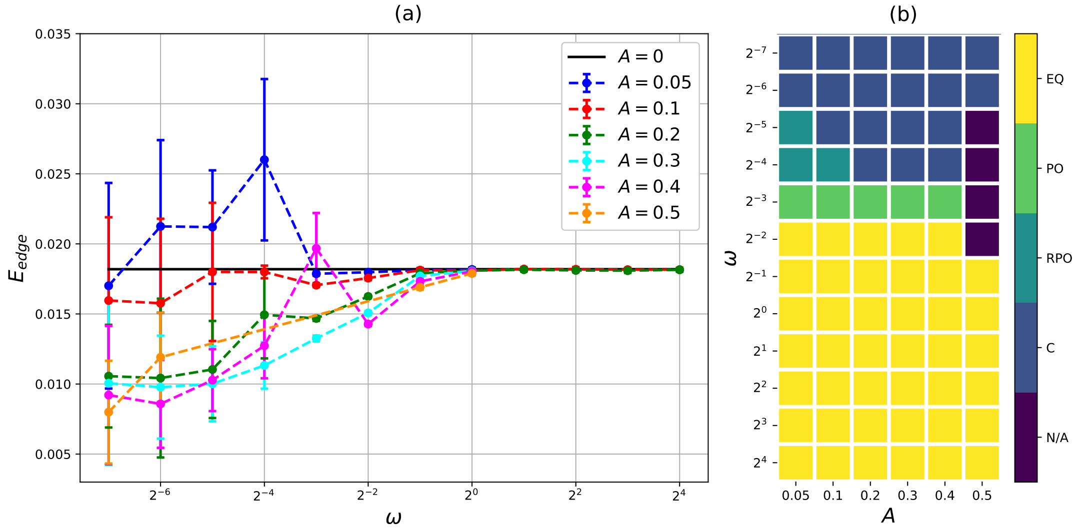

Figure 6.15: Plot (a) presents the dependence of the average edge state energy E_{edge} and associated standard deviation, shown in error bars, on the amplitude A and frequency ω of wall oscillations. Diagram (b) classifies the edge states as equilibria (EQ), periodic orbits (PO), relative periodic orbits (RPO) and chaotic trajectories (C) depending on A and ω. The edge state results are omitted for $A = 0.5, \omega = 1/4, 1/8, 1/16, 1/32$ in both (a) and (b) since the control strategy almost completely suppresses turbulence at these parameter values which makes the concept of the edge of chaos ill-defined.

ω A	1/128		1/64		1/32		1/16		1/8		1/4		1/2	
0.05	–	0.065	–	0.17	–	0.16	–	0.43	–	0.018	–	0.012	–	0.0040
0.1	–	0.12	–	0.13	0.17	0.011	0.46	0.011	−0.08	0.062	0.41	0.035	−0.10	0.0038
0.2	–	0.42	–	0.43	0.18	0.39	0.78	0.18	1.12	0.19	0.92	0.11	0.01	0.016
0.3	–	0.45	–	0.46	0.42	0.45	1.79	0.38	4.29	0.27	2.57	0.17	0.19	0.027
0.4	–	0.49	–	0.53	1.72	0.43	4.16	0.30	7.12	0.082	5.11	0.22	0.93	0.048
0.5	–	0.56	–	0.35	3.46	–	6.61	–	8.27	–	7.17	–	2.14	0.071

Table 6.2: Relative change of the laminarisation probability C_f (gray cells) and of the edge state energy (white cells excluding the top row and the leftmost column) calculated with respect to the uncontrolled plane Couette flow and reported as a function of the amplitude A and frequency ω of in-phase spanwise wall oscillations.

Chapter 7

Conclusion

In this thesis, we have investigated the dynamics of spatially localised states in plane Couette flow in a streamwise-confined spanwise-extended domain and suggested two approaches for the assessment of transition to turbulence and the efficiency of its control.

Homoclinic snaking

We started from the discussion of the snaking branches of exact localised equilibria and travelling waves in Chapter 3 and explained how they can be used as a source of initial conditions as an alternative to more conventional approaches where initial conditions are generated either using some analytical expressions [47, 63, 75, 92], linearly or nonlinearly optimal perturbations [52, 55, 176], turbulence at higher Reynolds numbers [92, 121, 122, 126] or a completely random sampling [119, 177, 178]. Closer inspection of the snaking branches allowed for the identification of a branch of spatially localised periodic orbits, PO5, bifurcating from the branch of localised equilibria. A thorough analysis of one of the PO5 solutions unveiled the interaction between the streak, rolls and their fluctuations, typical for the dynamics of spatially localised solutions in the vicinity of the snaking region and differing in important details from the famous self-sustained process [30]. Moreover, we showed that the “microscopic” dynamics of localised states, i.e., the dynamics on the spatial scale of streaks, can be associated with an approximate heteroclinic cycle between two spatially periodic solutions, lower and upper Nagata solutions, in a small-domain plane Couette flow. These findings reinforce the importance of studying invariant coherent solutions and coherent structures in general for understanding the dynamics of transitional and turbulent flows [34, 41, 198–201]. The presence of the Hopf bifurcations along the snaking branches also implies the usefulness of further studies of the extended Swift–Hohenberg equation (non-conservative in space and non-variational in time), where similar phenomena were observed, as a model for homoclinic snaking [181, 202].

Our preliminary stability analysis of the snaking branches, revealing the dominant oscillatory mode instead of the depinning mode, contribute to the existing body of research on homoclinic snaking in three-dimensional fluids [64, 87, 98, 99, 101] and encourages the comparative analysis of stability properities of localised solutions found on snaking branches in various systems exhibiting homoclinic snaking and their relations to homoclinic snaking in the context of the Swift–Hohenberg equation [2]. This will require the completion of the stability analysis in Section 3.2 which necessitates overcoming the existing numerical issues and paying a special attention to the connections of the unstable and stable manifolds of the localised solutions with different width. In addition, unveiling the dependence of the stability properties of our localised solutions on the domain size (in particular, on the streamwise wavelength of the domain) could explain why, contrary to our results, depinning was observed in the vicinity of the snaking region in the study by Duguet *et al.* [92], where a slightly smaller domain was used. This would also complement a recent study of the structure of homoclinic snaking and localised solutions in plane Couette flow as a function of the domain size [87].

Dynamics of localised states in plane Couette flow

Using then a discrete set of localised initial conditions sampled from the snaking branches, we built a map of their dynamics spanning a range of Reynolds numbers from $Re \approx 175$ to $Re = 350$ and quantified by the dependence of the relaminarisation time on Re for each initial condition (Chapter 4). In region R1 adjacent to the snaking region, the initial conditions were found to exhibit clear oscillations whose number decreased as a distance from the right boundary of the snaking region was increased. These oscillations were already understood in the context of PO5 and predicted by the linear analysis in Chapter 3. For larger Reynolds numbers, wide initial conditions were shown to split into two spots whose width typically coincided with the width of the edge states. For certain windows in Re shaping regions R2 and R3, the spots formed after the splitting got activated exhibiting oscillations resembling those in region R1. The relaminarisation times in region R3 were characterised statistically for all initial conditions for which this region can be defined. For $Re \gtrsim 280$, we identified an eventual transition of our localised initial conditions to long-lasting turbulent dynamics framed by region R4. The dynamics within this region were characterised by measuring the averaged front speed for each simulation which exhibited a weak dependence on Re within the considered range of Reynolds numbers ($280 \lesssim Re < 350$) whose sign varied among different inital conditions. Additionally, the front speed averaged among all Re and initial conditions was found to be consistent with the study by Duguet *et al.* in a similar streamwise-confined domain [92]. For the sake of completeness, we also studied transition from the EQ_LOW solutions, related to the edge states, and identified that the “laminar” and “turbulent” sides of the unstable manifold of the edge state switched erratically as the Reynolds number was varied which presents a new knowledge in the context of the edge of chaos in plane Couette flow [27, 50, 51, 62, 63]. The whole study, described in Chapter 4 and summarised in paper [159], complements research works on exact localised solutions in plane Couette flow [64, 82, 87, 203] and links them to the dynamical phenomena well-known from statistically inclined studies, namely, self-sustained oscillations, splitting, spontaneous decay and front propagation [17, 30, 92, 130, 204].

One of the aspects of our study requiring additional attention is the problem of the splitting or, generally speaking, the decay of a group of rolls (clusters). Even though we managed to link the splitting phenomenon to the crossing of the stable manifold of a two-pulse state, it is still unclear how the decay of roll clusters can be predicted based on the flow observations and whether it is linked to the break-up of the self-sustained mechanism associated with the PO5 dynamics. Two problems associated with the roll decay may be of particular interest: (1) the initial splitting of wide states ($t \propto O(10^2)$) and its dependence on the Reynolds number and (2) spontaneous decay of roll clusters in long-lasting simulations in regions R3 and R4 (see figure 4.15). Both questions are directly related to the estimation of the average size of spots with large lifetimes which are known as turbulent bands [182, 204]. Manipulating the splitting in the presence of the small-amplitude wall oscillation, as discussed in Chapter 5, may also help understand this phenomenon. In addition, one may try to mimic this behaviour via low-order modelling: for example, given the oscillatory streak-roll dynamics, one could model the flow as a system of coupled identical oscillators and investigate the relevance of chimera states [205, 206] to this problem.

The presence of splitting in the very beginning of most of the simulations of sufficiently wide localised states and the clear dependence of the averaged front speed on the distance between two spots occuring after initial splitting of the initial condition (see Section 4.5) highlights an alternative way of studying transition to turbulence in spatially extended domains. One may try to construct two-pulse solutions from the edge states or their steady companions taken from EQ_LOW as the smallest localised solutions and then investigate transition to turbulence from the two-pulse solutions, where the spacing between the pulses may act as a parameter of the solution unrestricted to any discrete set.

Finally, the methodology, presented in Chapter 4 and based on using exact solutions and relaminarisation time curves, can readily be employed to study transition to turbulence in more realistic domains extended both in the spanwise and streamwise directions and, thus, allowing for the existence of doubly localised solutions [65, 82].

Control of dynamics of localised states

The map of dynamics presented in Chapter 4 and all the estimates associated with it constitute a detailed quantitative description of the transitional properties of spatially extended plane Couette flow and, consequently, can be used as a point of reference with respect to which different control strategies should be compared. We give a particular example of such a comparison in Chapter 5 where we imposed a classical control, in-phase spanwise wall oscillations, on the system and investigated how the relaminarisation time curves changed for two deliberately chosen localised initial conditions S5 and S13 as a function of the amplitude and, in certain cases, frequency of oscillations. Studying the homotopy from the uncontrolled system, when the amplitude is gradually increased from zero, we tracked the modifications of regions R1, R2, R3(a), their joining, manifesting as a single peak in t_{relam}, and disappearance for $A \lesssim 6 \times 10^{-2}$. We noted that for small amplitudes, wall oscillations tend to increase the relaminarisation time thus destabilising the system until the amplitude is increased beyond a certain threshold which is close to the value at which regions R1, R2 and R3(a) disappear. By Fourier-decomposing one of the long-lasting oscillatory solutions belonging to region R1, we described its dynamics in terms of the PO5 dynamics, typical for the uncontrolled system, and strengthening/weakening of the streaks caused by wall oscillations which, via a nonlinear feedback mechanism, may provoke relaminarisation or transition to long-lasting dynamics depending on the phase of oscillations. At the smallest considered amplitude, $A = 10^{-3}$, wall oscillations were shown to increase significantly t_{relam} within region R3. At the same time, wall oscillations were found to reduce the averaged front speed, as the amplitude is increased from 0, so that the front speed nearly vanishes at $A = 5 \times 10^{-2}$ for S5. We also provided a detailed account of the dependence and the delay of onset of transition to transition, i.e., the left boundary of region R4, on the amplitude and frequency which revealed two important facts: (1) the larger the amplitude, the further the onset of transition; (2) the optimal frequency, delaying the onset of transition, is likely to belong to the interval $[1/16; 1/8]$. The outcome of this study is twofold. First of all, it establishes the framework for the quantitative assessment of the efficiency of a chosen control strategy: using exact solutions as reproducible initial conditions, one can reproduce the associated relaminarisation time curves and compare the uncontrolled and controlled systems by means of an appropriate metrics (t_{incr}, c_{incr} or merely the expected relaminarisation times) accounting for the uncertainty in measuring Re. Secondly, the study presents the first attempt to assess the effect of wall oscillations on spatially localised states in plane Couette flow and thus extends the existing bulk of research devoted to this type of flow control [153, 154].

Since the homotopy was performed with respect to the amplitude, it is natural to suggest a similar study with the frequency as a homotopy parameter. It is particularly inspired by the fact that the dependences of the laminarisation probability in the small domain (figure 6.11) and the critical Reynolds number for S5 and S13 in the wide domain (figure 5.14) on the amplitude of wall oscillations are essentially monotonic for $A \gtrsim 0.1$ whereas they are concave with respect to the frequency. Alternatively, one could consider a homotopy from the uncontrolled system using again the amplitude as a parameter, but setting the wall frequency at that of PO5 which can be thought of as an internal frequency of the uncontrolled flow. Such a study would necessitate to consider the influence of the phase in more details than we did in Chapter 5. In any of these homotopy configurations, it would be of prime importance to understand how the control affects the decay of roll clusters and front growth.

The framework for control assessment suggested in Chapter 5 can also be used to study other modes of wall oscillations and, of course, other control strategies. For example, one could attempt controlling the flow by antiphase wall oscillations or the walls oscillated at independent frequencies: the corresponding time-periodic laminar solutions are presented in Appendix A.

In addition, the sensitivity of the flow to small-amplitude wall oscillations encourages to explore the link between noise-driven excitable systems [207] and shear flows. In particular, our observations of the sensitivity can be related to the phenomenon of stochastic resonance indeed taking placing in the presence of a weak periodic forcing [207, 208]. This looks especially promising given the remarkably close connection between transitional flows and excitable media highlighted by Barkley [129, 130, 209].

Probabilistic protocol

An alternative method for assessment of the transitional properties and the efficiency of control strategies aimed at suppressing or triggering transition to turbulence was introduced in Chapter 6. It is based on the calculation of the laminarisation probability $P_{lam}(E)$, i.e., the probability that a random finite-amplitude perturbation (RP) decays as a function of its kinetic energy. An RP was expressed as a linear combination of the laminar solution and a random component orthogonal to it. For both the uncontrolled and controlled (in-phase spanwise wall oscillations at $A = 0.3, \omega = 1/16$) small-domain systems, we then sampled 8000 RPs spread between 40 energy levels and, after time-integration, classified them as laminarising or transitioning. This allowed for the discrete approximation of the dependence of the laminarisation probability on the kinetic energy of perturbations which was shown to be well-fitted by a modified gamma function. By comparing the fitting for the uncontrolled system with that in the presence of control, we demonstrated that the chosen flow control makes transition to turbulence less likely and quantitatively assessed the control efficiency by means of the relative probability change. We also demonstrated that more conventional scalar metrics of the control efficiency, namely the energy of the minimal seed or of the edge state, may easily be misleading and suggest the failure of control. To explore the parameter space of this control strategy further and find optimal control configurations, we suggested an algorithm for the estimation of the laminarisation probability using only 10 RPs per energy level. Its accuracy was tested using extensive sub-samplings from two relatively large datasets with 8000 RPs in each. By estimating the laminarisation probability for a range of amplitudes and frequencies, we identified that the dependence of the control efficiency, assessed by the relative probability change, on the amplitude and frequency of wall oscillations exhibits the trends very similar to that of the onset of transition of S5 and S13 studied in Chapter 5. Namely, we found that the relative probability change inevitably grows as a function of the amplitude and almost always finds its maximum at frequency $\omega = 1/8$. This result establishes an important connection between the optimal flow configurations found in small (preventing localisation) and wide (allowing for localisation in one spatial direction) periodic domains. Overall, the described probabilistic protocol represents a new method for the assessment of the robustness of the laminar flow to finite-amplitude perturbations and allows for a comparison of the efficiency of control strategies which put him in competition with a more conventional approach based on the maximisation of the minimal seed energy [154, 189]. Owing to its simplicity and generality, the protocol can be expected to find applications in other nonlinear systems exhibiting finite-amplitude instability.

By giving the description of the probabilistic protocol in Chapter 6 and paper [160], we have barely scratched the surface of open questions related to the laminarisation probability. On the one side, given its interpretation as an approximation of the size of the basin of attraction, the laminarisation probability may be used to investigate the deformation of the basin of attraction in plane Couette flow as a function of the Reynolds number and, possibly, relate the associated scalings to the known scalings of the edge states [26], minimal perturbations [52, 210, 211] and exact coherent states [203] with respect to Re. On the other side, one could continue exploring how the laminarisation probability changes when various control strategies are employed [134]. A particularly exciting direction would be to build a connection between the concept of the laminarisation probability and flourishing machine-learning approaches for controlling fluid flows [212–214]. Additionally, the laminarisation probability could be used to verify the adequacy of reduced-order models of transitional flows [31–33, 36, 214, 215].

There is also a series of aspects in which the probabilistic protocol needs to be improved. The most important one regards designing the sampling procedure which could enable computing the laminarisation probability in large domains allowing for the localisation of flow states. The larger spatial scales in this case make the sampling we presented in Chapter 6 infeasible, but the results in Chapters 4 and 5 seem to suggest an attractive way for an economic sampling of random perturbations in large domains. Namely, they imply that transition to turbulence occurs from small spots even when an initial condition is a wide state filling most of the domain which means that one could sample spatially localised random perturbations of only small width. However, this will be a correct way only if the laminarisation probability associated with wide localised initial conditions is sufficiently small which requires additional research to be demonstrated. One could also explore the possibility of using an alternative decomposition of random perturbations, e.g., more relevant to the turbulent attractor or the external noise giving rise to these perturbations in the flow. Furthermore, the very classification of random perturbations into laminarising and transitioning ones becomes much more complicated in large domains due to the larger time-scale associated with transition to turbulence: $O(10^2)$ in a small domain versus at least $O(10^3)$ in a wide domain. To overcome this issue, one needs to predict whether an initial condition transitions based on its early time-evolution, perhaps, by means of data-driven approaches [214, 216].

It is also clear that our approach to the estimation of the laminarisation probability requires further developments. Our choice of the function $p(E)$, used to fit the dependence of the laminarisation probability on the energy of random perturbations, was primarily motivated by its algebraic properties and lacks the proper justification in terms of some assumptions related to the laminarisation probability. Since the value of P_{lam} at a particular energy level is determined by the highly complicated and fractal structure of the edge in plane Couette flow, we could gain some knowledge about the nature of these assumptions, which could lead to a different fitting function, by studying the laminarisation probability in simple low-dimensional dynamical systems exhibiting bistability. On the algorithmic side, the estimation procedure could be improved by turning to Bayesian inference which suits well for the case of sequential updates of data without a fixed sample size and naturally incorporates the uncertainty of the estimation parameters in contrast to the frequentist approach we used.

Appendix A

Derivation of the laminar solution in wall-oscillated plane Couette flow

Consider the Navier–Stokes equation (NSE)

$$\partial_t \boldsymbol{u} + (\boldsymbol{u} \cdot \nabla)\boldsymbol{u} = -\nabla p + \frac{1}{Re}\nabla^2 \boldsymbol{u}, \tag{A.1}$$

accompanied by the continuity equation

$$\nabla \cdot \boldsymbol{u} = 0, \tag{A.2}$$

and the following boundary conditions:

$$\boldsymbol{u}(x, y, z) = \boldsymbol{u}(x + \Gamma_x, y, z + \Gamma_z), \tag{A.3}$$

$$\boldsymbol{u}(x, \pm 1, z, t) = \begin{bmatrix} \pm 1 \\ 0 \\ \gamma_{\pm}(t) \end{bmatrix}, \tag{A.4}$$

where $\gamma_{\pm}(t) = A_{\pm} \sin(\omega_{\pm} t + \phi_{\pm})$ and $A_{\pm}, \omega_{\pm}, \phi_{\pm}$ are parameters of wall oscillations.

Consider a solution in the form of a periodic parallel flow:

$$\boldsymbol{u}(x, y, z, t) = [U(y), 0, W(y, t)]. \tag{A.5}$$

After expanding the vector form of NSE into its coordinate form and substituting the parallel base flow, we get

$$0 = -\partial_x p + \frac{1}{Re}\partial_{yy} U, \tag{A.6}$$

$$0 = -\partial_y p, \tag{A.7}$$

$$\partial_t W = -\partial_z p + \frac{1}{Re}\partial_{yy} W. \tag{A.8}$$

It is easy to see that

$$\partial_x p = \text{const}, \tag{A.9}$$

$$\partial_y p = 0, \tag{A.10}$$

$$\partial_z p = \text{const}. \tag{A.11}$$

Since we would like to extend a simple plane Couette flow, we choose $p = \text{const}$. As a result, we have

$$\partial_{yy} U = 0, \tag{A.12}$$

$$\partial_t W = \frac{1}{Re}\partial_{yy} W. \tag{A.13}$$

The equation for U yields the laminar solution for a plane Couette flow:

$$U(y) = y. \tag{A.14}$$

The equations for W corresponds to a diffusion equation with the following boundary conditions:

$$W(\pm 1, t) = \gamma_{\pm}(t). \tag{A.15}$$

It is known that the solution for a diffusion equation with homogeneous Dirichlet boundary conditions can be found via a Fourier series expansion (essentially, it reduces to an eigenvalue problem). To transform (A.13) and (A.15) into aforementioned form, we introduce a function

$$g(y,t) = W(y,t) - \gamma_-(t) - \frac{y+1}{2}\left[\gamma_+(t) - \gamma_-(t)\right]. \tag{A.16}$$

which has zero values on the boundaries. Substituting $W(y,t)$, expressed through $g(y,t)$, into (A.15) then yields an inhomogeneous diffusion equation

$$\partial_t g = \frac{1}{Re}\partial_{yy} g - \frac{d\gamma_-}{dt} - \frac{y+1}{2}\left[\frac{d\gamma_+}{dt} - \frac{d\gamma_-}{dt}\right], \tag{A.17}$$

accompanied by the homogeneous Dirichlet boundary conditions and the following initial condition:

$$g(y,0) = W(y,0) - \gamma_-(0) - \frac{y+1}{2}\left[\gamma_+(0) - \gamma_-(0)\right]. \tag{A.18}$$

First consider the homogeneous version of this equation:

$$\partial_t g - \frac{1}{Re}\partial_{yy} g = 0, \tag{A.19}$$

which can be solved by the separation of variables:

$$g(y,t) = \theta(t)\psi(y). \tag{A.20}$$

Substiution yields:

$$\frac{\dot{\theta}}{\theta} = \frac{1}{Re}\frac{\psi''}{\psi}, \tag{A.21}$$

where dot and prime denote the derivation with respect to time and space respectively. Since the left hand side is a function of t and the right hand side is a function of y, they both must be equal to the same constant λ. This gives two eigenvalues problems for θ and ψ:

$$\dot{\theta} = \lambda\theta, \tag{A.22}$$

$$\psi'' = Re\lambda\psi. \tag{A.23}$$

Consider the eigenvalue problem for the second equation. Given the homogeneous boundary conditions, we get the following eigenfunction:

$$\psi(y) = \sin\left(\sqrt{-Re\lambda}y\right), \tag{A.24}$$

where $\sqrt{-Re\lambda} = k\pi$, $k \in \mathbb{N}$. The eigenvalue is then:

$$\lambda = -\frac{k^2\pi^2}{Re}, k \in \mathbb{N}. \tag{A.25}$$

To incorporate inhomogeneity in (A.17), instead of direct solution for $\theta(t)$ we consider the following expansion for $g(y,t)$:

$$g(y,t) = \sum_{\substack{k=1,\\ k\in\mathbb{N}}}^{\infty} A_k(t)\sin(k\pi y), \tag{A.26}$$

and decompose the right hand side of (A.17) into the same eigenfunctions. Let $F(y,t)$ denote the right hand side of (A.17). Then we have:

$$F(y,t) = \sum_{\substack{k=1,\\ k\in\mathbb{N}}}^{\infty} F_k(t)\sin(k\pi y). \tag{A.27}$$

Using the property of orthogonality, we find $F_k(t)$:

$$\begin{aligned} F_k(t) &= \int_{-1}^{1} F(t,y)\sin(k\pi y)dy \\ &= \int_{-1}^{1}\left[-\frac{d\gamma_-}{dt} - \frac{y+1}{2}\left(\frac{d\gamma_+}{dt} - \frac{d\gamma_-}{dt}\right)\right]\sin(k\pi y)dy \\ &= \frac{(-1)^k}{2k\pi}\left(3\frac{d\gamma_+}{dt} + \frac{d\gamma_-}{dt}\right). \end{aligned} \tag{A.28}$$

Substituting (A.28) into (A.27) and then the latter and (A.26) into (A.17) gives:

$$\begin{aligned} &\sum_{\substack{k=1,\\ k\in\mathbb{N}}}^{\infty} \frac{dA_k}{dt}\sin(k\pi y) + \frac{1}{Re}\sum_{\substack{k=1,\\ k\in\mathbb{N}}}^{\infty} k^2\pi^2 A_k\sin(k\pi y) \\ &\qquad = \sum_{\substack{k=1,\\ k\in\mathbb{N}}}^{\infty} \frac{(-1)^k}{2k\pi}\left(3\frac{d\gamma_+}{dt} + \frac{d\gamma_-}{dt}\right)\sin(k\pi y). \end{aligned} \tag{A.29}$$

Collecting the terms at $\sin(k\pi y)$ yields the first-order ODE for $A_k(t)$:

$$\frac{dA_k}{dt} + \frac{k^2\pi^2}{Re}A_k = \frac{(-1)^k}{2k\pi}\left(3\frac{d\gamma_+}{dt} + \frac{d\gamma_-}{dt}\right). \tag{A.30}$$

or, with explicit expressions for $\gamma_\pm$:

$$\frac{dA_k}{dt} + \frac{k^2\pi^2}{Re}A_k = \frac{(-1)^k}{2k\pi}\left[3\omega_+ A_+ \cos(\omega_+ t + \phi_+) + \omega_- A_- \cos(\omega_- t + \phi_-)\right]. \tag{A.31}$$

It has the following general solution:

$$\begin{aligned} A_k = a_k e^{-\frac{k^2\pi^2}{Re}t} + a_{+,k}\sin(\omega_+ t + \phi_+) + b_{+,k}\cos(\omega_+ t + \phi_+) \\ + a_{-,k}\sin(\omega_- t + \phi_-) + b_{-,k}\cos(\omega_- t + \phi_-), \end{aligned} \tag{A.32}$$

where $a_k, a_{+,k}, b_{+,k}, a_{-,k}, b_{-,k}$ are constants to be chosen. Since we are looking for a laminar solution of the flow, it is valid to consider $t \to \infty$ where A_k tends to a time-periodic solution:

$$\begin{aligned} A_k \approx a_{+,k}\sin(\omega_+ t + \phi_+) + b_{+,k}\cos(\omega_+ t + \phi_+) \\ + a_{-,k}\sin(\omega_- t + \phi_-) + b_{-,k}\cos(\omega_- t + \phi_-). \end{aligned} \tag{A.33}$$

Therefore, for large enough t, $g(y,t)$ has a form:

$$\begin{aligned} g(y,t) \approx \left(\sum_{\substack{k=1,\\ k\in\mathbb{N}}}^{\infty} a_{+,k}\sin(k\pi y)\right)\sin(\omega_+ t + \phi_+) + \left(\sum_{\substack{k=1,\\ k\in\mathbb{N}}}^{\infty} b_{+,k}\sin(k\pi y)\right)\cos(\omega_+ t + \phi_+) \\ + \left(\sum_{\substack{k=1,\\ k\in\mathbb{N}}}^{\infty} a_{-,k}\sin(k\pi y)\right)\sin(\omega_- t + \phi_-) + \left(\sum_{\substack{k=1,\\ k\in\mathbb{N}}}^{\infty} b_{-,k}\sin(k\pi y)\right)\cos(\omega_- t + \phi_-). \end{aligned} \tag{A.34}$$

Working with infinite series seems to be complex, so instead we can look for the solution in the following form:

$$\begin{aligned} g(y,t) = a(y)\sin(\omega_+ t + \phi_+) + b(y)\cos(\omega_+ t + \phi_+) \\ + c(y)\sin(\omega_- t + \phi_-) + d(y)\cos(\omega_- t + \phi_-), \end{aligned} \tag{A.35}$$

where $a(y), b(y), c(y), d(y)$ are functions to be found by substituting this ansatz into (A.17).

A.1 In-phase oscillations

Consider the simplest case: $\gamma_+(t) = \gamma_-(t) = A\sin(\omega t + \phi)$. This gives the equation for $g(t, y)$:

$$\partial_t g = \frac{1}{Re}\partial_{yy} g - A\omega\cos(\omega t + \phi). \tag{A.36}$$

The solutions can be sought in the form

$$g(t, y) = a(y)\sin(\omega t + \phi) + b(y)\cos(\omega t + \phi), \tag{A.37}$$

where both $a(y)$ and $b(y)$ must satisfy homogeneous Dirichlet boundary conditions. Substitution yields:

$$\begin{aligned}&\omega a\cos(\omega t + \phi) - \omega b\sin(\omega t + \phi)\\ &\qquad = \frac{a''}{Re}\sin(\omega t + \phi) + \frac{b''}{Re}\cos(\omega t + \phi) - A\omega\cos(\omega t + \phi).\end{aligned} \tag{A.38}$$

Collecting terms at sin and cos gives:

$$-\omega b = \frac{a''}{Re}, \tag{A.39}$$

$$\omega a = \frac{b''}{Re} - A\omega, \tag{A.40}$$

which leads to

$$b = -\frac{a''}{\omega Re}, \tag{A.41}$$

$$a'''' + \omega^2 Re^2 a = -A\omega^2 Re^2. \tag{A.42}$$

Note that the boundary conditions for the fourth-order equation are:

$$a(-1) = a(1) = 0, \tag{A.43}$$

$$a''(-1) = a''(1) = 0, \tag{A.44}$$

where the last pair of boundary conditions follow from (A.41). Consider first the homogeneous equation for $a(y)$:

$$a'''' + \omega^2 Re^2 a = 0. \tag{A.45}$$

The characteristic equation, obtained by substitution $e^{\lambda y}$, $\lambda \in \mathbb{C}$, is then:

$$\lambda^4 + \omega^2 Re^2 = 0, \tag{A.46}$$

from which we have:

$$\lambda = \pm\sqrt{\pm i\omega Re}. \tag{A.47}$$

After simplifying $\sqrt{i}$ we get:

$$\lambda_1 = \Omega(1+i), \lambda_2 = \Omega(1-i), \lambda_3 = \Omega(-1+i), \lambda_4 = \Omega(-1-i), \tag{A.48}$$

where $\Omega = \sqrt{\frac{\omega Re}{2}}$. Therefore, the homogeneous solution is:

$$a^h(y) = \hat{a}_1 e^{\Omega(1+i)y} + \hat{a}_2 e^{\Omega(1-i)y} + \hat{a}_3 e^{\Omega(-1+i)y} + \hat{a}_4 e^{\Omega(-1-i)y}, \tag{A.49}$$

where $\hat{a}_1, \hat{a}_2, \hat{a}_3, \hat{a}_4 \in \mathbb{C}$. Now we need to guarantee that the solution is a real-valued function. Expand all the terms in the solution into real and imaginary parts:

$$\begin{aligned}
a^h(y) = &\operatorname{Re}(\hat{a}_1)e^{\Omega y}\cos\Omega y + i\operatorname{Re}(\hat{a}_1)e^{\Omega y}\sin\Omega y + \\
&\quad i\operatorname{Im}(\hat{a}_1)e^{\Omega y}\cos\Omega y - \operatorname{Im}(\hat{a}_1)e^{\Omega y}\sin\Omega y + \\
&\operatorname{Re}(\hat{a}_2)e^{\Omega y}\cos\Omega y - i\operatorname{Re}(\hat{a}_2)e^{\Omega y}\sin\Omega y + \\
&\quad i\operatorname{Im}(\hat{a}_2)e^{\Omega y}\cos\Omega y + \operatorname{Im}(\hat{a}_2)e^{\Omega y}\sin\Omega y + \\
&\operatorname{Re}(\hat{a}_3)e^{-\Omega y}\cos\Omega y + i\operatorname{Re}(\hat{a}_3)e^{-\Omega y}\sin\Omega y + \\
&\quad i\operatorname{Im}(\hat{a}_3)e^{-\Omega y}\cos\Omega y - \operatorname{Im}(\hat{a}_3)e^{-\Omega y}\sin\Omega y + \\
&\operatorname{Re}(\hat{a}_4)e^{-\Omega y}\cos\Omega y - i\operatorname{Re}(\hat{a}_4)e^{-\Omega y}\sin\Omega y + \\
&\quad i\operatorname{Im}(\hat{a}_4)e^{-\Omega y}\cos\Omega y + \operatorname{Im}(\hat{a}_4)e^{-\Omega y}\sin\Omega y.
\end{aligned} \tag{A.50}$$

The imaginary part of $a^h(y)$ must be zero:

$$\begin{aligned}
\operatorname{Im}(a^h(y)) = &\operatorname{Re}(\hat{a}_1)e^{\Omega y}\sin\Omega y + \operatorname{Im}(\hat{a}_1)e^{\Omega y}\cos\Omega y - \\
&\quad \operatorname{Re}(\hat{a}_2)e^{\Omega y}\sin\Omega y + \operatorname{Im}(\hat{a}_2)e^{\Omega y}\cos\Omega y + \\
&\operatorname{Re}(\hat{a}_3)e^{-\Omega y}\sin\Omega y + \operatorname{Im}(\hat{a}_3)e^{-\Omega y}\cos\Omega y - \\
&\quad \operatorname{Re}(\hat{a}_4)e^{-\Omega y}\sin\Omega y + \operatorname{Im}(\hat{a}_4)e^{-\Omega y}\cos\Omega y \\
= &0.
\end{aligned} \tag{A.51}$$

Then we have four conditions for the coefficients:

$$\operatorname{Re}(\hat{a}_1) = \operatorname{Re}(\hat{a}_2), \tag{A.52}$$

$$\operatorname{Im}(\hat{a}_1) = -\operatorname{Im}(\hat{a}_2), \tag{A.53}$$

$$\operatorname{Re}(\hat{a}_3) = \operatorname{Re}(\hat{a}_3), \tag{A.54}$$

$$\operatorname{Im}(\hat{a}_3) = -\operatorname{Im}(\hat{a}_3), \tag{A.55}$$

i.e. $\hat{a}_2^* = \hat{a}_1$ and $\hat{a}_4^* = \hat{a}_3$. Therefore, by defining $a_1 = 2\,\mathrm{Re}(\hat{a}_1), a_2 = -2\,\mathrm{Im}(\hat{a}_1), a_3 = 2\,\mathrm{Re}(\hat{a}_3), a_4 = -2\,\mathrm{Im}(\hat{a}_3)$, we get the homogeneous solution:

$$a^h(y) = a_1 e^{\Omega y}\cos(\Omega y) + a_2 e^{\Omega y}\sin(\Omega y) + a_3 e^{-\Omega y}\cos(\Omega y) + a_4 e^{-\Omega y}\sin(\Omega y), \tag{A.56}$$

where $a_1, a_2, a_3, a_4 \in \mathbb{R}$. It is trivial to show that the general solution is then:

$$a(y) = a_1 e^{\Omega y}\cos(\Omega y) + a_2 e^{\Omega y}\sin(\Omega y) + a_3 e^{-\Omega y}\cos(\Omega y) + a_4 e^{-\Omega y}\sin(\Omega y) - A, \tag{A.57}$$

To simplify upcoming algebra, we shift y by 1:

$$\begin{aligned} a(y) = a_1 e^{\Omega(y-1)}\cos\Omega(y-1) &+ a_2 e^{\Omega(y-1)}\sin\Omega(y-1) \\ &+ a_3 e^{-\Omega(y-1)}\cos\Omega(y-1) + a_4 e^{-\Omega(y-1)}\sin\Omega(y-1) - A. \end{aligned} \tag{A.58}$$

This transformation does not affect the basis of the solution and only modifies unknown coefficients. The general solution for $b(y)$ is:

$$\begin{aligned} b(y) = a_1 e^{\Omega(y-1)}\sin\Omega(y-1) &- a_2 e^{\Omega(y-1)}\cos\Omega(y-1) \\ &- a_3 e^{-\Omega(y-1)}\sin\Omega(y-1) + a_4 e^{-\Omega(y-1)}\cos\Omega(y-1). \end{aligned} \tag{A.59}$$

The boundary conditions $a(1) = b(1) = 0$ immediately give:

$$a_3 = A - a_1, \tag{A.60}$$

$$a_4 = a_2. \tag{A.61}$$

Then the boundary conditions $a(-1) = b(-1) = 0$ give the following system with respect to a_1 and a_2:

$$a_1 e^{-2\Omega}\cos 2\Omega - a_2 e^{-2\Omega}\sin 2\Omega + (A - a_1)e^{2\Omega}\cos 2\Omega - a_2 e^{2\Omega}\sin 2\Omega - A = 0, \tag{A.62}$$

$$-a_1 e^{-2\Omega}\sin 2\Omega - a_2 e^{-2\Omega}\cos 2\Omega + (A - a_1)e^{2\Omega}\sin 2\Omega + a_2 e^{2\Omega}\cos 2\Omega = 0. \tag{A.63}$$

Using the definitions of hyperbolic functions, we get:

$$\begin{bmatrix} 2\sinh 2\Omega\cos 2\Omega & 2\cosh 2\Omega\sin 2\Omega \\ 2\cosh 2\Omega\sin 2\Omega & -2\sinh 2\Omega\cos 2\Omega \end{bmatrix} \begin{bmatrix} a_1 \\ a_2 \end{bmatrix} = \begin{bmatrix} A\left(e^{2\Omega}\cos 2\Omega - 1\right) \\ Ae^{2\Omega}\sin 2\Omega \end{bmatrix} \tag{A.64}$$

The determinant is calculated as follows:

$$\begin{aligned} \Delta &= -4\sinh^2 2\Omega\cos^2 2\Omega - 4\cosh^2 2\Omega\sin^2 2\Omega \\ &= 4(\cos 2\Omega - \cosh 2\Omega)(\cos 2\Omega + \cosh 2\Omega). \end{aligned} \tag{A.65}$$

The solution for a_1 is:

$$\begin{aligned}
a_1 &= \frac{1}{\Delta}\begin{vmatrix} A\left(e^{2\Omega}\cos 2\Omega - 1\right) & 2\cosh 2\Omega \sin 2\Omega \\ Ae^{2\Omega}\sin 2\Omega & -2\sinh 2\Omega \cos 2\Omega \end{vmatrix} \\
&= \frac{-2A}{\Delta}\left(e^{2\Omega}\sinh 2\Omega \cos^2 2\Omega + e^{2\Omega}\cosh 2\Omega \sin^2 2\Omega - \sinh 2\Omega \cos 2\Omega\right) \\
&= \frac{-2A}{\Delta}\left(-\cos^2 2\Omega + \cosh^2 2\Omega + \sinh 2\Omega \cosh 2\Omega - \sinh 2\Omega \cos 2\Omega\right) \\
&= \frac{A\left(e^{2\Omega} + \cos 2\Omega\right)}{2(\cosh 2\Omega + \cos 2\Omega)}.
\end{aligned} \tag{A.66}$$

The solution for a_2 is:

$$\begin{aligned}
a_2 &= \frac{1}{\Delta}\begin{vmatrix} 2\sinh 2\Omega \cos 2\Omega & A\left(e^{2\Omega}\cos 2\Omega - 1\right) \\ 2\cosh 2\Omega \sin 2\Omega & Ae^{2\Omega}\sin 2\Omega \end{vmatrix} \\
&= \frac{A}{\Delta}\left(e^{2\Omega}\sinh 2\Omega \sin 4\Omega - e^{2\Omega}\cosh 2\Omega \sin 4\Omega + 2\cosh 2\Omega \sin 2\Omega\right) \\
&= \frac{A}{\Delta}\left(-2\sin 2\Omega \cos 2\Omega + 2\cosh 2\Omega \sin 2\Omega\right) \\
&= -\frac{A\sin 2\Omega}{2(\cosh 2\Omega + \cos 2\Omega)}.
\end{aligned} \tag{A.67}$$

By substituting the expressions for a_1 and a_2 into (A.58), we obtain the full expression for $a(y)$:

$$\begin{aligned}
a(y) = \frac{A}{2(\cosh 2\Omega + \cos 2\Omega)} \Big[&\left(e^{2\Omega} + \cos 2\Omega\right) e^{\Omega(y-1)} \cos \Omega(y-1) \\
&- \sin 2\Omega e^{\Omega(y-1)} \sin \Omega(y-1) + \Big(2\cos 2\Omega + 2\cosh 2\Omega - e^{2\Omega} \\
&- \cos 2\Omega\Big) e^{-\Omega(y-1)} \cos \Omega(y-1) \\
&- \sin 2\Omega e^{-\Omega(y-1)} \sin \Omega(y-1)\Big] - A.
\end{aligned} \tag{A.68}$$

After few simplifications, we have:

$$\begin{aligned}
a(y) = \frac{A}{\cosh 2\Omega + \cos 2\Omega} &\left[\cosh \Omega(y+1) \cos \Omega(y-1)\right. \\
&\left. + \cosh \Omega(y-1) \cos \Omega(y+1)\right] - A,
\end{aligned} \tag{A.69}$$

which immediately gives the expression for $b(y)$:

$$\begin{aligned}
b(y) = \frac{A}{\cosh 2\Omega + \cos 2\Omega} &\left[\sinh \Omega(y+1) \sin \Omega(y-1)\right. \\
&\left. + \sinh \Omega(y-1) \sin \Omega(y+1)\right].
\end{aligned} \tag{A.70}$$

It allows us to write down the expression for $g(y,t)$:

$$\begin{aligned}g(y,t) = \frac{A}{\cosh 2\Omega + \cos 2\Omega}\,&[[\cosh \Omega(y+1)\cos \Omega(y-1)\\ &+ \cosh \Omega(y-1)\cos \Omega(y+1)]\sin(\omega t + \phi)\\ &+ [\sinh \Omega(y+1)\sin \Omega(y-1) + \sinh \Omega(y-1)\sin \Omega(y+1)]\cos(\omega t+\phi)]\\ &- A\sin(\omega t+\phi), \end{aligned} \quad (A.71)$$

and then for $W(t,y)$:

$$\begin{aligned}W(t,y) = \frac{A}{\cosh 2\Omega + \cos 2\Omega}\,&[[\cosh \Omega(y+1)\cos \Omega(y-1)\\ &\cosh \Omega(y-1)\cos \Omega(y+1)]\sin(\omega t + \phi)\\ &+ [\sinh \Omega(y+1)\sin \Omega(y-1) + \sinh \Omega(y-1)\sin \Omega(y+1)]\cos(\omega t+\phi)]\,. \end{aligned} \quad (A.72)$$

A.2 Antiphase oscillations

Another important case is antiphase oscillations:

$$\gamma_+(t) = A\sin(\omega t + \phi) \quad (A.73)$$

$$\gamma_-(t) = A\sin(\omega t + \phi + \pi) = -A\sin(\omega t+\phi). \quad (A.74)$$

In this case, the equation for $g(t,y)$ is given by (A.17):

$$\partial_t g = \frac{1}{Re}\partial_{yy} g - y\omega A\cos(\omega t+\phi), \quad (A.75)$$

The solutions is sought in the form

$$g(t,y) = a(y)\sin(\omega t+\phi) + b(y)\cos(\omega t+\phi). \quad (A.76)$$

Since the derivation is similar to the in-phase oscillations, we only present the result:

$$\begin{aligned}a(y) &= \frac{A}{\cosh 2\Omega - \cos 2\Omega}[\cosh \Omega(y+1)\cos \Omega(y-1)\\ &\quad - \cosh \Omega(y-1)\cos \Omega(y+1)] - Ay, \end{aligned} \quad (A.77)$$

$$\begin{aligned}b(y) &= \frac{A}{\cosh 2\Omega - \cos 2\Omega}[\sinh \Omega(y+1)\sin \Omega(y-1)\\ &\quad - \sinh \Omega(y-1)\sin \Omega(y+1)]\,. \end{aligned} \quad (A.78)$$

which gives

$$\begin{aligned} W(t,y) = \frac{A}{\cosh 2\Omega - \cos 2\Omega} &\left[[\cosh \Omega(y+1) \cos \Omega(y-1) \right. \\ &- \cosh \Omega(y-1) \cos \Omega(y+1)] \sin(\omega t + \phi) \\ &\left. + [\sinh \Omega(y+1) \sin \Omega(y-1) - \sinh \Omega(y-1) \sin \Omega(y+1)] \cos(\omega t + \phi) \right], \end{aligned} \tag{A.79}$$

A.3 Oscillations with equal frequencies

The last exceptional case is the oscillations with equal frequencies:

$$\gamma_+(t) = A_+ \sin(\omega t + \phi_+), \tag{A.80}$$

$$\begin{aligned} \gamma_-(t) &= A_- \sin(\omega t + \phi_-) \\ &= A_- \cos(\phi_- - \phi_+) \sin(\omega t + \phi_+) + A_- \sin(\phi_- - \phi_+) \cos(\omega t + \phi_+). \end{aligned} \tag{A.81}$$

The solutions is sought in the form

$$g(t,y) = a(y) \sin(\omega t + \phi_+) + b(y) \cos(\omega t + \phi_+). \tag{A.82}$$

We only show the result. The constant coefficients are:

$$\begin{aligned} a_1 = \frac{2}{\Delta} &\left[\widetilde{A} \left(\cos^2 2\Omega - \sinh 2\Omega \cosh 2\Omega - \cosh^2 2\Omega \right) \right. \\ &\left. + A_- \cos(\phi_- - \phi_+) \sinh 2\Omega \cos 2\Omega - A_- \sin(\phi_- - \phi_+) \cosh 2\Omega \sin 2\Omega \right], \end{aligned} \tag{A.83}$$

$$\begin{aligned} a_2 = \frac{2}{\Delta} &\left(-\widetilde{A} \sin 2\Omega \cos 2\Omega + A_- \sin(\phi_- - \phi_+) \sinh 2\Omega \cos 2\Omega \right. \\ &\left. + A_- \cos(\phi_- - \phi_+) \cosh 2\Omega \sin 2\Omega \right), \end{aligned} \tag{A.84}$$

where $\widetilde{A} = A_+ + 2A_- \cos(\phi_- - \phi_+)$. The expression for $a(y)$ is:

$$\begin{aligned} a(y) = 2a_1 \sinh \Omega(y-1) \cos \Omega(y-1) &+ 2a_2 \cosh \Omega(y-1) \sin \Omega(y-1) \\ &+ \widetilde{A} e^{-\Omega(y-1)} \cos \Omega(y-1) - A_- \cos(\phi_- - \phi_+) \\ &- \frac{y+1}{2} [A_+ + A_- \cos(\phi_- - \phi_+)], \end{aligned} \tag{A.85}$$

The expression for $b(y)$ is:

$$\begin{aligned} b(y) = 2a_1 \cosh \Omega(y-1) \sin \Omega(y-1) &- 2a_2 \sinh \Omega(y-1) \cos \Omega(y-1) \\ &- \widetilde{A} e^{-\Omega(y-1)} \sin \Omega(y-1) - \frac{y-1}{2} A_- \sin(\phi_- - \phi_+). \end{aligned} \tag{A.86}$$

The expression for $W(y,t)$ is then:

$$\begin{aligned} W(y,t) = {} & [2a_1 \sinh \Omega(y-1) \cos \Omega(y-1) + 2a_2 \cosh \Omega(y-1) \sin \Omega(y-1) \\ & +\widetilde{A} e^{-\Omega(y-1)} \cos \Omega(y-1) - (y+1) A_- \cos(\phi_- - \phi_+) \big] \sin(\omega t + \phi_+) \\ & + [2a_1 \cosh \Omega(y-1) \sin \Omega(y-1) - 2a_2 \sinh \Omega(y-1) \cos \Omega(y-1) \\ & -\widetilde{A} e^{-\Omega(y-1)} \sin \Omega(y-1) - (y-1) A_- \sin(\phi_- - \phi_+) \big] \cos(\omega t + \phi_+). \end{aligned} \tag{A.87}$$

A.4 General case

After recovering the Rabin's solution, we can turn to the most general case, i.e.:

$$\gamma_+(t) = A_+ \sin(\omega_+ t + \phi_+) \tag{A.88}$$

$$\gamma_-(t) = A_- \sin(\omega_- t + \phi_-). \tag{A.89}$$

In this case, the equation for $g(t,y)$ is given by (A.17):

$$\partial_t g = \frac{1}{Re} \partial_{yy} g - \frac{d\gamma_-}{dt} - \frac{y+1}{2} \left[\frac{d\gamma_+}{dt} - \frac{d\gamma_-}{dt} \right], \tag{A.90}$$

and the solution is sought in the form of (A.35):

$$\begin{aligned} g(y,t) = {} & a(y) \sin(\omega_+ t + \phi_+) + b(y) \cos(\omega_+ t + \phi_+) \\ & + c(y) \sin(\omega_- t + \phi_-) + d(y) \cos(\omega_- t + \phi_-). \end{aligned} \tag{A.91}$$

Here all $a(y), b(y), c(y)$ and $d(y)$ must satisfy homogeneous Dirichlet boundary conditions since the set of functions $\{\sin(\omega_+ t + \phi_+), \cos(\omega_+ t + \phi_+), \sin(\omega_- t + \phi_-), \cos(\omega_- t + \phi_-)\}$ is linearly independent for distinct and non-zero $\omega_+, \omega_- \in \mathbb{R}$. Substitution yields:

$$\begin{aligned} & \omega_+ a \cos(\omega + t + \phi_+) - \omega_+ b \sin(\omega_+ t + \phi_+) + \omega_- a \cos(\omega - t + \phi_-) \\ & - \omega_- b \sin(\omega_- t + \phi_-) = \frac{1}{Re} \left[a'' \sin(\omega_+ t + \phi_+) + b'' \cos(\omega_+ t + \phi_+) \right. \\ & \left. + c'' \sin(\omega_- t + \phi_-) + d'' \cos(\omega_- t + \phi_-) \right] - \omega_- A_- \cos(\omega_- t + \phi_-) \\ & - \frac{y+1}{2} \left[\omega_+ A_+ \cos(\omega_+ t + \phi_+) - \omega_- A_- \cos(\omega_- t + \phi_-) \right]. \end{aligned} \tag{A.92}$$

Collecting terms at sin and cos gives a system of equations:

$$-\omega_+ b = \frac{1}{Re} a'', \tag{A.93}$$

$$\omega_+ a = \frac{1}{Re} b'' - \frac{y+1}{2}\omega_+ A_+, \tag{A.94}$$

$$-\omega_- d = \frac{1}{Re} c'', \tag{A.95}$$

$$\omega_- c = \frac{1}{Re} d'' - \omega_- A_- + \frac{y+1}{2}\omega_- A_-, \tag{A.96}$$

from which we get the following decoupling:

$$b = -\frac{1}{\omega_+ Re} a'', \tag{A.97}$$

$$a'''' + \omega_+^2 Re^2 a = -\frac{y+1}{2}\omega_+^2 Re^2 A_+, \tag{A.98}$$

$$d = -\frac{1}{\omega_- Re} c'', \tag{A.99}$$

$$c'''' + \omega_-^2 Re^2 c = \frac{y-1}{2}\omega_-^2 Re^2 A_-, \tag{A.100}$$

which allows us to solve only equations for a and c.

We start from the fourth-order differential equations for a and then, given the similarity of equations, quickly derive the result for c. It has the following boundary conditions (similar for c):

$$a(-1) = a(1) = 0, \tag{A.101}$$

$$a''(-1) = a''(1) = 0. \tag{A.102}$$

The general solution is

$$\begin{aligned} a(y) &= a_1 e^{\Omega_+(y-1)} \cos \Omega_+(y-1) + a_2 e^{\Omega_+(y-1)} \sin \Omega_+(y-1) \\ &\quad + a_3 e^{-\Omega_+(y-1)} \cos \Omega_+(y-1) + a_4 e^{-\Omega_+(y-1)} \sin \Omega_+(y-1) - \frac{A_+}{2}(y+1), \end{aligned} \tag{A.103}$$

where $\Omega_+ = \sqrt{\frac{\omega_+ Re}{2}}$. The solution for b is then:

$$\begin{aligned} b(y) &= a_1 e^{\Omega_+(y-1)} \sin \Omega_+(y-1) - a_2 e^{\Omega_+(y-1)} \cos \Omega_+(y-1) \\ &\quad - a_3 e^{-\Omega_+(y-1)} \sin \Omega_+(y-1) + a_4 e^{-\Omega_+(y-1)} \cos \Omega_+(y-1). \end{aligned} \tag{A.104}$$

Applying boundary conditions at $y = 1$ immediately gives $a_3 = A_+ - a_1$ and $a_4 = a_2$. Applying boundary conditions at $y = -1$ yields the following system of equations:

$$\begin{bmatrix} 2\sinh 2\Omega_+ \cos 2\Omega_+ & 2\cosh 2\Omega_+ \sin 2\Omega_+ \\ 2\cosh 2\Omega_+ \sin 2\Omega_+ & -2\sinh 2\Omega_+ \cos 2\Omega_+ \end{bmatrix} \begin{bmatrix} a_1 \\ a_2 \end{bmatrix} = \begin{bmatrix} A_+ e^{2\Omega_+} \cos 2\Omega_+ \\ A_+ e^{2\Omega_+} \sin 2\Omega_+ \end{bmatrix} \tag{A.105}$$

Note that it has the same matrix as in the case of in-phase oscillations and only right-hand side is different. The determinant is then calculated according to (A.65). The solutions for a_1 and a_2 are:

$$a_1 = \frac{2A_+}{\Delta_+}\left(\cos^2 2\Omega_+ - \sinh 2\Omega_+ \cosh 2\Omega_+ - \cosh^2 2\Omega_+\right), \tag{A.106}$$

$$a_2 = \frac{-2A_+}{\Delta_+}\sin 2\Omega_+ \cos 2\Omega_+. \tag{A.107}$$

In turn, the expression for $a(y)$ can be simplified:

$$\begin{aligned} a(y) = \frac{A_+}{\cosh^2 2\Omega_+ - \cos^2 2\Omega_+} & [\sin 2\Omega_+ \cosh \Omega_+(y-1) \sin \Omega_+(y+1) \\ & + \sinh 2\Omega_+ \sinh \Omega_+(y+1) \cos \Omega_+(y-1)] - \frac{A_+}{2}(y+1). \end{aligned} \tag{A.108}$$

Similarly for $b(y)$:

$$\begin{aligned} b(y) = \frac{A_+}{\cosh^2 2\Omega_+ - \cos^2 2\Omega_+} & [\sinh 2\Omega_+ \cosh \Omega_+(y+1) \sin \Omega_+(y-1) \\ & - \sin 2\Omega_+ \sinh \Omega_+(y-1) \cos \Omega_+(y+1)]. \end{aligned} \tag{A.109}$$

Now consider the general solution for $c(y)$:

$$\begin{aligned} c(y) = {} & c_1 e^{\Omega_-(y-1)} \cos \Omega_-(y-1) + c_2 e^{\Omega_-(y-1)} \sin \Omega_-(y-1) \\ & + c_3 e^{-\Omega_-(y-1)} \cos \Omega_-(y-1) + c_4 e^{-\Omega_-(y-1)} \sin \Omega_-(y-1) + \frac{A_-}{2}(y-1), \end{aligned} \tag{A.110}$$

where $\Omega_- = \sqrt{\frac{\omega_- Re}{2}}$. The solution for $d(y)$ is then:

$$\begin{aligned} d(y) = {} & c_1 e^{\Omega_-(y-1)} \sin \Omega_-(y-1) - c_2 e^{\Omega_-(y-1)} \cos \Omega_-(y-1) \\ & - c_3 e^{-\Omega_-(y-1)} \sin \Omega_-(y-1) + c_4 e^{-\Omega_-(y-1)} \cos \Omega_-(y-1). \end{aligned} \tag{A.111}$$

Applying boundary conditions at $y = 1$ immediately gives $c_3 = -c_1$ and $c_2 = c_4$. Applying boundary conditions at $y = -1$ yields the following system of equations:

$$\begin{bmatrix} 2\sinh 2\Omega_- \cos 2\Omega_- & 2\cosh 2\Omega_- \sin 2\Omega_- \\ 2\cosh 2\Omega_- \sin 2\Omega_- & -2\sinh 2\Omega_- \cos 2\Omega_- \end{bmatrix} \begin{bmatrix} c_1 \\ c_2 \end{bmatrix} = \begin{bmatrix} -A_- \\ 0 \end{bmatrix} \tag{A.112}$$

The solutions for c_1 and c_2 are:

$$c_1 = \frac{2A_-}{\Delta_-}\sinh 2\Omega_- \cos 2\Omega_-, \tag{A.113}$$

$$c_2 = \frac{2A_-}{\Delta_-}\cosh 2\Omega_- \sin 2\Omega_-. \tag{A.114}$$

The expression for $c(y)$ can be slightly simplified:

$$\begin{aligned} c(y) = \frac{A_-}{\cosh^2 2\Omega_- - \cos^2 2\Omega_-} & \left[-\sinh 2\Omega_- \cos 2\Omega_- \sinh \Omega_-(y-1) \cos \Omega_-(y-1)\right. \\ & \left. - \cosh 2\Omega_- \sin 2\Omega_- \cosh \Omega_-(y-1) \sin \Omega_-(y-1)\right] + \frac{A_-}{2}(y-1). \end{aligned} \tag{A.115}$$

Similarly for $d(y)$:

$$\begin{aligned} d(y) = \frac{A_-}{\cosh^2 2\Omega_- - \cos^2 2\Omega_-} & \left[-\sinh 2\Omega_- \cos 2\Omega_- \cosh \Omega_-(y-1) \sin \Omega_-(y-1)\right. \\ & \left. + \cosh 2\Omega_- \sin 2\Omega_- \sinh \Omega_-(y-1) \cos \Omega_-(y-1)\right]. \end{aligned} \tag{A.116}$$

As we derived all needed functions $a(y), b(y), c(y), d(y)$, we can write the expression for $W(y,t)$:

$$\begin{aligned} W(y,t) = \frac{A_+}{\cosh^2 2\Omega_+ - \cos^2 2\Omega_+} & \left[(\sin 2\Omega_+ \cosh \Omega_+(y-1) \sin \Omega_+(y+1)\right. \\ & + \sinh 2\Omega_+ \sinh \Omega_+(y+1) \cos \Omega_+(y-1)) \sin(\omega_+ t + \phi_+) \\ & + (\sinh 2\Omega_+ \cosh \Omega_+(y+1) \sin \Omega_+(y-1) \\ & \left. - \sin 2\Omega_+ \sinh \Omega_+(y-1) \cos \Omega_+(y+1)) \cos(\omega_+ t + \phi_+)\right] \\ + \frac{A_-}{\cosh^2 2\Omega_- - \cos^2 2\Omega_-} & \left[(-\sinh 2\Omega_- \cos 2\Omega_- \sinh \Omega_-(y-1) \cos \Omega_-(y-1)\right. \\ & - \cosh 2\Omega_- \sin 2\Omega_- \cosh \Omega_-(y-1) \sin \Omega_-(y-1)) \sin(\omega_- t + \phi_-) \\ & + (-\sinh 2\Omega_- \cos 2\Omega_- \cosh \Omega_-(y-1) \sin \Omega_-(y-1) \\ & \left. + \cosh 2\Omega_- \sin 2\Omega_- \sinh \Omega_-(y-1) \cos \Omega_-(y-1)) \cos(\omega_- t + \phi_-)\right]. \end{aligned} \tag{A.117}$$

Bibliography

[1] H. Kao, C. Beaume, and E. Knobloch. Spatial localization in heterogeneous systems. *Physical Review E*, 89(1):012903, 2014.

[2] J. Burke and E. Knobloch. Localized states in the generalized Swift–Hohenberg equation. *Physical Review E*, 73(5):056211, 2006.

[3] O. Reynolds. An experimental investigation of the circumstances which determine whether the motion of water shall he direct or sinuous, and of the law of resistance in parallel channels. *Philosophical Transactions of the Royal Society of London*, 174:935–982, 1884.

[4] P. J. Schmid and D. S. Henningson. *Stability and transition in shear flows*, volume 142. Springer-Verlag New York, Inc., 2001.

[5] L. D. Landau. On the problem of turbulence. In *Dokl. Akad. Nauk SSSR*, volume 44, pages 339–349, 1944.

[6] E. Hopf. A mathematical example displaying features of turbulence. *Communications on Pure and Applied Mathematics*, 1(4):303–322, 1948.

[7] S. Newhouse, D. Ruelle, and F. Takens. Occurrence of strange Axiom A attractors near quasi periodic flows on $t^m, m \geq 3$. *Communications in Mathematical Physics*, 64(1):35–40, 1978.

[8] M. J. Feigenbaum. The transition to aperiodic behavior in turbulent systems. *Communications in Mathematical Physics*, 77(1):65–86, 1980.

[9] A. Libchaber, C. Laroche, and S. Fauve. Period doubling cascade in mercury, a quantitative measurement. *Journal de Physique Lettres*, 43(7):211–216, 1982.

[10] T. Kreilos and B. Eckhardt. Periodic orbits near onset of chaos in plane Couette flow. *Chaos: An Interdisciplinary Journal of Nonlinear Science*, 22(4):047505, 2012.

[11] A. S. Everhardt, S. Damerio, J. A. Zorn, S. Zhou, N. Domingo, G. Catalan, E. K. H. Salje, L. Chen, and B. Noheda. Periodicity-doubling cascades: Direct observation in ferroelastic materials. *Physical Review Letters*, 123:087603, 2019.

[12] Y. Pomeau and P. Manneville. Intermittent transition to turbulence in dissipative dynamical systems. *Communications in Mathematical Physics*, 74(2):189–197, 1980.

[13] P. Bergé, M. Dubois, P. Manneville, and Y. Pomeau. Intermittency in Rayleigh-Bénard convection. *Journal de Physique Lettres*, 41(15):341–345, 1980.

[14] V. A. Romanov. Stability of plane-parallel Couette flow. *Functional analysis and its applications*, 7(2):137–146, 1973.

[15] A. Meseguer and L. N. Trefethen. Linearized pipe flow to Reynolds number 10^7. *Journal of Computational Physics*, 186:178–197, 2003.

[16] O. Dauchot and F. Daviaud. Streamwise vortices in plane Couette flow. *Physics of Fluids*, 7(5):901–903, 1995.

[17] K. Avila, D. Moxey, A. de Lozar, M. Avila, D. Barkley, and B. Hof. The onset of turbulence in pipe flow. *Science*, 333(6039):192–196, 2011.

[18] S. A. Orszag. Accurate solution of the Orr–Sommerfeld stability equation. *Journal of Fluid Mechanics*, 50:689–703, 1971.

[19] M. Sano and K. Tamai. A universal transition to turbulence in channel flow. *Nature Physics*, 12(3):249, 2016.

[20] P. Falsaperla, A. Giacobbe, and G. Mulone. Nonlinear stability results for plane Couette and Poiseuille flows. *Physical Review E*, 100(1):013113, 2019.

[21] K. M. Butler and B. F. Farrell. Three-dimensional optimal perturbations in viscous shear flow. *Physics of Fluids A: Fluid Dynamics*, 4(8):1637–1650, 1992.

[22] P. Cvitanovic, R. Artuso, R. Mainieri, G. Tanner, G. Vattay, N. Whelan, and A. Wirzba. *Chaos: Classical and Quantum.* Niels Bohr Inst., Copenhagen, 2016. URL `http://ChaosBook.org/`.

[23] F. Waleffe. Exact coherent structures in channel flow. *Journal of Fluid Mechanics*, 435:93–102, 2001.

[24] M. Nagata. Three-dimensional finite-amplitude solutions in plane Couette flow: bifurcation from infinity. *Journal of Fluid Mechanics*, 217:519–527, 1990.

[25] R. M. Clever and F. H. Busse. Three-dimensional convection in a horizontal fluid layer subjected to a constant shear. *Journal of Fluid Mechanics*, 234:511–527, 1992.

[26] J. Wang, J. Gibson, and F. Waleffe. Lower branch coherent states in shear flows: transition and control. *Physical Review Letters*, 98(20):204501, 2007.

[27] T. M. Schneider, J. F. Gibson, M. Lagha, F. De Lillo, and B. Eckhardt. Laminar-turbulent boundary in plane Couette flow. *Physical Review E*, 78(3):037301, 2008.

[28] J. M. Hamilton, J. Kim, and F. Waleffe. Regeneration mechanisms of near-wall turbulence structures. *Journal of Fluid Mechanics*, 287:317–348, 1995.

[29] J. Jiménez and P. Moin. The minimal flow unit in near-wall turbulence. *Journal of Fluid Mechanics*, 225:213–240, 1991.

[30] F. Waleffe. On a self-sustaining process in shear flows. *Physics of Fluids*, 9(4): 883–900, 1997.

[31] C. Beaume. A reduced model for exact coherent states in high Reynolds numbers shear flows. *Proc. Geophysical Fluid Dynamics Program (Woods Hole Oceanographic Institution)*, pages 389–412, 2012.

[32] C. Beaume, E. Knobloch, G. P. Chini, and K. Julien. Exact coherent structures in an asymptotically reduced description of parallel shear flows. *Fluid Dynamics Research*, 47(1):015504, 2014.

[33] M. Chantry, L. S. Tuckerman, and D. Barkley. Turbulent–laminar patterns in shear flows without walls. *Journal of Fluid Mechanics*, 791, 2016.

[34] F. Waleffe. Three-dimensional coherent states in plane shear flows. *Physical Review Letters*, 81(19):4140, 1998.

[35] F. Waleffe. Homotopy of exact coherent structures in plane shear flows. *Physics of Fluids*, 15(6):1517–1534, 2003.

[36] C. Beaume, E. Knobloch, G. P. Chini, and K. Julien. Modulated patterns in a reduced model of a transitional shear flow. *Physica Scripta*, 91(2):024003, 2016.

[37] A. Schmiegel. *Transition to turbulence in linearly stable shear flows.* PhD thesis, 1999.

[38] M. Nagata. Three-dimensional traveling-wave solutions in plane Couette flow. *Physical Review E*, 55(2):2023, 1997.

[39] J. F. Gibson, J. Halcrow, and P. Cvitanović. Equilibrium and travelling-wave solutions of plane Couette flow. *Journal of Fluid Mechanics*, 638:243–266, 2009.

[40] J. Halcrow, J. F. Gibson, P. Cvitanović, and D. Viswanath. Heteroclinic connections in plane Couette flow. *Journal of Fluid Mechanics*, 621:365–376, 2009.

[41] G. Kawahara, M. Uhlmann, and L. Van Veen. The significance of simple invariant solutions in turbulent flows. *Annual Review of Fluid Mechanics*, 44:203–225, 2012.

[42] G. Kawahara and S. Kida. Periodic motion embedded in plane Couette turbulence: regeneration cycle and burst. *Journal of Fluid Mechanics*, 449:291–300, 2001.

[43] D. Viswanath. Recurrent motions within plane Couette turbulence. *Journal of Fluid Mechanics*, 580:339–358, 2007.

[44] P. Cvitanović and J. F. Gibson. Geometry of the turbulence in wall-bounded shear flows: periodic orbits. *Physica Scripta*, 2010(T142):014007, 2010.

[45] G. J. Chandler and R. R. Kerswell. Invariant recurrent solutions embedded in a turbulent two-dimensional Kolmogorov flow. *Journal of Fluid Mechanics*, 722: 554–595, 2013.

[46] D. Lucas and R. R. Kerswell. Recurrent flow analysis in spatiotemporally chaotic 2-dimensional Kolmogorov flow. *Physics of Fluids*, 27(4):045106, 2015.

[47] A. Schmiegel and B. Eckhardt. Fractal stability border in plane Couette flow. *Physical Review Letters*, 79(26):5250, 1997.

[48] B. Hof, J. Westerweel, T. M. Schneider, and B. Eckhardt. Finite lifetime of turbulence in shear flows. *Nature*, 443(7107):59, 2006.

[49] B. Hof, A. de Lozar, D. J. Kuik, and J. Westerweel. Repeller or attractor? Selecting the dynamical model for the onset of turbulence in pipe flow. *Physical Review Letters*, 101(21):214501, 2008.

[50] J. D. Skufca, J. A. Yorke, and B. Eckhardt. Edge of chaos in a parallel shear flow. *Physical Review Letters*, 96(17):174101, 2006.

[51] M. Chantry and T. M. Schneider. Studying edge geometry in transiently turbulent shear flows. *Journal of Fluid Mechanics*, 747:506–517, 2014.

[52] T. M. Schneider, B. Eckhardt, and J. A. Yorke. Turbulence transition and the edge of chaos in pipe flow. *Physical Review Letters*, 99(3):034502, 2007.

[53] Y. Duguet, A. P. Willis, and R. R. Kerswell. Transition in pipe flow: the saddle structure on the boundary of turbulence. *Journal of Fluid Mechanics*, 613:255–274, 2008.

[54] N. B. Budanur and B. Hof. Complexity of the laminar-turbulent boundary in pipe flow. *Physical Review Fluids*, 3(5):054401, 2018.

[55] S. Cherubini, P. D. Palma, J. Robinet, and A. Bottaro. Edge states in a boundary layer. *Physics Of Fluids*, 23(5):051705, 2011.

[56] Y. Duguet, P. Schlatter, D. S. Henningson, and B. Eckhardt. Self-sustained localized structures in a boundary-layer flow. *Physical Review Letters*, 108(4):044501, 2012.

[57] T. Kreilos, G. Veble, T. M. Schneider, and B. Eckhardt. Edge states for the turbulence transition in the asymptotic suction boundary layer. *Journal of Fluid Mechanics*, 726:100–122, 2013.

[58] T. Khapko, T. Kreilos, P. Schlatter, Y. Duguet, B. Eckhardt, and D. S. Henningson. Localized edge states in the asymptotic suction boundary layer. *Journal of Fluid Mechanics*, 717, 2013.

[59] T. Khapko, T. Kreilos, P. Schlatter, Y. Duguet, B. Eckhardt, and D. S. Henningson. Edge states as mediators of bypass transition in boundary-layer flows. *Journal of Fluid Mechanics*, 801, 2016.

[60] T. Kreilos, T. Khapko, P. Schlatter, Y. Duguet, D. S. Henningson, and B. Eckhardt. Bypass transition and spot nucleation in boundary layers. *Physical Review Fluids*, 1(4):043602, 2016.

[61] F Mellibovsky, A. Meseguer, T. M. Schneider, and B. Eckhardt. Transition in localized pipe flow turbulence. *Physical Review Letters*, 103(5):054502, 2009.

[62] T. M. Schneider, D. Marinc, and B. Eckhardt. Localized edge states nucleate turbulence in extended plane Couette cells. *Journal of Fluid Mechanics*, 646: 441–451, 2010.

[63] Y. Duguet, P. Schlatter, and D. S. Henningson. Localized edge states in plane Couette flow. *Physics of Fluids*, 21(11):111701, 2009.

[64] T. M. Schneider, J. F. Gibson, and J. Burke. Snakes and ladders: localized solutions of plane Couette flow. *Physical Review Letters*, 104(10):104501, 2010.

[65] S. Zammert and B. Eckhardt. Streamwise and doubly-localised periodic orbits in plane Poiseuille flow. *Journal of Fluid Mechanics*, 761:348–359, 2014.

[66] A. Guseva, A. P. Willis, R. Hollerbach, and M. Avila. Transition to magnetorotational turbulence in Taylor–Couette flow with imposed azimuthal magnetic field. *New Journal of Physics*, 17(9):093018, 2015.

[67] L. Xi and X. Bai. Marginal turbulent state of viscoelastic fluids: A polymer drag reduction perspective. *Physical Review E*, 93(4):043118, 2016.

[68] P. R. Munoz, J. J. Barroso, A. C. Chian, and E. L. Rempel. Edge state and crisis in the Pierce diode. *Chaos: An Interdisciplinary Journal of Nonlinear Science*, 22(3):033120, 2012.

[69] B. F. McMillan, C. C. T. Pringle, and B. Teaca. Simple advecting structures and the edge of chaos in subcritical tokamak plasmas. *Journal of Plasma Physics*, 84 (6), 2018.

[70] V. Lucarini and T. Bódai. Edge states in the climate system: exploring global instabilities and critical transitions. *Nonlinearity*, 30(7):R32, 2017.

[71] G. Gallino, T. M. Schneider, and F. Gallaire. Edge states control droplet breakup in subcritical extensional flows. *Physical Review Fluids*, 3(7):073603, 2018.

[72] P. A. Cassak, J. F. Drake, M. A. Shay, and B. Eckhardt. Onset of fast magnetic reconnection. *Physical Review Letters*, 98(21):215001, 2007.

[73] T. Kreilos and T. M. Schneider. Fully localized post-buckling states of cylindrical shells under axial compression. *Proceedings of the Royal Society A: Mathematical, Physical and Engineering Sciences*, 473(2205):20170177, 2017.

[74] H. W. Emmons. The laminar-turbulent transition in a boundary layer - Part I. *Journal of the Aeronautical Sciences*, 18(7):490–498, 1951.

[75] A. Lundbladh and A. V. Johansson. Direct simulation of turbulent spots in plane Couette flow. *Journal of Fluid Mechanics*, 229:499–516, 1991.

[76] N. Tillmark and P. H. Alfredsson. Experiments on transition in plane Couette flow. *Journal of Fluid Mechanics*, 235:89–102, 1992.

[77] F. Daviaud, J. Hegseth, and P. Bergé. Subcritical transition to turbulence in plane Couette flow. *Physical Review Letters*, 69(17):2511, 1992.

[78] N. Tillmark. On the spreading mechanisms of a turbulent spot in plane Couette flow. *EPL (Europhysics Letters)*, 32(6):481, 1995.

[79] J. Schumacher and B. Eckhardt. Evolution of turbulent spots in a parallel shear flow. *Physical Review E*, 63(4):046307, 2001.

[80] M. Lagha and P. Manneville. Modeling of plane Couette flow. I. Large scale flow around turbulent spots. *Physics of Fluids*, 19(9):094105, 2007.

[81] Y. Duguet and P. Schlatter. Oblique laminar-turbulent interfaces in plane shear flows. *Physical Review Letters*, 110(3):034502, 2013.

[82] E. Brand and J. F. Gibson. A doubly localized equilibrium solution of plane Couette flow. *Journal of Fluid Mechanics*, 750, 2014.

[83] M. Couliou and R. Monchaux. Large-scale flows in transitional plane Couette flow: a key ingredient of the spot growth mechanism. *Physics of Fluids*, 27(3): 034101, 2015.

[84] M. Couliou and R. Monchaux. Growth dynamics of turbulent spots in plane Couette flow. *Journal of Fluid Mechanics*, 819:1–20, 2017.

[85] M. Couliou and R. Monchaux. Childhood of turbulent spots in a shear flow. *Physical Review Fluids*, 3(12):123901, 2018.

[86] Z. Wang, C. Guet, R. Monchaux, Y. Duguet, and B. Eckhardt. Quadrupolar flows around spots in internal shear flows. *Journal of Fluid Mechanics*, 892:A27, 2020.

[87] J. F. Gibson and T. M. Schneider. Homoclinic snaking in plane Couette flow: bending, skewing and finite-size effects. *Journal of Fluid Mechanics*, 794:530–551, 2016.

[88] E. Knobloch. Spatial localization in dissipative systems. *Annual Review of Condensed Matter Physics*, 6(1):325–359, 2015.

[89] J. Swift and P. C. Hohenberg. Hydrodynamic fluctuations at the convective instability. *Physical Review A*, 15(1):319, 1977.

[90] M. C. Cross and P. C. Hohenberg. Pattern formation outside of equilibrium. *Reviews of Modern Physics*, 65(3):851, 1993.

[91] P. D. Woods and A. R. Champneys. Heteroclinic tangles and homoclinic snaking in the unfolding of a degenerate reversible Hamiltonian–Hopf bifurcation. *Physica D*, 129:147–170, 1999.

[92] Y. Duguet, O. Le Maître, and P. Schlatter. Stochastic and deterministic motion of a laminar-turbulent front in a spanwisely extended Couette flow. *Physical Review E*, 84(6):066315, 2011.

[93] D. Olvera and R. R. Kerswell. Optimizing energy growth as a tool for finding exact coherent structures. *Physical Review Fluids*, 2:083902, 2017.

[94] O. Batiste, E. Knobloch, A. Alonso, and I. Mercader. Spatially localized binary-fluid convection. *Journal of Fluid Mechanics*, 560:149–158, 2006.

[95] A. Bergeon and E. Knobloch. Spatially localized states in natural doubly diffusive convection. *Physics of Fluids*, 20(3):034102, 2008.

[96] I. Mercader, O. Batiste, A. Alonso, and E. Knobloch. Convectons, anticonvectons and multiconvectons in binary fluid convection. *Journal of Fluid Mechanics*, 667: 586–606, 2011.

[97] C. Beaume, A. Bergeon, and E. Knobloch. Homoclinic snaking of localized states in doubly diffusive convection. *Physics of Fluids*, 23(9):094102, 2011.

[98] C. Beaume, A. Bergeon, and E. Knobloch. Convectons and secondary snaking in three-dimensional natural doubly diffusive convection. *Physics of Fluids*, 25(2): 024105, 2013.

[99] C. Beaume, A. Bergeon, and E. Knobloch. Three-dimensional doubly diffusive convectons: instability and transition to complex dynamics. *Journal of Fluid Mechanics*, 840:74–105, 2018.

[100] P. Assemat, A. Bergeon, and E. Knobloch. Spatially localized states in Marangoni convection in binary mixtures. *Fluid Dynamics Research*, 40(11-12):852, 2008.

[101] D. J. B. Lloyd, C. Gollwitzer, I. Rehberg, and R. Richter. Homoclinic snaking near the surface instability of a polarizable fluid. *Journal of Fluid Mechanics*, 783:283–305, 2015.

[102] G. W. Hunt, M. A. Peletier, A. R. Champneys, P. D. Woods, M. A. Wadee, C. J. Budd, and G. J. Lord. Cellular buckling in long structures. *Nonlinear Dynamics*, 21(1):3–29, 2000.

[103] M. A. Peletier. Sequential buckling: a variational analysis. *SIAM Journal on Mathematical Analysis*, 32(5):1142–1168, 2001.

[104] C. R. Laing, W. C. Troy, B. Gutkin, and G. B. Ermentrout. Multiple bumps in a neuronal model of working memory. *SIAM Journal on Applied Mathematics*, 63 (1):62–97, 2002.

[105] S. Coombes, G. J. Lord, and M. R. Owen. Waves and bumps in neuronal networks with axo-dendritic synaptic interactions. *Physica D: Nonlinear Phenomena*, 178 (3-4):219–241, 2003.

[106] G. Faye, J. Rankin, and P. Chossat. Localized states in an unbounded neural field equation with smooth firing rate function: a multi-parameter analysis. *Journal of Mathematical Biology*, 66(6):1303–1338, 2013.

[107] J. Rankin, D. Avitabile, J. Baladron, G. Faye, and D. J. B. Lloyd. Continuation of localized coherent structures in nonlocal neural field equations. *SIAM Journal on Scientific Computing*, 36(1):B70–B93, 2014.

[108] D. Avitabile and H. Schmidt. Snakes and ladders in an inhomogeneous neural field model. *Physica D: Nonlinear Phenomena*, 294:24–36, 2015.

[109] J. M. McSloy, W. J. Firth, G. K. Harkness, and G. Oppo. Computationally determined existence and stability of transverse structures. II. Multipeaked cavity solitons. *Physical Review E*, 66(4):046606, 2002.

[110] D. Gomila, A. J. Scroggie, and W. J. Firth. Bifurcation structure of dissipative solitons. *Physica D: Nonlinear Phenomena*, 227(1):70–77, 2007.

[111] A. Yochelis and A. Garfinkel. Front motion and localized states in an asymmetric bistable activator-inhibitor system with saturation. *Physical Review E*, 77:035204, 2008.

[112] D. J. B. Lloyd and H. O'Farrell. On localised hotspots of an urban crime model. *Physica D: Nonlinear Phenomena*, 253:23–39, 2013.

[113] P. Gandhi, Y. R. Zelnik, and E. Knobloch. Spatially localized structures in the Gray–Scott model. *Philosophical Transactions of the Royal Society A: Mathematical, Physical and Engineering Sciences*, 376(2135):20170375, 2018.

[114] N. Verschueren and A. Champneys. A model for cell polarization without mass conservation. *SIAM Journal on Applied Dynamical Systems*, 16(4):1797–1830, 2017.

[115] G. Bel, A. Hagberg, and E. Meron. Gradual regime shifts in spatially extended ecosystems. *Theoretical Ecology*, 5(4):591–604, 2012.

[116] Y. R. Zelnik, E. Meron, and G. Bel. Gradual regime shifts in fairy circles. *Proceedings of the National Academy of Sciences*, 112(40):12327–12331, 2015.

[117] Y. R. Zelnik, H. Uecker, U. Feudel, and E. Meron. Desertification by front propagation? *Journal of theoretical biology*, 418:27–35, 2017.

[118] Y. R. Zelnik, P. Gandhi, E. Knobloch, and E. Meron. Implications of tristability in pattern-forming ecosystems. *Chaos: An Interdisciplinary Journal of Nonlinear Science*, 28(3):033609, 2018.

[119] H. Faisst and B. Eckhardt. Sensitive dependence on initial conditions in transition to turbulence in pipe flow. *Journal of Fluid Mechanics*, 504:343–352, 2004.

[120] J. Peixinho and T. Mullin. Decay of turbulence in pipe flow. *Physical Review Letters*, 96(9):094501, 2006.

[121] A. P. Willis and R. R. Kerswell. Critical behavior in the relaminarization of localized turbulence in pipe flow. *Physical Review Letters*, 98(1):014501, 2007.

[122] M. Avila, A. P. Willis, and B. Hof. On the transient nature of localized pipe flow turbulence. *Journal of Fluid Mechanics*, 646:127–136, 2010.

[123] J. P. Crutchfield and K. Kaneko. Are attractors relevant to turbulence? *Physical Review Letters*, 60(26):2715, 1988.

[124] N. Goldenfeld, N. Guttenberg, and G. Gioia. Extreme fluctuations and the finite lifetime of the turbulent state. *Physical Review E*, 81(3):035304, 2010.

[125] D. Moxey and D. Barkley. Distinct large-scale turbulent-laminar states in transitional pipe flow. *Proceedings of the National Academy of Sciences*, 107(18): 8091–8096, 2010.

[126] L. Shi, M. Avila, and B. Hof. Scale invariance at the onset of turbulence in Couette flow. *Physical Review Letters*, 110(20):204502, 2013.

[127] Y. Pomeau. Front motion, metastability and subcritical bifurcations in hydrodynamics. *Physica D: Nonlinear Phenomena*, 23(1-3):3–11, 1986.

[128] M. Sipos and N. Goldenfeld. Directed percolation describes lifetime and growth of turbulent puffs and slugs. *Physical Review E*, 84(3):035304, 2011.

[129] D. Barkley. Simplifying the complexity of pipe flow. *Physical Review E*, 84(1): 016309, 2011.

[130] D. Barkley. Theoretical perspective on the route to turbulence in a pipe. *Journal of Fluid Mechanics*, 803:P1, 2016.

[131] H. Shih, T. Hsieh, and N. Goldenfeld. Ecological collapse and the emergence of travelling waves at the onset of shear turbulence. *Nature Physics*, 12(3):245, 2016.

[132] M. Chantry, L. S. Tuckerman, and D. Barkley. Universal continuous transition to turbulence in a planar shear flow. *Journal of Fluid Mechanics*, 824, 2017. doi: 10.1017/jfm.2017.405.

[133] D. Traphan, T. T. B. Wester, G. Gülker, J. Peinke, and P. G. Lind. Aerodynamics and percolation: Unfolding laminar separation bubble on airfoils. *Physical Review X*, 8(2):021015, 2018.

[134] K. R. Sreenivasan. Laminarescent, relaminarizing and retransitional flows. *Acta Mechanica*, 44(1-2):1–48, 1982.

[135] B. E. Launder. Laminarization of the turbulent boundary layer in a severe acceleration. *Journal of Applied Mechanics*, 31(4):707–708, 1964.

[136] R. Narasimha and K. R. Sreenivasan. Relaminarization in highly accelerated turbulent boundary layers. *Journal of Fluid Mechanics*, 61(3):417–447, 1973.

[137] V. J. Modi. Moving surface boundary-layer control: A review. *Journal of Fluids and Structures*, 11(6):627–663, 1997.

[138] P. J. Lefebvre and F. M. White. Experiments on transition to turbulence in a constant-acceleration pipe flow. *Transactions of the ASME Journal of Fluids Engineering*, 111(4):428–432, 1989.

[139] P. Corbett and A. Bottaro. Optimal perturbations for boundary layers subject to stream-wise pressure gradient. *Physics of Fluids*, 12(1):120–130, 2000.

[140] L. Sirovich and S. Karlsson. Turbulent drag reduction by passive mechanisms. *Nature*, 388(6644):753, 1997.

[141] K. Watanabe, Y. Udagawa, and H. Udagawa. Drag reduction of Newtonian fluid in a circular pipe with a highly water-repellent wall. *Journal of Fluid Mechanics*, 381:225–238, 1999.

[142] J. H. M. Fransson, A. Talamelli, L. Brandt, and C. Cossu. Delaying transition to turbulence by a passive mechanism. *Physical Review Letters*, 96(6):064501, 2006.

[143] J. Kim and T. R. Bewley. A linear systems approach to flow control. *Annual Review of Fluid Mechanics*, 39:383–417, 2007.

[144] S. Bagheri and D. S. Henningson. Transition delay using control theory. *Philosophical Transactions of the Royal Society A: Mathematical, Physical and Engineering Sciences*, 369(1940):1365–1381, 2011.

[145] M. Högberg, T. R. Bewley, and D. S. Henningson. Linear feedback control and estimation of transition in plane channel flow. *Journal of Fluid Mechanics*, 481: 149–175, 2003.

[146] A. S. Sharma, J. F. Morrison, B. J. McKeon, D. J. N. Limebeer, W. H. Koberg, and S. J. Sherwin. Relaminarisation of $Re_\tau = 100$ channel flow with globally stabilising linear feedback control. *Physics of Fluids*, 23(12):125105, 2011.

[147] Y. Du and G. E. Karniadakis. Suppressing wall turbulence by means of a transverse traveling wave. *Science*, 288(5469):1230–1234, 2000.

[148] R. Moarref and M. R. Jovanović. Controlling the onset of turbulence by streamwise travelling waves. Part 1. Receptivity analysis. *Journal of Fluid Mechanics*, 663:70–99, 2010.

[149] B. K. Lieu, R. Moarref, and M. R. Jovanović. Controlling the onset of turbulence by streamwise travelling waves. Part 2. Direct numerical simulation. *Journal of Fluid Mechanics*, 663:100–119, 2010.

[150] W. J. Jung, N. Mangiavacchi, and R. Akhavan. Suppression of turbulence in wall-bounded flows by high-frequency spanwise oscillations. *Physics of Fluids A: Fluid Dynamics*, 4(8):1605–1607, 1992.

[151] M. Quadrio, P. Ricco, and C. Viotti. Streamwise-travelling waves of spanwise wall velocity for turbulent drag reduction. *Journal of Fluid Mechanics*, 627:161–178, 2009.

[152] M. Quadrio and S. Sibilla. Numerical simulation of turbulent flow in a pipe oscillating around its axis. *Journal of Fluid Mechanics*, 424:217–241, 2000.

[153] M. Quadrio. Drag reduction in turbulent boundary layers by in-plane wall motion. *Philosophical Transactions of the Royal Society A: Mathematical, Physical and Engineering Sciences*, 369(1940):1428–1442, 2011.

[154] S. M. E. Rabin, C. P. Caulfield, and R. R. Kerswell. Designing a more nonlinearly stable laminar flow via boundary manipulation. *Journal of Fluid Mechanics*, 738, 2014.

[155] B. Hof, A. De Lozar, M. Avila, X. Tu, and T. M. Schneider. Eliminating turbulence in spatially intermittent flows. *Science*, 327(5972):1491–1494, 2010.

[156] J. Kühnen, D. Scarselli, M. Schaner, and B. Hof. Relaminarization by steady modification of the streamwise velocity profile in a pipe. *Flow, Turbulence and Combustion*, 100(4):919–943, 2018.

[157] J. Kühnen, B. Song, D. Scarselli, N. B. Budanur, M. Riedl, A. P. Willis, M. Avila, and B. Hof. Destabilizing turbulence in pipe flow. *Nature Physics*, 14(4):386, 2018.

[158] E. Marensi, A. P. Willis, and R. R. Kerswell. Stabilisation and drag reduction of pipe flows by flattening the base profile. *Journal of Fluid Mechanics*, 863: 850–875, 2019.

[159] A. Pershin, C. Beaume, and S. M. Tobias. Dynamics of spatially localized states in transitional plane Couette flow. *Journal of Fluid Mechanics*, 867:414–437, 2019.

[160] A. Pershin, C. Beaume, and S. M. Tobias. A probabilistic protocol for the assessment of transition and control. *Journal of Fluid Mechanics*, 895:A16, 2020.

[161] S. B. Pope. *Turbulent Flows*. Cambridge University Press, 2000.

[162] J. F. Gibson. Channelflow: A spectral Navier–Stokes simulator in C++. Technical report, U. New Hampshire, 2014. `Channelflow.org`.

[163] S. A. Orszag. Numerical simulation of incompressible flows within simple boundaries. I. Galerkin (spectral) representations. *Studies in Applied Mathematics*, 50 (4):293–327, 1971.

[164] T. A. Zang. On the rotation and skew-symmetric forms for incompressible flow simulations. *Applied Numerical Mathematics*, 7(1):27–40, 1991.

[165] C. Canuto, M. Y. Hussaini, A. Quarteroni, and A. Thomas Jr. *Spectral methods in fluid dynamics.* Springer-Verlag Berlin Heidelberg, 1988.

[166] L. Kleiser and U. Schumann. Treatment of incompressibility and boundary conditions in 3-D numerical spectral simulations of plane channel flows. In *Proceedings of the Third GAMM–Conference on Numerical Methods in Fluid Mechanics*, pages 165–173. Springer, 1980.

[167] P. J. Olver. *Applications of Lie groups to differential equations*, volume 107. Springer Science & Business Media, 2012.

[168] W. S. Edwards, L. S. Tuckerman, R. A. Friesner, and D. C. Sorensen. Krylov methods for the incompressible Navier–Stokes equations. *Journal of Computational Physics*, 110(1):82–102, 1994.

[169] L. N. Trefethen and D. Bau III. *Numerical linear algebra*, volume 50. SIAM, 1997.

[170] J. E. Dennis Jr and R. B. Schnabel. *Numerical methods for unconstrained optimization and nonlinear equations*, volume 16. SIAM, 1996.

[171] A. Bergeon, J. Burke, E. Knobloch, and I. Mercader. Eckhaus instability and homoclinic snaking. *Physical Review E*, 78:046201, 2008.

[172] C. R. Smith and S. P. Metzler. The characteristics of low-speed streaks in the near-wall region of a turbulent boundary layer. *Journal of Fluid Mechanics*, 129: 27–54, 1983.

[173] J. Kim, P. Moin, and R. Moser. Turbulence statistics in fully developed channel flow at low Reynolds number. *Journal of Fluid Mechanics*, 177:133–166, 1987.

[174] S. Bottin, O. Dauchot, and F. Daviaud. Intermittency in a locally forced plane Couette flow. *Physical Review Letters*, 79(22):4377, 1997.

[175] S. Bottin, O. Dauchot, F. Daviaud, and P. Manneville. Experimental evidence of streamwise vortices as finite amplitude solutions in transitional plane Couette flow. *Physics of Fluids*, 10(10):2597–2607, 1998.

[176] S. C. Reddy, P. J. Schmid, J. S. Baggett, and D. S. Henningson. On stability of streamwise streaks and transition thresholds in plane channel flows. *Journal of Fluid Mechanics*, 365:269–303, 1998.

[177] Y. Duguet, P. Schlatter, and D. S. Henningson. Formation of turbulent patterns near the onset of transition in plane Couette flow. *Journal of Fluid Mechanics*, 650:119–129, 2010.

[178] J. Rolland. Turbulent spot growth in plane Couette flow: statistical study and formation of spanwise vorticity. *Fluid Dynamics Research*, 46(1):015512, 2014.

[179] J. Burke and E. Knobloch. Homoclinic snaking: structure and stability. *Chaos: An Interdisciplinary Journal of Nonlinear Science*, 17(3):037102, 2007.

[180] T. Watanabe, M. Iima, and Y. Nishiura. A skeleton of collision dynamics: Hierarchical network structure among even-symmetric steady pulses in binary fluid convection. *SIAM Journal on Applied Dynamical Systems*, 15(2):789–806, 2016.

[181] J. Burke and J. H. P. Dawes. Localized states in an extended Swift–Hohenberg equation. *SIAM Journal on Applied Dynamical Systems*, 11(1):261–284, 2012.

[182] D. Barkley and L. S. Tuckerman. Turbulent-laminar patterns in plane Couette flow. In *IUTAM Symposium on Laminar-Turbulent Transition and Finite Amplitude Solutions*, pages 107–127. Springer, 2005.

[183] W. Fabian. *Turbulence and interactions – Exact coherent stuctures in turbulent shear flows.* Springer Berlin, Heidelberg, 2009.

[184] J. Philip and P. Manneville. From temporal to spatiotemporal dynamics in transitional plane Couette flow. *Physical Review E*, 83(3):036308, 2011.

[185] G. Lemoult, L. Shi, K. Avila, S. V. Jalikop, M. Avila, and B. Hof. Directed percolation phase transition to sustained turbulence in Couette flow. *Nature Physics*, 12(3):254–258, 2016.

[186] A. Schmiegel and B. Eckhardt. Persistent turbulence in annealed plane Couette flow. *EPL (Europhysics Letters)*, 51(4):395, 2000.

[187] I. G. Kevrekidis, B. Nicolaenko, and J. C. Scovel. Back in the saddle again: a computer assisted study of the Kuramoto–Sivashinsky equation. *SIAM Journal on Applied Mathematics*, 50(3):760–790, 1990.

[188] B. Suri, R. K. Pallantla, M. F. Schatz, and R. O. Grigoriev. Heteroclinic and homoclinic connections in a Kolmogorov-like flow. *Physical Review E*, 100(1): 013112, 2019.

[189] R. R. Kerswell. Nonlinear nonmodal stability theory. *Annual Review of Fluid Mechanics*, 50:319–345, 2018.

[190] P. J. Menck, J. Heitzig, N. Marwan, and J. Kurths. How basin stability complements the linear-stability paradigm. *Nature Physics*, 9(2):89–92, 2013.

[191] G. Casella and R. L. Berger. *Statistical inference*, volume 2. Duxbury Pacific Grove, CA, 2002.

[192] V. A. Sposito, M. L. Hand, and B. Skarpness. On the efficiency of using the sample kurtosis in selecting optimal l_p estimators. *Communications in Statistics-Simulation and Computation*, 12(3):265–272, 1983.

[193] R. Gonin and A. H. Money. Nonlinear l_p-norm estimation: part I - on the choice of the exponent, p, where the errors are additive. *Communications in Statistics-Theory and Methods*, 14(4):827–840, 1985.

[194] D. M. Bates and D. G. Watts. *Nonlinear regression analysis and its applications*, volume 2. Wiley New York, 1988.

[195] J. R. Donaldson and R. B. Schnabel. Computational experience with confidence regions and confidence intervals for nonlinear least squares. *Technometrics*, 29 (1):67–82, 1987.

[196] A. C. Davison and D. V. Hinkley. *Bootstrap methods and their application*, volume 1. Cambridge university press, 1997.

[197] M. Quadrio and P. Ricco. Critical assessment of turbulent drag reduction through spanwise wall oscillations. *Journal of Fluid Mechanics*, 521:251–271, 2004.

[198] R. R. Kerswell. Recent progress in understanding the transition to turbulence in a pipe. *Nonlinearity*, 18(6):R17, 2005.

[199] B. Eckhardt, T. M. Schneider, B. Hof, and J. Westerweel. Turbulence transition in pipe flow. *Annual Review of Fluid Mechanics*, 39:447–468, 2007.

[200] M. Avila, F. Mellibovsky, N. Roland, and B. Hof. Streamwise-localized solutions at the onset of turbulence in pipe flow. *Physical Review Letters*, 110(22):224502, 2013.

[201] J. Jiménez. Coherent structures in wall-bounded turbulence. *Journal of Fluid Mechanics*, 842, 2018.

[202] E. Makrides and B. Sandstede. Predicting the bifurcation structure of localized snaking patterns. *Physica D: Nonlinear Phenomena*, 268:59–78, 2014.

[203] J. F. Gibson and E. Brand. Spanwise-localized solutions of planar shear flows. *Journal of Fluid Mechanics*, 745:25–61, 2014.

[204] L. S. Tuckerman, M. Chantry, and D. Barkley. Patterns in wall-bounded shear flows. *Annual Review of Fluid Mechanics*, 52, 2020.

[205] D. M. Abrams and S. H. Strogatz. Chimera states for coupled oscillators. *Physical Review Letters*, 93(17):174102, 2004.

[206] M. Wolfrum and E. Omel'chenko. Chimera states are chaotic transients. *Physical Review E*, 84(1):015201, 2011.

[207] B. Lindner, J. Garcıa-Ojalvo, A. Neiman, and L. Schimansky-Geier. Effects of noise in excitable systems. *Physics Reports*, 392(6):321–424, 2004.

[208] V. Lucarini. Stochastic resonance for nonequilibrium systems. *Physical Review E*, 100(6):062124, 2019.

[209] D. Barkley, B. Song, V. Mukund, G. Lemoult, M. Avila, and B. Hof. The rise of fully turbulent flow. *Nature*, 526(7574):550–553, 2015.

[210] Y. Duguet, L. Brandt, and B. R. J. Larsson. Towards minimal perturbations in transitional plane Couette flow. *Physical Review E*, 82(2):026316, 2010.

[211] Y. Duguet, A. Monokrousos, L. Brandt, and D. S. Henningson. Minimal transition thresholds in plane Couette flow. *Physics of Fluids*, 25(8):084103, 2013.

[212] T. Duriez, S. L. Brunton, and B. R. Noack. *Machine learning control-taming nonlinear dynamics and turbulence*, volume 116. Springer, 2017.

[213] M. A. Bucci, O. Semeraro, A. Allauzen, G. Wisniewski, L. Cordier, and L. Mathelin. Control of chaotic systems by deep reinforcement learning. *Proceedings of the Royal Society A*, 475(2231):20190351, 2019.

[214] S. L. Brunton, B. R. Noack, and P. Koumoutsakos. Machine learning for fluid mechanics. *Annual Review of Fluid Mechanics*, 52:477–508, 2020.

[215] C. W. Rowley and S. T. M. Dawson. Model reduction for flow analysis and control. *Annual Review of Fluid Mechanics*, 49:387–417, 2017.

[216] J. N. Kutz, S. L. Brunton, B. W. Brunton, and J. L. Proctor. *Dynamic mode decomposition: data-driven modeling of complex systems*. SIAM, 2016.